



DOE Award No.: DE-FE0028973

OIL & GAS

**Final Project Scientific / Technical Report**  
**Advanced Simulation and Experiments of Strongly**  
**Coupled Geomechanics and Flow for Gas Hydrate**  
**Deposits: Validation and Field Application**  
**Project Period (10/01/2016 to 12/31/2019)**

Submitted by:  
PI: Dr. Jihoon Kim

*Jihoon Kim*

The Harold Vance Department of Petroleum Engineering,  
College of Engineering  
Texas A&M University  
501L Richardson Building  
3116 College Station TX, 77843-3136  
Email: jihoon.kim@tamu.edu  
Phone number: (979) 845-2205

Co-PI's:

Dr. I. Yucel Akkutlu, Texas A&M University (TAMU)  
Dr. Tim Kneafsey, Lawrence Berkeley National Laboratory (LBNL)  
Dr. Joo Yong Lee, Korea Institute of Geoscience and Mineral Resources (KIGAM)  
Dr. George J. Moridis, Lawrence Berkeley National Laboratory (LBNL)

Researchers: Jeremy Adams (TAMU), Dr. Tae Woong Ahn (KIGAM), Dr. Sharon Borglin (LBNL), Dr. Bin Wang (LBNL), Dr. Hyun Chul Yoon (TAMU), Sangcheol Yoon (TAMU) with courtesy contributions from Dr. Xuyang Guo (TAMU), Dr. John Killough (TAMU), Dr. Peng Zhou (TAMU)

Prepared for:  
United States Department of Energy  
National Energy Technology Laboratory

December 31, 2019



U.S. DEPARTMENT OF  
**ENERGY**

**NATIONAL ENERGY  
TECHNOLOGY LABORATORY**

**Office of Fossil Energy**

## **DISCLAIMER**

This report was prepared as an account of work sponsored by an agency of the United States Government. Neither the United States Government nor any agency thereof, nor any of their employees, makes any warranty, express or implied, or assumes any legal liability or responsibility for the accuracy, completeness, or usefulness of any information, apparatus, product, or process disclosed, or represents that its use would not infringe privately owned rights. Reference herein to any specific commercial product, process, or service by trade name, trademark, manufacturer, or otherwise does not necessarily constitute or imply its endorsement, recommendation, or favoring by the United States Government or any agency thereof. The views and opinions of authors expressed herein do not necessarily state or reflect those of the United States Government or any agency thereof.

# TABLE OF CONTENTS

	<u>Page</u>
DISCLAIMER .....	2
TABLE OF CONTENTS .....	3
ACCOMPLISHMENTS .....	4
Objectives of the project.....	4
Accomplished .....	4
Section 1 .....	6
Section 2 .....	24
Section 3 .....	52
Section 4 .....	96
Section 5 .....	135
Section 6 .....	163
PRODUCTS .....	165
REFERENCES.....	166

## ACCOMPLISHMENTS

### Objectives of the project

The objectives of the proposed research are (1) to investigate geomechanical responses induced by depressurization experimentally and numerically; (2) to enhance the current numerical simulation technology in order to simulate complex physically coupled processes by depressurization and (3) to perform in-depth numerical analyses of two selected potential production test sites: one based on the deposits observed at the Ulleung basin UBGH2-6 site; and the other based on well-characterized accumulations from the westend Prudhoe Bay. To these ends, the recipient will have the following specific objectives:

1). Information obtained from multi-scale experiments previously conducted at the recipient's research partner (the Korean Institute of Geoscience and Mineral Resources (KIGAM)) that were designed to represent the most promising known Ulleung Basin gas hydrate deposit as drilled at site UBGH2-6 will be evaluated (Task 2). These findings will be further tested by new experimental studies at Lawrence Berkeley National Laboratory (LBNL) and Texas A&M (TAMU) (Task 3) that are designed capture complex coupled physical processes between flow and geomechanics, such as sand production, capillarity, and formation of secondary hydrates. The findings of Tasks 2 and 3 will be used to further improve numerical codes.

2) Develop (in Tasks 4 through 6) an advanced coupled geomechanics and non-isothermal flow simulator (T+M<sup>AM</sup>) to account for large deformation and strong capillarity. This new code will be validated using data from the literature, from previous work by the project team, and with the results of the proposed experimental studies. The developed simulator will be applied to both Ulleung Basin and Prudhoe Bay sites, effectively addressing complex geomechanical and petrophysical changes induced by depressurization (e.g., frost-heave, strong capillarity, cryo-suction, induced fracturing, and dynamic permeability).

### Accomplished

We have completed the following tasks, as planned in the proposal. The names of researchers involved in a specific topic are also listed next to the title of the topic. We organize this final report by research topics while indicating the specific tasks that correspond to the topics.

Task 1: Project management and planning (Lead: Kim, J., Participants: Akkutlu, I.Y., Kneafsey, T., Lee, J.Y., Moridis, G.J.)

Task 2: Review and evaluation of experimental data of gas hydrate at various scales for gas production of Ulleung Basin (Lead: Lee, J.Y., Participants: Ahn, T.W., Kim, J., Yoon, H.C., Yoon, S.)

Subtask 2.1 Evaluation of Gas hydrate depressurization experiment of 1-m scale

Subtask 2.2 Evaluation of Gas hydrate depressurization experiment of 10-m scale

Subtask 2.3 Evaluation of Gas hydrate depressurization experiment of 1.5-m scale system in 3D

Subtask 2.4 Evaluation of gas hydrate production experiment of the centimeter-scale system

Task 3: Laboratory Experiments for Numerical Model Verification (Lead: Akkutlu, I.Y., Participants: Adams, J., Borglin, S., Kneafsey, T., Moridis, G.J., Wang, B.)

Subtask 3.1 Geomechanical changes from effective stress changes during dissociation

Subtask 3.2 Geomechanical changes from effective stress changes during dissociation – sand production

Subtask 3.3 Geomechanical changes resulting from secondary hydrate and capillary pressure changes

Subtask 3.4 Construction of the Relative Permeability Data in Presence of Hydrate

Subtask 3.5 Identification of Hysteresis in Hydrate Stability

Task 4: Incorporation of Laboratory Data into Numerical Simulation Model (Lead: Kim, J., Participants: All team members)

Subtask 4.1 Inputs and Preliminary Scoping Calculations

Subtask 4.2 Determination of New Constitutive Relationships

Subtask 4.3 Development of Geological Model

Task 5: Modeling of coupled flow and geomechanics in gas hydrate deposits (Lead: Kim, J., Participants: Ahn T.W., Guo, X., Killough, J., Lee, J.Y., Yoon, H.C., Yoon, S., Zhou, P.)

Subtask 5.1 Development of a coupled flow and geomechanics simulator for large deformation

Subtask 5.2 Validation with experimental tests of depressurization

Subtask 5.3 Modeling of sand production and plastic behavior

Subtask 5.4 Modeling of induced changes by formation of secondary hydrates: Frost-heave, strong capillarity, and induced fracturing

Subtasks 5.5 Field-scale simulation of PBU L106

Subtasks 5.6 Field-scale simulation of Ulleung Basin

Task 6: Simulation-Based Analysis of System Behavior at the Ignik-Sikumi and Ulleung Hydrate Deposits (Lead: Moridis, G.J., Participants: Kneafsey, T)

# 1. Experimental study of gas hydrate in various scales for gas production of Ulleung Basin (Task 2- Subtask 2.1, Subtask 2.2, Subtask 2.3, Subtask 2.4 by Ahn T.W., Kim, J., Lee, J.Y., Yoon, H.C., Yoon, S.)

## 1.1 Evaluation of gas hydrate production experiment of the centimeter-scale system (Subtask 2.4)

### 1.1.1 Introduction

For subtask 2.4, we revisited the experimental study on core-scale permeability measurements according to hydrate saturations, in order to make use of numerical simulation. In the experiment, we took specimens, choosing artificial samples and measuring porosity, of 98% SiO<sub>2</sub> of HAMA#5, 6, 7, 8 (grain density=2.68g/cm<sup>3</sup>, mean particle size 106~774 μm. Porosity of HAMA #5, 6, and 8 ranges from 0.39 to 0.40, while that of HAMA #7 is 0.43. We measured permeability with different hydrate saturation, ranging from 0.05 to 0.2 and pre-processed the data for numerical simulation

### 1.1.2 Experimental setups

#### 1.1.2.1 Specimens

Four different artificial sands (Hama #5, 6, 7, and 8) were used for the experiments. More than 98% of the sands are SiO<sub>2</sub> according to the XRF analyses. The grain density of sands were about 2.69g/cm<sup>3</sup>, according to the pycnometer measurements. The grain size distributions of four sands, measured by the laser diffraction particle analyzer are shown in Fig. 1.1 The mean particle sizes vary from 106 to 774 μm. The specimens were packed in cells with water pluviation methods in a vibrator. The initial porosity after specimens packing ranges from 0.39 to 0.43.

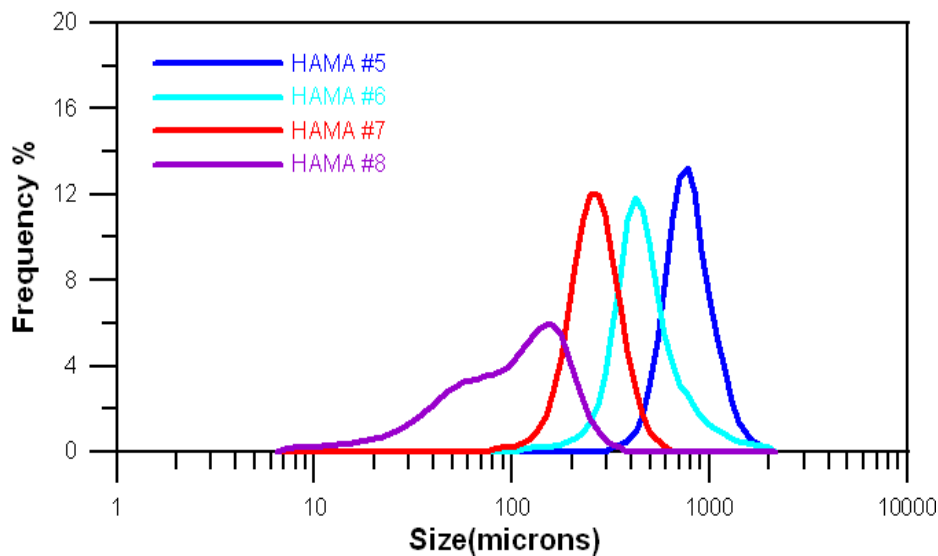


Fig. 1.1 Particle size distribution of the four sands (KIGAM 2007)

### 1.1.2.2 Experimental settings

A permeability measurement system that can maintain low temperature and high pressure for hydrate specimen were established. The system has four pressure vessels so that four experiments can be performed simultaneously. The system is largely comprised of four units: pressure vessels, the data acquisition unit, the flow and pressure control unit, and the temperature control unit (Fig. 1.2).

The working pressure of the pressure vessel is 3500 psia, and the inner dimension of the vessel is 2.54cm in diameter and 30cm in length. A cooling jacket is attached outside of each vessel and the temperatures of the pressure vessels were maintained by circulating fluid in the cooling jacket with refrigerating bath circulator.

The data acquisition unit has absolute pressure transducers that measure pressures from the top and bottom of a specimen, differential pressure transducers that measure differential pressures between the top and bottom of a specimen, and mass flow meters that measure the volume of the produced gas.

The flow and pressure control unit has mass flow controllers for controlled injection of gases, and a reciprocating pump for controlled water injections. The maximum flow rate for the mass flow controller is 1600sccm, and that of the reciprocating pump is 10ml/min.

The temperature control unit has refrigerating bath circulators connected to cooling jackets of pressure vessels.

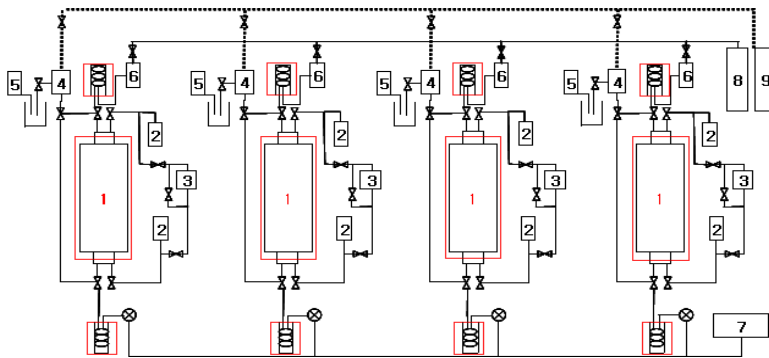




**Fig. 1.2 Permeability measurement system of hydrate-bearing sediments (1. Sand column 2. Heise Transducer, 3. Differential Pressure Transducer, 4. Back Pressure Regulator, 5. Mass Flow Meter, 6. Mass Flow Controller, 7. Reciprocating Pump, 8. CH<sub>4</sub> Cylinder, 9. Syringe Pump, 10. Displacement gauge, Red Rectangles: Temperature controlled unit) (KIGAM 2007)**

### **1.1.2.3 Experimental procedures**

After packing a specimen and assemble a pressure vessel, the temperature of a specimen was equilibrated at 11°C. The absolute water permeability of a specimen was measured by injecting water at several stages of flow rates. Methane gas was injected to a pre-determined initial water saturation and the specimen was pressurized with methane gas to about 700 psia. The temperature was lowered to 1°C to form hydrates in the specimen. Re-pressurizing the specimen with methane gas and forming hydrates were repeated until the pre-determined hydrate saturation was reached. After hydrate formation, effective permeability of methane gas was measured at several stages of flow rates. The permeability measurements were repeated four times per a specimen. After the effective permeability measurements, the hydrates in the specimens were dissociated by depressurization.

### **1.1.3 Results**

The permeability as a function of hydrate saturation is plotted in Fig. 1.3 The permeability differences in same type of sand specimens with similar hydrate saturations could have been induced from heterogeneous character of hydrate formation in specimens. The effective permeability of methane gas in hydrate-bearing sediments tends to decrease with the increase of hydrate saturations and the decrease of mean grain sizes of specimens.

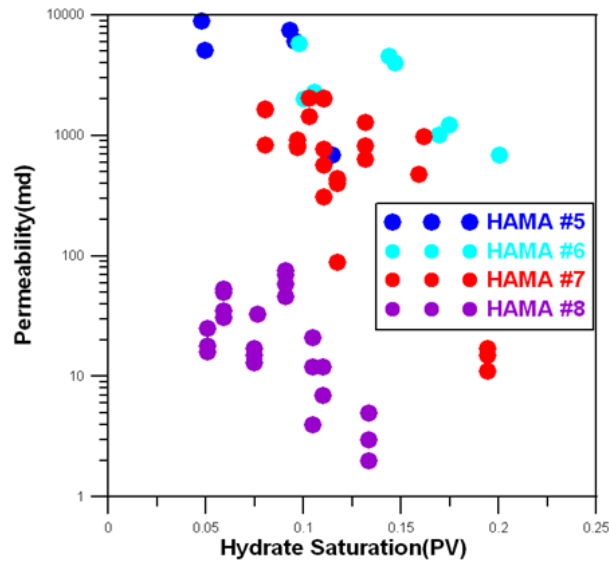


**Fig. 1.3 Permeability versus hydrate saturation (KIGAM 2007)**

## 1.2 Depressurization of 1m scale in 1D (Subtask 2.1)

### 1.2.1 Introduction

The experimental apparatus for the production test of gas hydrate (GH) have been used in cm-scale, typically. The cm-scale apparatus have limitations, such as the difficulty in getting an accurate production efficiency of GH on the variation of GH saturation due to the small quantity of in-situ GH in a specimen, difficulty of measuring propagation velocity of driving forces for GH production due to the short propagation distance of specimens, and difficulty of optical observation of specimen deformation and flow pattern in production well.

To overcome the limitations in cm-scale experimental apparatus, we developed meter-scale high pressure cell, and the system includes fluid/pressure control system, data acquisition system, temperature control system, and production control system to simulate GH production in sediment specimens. The cell can simulate flow phenomena during production only in uni-direction. In this study, we packed sediment sample into the meter-scale pressure cell. The packed sediments consisted of alternate layers of clay-sand-clay representing the layering system in the Ulleung Basin geological structure. After forming GH, we investigated the production behavior of hydrate-bearing alternate layers of sand and mud under depressurization process.

### 1.2.2 Experimental setup

#### 1.2.2.1 Apparatus

The meter scale GH production system is composed of 4 major modules, which are meterscale high pressure cell, fluid control unit, data acquisition unit, and temperature control unit. Fig. 1.4 shows a picture of the system modules. The meter-scale high pressure cell made of 316 stainless steel was constructed with the working pressure of 20 MPa in order to simulate a hydrate reservoir. The dimensions of sediment specimens are 10 cm of the diameter and 100 cm of the length. Two K-type thermocouples

for the temperature measurement at inlet and outlet and three K-Type multi-thermocouples for the internal temperature measurement of the specimen. Eleven Heise transducers and custom-made electrodes are equipped in every 10cm from the top end piece to the bottom for pressure and resistance measurements, respectively. Also, CCD cameras to visually monitor the surface of the specimen and 10  $\mu\text{m}$  pore-sized filters to prevent intrusion of the soil particles into the flow line were installed at the upper and the lower end-caps.

In injection module, two syringe pumps were used to inject water into the specimen and to control system pressure by dome-type back pressure regulator. Mass flow controllers were used to inject methane gas into the system. A wet test meter and a balance were used for the calculation of gas and water saturation change, respectively. We developed data acquisition module to control injection module and acquire the data including picture or videos of the sediment change using LabVIEW in real time, during the whole sequence of experiments. The temperature of the most part of the system, especially the high pressure cell, was controlled using heat convection oven. The remaining parts related with fluid flows were insulated and their temperatures were controlled by circulating coolants. Heat exchanger was installed to prevent hydrate reformation in pipes outside of the cell, especially often occurred in back pressure regulator due to Joule-Thompson effect.



**Fig. 1.4** Picture of the experimental setup for 1D 1-m scale GH production (KIGAM 2011)

### **1.2.2.2 Procedure**

#### **Sediment specimen preparation**

We used artificial sand that mimic the grain size distribution of sandy layers found in the Ulleung Basin, East Sea, Korea. The dry sand-grains were slowly poured into the vibrated high pressure cell filled with water. After compaction, porosity and absolute permeability of the sand specimen saturated with water were measured. To establish initial water saturation, we injected methane gas into the specimen with

constant flow rate. To minimize water flow in the specimens, methane injection rate was increased up to the highest flowing rate expected during production test. The system temperature was maintained at around 11°C.

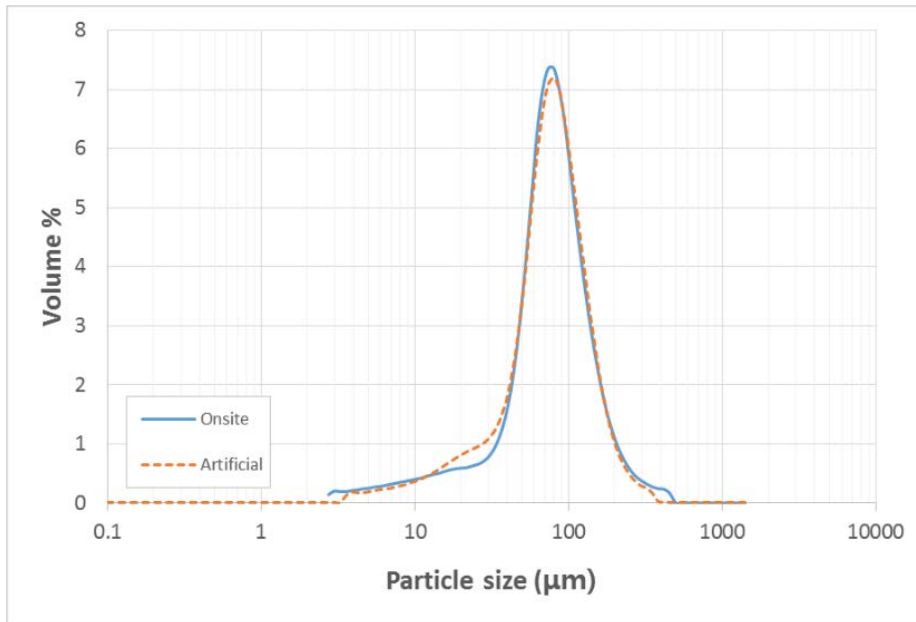


**Fig. 1.5 Particle size distributions of onsite (Ulleung Basin) and artificial samples (KIGAM 2011)**

### **Gas hydrate formation**

Methane hydrate was formed at the initial water saturation from the specimen preparation step as following orders; pressurizing the cell by injecting methane, and cooled down system temperature from 11 to 2°C. An abrupt decrease in the fluid pressure indicated the hydrate formation.

### **Depressurization**

The depressurization method was applied at the hydrate-bearing specimen to check the validity and applicability of the system. By controlling back pressure regulator, the fluid pressure of the cell was decreased from the stabilized pressure during GH formation to designated pressure, which is lower than equilibrium pressure at 2°C. The pressure, temperature, the volume of produced water and dissociated methane, and images of upper and lower specimen surfaces were recorded throughout the test.

### **1.2.3 Results and discussion**

After GH formation, three depressurization tests were conducted by decreasing system pressure down to 10, 20, and 30% against the equilibrium pressure of methane hydrate at constant temperature condition. Among the various results, we introduce production pattern and deformation of the specimen results from the three tests.

### **Production pattern**

Fig. 1.6 illustrated the cumulative methane production of three test cases (DP 10, DP 20, and DP 30%). In this figure, methane production was normalized to initial methane content in the cell. At all cases, normalized final gas production reach around 80% after the dissociation of GH. In this experiment, the effect of depressurization level was insignificant on the final gas production volume. After reaching 80% gas recovery, the system pressure was lowered to ambient condition, and gas recovery from 80% to 99% was obtained by producing remained free gas in the cell. Elapsed times to reach 80% gas recovery were compared in Fig. 1.6. The time of DP 20 was decreased drastically compared with that of DP 10 and the time difference between DP 20 and DP 30 was not significant. As expected, consumed time for the reaching final gas production shows exponential decrease pattern with increasing the level of depressurization.

In this preliminary study, we could not observe hydrate reformation phenomena unlike the results (not included in this article) of depressurization method applied with similar test condition in the cm-scale apparatus. Because the hydrate reformation can cause severe reduction of production efficiency, it should be avoided or minimized in designing production method. [1, 2, 3]

However this might be different in case of field condition, such that the fluid system in the pore is composed of hydrate and water only and heat sources for the depressurization is limited.

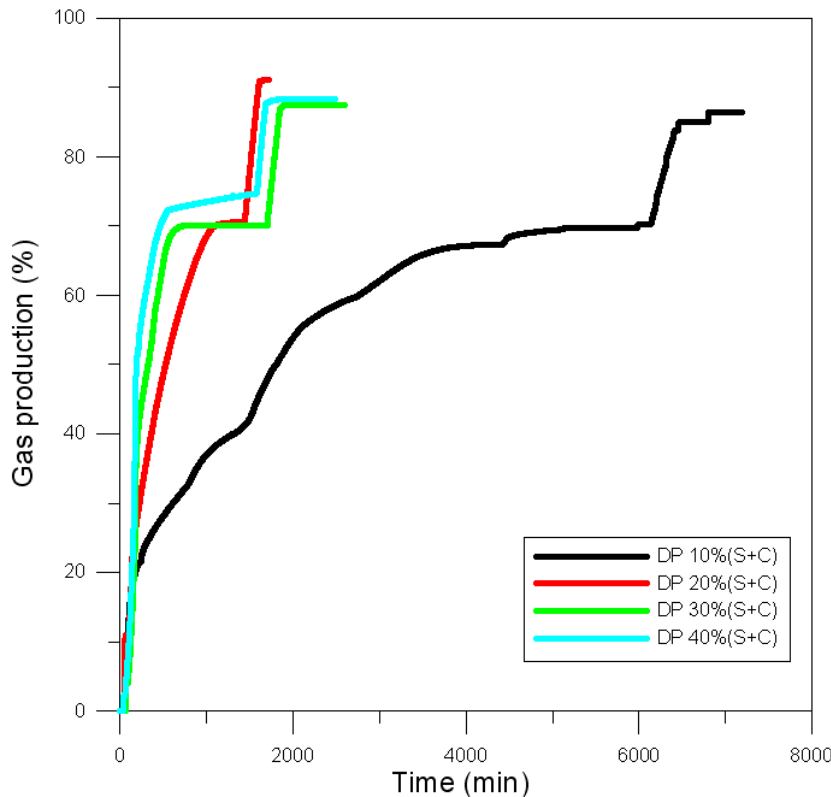


**Fig. 1.6 Cumulative production profiles at four different depressurization cases (KIGAM 2011)**

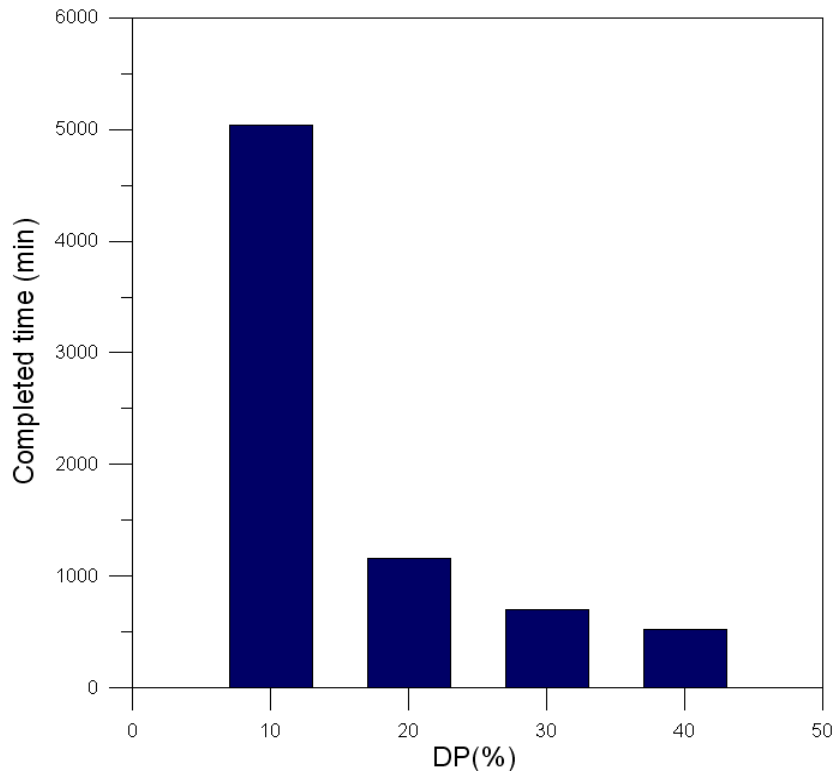


**Fig. 1.7 Time to reach 70% gas recovery at four different depressurization cases (KIGAM 2011)**

### **1.3 Depressurization of 10-m scale in 1D (Subtask 2.2)**

#### **1.3.1 Introduction**

In this study, a 10 meter-scale apparatus was developed to simulate the depressurization-induced gas hydrate production of a field-scale reservoir. We investigate the gas production behavior from the viewpoint of the dominating factor by observing the pressure, temperature, and gas production over time in the depressurizing process.

The 10 meter-scale apparatus is composed of four major modules, which are tube reactor, fluid control unit, data acquisition unit, and temperature control unit. Fig. 1.8 presents a schematic diagram of the experimental apparatus.

#### **1.3.2 Experimental setup**

##### **1.3.2.1 Apparatus**

The tube reactor in which the unconsolidated sedimentary sample is located is sequentially combined with six steel tubes of 2 m long. The dimensions of the sediment sample are 1.67 cm of the diameter and 13.3 m of the length. Seven K-type thermocouples (from T\_1 to T\_7) and seven pressure transducers (from P\_1 to P\_7) for the internal temperature and pressure measurement, respectively, of the sample are equipped at regular intervals in the tube reactor. Each tube is modularized to easily expand the scale of the sample. In the injection module, two syringe pumps were used to inject water into the sample and to

control system pressure using a dome-type back pressure regulator. Mass flow controllers were used to inject methane gas into the system. A wet test meter and a balance were used for the calculation of gas and water saturation change, respectively. We developed a data acquisition module to control the injection module and acquire the data using LabVIEW in real time, during the whole sequence of experiments. The temperature of the sample was controlled by circulating coolants through the outer space of the tube reactor.

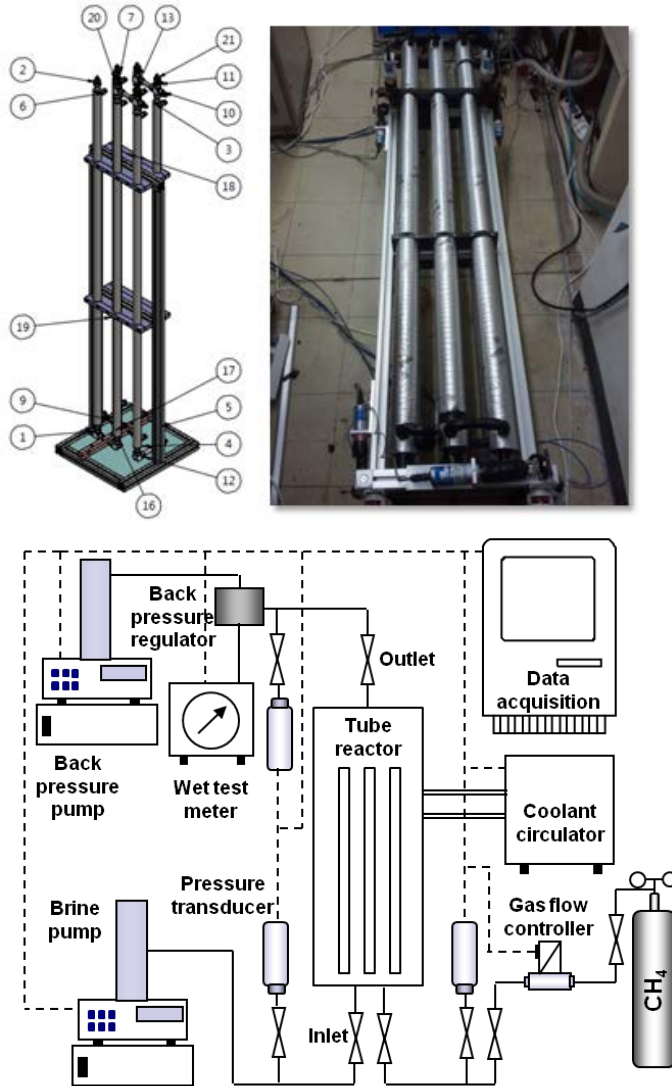


Fig. 1.8 Picture of the experimental setup for 1D 1-m scale GH production (KIGAM 2011)

### 1.3.2.2 Procedure

#### Experimental procedure

We used artificial particles that mimic the grain-size distribution of hydrate-bearing sandy layers found in the Ulleung Basin, East Sea, Korea. The hydrate-bearing sand column was prepared using the following

procedure. First, the dry particles were slowly poured into the vibrated tube reactor, and then the packed sample was fully saturated through water, of which porosity and absolute permeability were measured during this process. Second, the methane hydrate was formed at the state of initial water saturation; this state could be obtained by increasing the rate of methane injection into the sample.

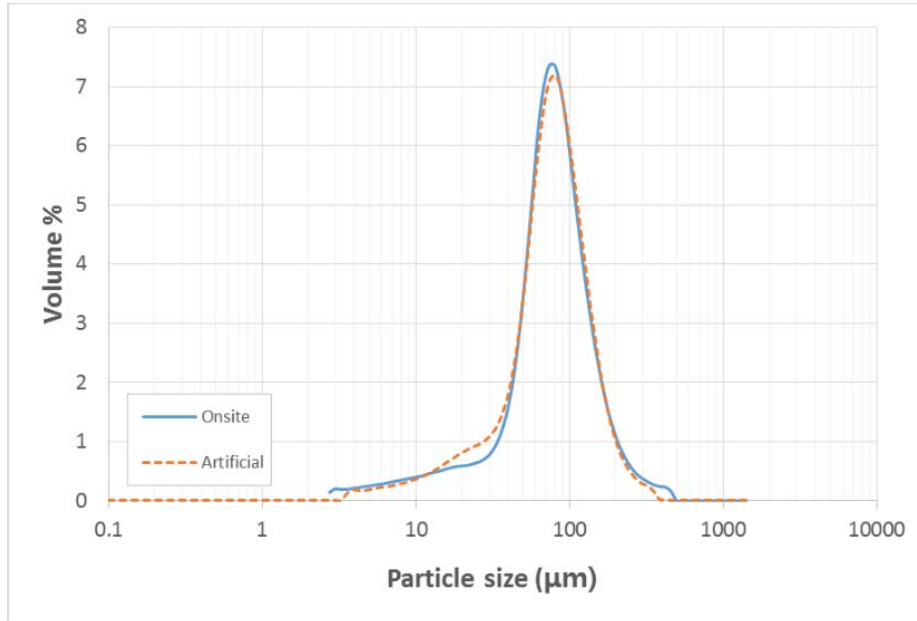


**Fig. 1.9 Particle size distributions of onsite (Ulleung Basin) and artificial samples (KIGAM 2011)**

The system temperature is maintained at around 11oC, the system is pressurized by methane injection, and then cooled to a given temperature. An abrupt decrease in the fluid pressure indicates hydrate formation. The depressurization is carried out to dissociate the hydrate-bearing sedimentary sample. By controlling the back pressure regulator, the fluid pressure of the sample is decreased from the stabilized pressure during hydrate formation to a designated pressure, which is lower than the equilibrium pressure. The pressure, temperature, and volume of the gas and water produced are recorded throughout the experimental process.

### **Experimental condition**

The porosity of the prepared sample was 47.7%, and the absolute permeability was approximately 10.5 Darcy (( $\mu\text{m}$ )<sup>2</sup>). The average particle size was approximately 150  $\mu\text{m}$ . Hydrates were formed in almost the same conditions; the initial pressure, formation temperature, and the initial water saturation were approximately 7.8 MPa, 1.0oC, and 32.1%, respectively. The equilibrium pressure corresponding to the given temperature was approximately 2.90 MPa.

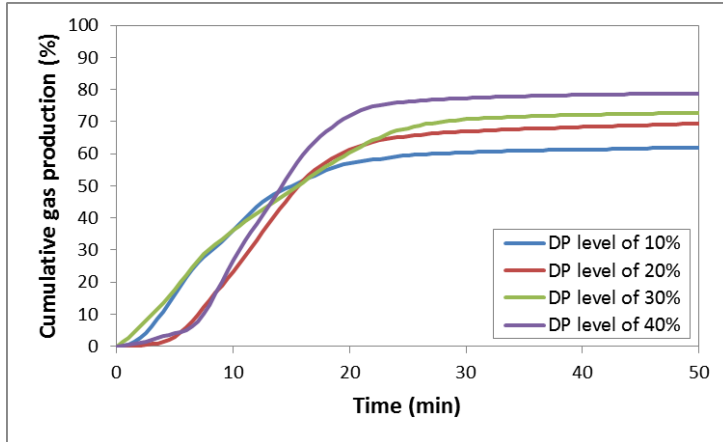
### **Depressurization test**

Four depressurization tests will be conducted by decreasing system pressure down to 10 (DP 10%), 20 (DP 20%), 30 (DP 30%), and 40% (DP 40%) against the equilibrium pressure of methane hydrate at a constant temperature condition. The pressure, temperature, and gas production behavior over the elapsed time will be analyzed during the dissociation process.

### 1.3.3 Results and discussion

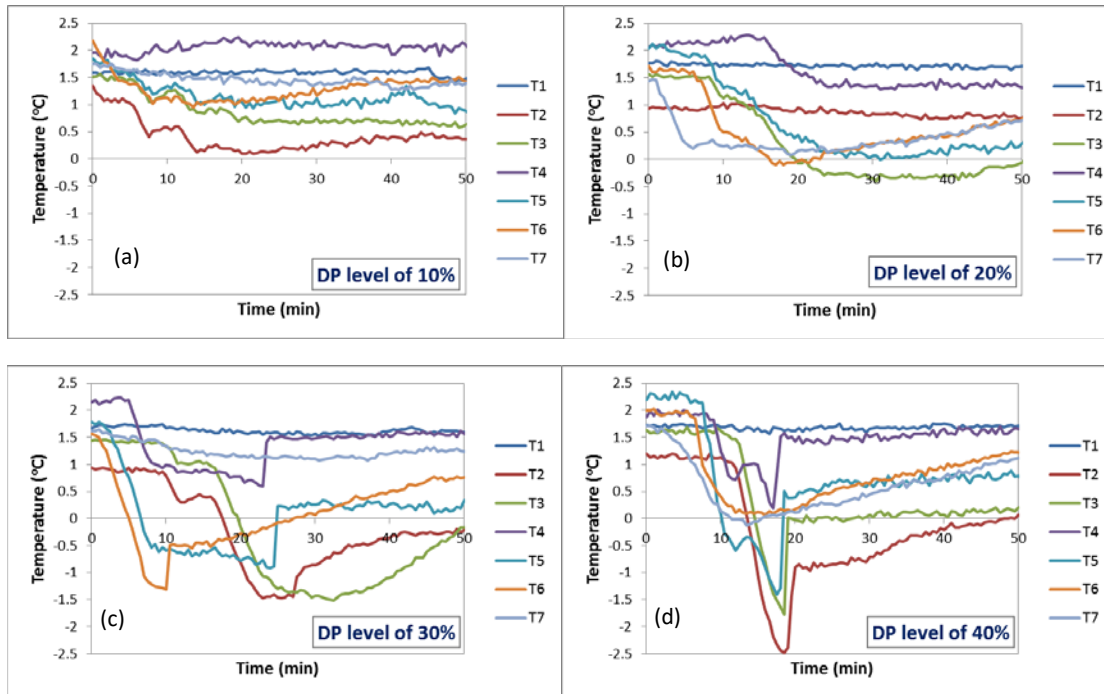
#### Effect of the level of depressurization

Fig. 1.10 show the cumulative gas production according to the level of depressurization (DP) ranging from 10 to 40%. There was no consistent tendency of gas production according to the level of depressurization. This behavior indicates that the level of depressurization was insignificant in relation to the gas production behavior. These results are different from the general trends resulting from small-scale experiments which have demonstrated the predominant effect of the level of depressurization on gas production behavior.



**Fig. 1.10 Cumulative volume of gas produced according to the level of depressurization (DP) ranging from 10 to 40% (KIGAM 2011)**

On the other hand, the level of depressurization strongly affected temperature changes during the dissociation process. Fig. 1.11 describes the temperature changes with an increasing level of depressurization from 10 to 40%. Temperature drops commonly occurred, as shown in Fig 1.11. The reason for this, as is well known, is that the latent heat of endothermic reaction of dissociation reduced the temperature, when the sensible heat of the sample was insufficient to decompose the hydrate in the dissociating zone. Subsequently, the reduced temperature commonly returned to the initial value, because heat was continuously transferred from the surroundings; this means that the dissociation lasted thanks to the heat transfer. Remarkably, the higher level of depressurization caused faster changes of temperature reduction and restoration. This was owing to the higher driving force of dissociation for a higher level of depressurization, which accelerated the dissociation process. For this reason, the duration of temperature reduction became shorter while the degree of temperature reduction became larger.



**Fig. 1.11 Temperature changes with increasing levels of depressurization from 10 to 40% (KIGAM 2011)**

### Effect of the rate of depressurization

Fig. 1.12 shows the average production rate until reaching 90% of final production according to a rate of depressurization ranging from 2.5 to 100 psi/min with a constant DP level of 40%. In contrast with the level of depressurization, the rate of depressurization significantly affected the gas production behavior during depressurization. As shown in Fig. 1.12, the gas production was delayed with a decreasing level of depressurization. This can be explained as follows: A higher rate of depressurization accelerated the hydrate dissociation rate with a higher concentration of driving force in a short period of time. A corresponding increase in gas production occurred.

The results confirm that it could be possible to control the depressurization-induced gas production behavior by adjusting the rate of depressurization in 10-meter-scale sediment that exhibits flow-dominated characteristics. It is commonly known that the pore spaces of marine hydrate fields are initially saturated with two phases, i.e. water and hydrate, without a free gas phase. Therefore, depressurization would be implemented by pumping water out of the hydrate-bearing layer. However, all the experiments of this study performed in the partially-gas-saturated sediment owing to the limitation of experimental methodology to form hydrate. To expand the in-situ applicability of depressurization, it is necessary to determine the characteristics of depressurization-induced gas production behavior in the sediment without a free gas phase.

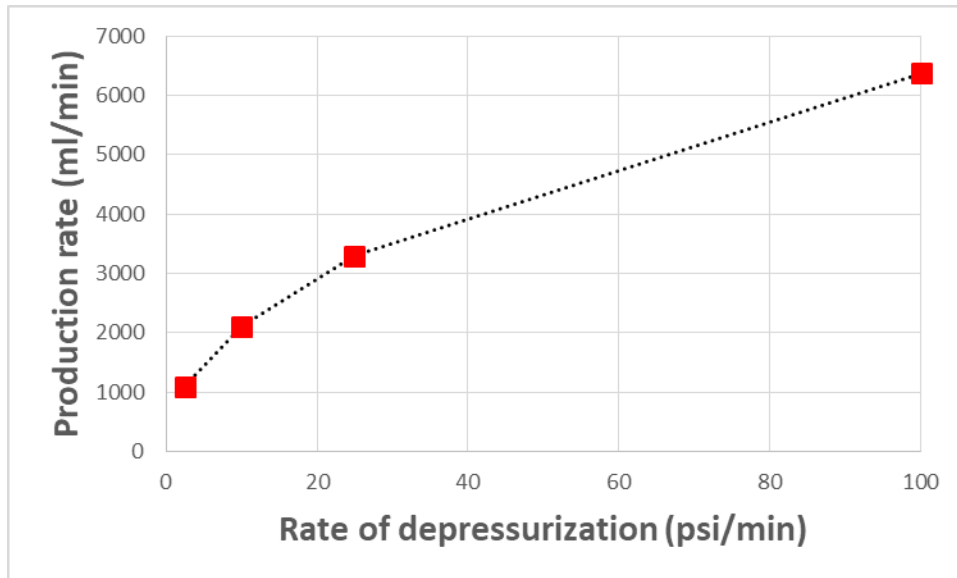


**Fig. 1.12. Cumulative volume of gas produced with different rates of depressurization (KIGAM 2011)**

## **1.4 Depressurization of 1.5 m scale in 3D (Subtask 2.3)**

### **1.4.1 Introduction**

To overcome the limitations in small scale experimental apparatus, such as cm-scale and 1D m-scale, we developed 3D meter-scale high pressure cell. The depressurization test was conducted in three stages. The depressurization range of the first stage was from 20.1MPa to 10.1MPa, and the range of the second stage was from 10.1MPa to 7.6MPa. The depressurization rate was -0.42MPa/h in both stages. The last stage was to reduce the pressure to atmospheric pressure.

### **1.4.2 Experimental setups**

#### **1.4.2.1 Apparatus**

The system is composed of 4 major modules, which are 3D meter-scale high pressure cell, fluid control unit, data acquisition unit, and temperature control unit to simulate gas hydrate production in sediment specimens. Fig. 1.13 shows a schematic diagram of 3D meter-scale GH production system.

The 3D meter-scale high pressure cell made of 316 stainless steel was constructed with the working pressure of 20 MPa in order to simulate a hydrate reservoir. The dimensions of sediment specimens were 1 meter of the diameter and 1 meter of the length. Five K-type thermocouples for the temperature measurement were equipped in every 20 cm from the bottom of the cell. Twenty pressure transducers were equipped in two places on the edge of cylindrical cell with 10 cm interval in the vertical direction. Custom-made electrodes were also equipped in every 10 cm in the vertical direction for resistance measurement. A coolant circulation jacket was installed outside the high-pressure cell for direct temperature control of the cell. A CCD camera and a laser displacement sensor were installed at the top of the high pressure cell lid to observe sediment deformations. The fluid control system used mass flow controllers and a circulation pump for the injection and circulation of gas and water. Specifically, two

autoclaves were installed to provide methane-dissolved water for gas hydrate formation. All of the above equipment was located in a large environmental chamber, which controls the temperature in the range from 0°C to 25°C. Data acquisition system has been constructed for real time storage and processing of experimental data such as temperature, pressure, volume of production fluid, internal image of high pressure cell, and control of various measurement equipment obtained during depressurization production test.

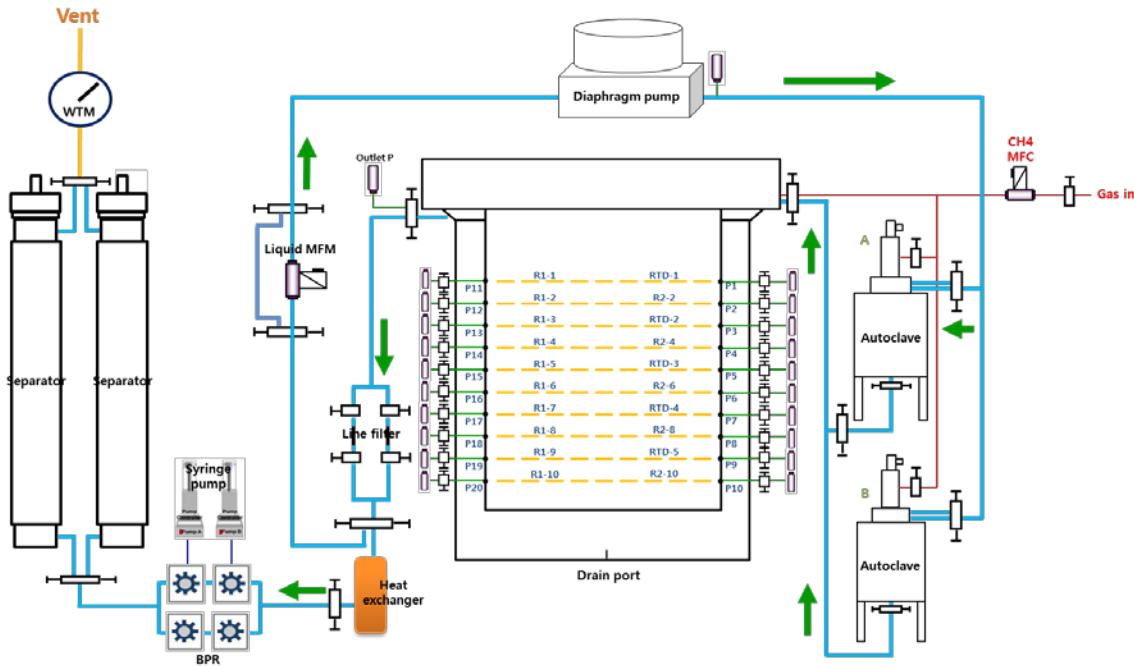
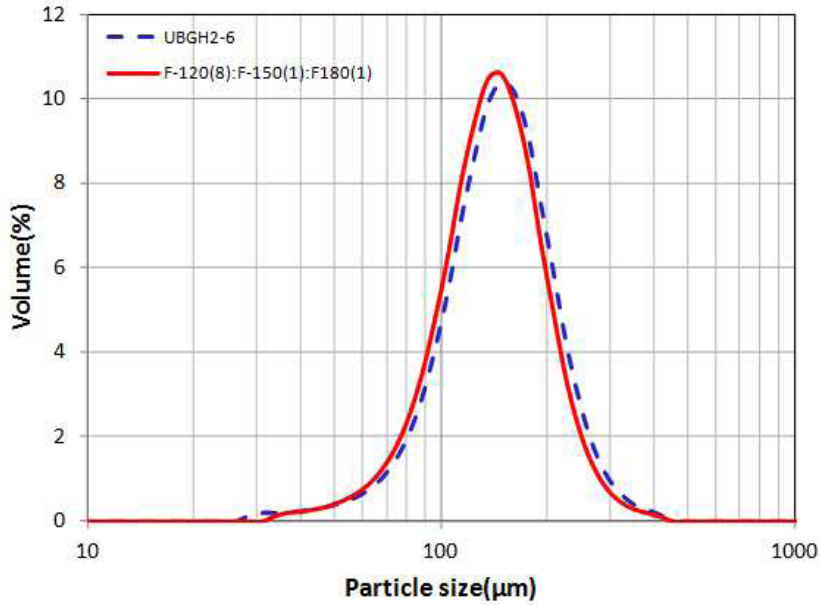


Fig. 1.13 Schematic diagram of 3D meter-scale GH production system (after KIGAM 2014)

#### 1.4.2.2 Procedure

##### Sediment specimen preparation

We inspected our 3D meter-scale system which includes high pressure cell, data acquisition equipment, fluid control equipment, and temperature control equipment. After confirming that there was no leakage of pressure during the inspection, we packed sediment sample into the 3D meter-scale pressure cell. The packed sediments consisted of alternate layers of clay (30 cm)-sand(60 cm)-clay(25 cm) representing the layering system in the Ulleung Basin geological structure. We also used artificial particles that mimic the grain size distribution of sandy layers found in the Ulleung Basin, as shown in Fig. 1.14



**Fig. 1.14 Particle size distributions of onsite (Ulleung Basin) and artificial samples (KIGAM 2014)**

### Gas hydrate formation

To simulate realistic phenomenon of hydrate formation in nature, water containing dissolved methane was continuously circulated through the sediment in closed flow system. Under a certain condition satisfying a hydrate equilibrium condition, hydrate starts to form in fully water-saturated condition with no gas phase, but the hydrate growth rate is very slow. Fig. 1.15 shows pressure changes and estimated hydrate saturation during circulation of methane-dissolved water. At the end of 118 days of circulation, water circulation was stopped. During hydrate formation, salinity of circulating water gradually increases due to the ion exclusion effect. Hydrate saturation could be estimated by measuring concentration of chlorine ion of circulating water. In our experiment, the hydrate saturation was determined as about 25%.

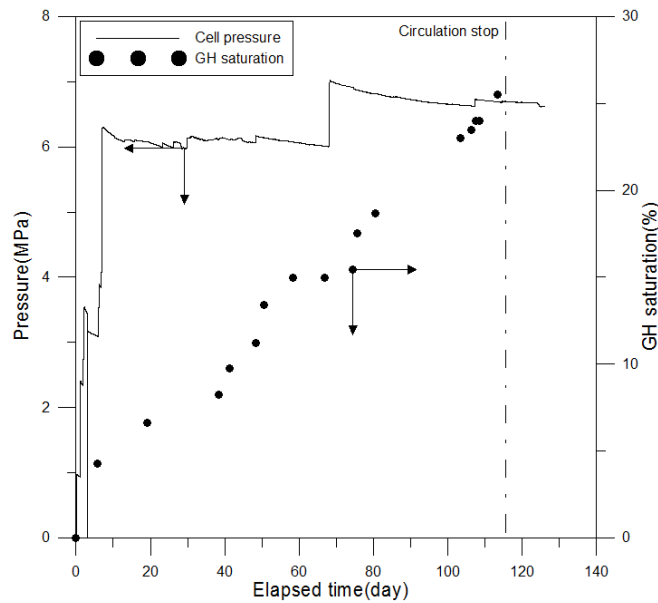


**Fig. 1.15 Pressure changes and estimated hydrate saturation during circulation of methane-dissolved water (KIGAM 2015)**

### Depressurization

The initial temperature and pressure was 15.2 °C and 20.1 MPa, respectively. The depressurization test was conducted in three stages. The depressurization range of the first stage was from 20.1MPa to 10.1MPa, and the range of the second stage was from 10.1MPa to 7.6MPa. The depressurization rate was -0.42MPa/h in both stages. The last stage was to reduce the pressure to atmospheric pressure, which was the step for mass balance calculation, not dissociation.

### 1.4.3 Results and discussion

#### Production pattern

Fig. 1.16, Fig. 1.17, and Fig. 1.18 show the pressure change, water production and total gas production of the high-pressure cell during the depressurization test, respectively. In Fig. 1.16, the pressure responses measured at the edge (50 cm from the center) and inside (5 cm from the center) of the sediment were almost similar, and the pressure at each height of the sediment layer was similar, although not shown here.

The total amount of water produced during the first, second and the third depressurization were about 190 L, 28L, and 16L, respectively. Most of the water was produced during the first depressurization in which the gas hydrate dissociation started, and the water production during the second depressurization after completion of the dissociation was only 18% of the total production. This could be explained as follows. The pores of sediment sample are initially saturated with water and gas hydrates. When the dissociation starts, water is preferentially produced by the dissociated gas from hydrates in the pores. Water production is significantly reduced after completion of the dissociation, because the majority of the pores is saturated with the gas phase.

Total gas production at the first stage begins to increase at the beginning of depressurization, but the gas production is the amount of dissolved gas that escapes from the produced water in atmospheric pressure, not the amount dissociated from hydrates in the sediment. The gas production from hydrate dissociation is delayed after the first stage. Gas production at the second stage includes dissolved gas and free gas, but mainly due to the gas dissociated from the first depressurization. The total amount of gas produced during the first, second and the third depressurization are about 2,328 L, 11,426L, and 35,790L, respectively.

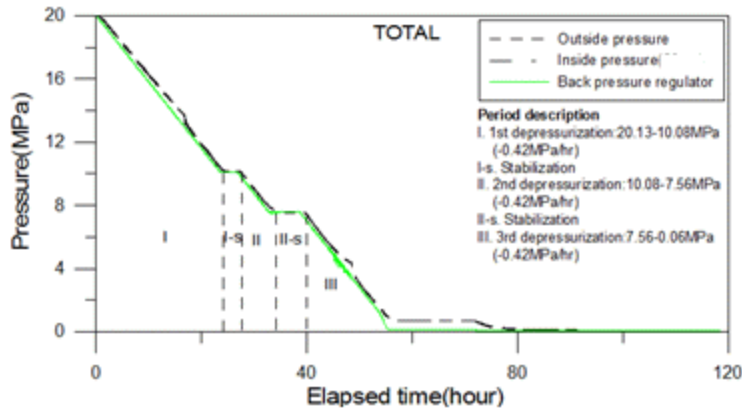


Fig. 1.16 Sediment pressure and back pressure during the depressurization test (KIGAM 2015)

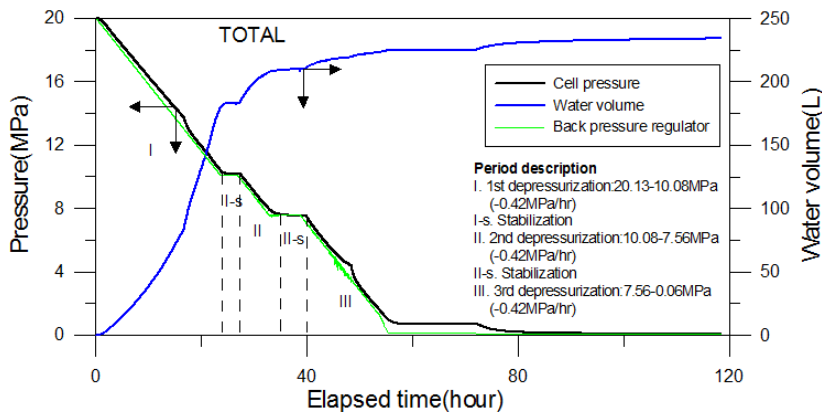
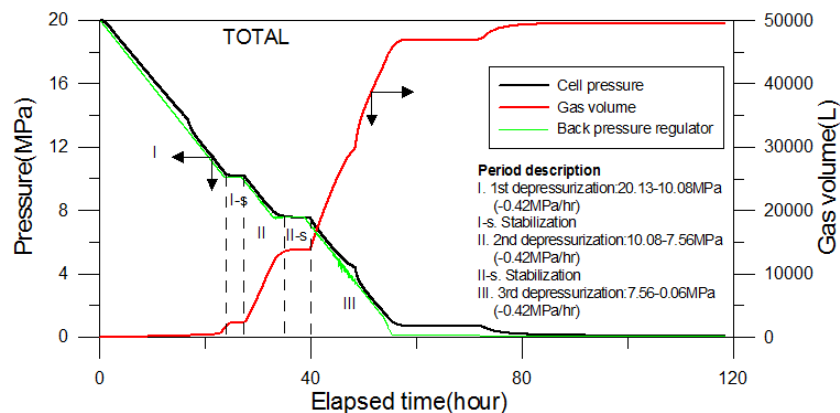


Fig. 1.17 Total water production during the depressurization test (KIGAM 2015)



**Fig. 1.18 Total gas production during the depressurization test (KIGAM 2015)**

### Observation of Sediment deformation

Deformation of the sediment sample during the experiment was measured using a laser displacement gauge mounted on a high pressure cell cover. The vertical deformation of the sediments measured from the laser displacement meter during the entire period from the saline circulation to the depressurization test is shown in Fig. 1.19 Vertical deformation was measured only during the first depressurization due to measurement errors, and it was observed that sediment layer shrinkage of about 35 mm occurred. The first depressurization is the period during which most of the water is produced by the GH dissociation. It is inferred that the sediment sample shrinkage occurred due to the dissociation of load-bearing hydrate.

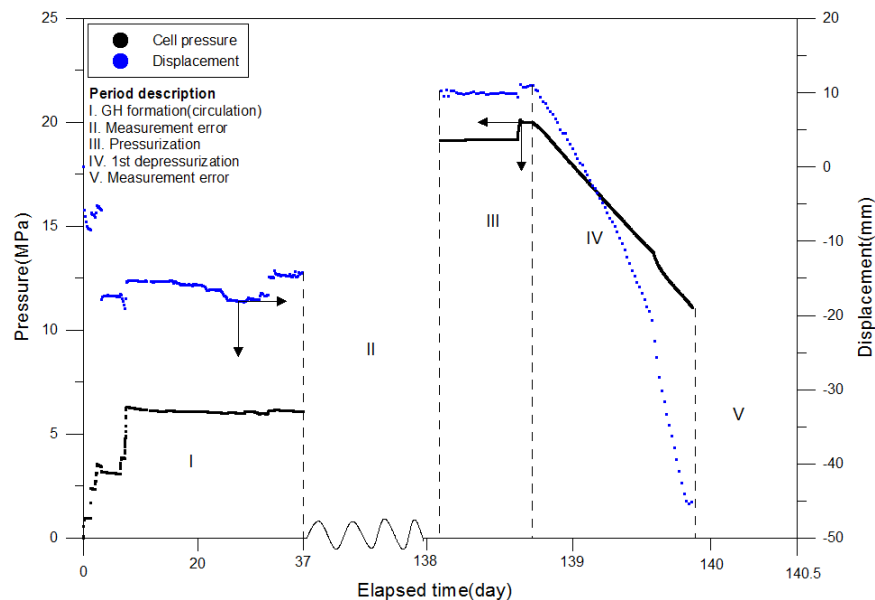


**Fig. 1.19 Vertical deformation of the sediment sample measured by a laser displacement meter during the entire experiment (KIGAM 2015)**

## **2. LBNL Laboratory tests investigating geomechanical changes in hydrate-bearing sediments (Task 3-Subtask 3.1, Subtask 3.2, Subtask 3.3 by Borglin, S., Kneafsey, T., Wang, B.)**

### **2.1 Objectives**

The objective of this task was to experimentally investigate geomechanical responses induced by depressurization of hydrate bearing sediment by performing new experimental studies at Lawrence Berkeley National Laboratory (LBNL). These experiments were designed to capture complex coupled physical processes between flow and geomechanics, such as sand production, capillarity, and formation of secondary hydrates. These findings were to be used to further improve numerical codes.

### **2.2 Scope of work**

To perform these experiments we considered conditions in two field sites; Ulleung basin UBGH2-6 and Prudhoe Bay, Alaska PBU-L106. Because the Ulleung Basin is located in the deep sea, depressurization can cause significant deformation, which implies that geomechanical responses such as substantial subsidence, sand production, and well instability become critical for both feasibility of gas production and environmental protection. Previous work has indicated that production at the PBU-L106 location is unlikely to induce significant subsidence, particularly as compared to the Ulleung Basin cases. However, sand production is another geomechanical concern during production, because the hydrate dissociation induces grain movement within unconsolidated formations with low Young's modulus. In the discussions below, the sand samples are intended to model the sands in the PBU and Ulleung Basin regions, and our mud/sand samples are intended to model mud/sand sediments found in the Ulleung basin.

To provide additional experimental data for numerical model verification, experiments examining the following were conducted at LBNL:

1. Geomechanical changes resulting from effective stress changes during depressurization,
2. Geomechanical changes resulting sand production during depressurization, and
3. Geomechanical changes resulting from capillary pressure changes during hydrate formation, dissociation, and combined formation and dissociation while attempting secondary hydrate formation.

These tests are performed by packing a sediment/water medium inside an elastomer sleeve between endcaps which are attached to the sleeve once the sample is emplaced. The elastomer sleeve and endcaps are sealed such that an external pressure can be applied (confining stress). The endcaps allow flow into and out of the sample, and may also contain thermocouples for temperature measurement. This assembly is submerged in a confining fluid and placed inside an X-ray transparent (radiolucent) pressure vessel, which is contained in a temperature-controlled liquid (Fig. 2.1). The pressure vessel is mounted to the location-controllable table of a medical X-ray computed tomography (CT) scanner for visualization of the processes occurring in the sample. The highest spatial resolution of the CT scanner is about 193 x 193 microns in the scan plane, and 625 microns in the axial direction. Sequential X-ray CT scans can be numerically compared to examine physical density changes, as well as location changes over time indicating translation or strain.

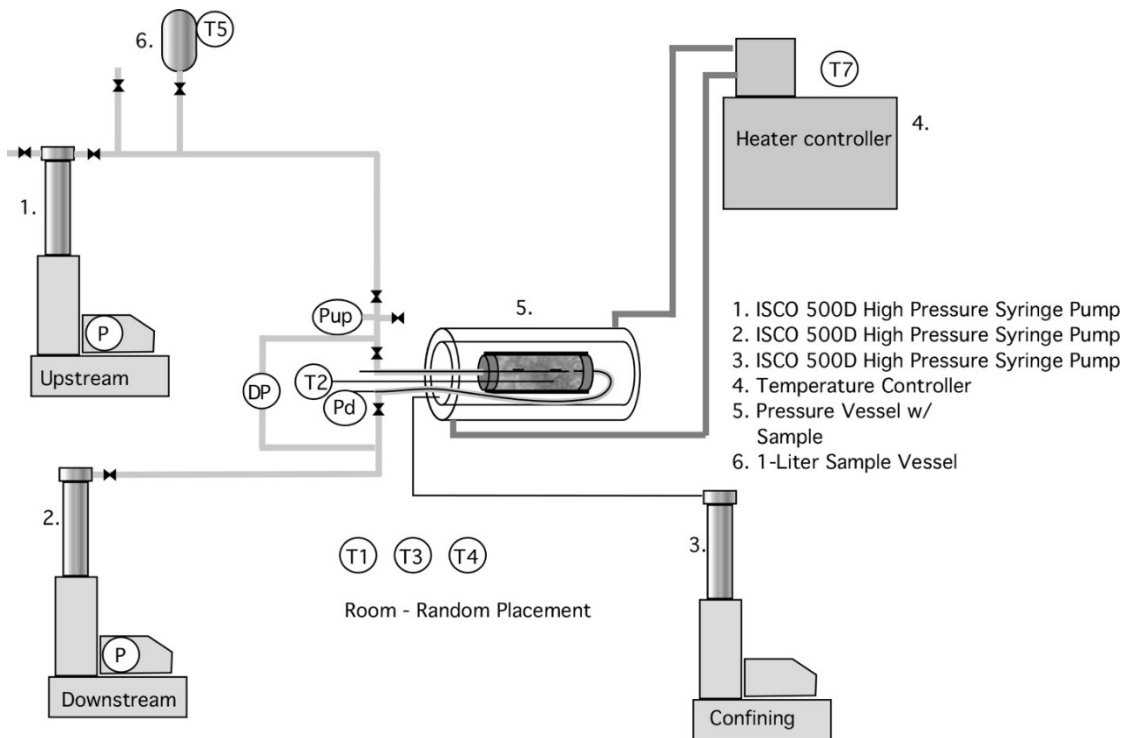


**Fig. 2.1. Typical experiment setup.**

### 2.3 Geomechanical changes from effective stress changes during dissociation (Subtask 3.1)

For this subtask, several experiments were performed to observe geomechanical changes in hydrate-bearing sediments during dissociation. Hydrate-bearing sediment samples were formed in an elastomeric tube (sleeve) with “fixed” endcaps, i.e., the endcaps were attached to the sleeve but not allowed to slide within the tube. The tests included geomechanical changes in sand 1. without hydrate to provide a baseline, 2. during hydrate formation in layered sand/mud systems, and 3. during hydrate formation in sand.

#### 2.3.1 Geomechanical changes from effective stress changes without hydrate formation

Simplified preliminary tests without hydrate were necessary to understand the baseline changes in geomechanics in the system due to flow and effective stress changes. The sample was reconstructed from partially saturated fine sand and the outlet was plugged with a porous plug to prevent the flow of sand from the system while allowing fluid flow. These sand systems can be viewed as being akin to the sands in the subsurface at Prudhoe Bay or sand layers in the Ullung Basin. To improve the visualization of minor shifting or movement of the sample, materials with different X-ray transparency were mixed with the sand placed in locations the sand column. Lower density areas were formed by mixing sand with diatomaceous earth (average particle size 100  $\mu\text{m}$ ) and higher density areas with barite (particle sizes range from 1 to 11 microns, mean particle size 4.5 microns,  $\text{BaSO}_4$ ). The sample was placed in an X-ray transparent vessel and subjected to an initial effective stress. The effective stress (external pressure –

pore pressure) was increased from an initial value of 100 psi to a value of 300 psi and changes in the sample geometry were monitored. Subsequent to the effective stress changes, both gas and air flow were forced through the sample. Despite all the perturbations, only minor changes were seen in the sample over time. Fig. 2.2 shows a cross section of the initial sample, and the sample after changes in effective stress and water flow. Within the limits of the CT information, no overall volume changes were observed. Images presented represent a representative slice and axial cross sections cut the length of the sample.

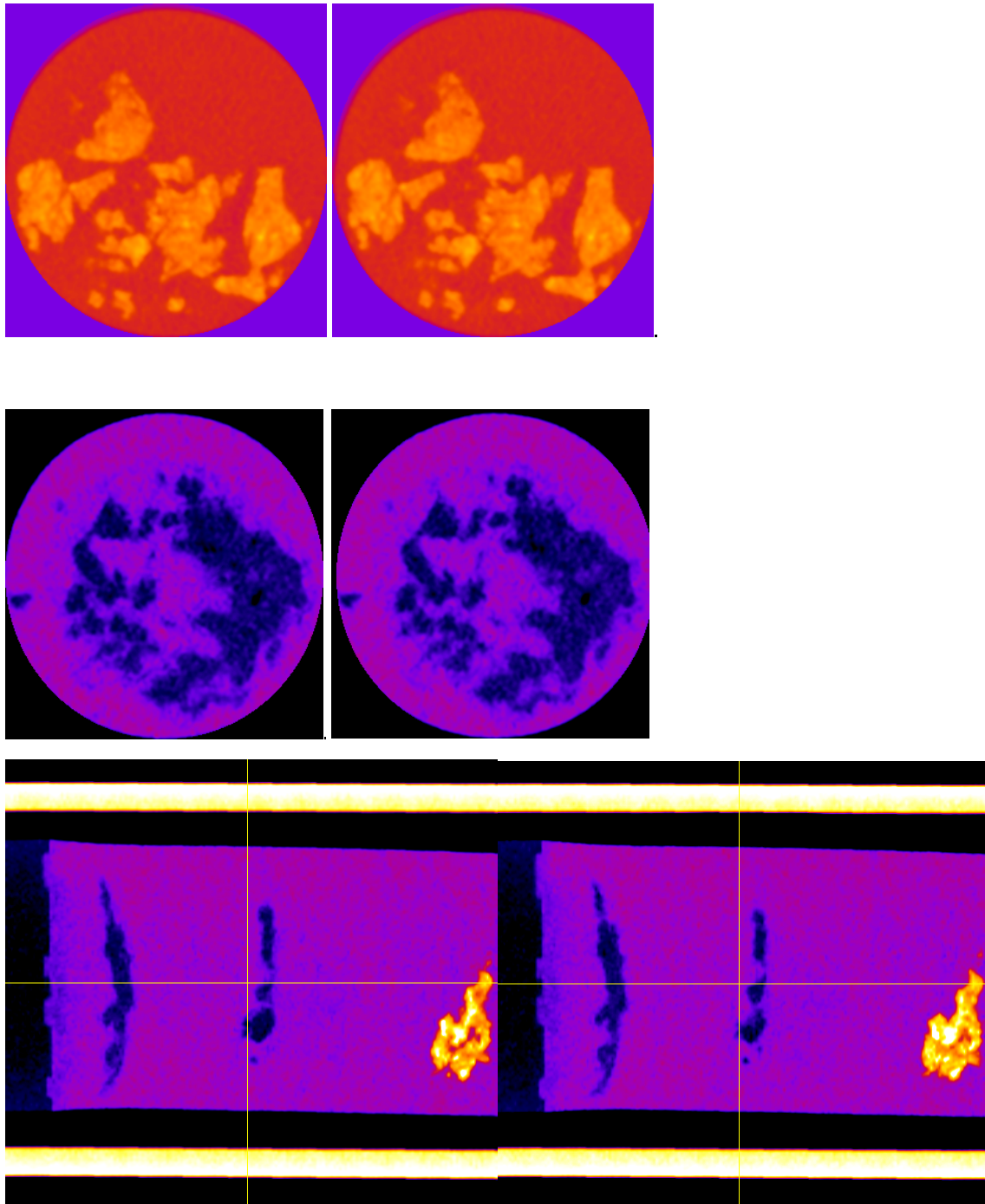


**Fig. 2.2** A cross section of the sand sample through an area mixed with barite (top), and mixed with diatomaceous earth (middle) and cross section through the sample (bottom) before and after completion of the test. Very little to no change in sample size was observed.

**2.3.2 Geomechanical changes from hydrate formation/dissociation in sand/mud layered systems**

These tests were performed to further examine geomechanical changes hydrate was formed in sand/mud layered systems more akin to the sand/mud layering in the Ulleung Basin. The mud layer was composed of 200g silt, 50g kaolinite, 2.5g diatomaceous earth, and 50 mL water. Barium sulfate powder (3 g) was added to the mixture to enhance contrast between the sand and mud layers during CT scanning. The sand layer was US Silica F110 sand moistened to make a 30% water saturation when compacted. Particle size analyses (Malvern Mastersizer, Malvern Panalytical, UK) of the two samples are listed in Table 2.1. To make the layered system the samples were packed into half cylinder forms and frozen (see Fig. 2.3) in a standard chest freezer. The frozen half cylinders were mated and placed in an elastomer sleeve with the mud layer on top and placed into an X-ray transparent pressure vessel as performed in tests described above (Fig. 2.4). The confining, inlet and outlet pressures were controlled with syringe pumps, and the temperature and pressure monitored continuously through the experiment. The entire system was placed on a table in a medical CT scanner and geomechanical changes were monitored by scanning the sample periodically throughout the processes of hydrate formation, saturation, and dissociation. The outlet tube was positioned in the center of the sample, and to prevent sand migration the outlet tube was plugged with an X-ray transparent porous material (aluminum wool).

Results show that in this layered system hydrate primarily formed in the sand layer, expected as gas transport in the sand was not severely hampered and in the mud was limited to mostly diffusive transport by the lack of advective flow pathways. To dissociate hydrate as an analog to depressurization of a natural system where the geological stresses would remain and the fluid pressures decreased, the confining pressure was held constant and pore pressure reduced to a value below the hydrate stability point. This caused an effective stress increase from 120 psi to 320 psi, similar to that in Section 2.1.1. During depressurization, dissociation of hydrate (in the sand) occurs without any appreciable geomechanical changes – the sample density changes were consistent with changes in hydrate/water and size did not shift. Compaction in the mud was evident, however, as the sampled bent slightly as the compaction of the mud was relatively higher than the sand. Effluent samples were taken to observe fines migration, however no particles were observed in these samples and the turbidity appeared to be close background.

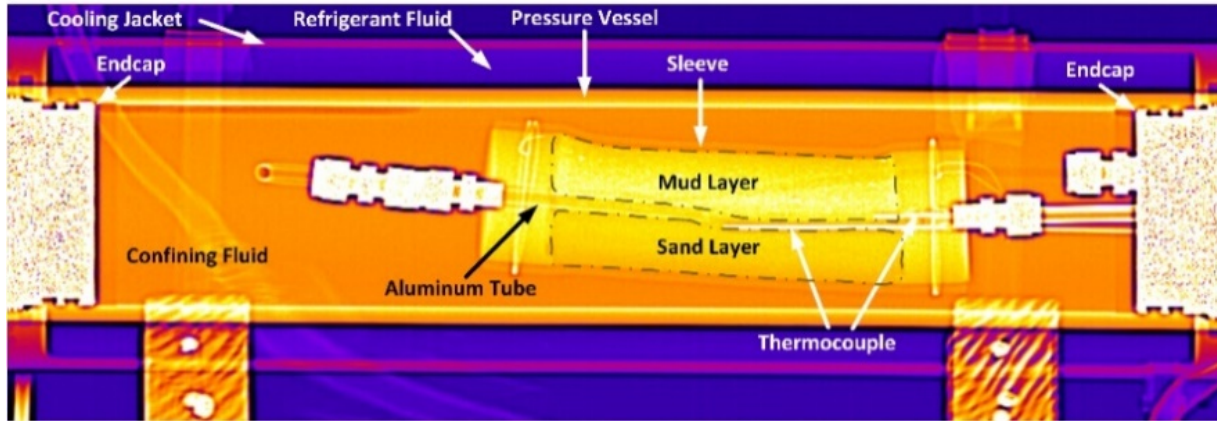
**Table 2.1.** Particle size of mud and sand samples.

Size Classification	Size range	% in mud	% in sand
Clay	Less than 2 um	6.84	0
Silt	2-50 um	59.41	0.03
Very fine sand	50 – 100 um	15.7	18.51

Fine sand	100-250 um	15.9	74.18
Medium sand	250-500 um	2.16	7.28
Coarse sand	500-1000 um	0	0
Very coarse sand	1000-2000 um	0	0



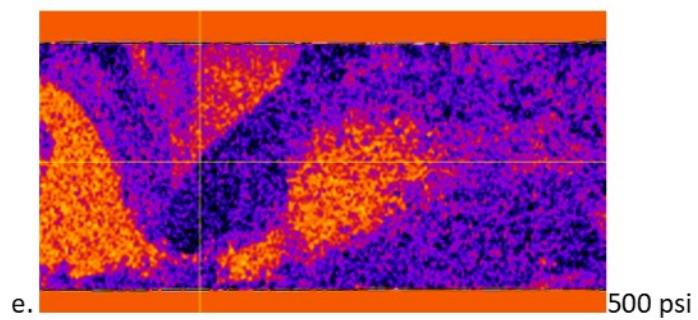
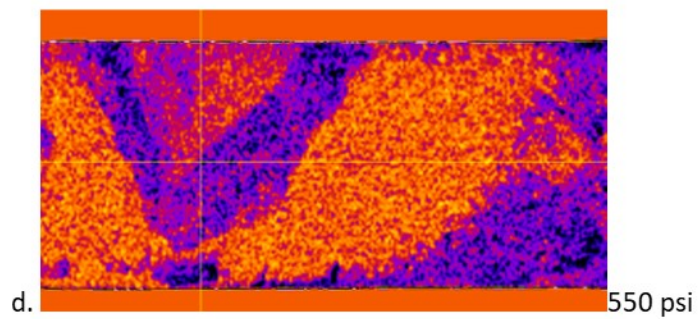
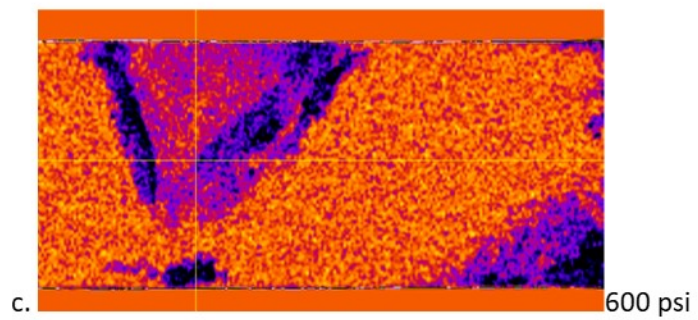
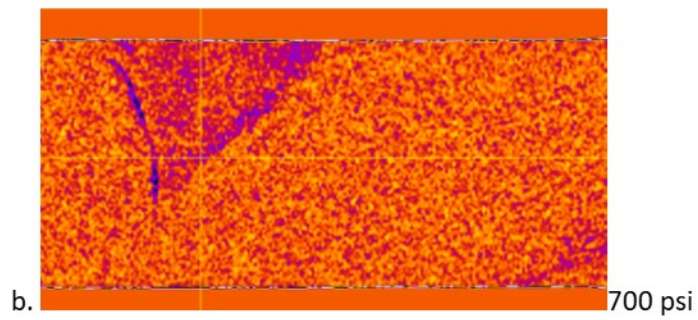
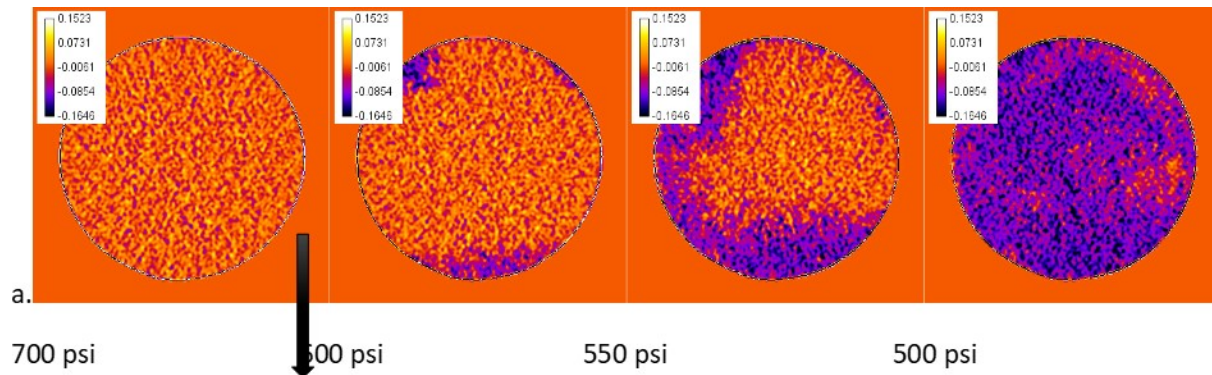
**Fig. 2.3. Layered sample preparation. Top - sand in half-cylinder mold, middle - mud sample, bottom - both. Plastic wrap was used to protect sample and prevent evaporation during freezing.**



**Fig. 2.4. Details of sample installation in pressure vessel. Sample curvature occurs due to mud compaction.**

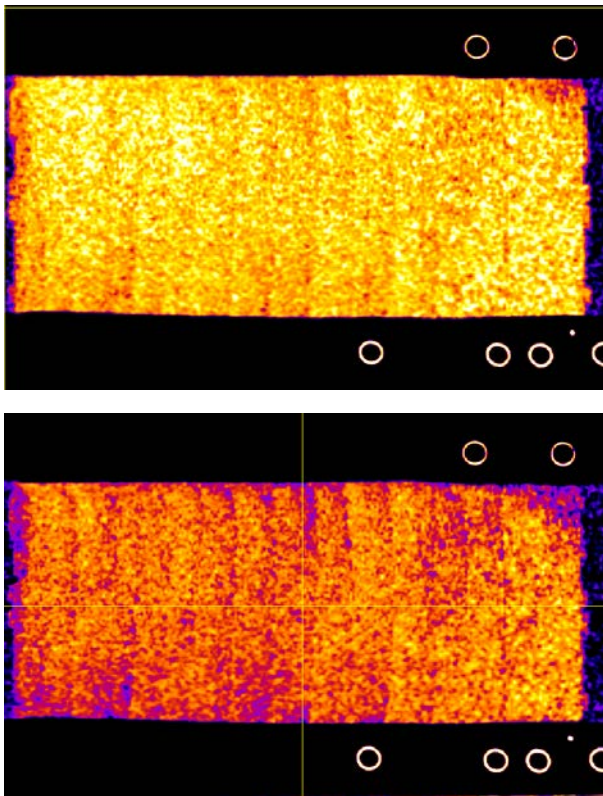
### **2.3.3 Geomechanical changes with hydrate formation and dissociation in sand**

Methane hydrate was formed in the pore space of a fine sand sample in an elastomer sleeve in an X-ray transparent pressure vessel using the excess gas method, with an initial water content of 30% of the pore space. Very few laboratory-formed hydrate-bearing samples contain a uniform distribution of hydrate, and the distribution in this test was heterogenous as well, with a region at the top having a higher saturation than the rest of the sample (Fig. 2.5). The sample was subjected to an initial effective stress of 200 psi. After hydrate formed in the sand, water was injected into the pore space to re-saturate the sample with water. This has been shown to alter the grain cementing hydrate formed by the excess gas method to a pore filling hydrate (Lei et al., 2019). Methane gas was produced by depressurization. This lowering of pore pressure increased the effective stress as the confining stress was held constant. Sample changes were monitored using X-ray CT and confining fluid volume changes. Volume changes are sensitive to changes in sample size (the desired measurement), but can also be affected by room temperature and leaks that might occur. Sand production was prohibited using porous plugs in the tubes. Fig. 2.5 shows a cross section of changes in density of the sample during depressurization. Difference images are created by subtracting a set of calibrated CT images from the initial set of calibrated images, highlighting changes in density. Here, the orange color indicates no change, whereas the purple color indicates a decrease in density typically caused from gas replacing water. The initial confining stress was 900 psi so the sequence in Fig. 2.5 represents an increase of effective stress from 200 to 400 psi. The temperature of the sample was maintained at 4°C. The hydrate dissociation resulted in the density decrease, indicated by the purple color. From these images, we can observe that the hydrate dissociation front moved from the outside of the hydrate rich region towards the center of the “V” shape hydrate-rich region indicated in the top axial cross section in Fig. 2.5. *No significant volume change* was observed in this test, although an effective stress of 400 psi was applied to the sample while dissociation occurred. It is important to note that the sample retained its shape throughout the process, indicating that the hydrate-bearing sand was mechanically stable. Recall however that the hydrate formation in the sample began with grain to grain sand contacts. These apparently were not disturbed by the hydrate formation or dissociation.



**Fig. 2.5. a. - From left to right, the images show the density change at one cross section with hydrate dissociation at the pressure of 700 psi, 600 psi, 550 psi, 500 psi, respectively. b - e. present axial slices at the listed fluid pressure (effective stress = 900 psi – the fluid pressure). The arrow in b. indicates the approximate location of the cross sections shown in a.**

A second dissociation experiment was performed using a hydrate-bearing sand sample. Before dissociation the sample was at 620 psi pore pressure, 830 psi confining pressure (190 psi effective stress). The sample was maintained at 4°C and was dissociated by dropping the pore pressure to 450 psi (380 psi effective stress). The sample was not rehydrated prior to the dissociation. In this system the outlet and inlet contained porous plugs to prevent sand movement. Fig. 2.6 shows the sample before dissociation at 620 psi, after dissociation at 450 psi, and the difference between the two images. Loss of hydrate is evident throughout the sample (purple color in the bottom image in Fig. 2.6), but no overall size changes indicating geomechanical changes were observed. Another observation in the bottom image of Fig. 2.6 is that there is a shift in the sample position (white bands at the sample top *and* black bands at the sample bottom). Because these are the same magnitude, a translation of the sample explains the difference (note other objects experiencing the same translation). This can occur when the CT scanner table height is adjusted. The manual adjustment is in 0.5 mm increments, which is about 2.5 voxels. The key observation again, is that the sand did not experience failure under 380 psi effective stress.



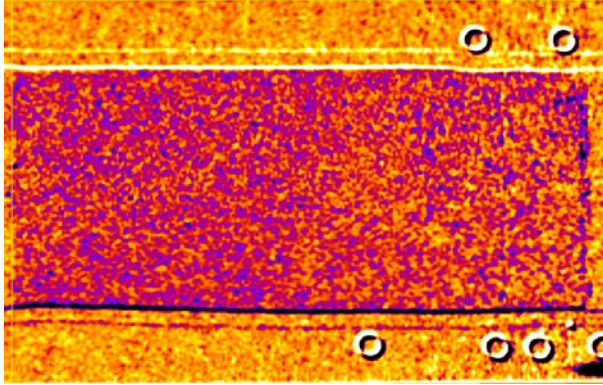
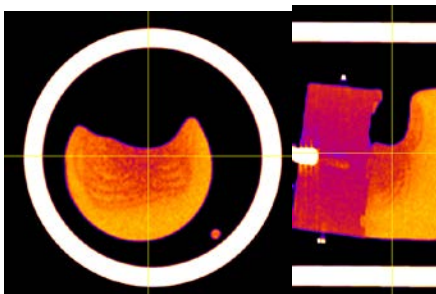


**Fig. 2.6 Axial cross section of CT images of hydrate sample before dissociation (top), after dissociation (middle), and difference (bottom).**

#### **2.4 Geomechanical changes from effective stress changes during dissociation allowing sand production (Subtask 3.2)**

To examine the effect of sand production, the same setup and general concept used in Swrcrtion 2.2 was used, however the plug preventing sand flow was removed and a sand trap was assembled so that flowing sand was not allowed to ruin experimental equipment.

Initial pre-tests were performed in hydrate-free systems to examine the direct effect of effective stress on the medium while water is flowing. Initially we used 1/8 in diameter tubing, but the flow was limited by the inner diameter of the tubing, so the tubing size was increased to 1/4 inch. Two configurations were tried, one with the outlet at the endcap and one with the outlet near the center of the sample. (Fig. 2.7). Both show significant sand flow and deformation of the sample. After set up the sample was initially exposed to increasing effective stress followed by a set confining pressure with increasing flow. The majority of the sand movement occurs during flow, not confining pressure changes. This rapid deformation was also shown in a layered sample Fig. 2.8 (top mud, bottom sand) with the sand rapidly flowing outward when an effective stress of 100 psi was applied.



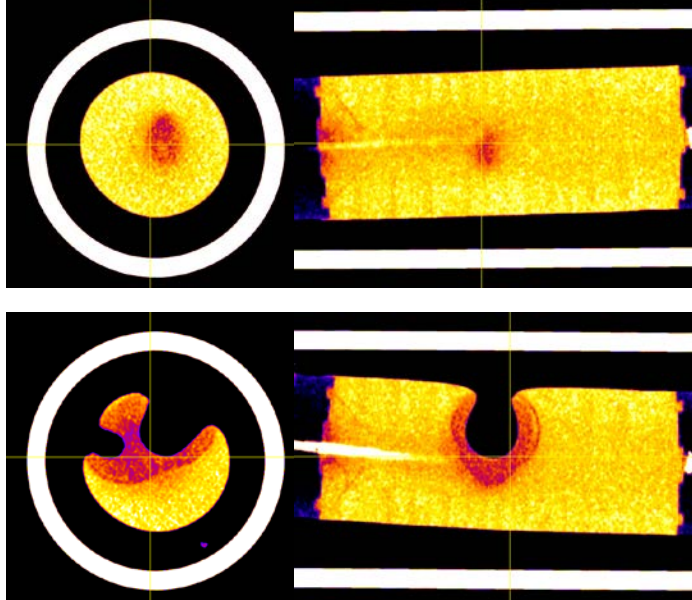
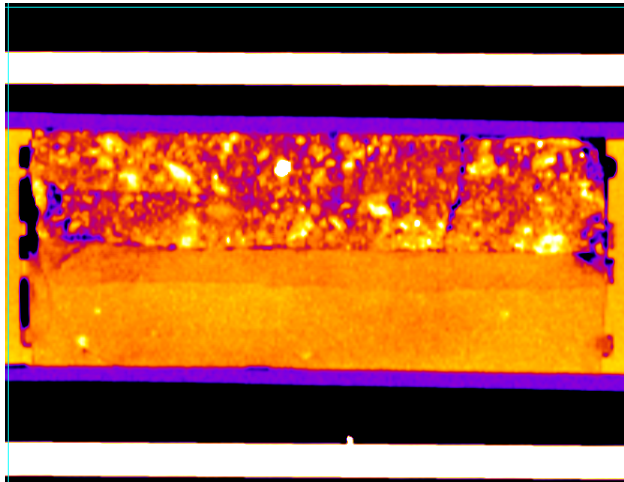
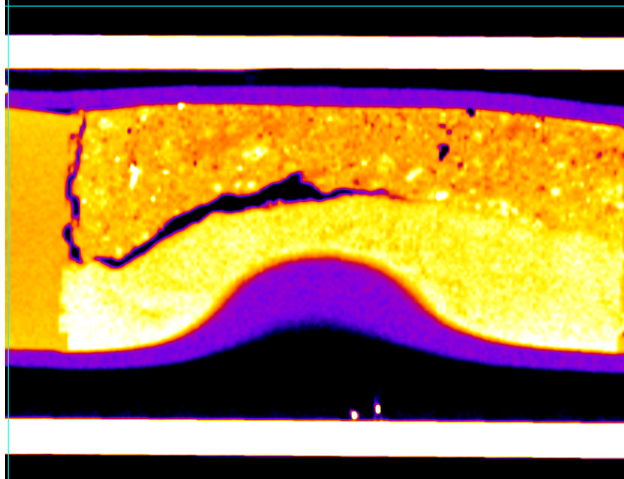


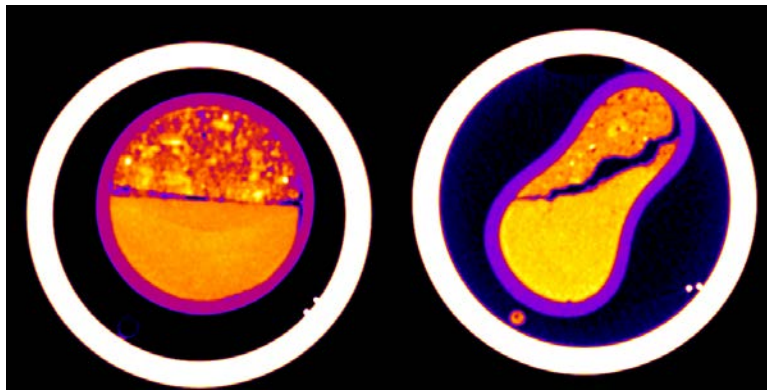
Fig. 2.7. Top - flow of sand from sample when outlet is located at the end of the sample. Note the dilatant (lower density i.e. reddish) shear bands that formed during failure. Middle and bottom - flow of sand from sample when outlet is located mid-sample. Middle configuration observed due to a 300 psi increase in effective stress. Note the red lower density region in the center from sand production. Bottom is change in sample due to flow at 2 mL/min.



a.



b.



c.

d.

**Fig. 2.8 shows the results of sample that failed during setup. In this case, a mud layer was placed over a sand layer (cross sections a. and c.). Upon application of an effective stress, the sample failed as sand flowed out of the sample (cross sections b and d). The aluminum pressure vessel is shown by the thick white lines in a. and b., as thick white circles in c. and d.**

To avoid the rapid flow of sand, an aluminum X-ray transparent screen with mesh size of 0.009 in (0.23 mm) was placed between the sample and the endcap on the outlet end of sample to restrict sand flow but allow for the movement of finer particles. Geomechanical changes were monitored using CT scanning after hydrate formation. The sample was saturated with water, followed by water flow (0.5 mL/min) and methane flow (2 mL/min). In addition, samples were collected from the installed sand trap downstream from the outlet and saved for further analysis of turbidity, particle size, and total dissolved solids.

This sample showed little or no sand or fines production throughout the experiment, possibly due to the mesh size being too small to allow for migration. A second experiment was performed with a larger mesh screen, this one with a mesh of 0.011 in (0.28 mm). Both screens are larger than the mean particle size of the sand (~110  $\mu\text{m}$ ). The second experiment showed some density decrease near the outlet (see Fig. 2.9)

indicating some particle movement. Upon disassembly, sand was observed to have moved through the screen and collect on the endcap. Fig. 2.10 shows the endcap and screen after the experiment.

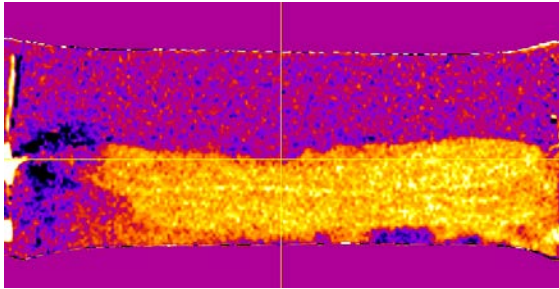


**Fig. 2.9. Layered mud/sand sample after hydrate dissociation. Image was formed by subtracting an image of dissociated hydrate from an image of fully formed hydrate in the sample. Bright yellow areas indicates mud compaction. Dark areas indicate little or no change between samples.**

These results indicate that the sand/mud layered sample is stable during dissociation with only minimal geomechanical changes observed. This may be due to stabilization by the mud layer.



**Fig. 2.10. Outlet endcap and screen after disassembly showing some sand migration through the screen.**

## **2.5 Takeaway**

The key takeaway from these tests is that erosion of the mud, previously thought to be a major problem, is probably secondary to sand control. Compaction of mud layers was observed and this could be significant, however when sand was not controlled, failure was dramatic.

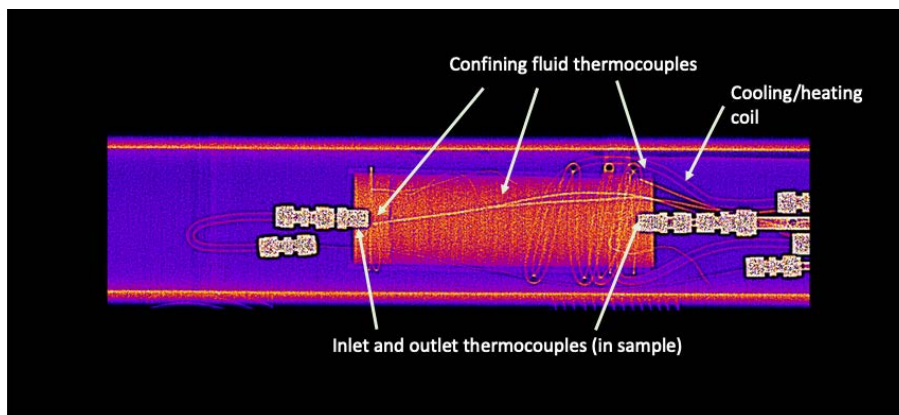
## **2.5 Geomechanical changes resulting from secondary hydrate and capillary pressure changes (Subtask 3.3)**

Two sets of experiments were performed to investigate geomechanical changes caused by the changes in a hydrate-bearing sediment experiencing a thermal gradient. Both used a custom LBNL core holder that allowed for the formation and dissociation of hydrate by warming and cooling opposite sides of the

sample, with the second set of tests further modifying the apparatus to include capillary pressure sensors embedded in the sand for further characterization of the hydrate system. These tests are unique.

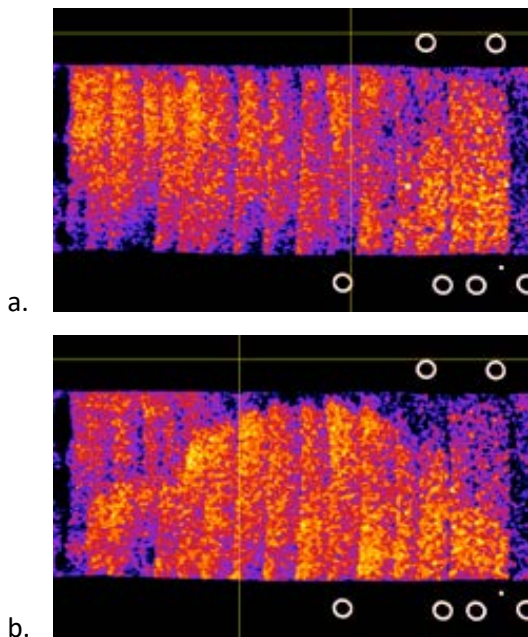
### 2.5.1 Application of a temperature gradient

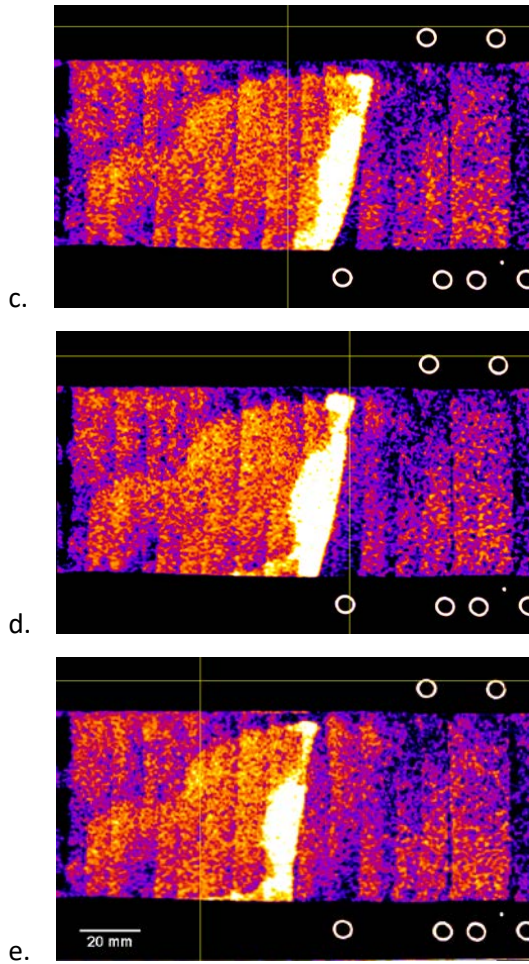
A temperature gradient was created in the sample by flowing a temperature controlled fluid through an aluminum coil (gradient coil) located outside the elastomer sleeve near the inlet (see Fig. 2.11). The confining fluid consisting of 1:1 water and propylene glycol with 1% gelatin added to increase viscosity to prevent convective heat transfer in the confining fluid. Monitoring the temperature gradient was accomplished by placing thermocouples in the inlet and outlet of the sample, as well as in the confining fluid near the inlet, middle, and outlet of the sample. For these experiments the confining fluid was maintained at a constant temperature (nominally 4°C) and hydrate instability was caused by raising the temperature in the gradient coil to 6.4°C. When the coil was activated the outlet temp increased slightly (from 3.7°C to 4.0°C) and the inlet temperature increased from 4.2°C to 6.4°C. The confining fluid middle location thermocouple was at the same temperature as the thermocouple located near the outlet in the confining fluid, indicating that convective heat transfer was minimized. There was no temperature measurement in the sample between the inlet and the outlet, but it is assumed that the temperature has a decline curve from the inlet to the outlet similar to the external thermocouples.



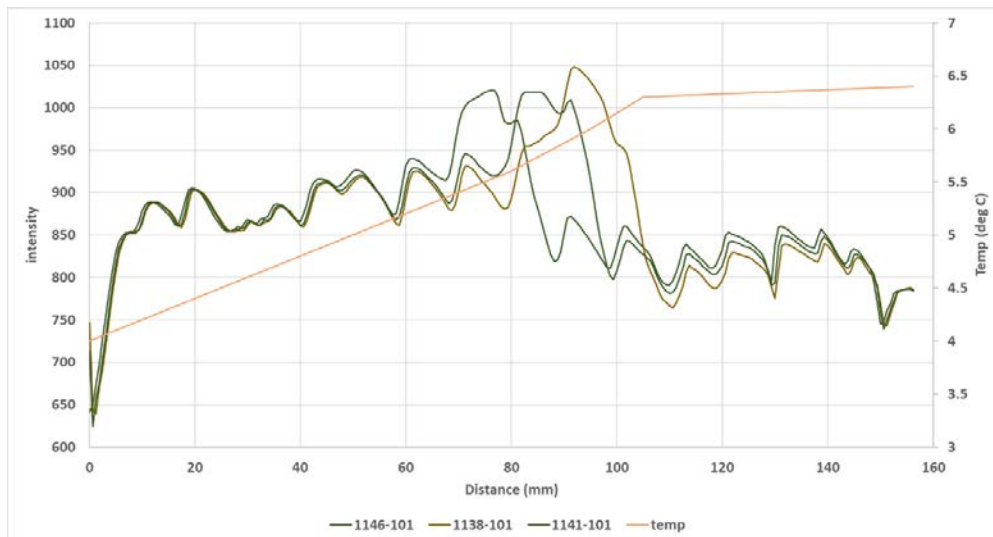
**Fig. 2.11 Top - custom core holder designed to apply a thermal gradient. Bottom – X-ray image of sample in the core holder. The entire sample was cooled to a uniform temperature to allow hydrate formation. Fluid flowing at a higher or lower temperature through the aluminum coil imparts a temperature gradient.**

Fig. 2.12 shows a series of CT images collected during warming and depressurization tests that were performed on the sample. Fig. 2.12 a. shows a cross section of the initial condition. Bands indicate packing density as the sample was packed in layers. Bright colors are higher density, resulting from packing and water redistribution from capillary pressure inhomogeneity. Fig. 2.12 b. shows the density distribution following hydrate formation. Note the automobile-shaped brighter region (compared to the top image) indicating elevated hydrate abundance. Once the heater coil was activated using 6.4°C water, hydrate near the heater began to dissociate. The water released by dissociation was drawn by capillarity towards the cooler end of the vessel by the narrower pore sizes and cryosuction, and upon reaching hydrate-stable conditions, formed a more dense band of hydrate (white subvertical band). As the pressure was stepwise decreased, the stability region moved farther and farther to the left (Fig. 2.12 d, and e.). It should be noted that this capability is unique, and although temperature control is rough, using temperature control with precise temperature control allows easy system manipulation around the equilibrium point. At 710 psi the stability point is around 6.3°C, at 680 psi it is 6°C, and at 650 psi it is 5.6°C. Using the position of the leading edge of the formed hydrate band, an estimate of the temperature gradient can be made (see Fig. 2.13). Temperature appears to be somewhat uniform in the sample surrounded by coils and is estimated to drop off linearly towards the cooler end of the vessel. The location of the coils can be seen in Fig. 2.12 by the white circles above and below the sample on the right side of the image. These circles are cross sections of the heater coil.





**Fig. 2.12. X-ray CT cross sections through a. initial condition, b. after hydrate formation, c. – e. with the heating coil turned on (6.4°C), c. 710 psi, d. 680 psi, and e. 650 psi. Flow is from the inlet (right) to outlet (left).**



**Fig. 2.13. Estimated temperature gradient along the sample. Inlet is at position 156.25 mm, outlet at position 0 mm. Temperature at inlet and outlet were recorded by thermocouples, in the middle by position of the hydrate plug as seen in Fig. 2.12.**

### **2.5.2 Measurement of capillary pressure during hydrate formation**

The next set of experiments incorporated the use of capillary pressure sensors in the sample which necessitated re-designing of the endcap and the temperature control coil system. Due to the complexity of the setup, multiple iterations of the system were built before the final design was used for experimental testing. The concept behind the capillary pressure measurement is that under conditions where the capillary pressure is less than the “air entry pressure” (these sensors are typically used for unsaturated zone measurements) and the medium grains are water wetting thus the water film is continuous, the sensor saturated with water will be in direct contact with water distributed in the sample. We assumed that the gas phase was continuous throughout the sample, which is logical for the unsaturated system. Since the capillary pressure is defined as  $P_c = P_{nw} - P_w$  (here  $P_{gas} - P_{water}$ ), we measure the differential pressure between the gas phase in the sample and the water phase in the sensor. The capillary pressure sensors consisted of a small porous ceramic cylinders (0.25 in diameter, 0.5 in long) with 5 bar air entry pressure connected to 1/16 in nylon tubing (Fig. 2.14) (SoilMoisture Equipment Corp.).

To prepare the sample, moistened sand was packed in an elastomeric sleeve (to end up with 30% water saturation), incorporating three capillary sensors in the sand at positions near the inlet, mid-sample, and near the outlet (Fig. 2.15). Thermocouples were located in the confining fluid, with the exception of one located in the inlet line, and one located in the outlet line. The sample was 5.7 in (14.5 cm) long and 2.5 in (6.3 cm) in diameter. With the additional sensor connections, the vessel endcaps were modified so most of the thermocouples, confining fluid ports, and aluminum tubing for cooling/heating were located on one endcap, and the inlet/outlet and capillary pressure sensors were located on the other endcap (See Fig. 2.16). The aluminum tubing used for creating the temperature gradient along the sample also was reduced to 3/16 in OD to better fit around the large diameter sample. Once assembled, confining fluid consisting of 1:1 solution of propylene glycol and water, with 1% gelatin added to increase viscosity. Confining pressure was set to 100 psi and after confirming the absence of leaks, the system was X-ray CT scanned to check packing and sensor placement. (Fig. 2.17). Note that two of the capillary sensors were located in the region with the warming coil and the third sensor was located near the inlet and outside the coil.



**Fig. 2.14. Porous ceramic capillary pressure sensor.**

(a) (b)



**Fig.2.15. (a) . Packing sensor and sand inside elastomer sleeve. (b) Packed elastomer sleeve, showing inlet end cap with two inlets, a central one for fluid flow and temperature measurement, the other to accommodate the three capillary sensors.**

To monitor the system, three differential pressure transducers were added as well as gage pressure sensors for the confining, inlet, and outlet pressures. Three syringe pumps controlled fluid pressures (inlet, outlet, and confining) and their conditions were also electronically logged for flow rate, volume, and pressure. At the start of the experiment methane hydrate was formed using the excess gas method by setting confining and pore pressure to 800 psi and 700 psi, respectively, setting the temperature to the within hydrate stability region, 4°C, to allow hydrate to form.

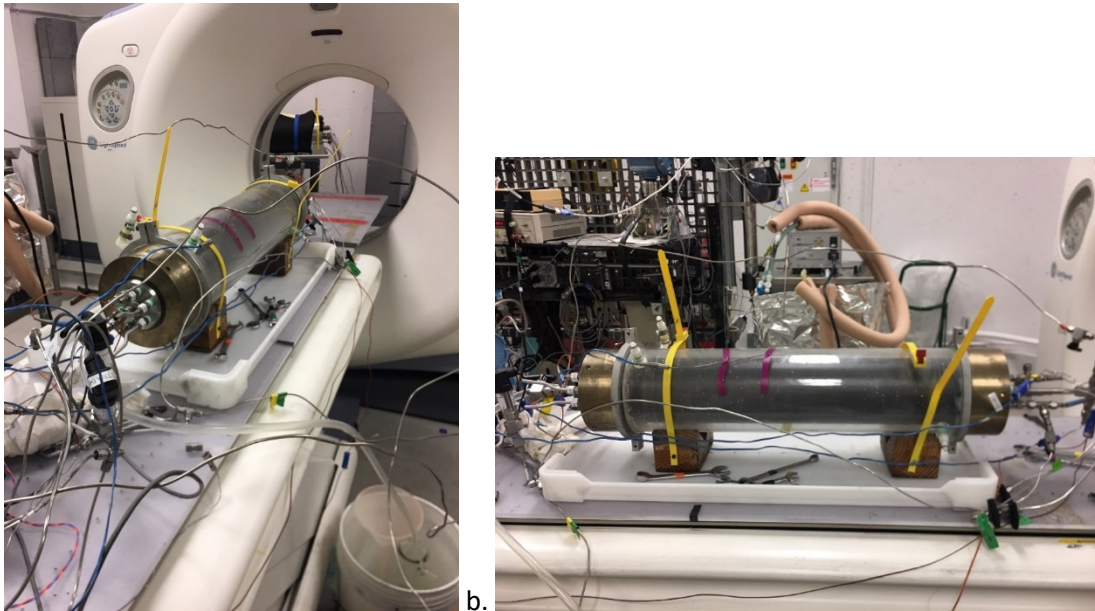


**Fig.2.16. Assembled aluminum pressure vessel. The left end has ports for interior coolant flow, confining pressure inlet and outlet, and 4 thermocouples. The right end has an inlet port, outlet ports, the three capillary sensor ports, and 4 additional thermocouples. (b) Vessel on table prepared for scanning.**

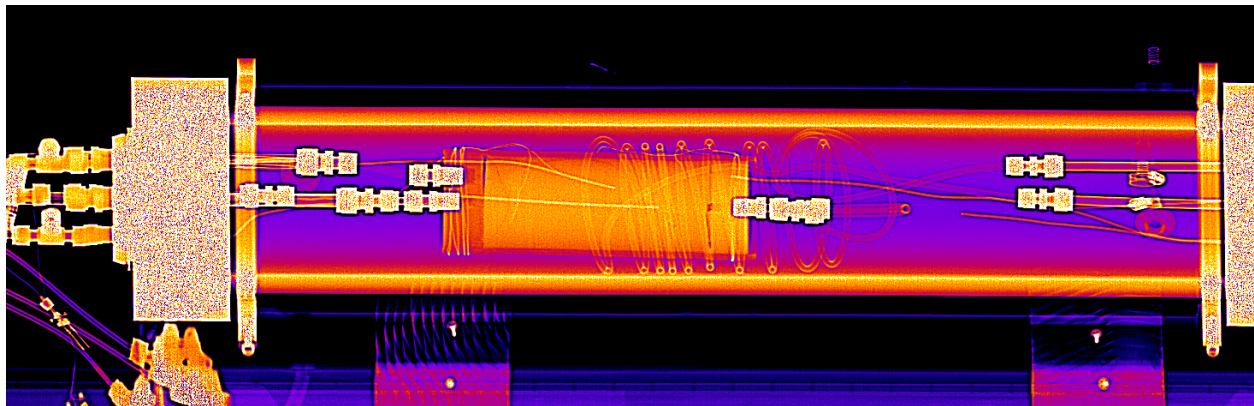
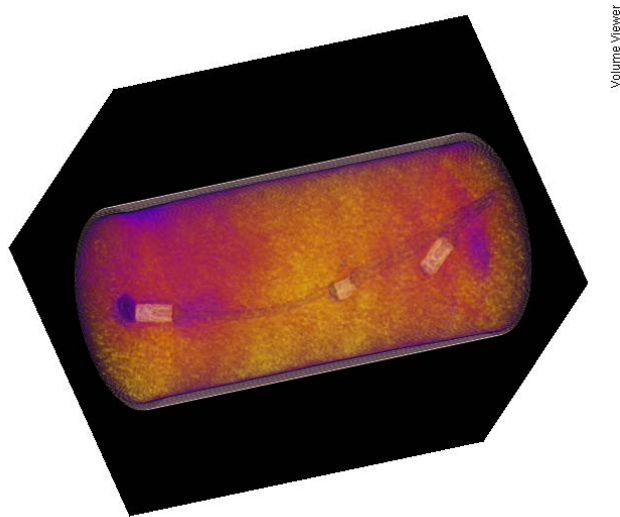
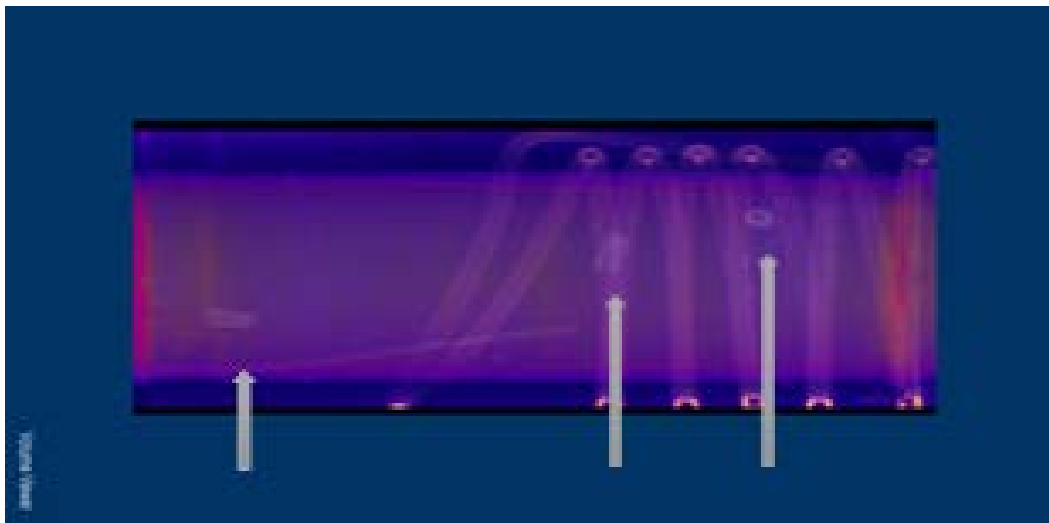


**Fig.2.17. Initial scan of system to check sensor position and packing. Visible on the right are the two inlet ports. The spiral tubing around the outlet end of the sample is for creating a temperature gradient. Outlet is located to the left of the sample.**



a.



b.

**Fig.2.18. Scans of sand pack showing location of capillary pressure sensors within the sand. For (a) inlet is at the bottom of the sample. (b) inlet is to the right of the sample. Arrows indicate location of capillary sensors.**

After hydrate formation the sample was saturated with water and the temperature gradient was adjusted such that one end of the sample was outside of hydrate equilibrium ( $T_{eq}$  for 700 psi  $\sim 6.1^{\circ}\text{C}$ ), while the other end was still in equilibrium (Fig. 2.19). Because the majority of thermocouples were located in the confining fluid, not the sample, these temperatures are a best estimate of the sample temperature. During the temperature modifications, effects of the secondary hydrate formation resulting from the thermal dissociation were monitored by X-ray CT scanning, changes in methane volume, and capillary pressures changes. The first temperature gradient was applied on Day 6, when the temperature of the fluid in the aluminum coil was raised elevating the temperature of a region in the sample to outside the hydrate stability zone for approximately 1 day, then lowered again so the entire system was in the stable hydrate

zone. This was repeated 3 more times, for a total of 4 cycles over a period of 30 days (Fig. 2.20). Before final dissociation by warming, the system was set at a 'mid' point temperature.

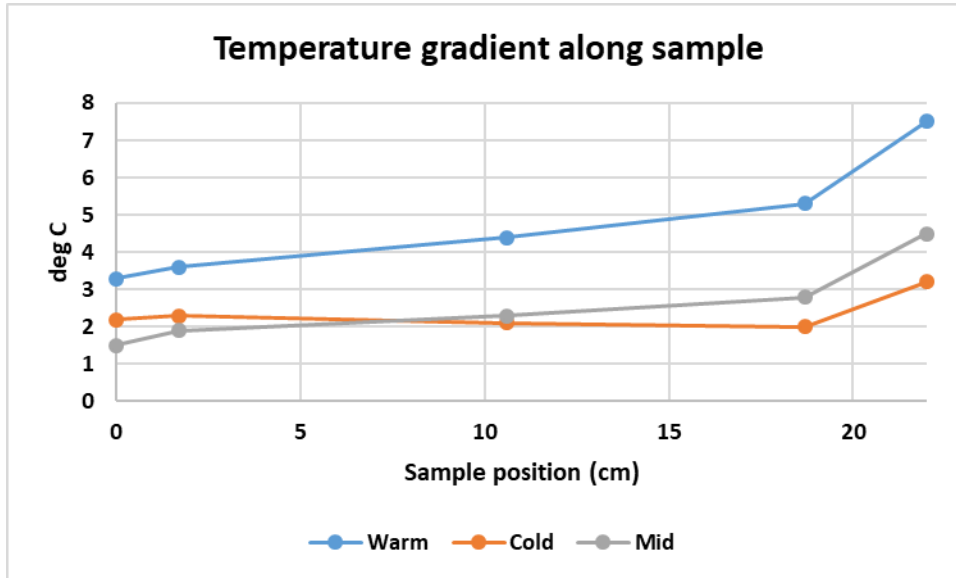


Fig. 2.19. Temperature profiles along sample. Position of the thermocouples are measured endcap next to the sample.

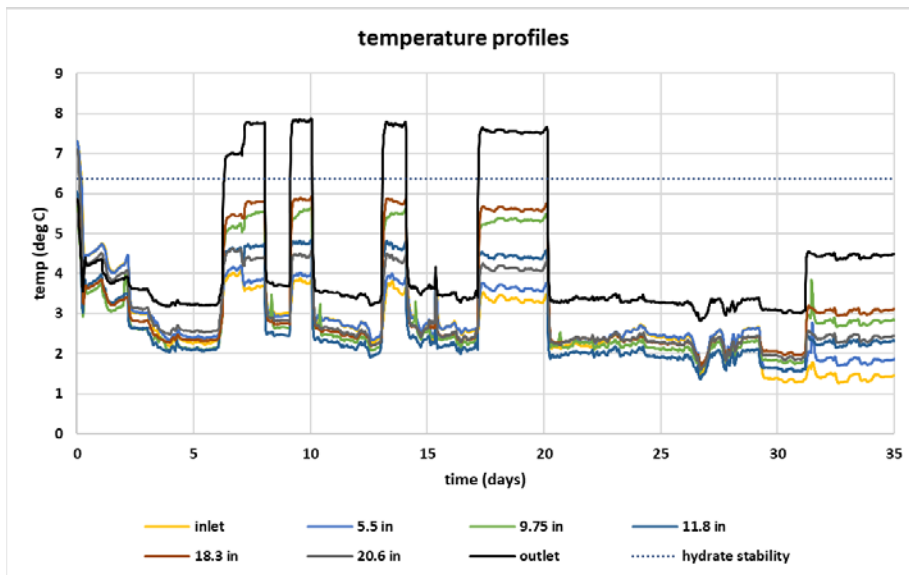


Fig. 2.20. Temperature profiles in sample. Position of the thermocouples are measured from the inlet endcap of the large vessel. Dashed line indicates temperature where hydrate becomes unstable (pore pressure 700 psi)

The capillary pressure sensors were connected to the negative side of a differential pressure transducer (DPT), and the positive side was connected to sample inlet. The ranges on the DPTs varied. The expected capillary pressures were < 10 psi, and one DPT had a 10 psi range. The other two DPTs had ranges exceeding 60 psi. The expected behavior of the system would be that when water saturated, the capillary pressure would be near zero. When gas is present, a capillary pressure could be recorded.

When the temperature was above the equilibrium temperature, the DPTs showed low values indicating that water was freed from the hydrate (Fig. 2.21). When the sample was cold, the DPT showed large positive differential pressure indicating the sample was dry due to water being consumed by hydrate. The three sensors behaved similarly. The sensor 'middle DPT' (DelP mid in Fig. 2.21) was connected to a sensor with a maximum range of 10 psi which resulted in lower apparent readings for that position. Despite differences in hydrate conditions in the sample, the capillary sensors did not show differences in the values depending on position within the sample. One exception is during the mid-temperature cycle during the end of the experiment, there seemed to be some variation in the values of the three sensors. During this the mid-temperature setting, which started around day 32 (Fig. 2.20), a different pattern was observed in the sensors (Fig. 3.1.1), which was likely due to a pressure drop in the inlet (data not shown), and was unrelated to hydrate formation.

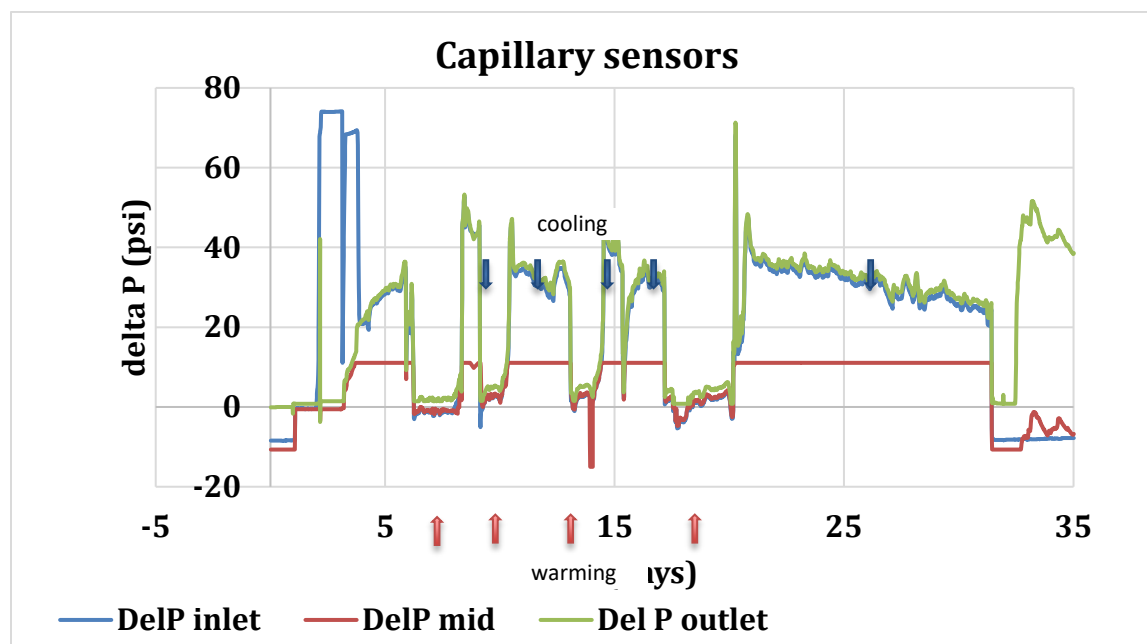


Fig. 2.21. Capillary pressures at the sensors as measured by differential pressure transducers.

During the warming and cooling process, X-ray CT was used to monitor methane hydrate formation in the sample (Fig. 2.22). The brighter colors (yellow) indicate higher density, and the darker colors (purple) indicate lower density (e.g. more gas present). As hydrate forms, the density of the sample increases slightly. After hydrate formation is complete the sample is saturated with water. Comparing panels Fig. 2.22 (b) and (c), hydrate dissociation during warming is shown by the lower density region to the right.

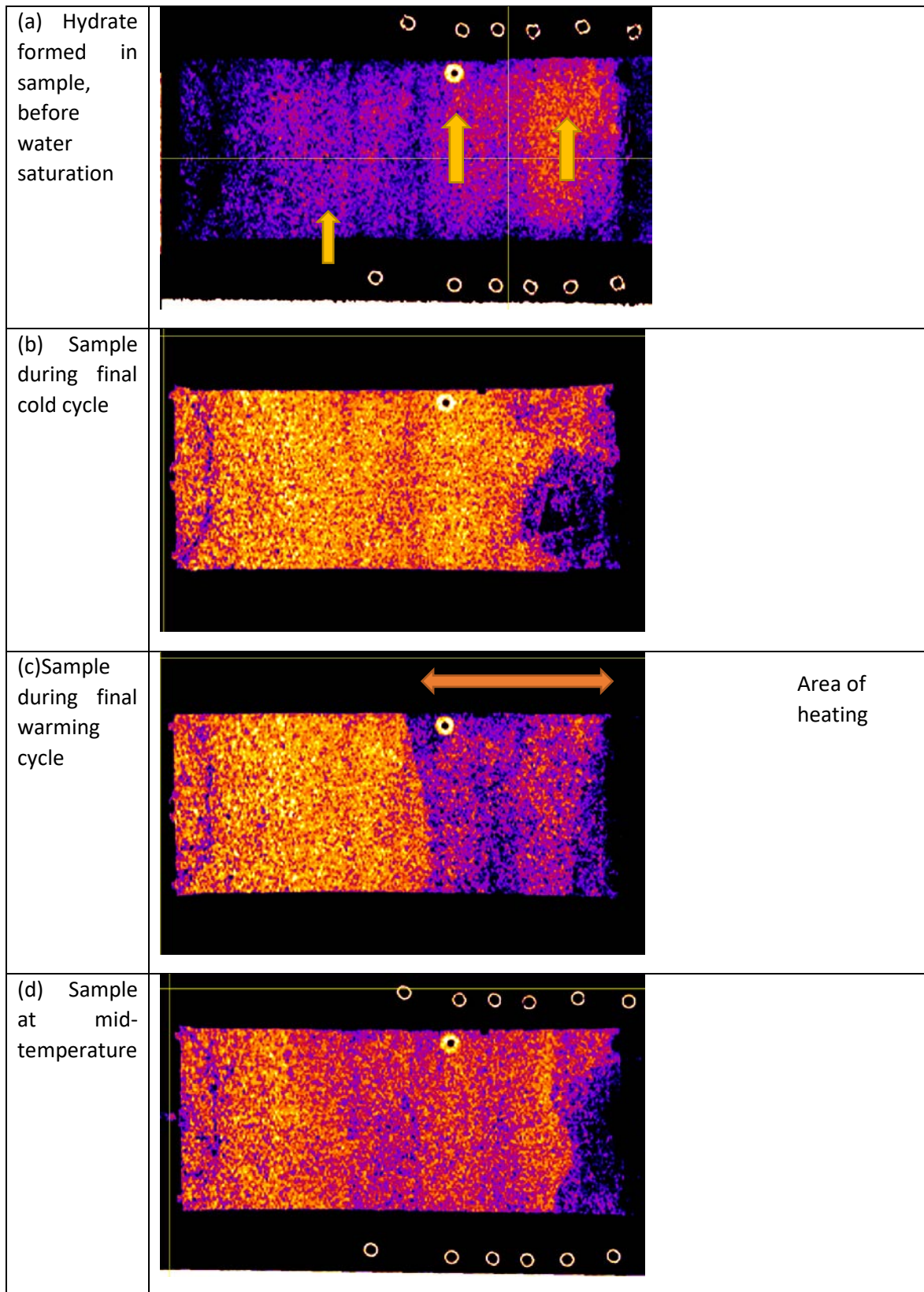
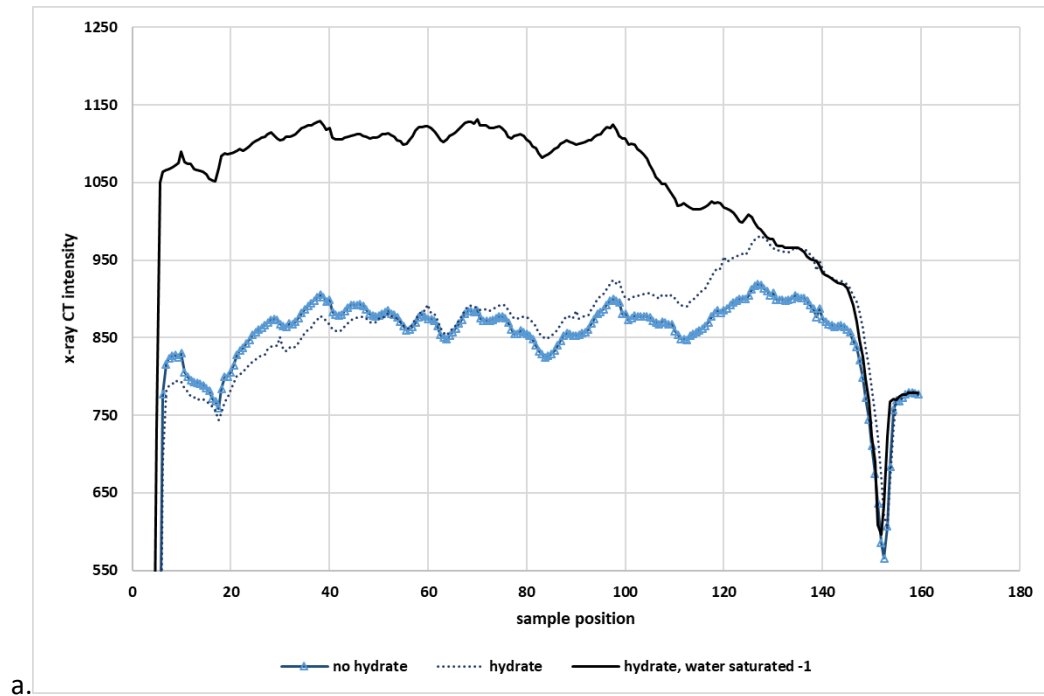


Fig. 2.22. Density cross sections of sample under different conditions (a) hydrate formation (b) water saturated, cold (c) water saturated, warm (d) mid-temperature. Arrows indicate approximate location

of capillary sensors – the middle sensor (white circle at the top center of the sample) is visible in all four panels.

Fig. 2.23 (a) shows the average change in intensity along the axis of the sample during hydrate formation and saturation. Fig. 2.23 (b) shows average z-axis profiles during warm and cold states. The intensity change is correlated to the average density of each slice along the sample during the experiment. When the sample is entirely within the hydrate stability zone (cold state) the average intensity is higher, and when hydrate dissociated during the warm state, the average intensity of the sample in the heated zone decreases. Note that during each cycle hydrate formation patterns change as shown by changes in the shape of the curves, while for in the warm state, the pattern remains relatively unchanged. This indicates that hydrate distribution can change during each cycle, but the sand in the column is stable. The change in hydrate distribution is most likely due to redistribution of water in the sample during each cycle (Fig. 2.24).



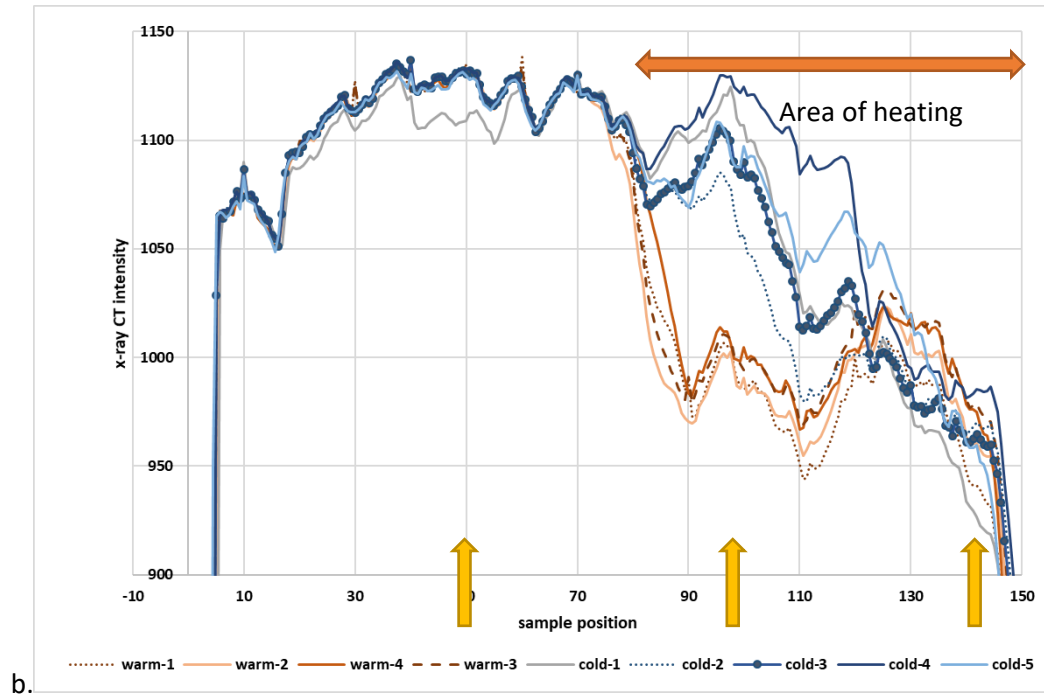
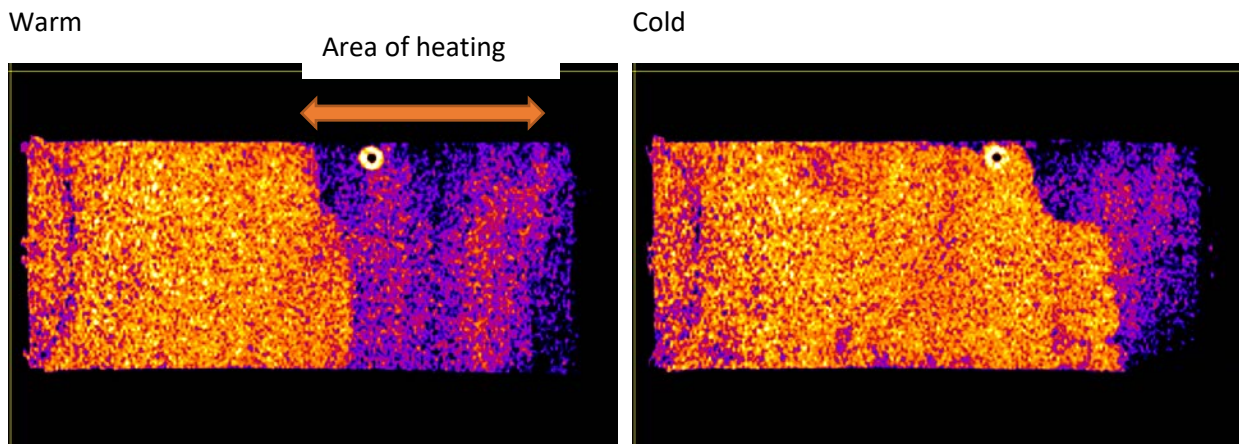
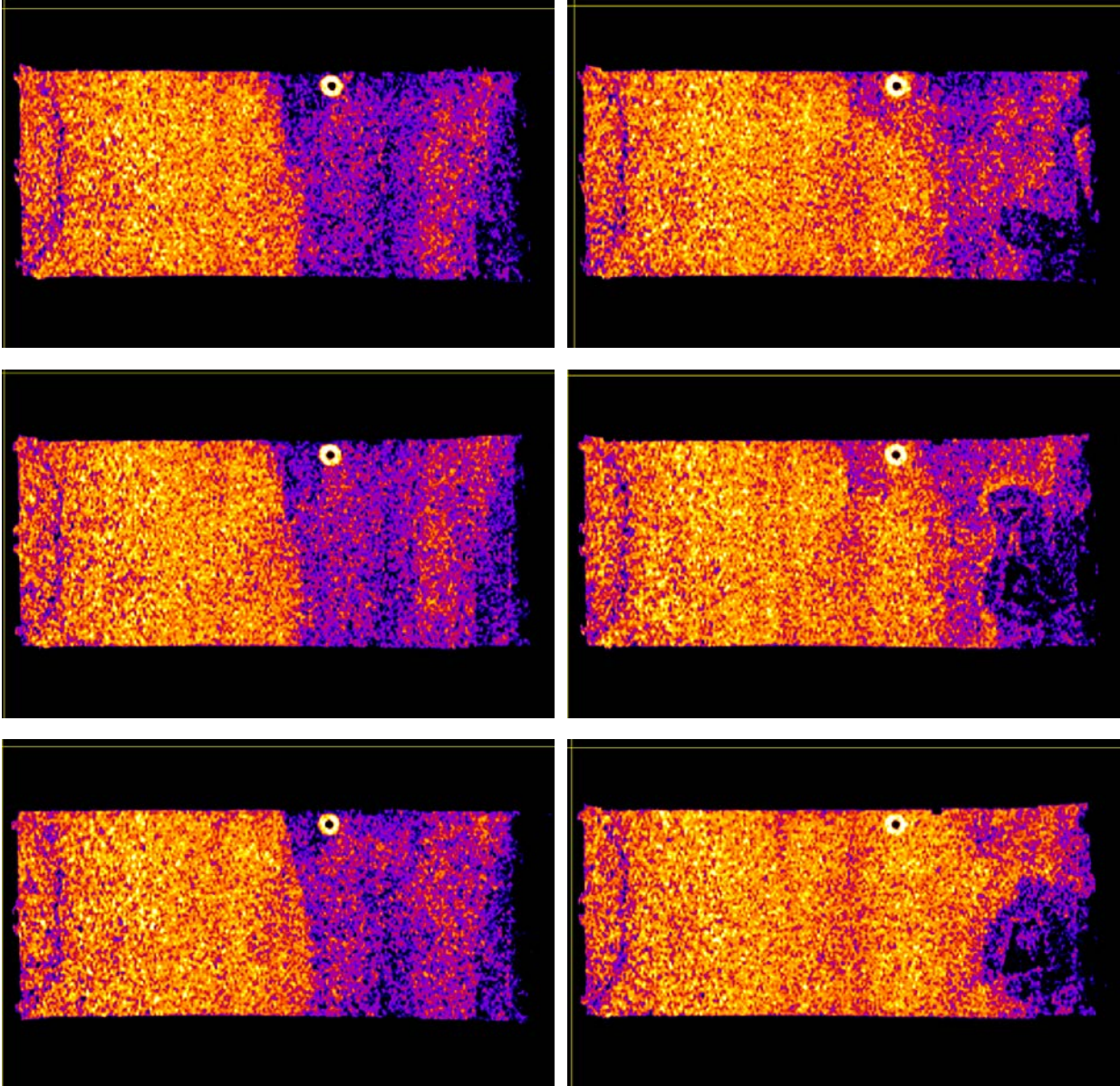


Fig. 2.23. (a) profile of average intensity during hydrate formation and water saturation. (b) profiles of average intensity of the sample during warming and cooling cycles. Arrows indicate approximate location of capillary sensors.





**Fig. 2.24. X-ray CT image cross sections of the warm and cold states for the four cycles. Changes in hydrate distribution in the cold state (sample all one temperature) was probably due to redistribution of the water in the sample during each cycle.**

During each cycle methane volume changes were measured (Table 2.2, Fig. 2.25) and each cycle was relatively consistent. The first cold cycle has higher methane consumption because this volume represents hydrate formation throughout the sample. The second cycle had lower methane uptake/release than the following cycles, probably due to better water saturation at the outlet. The confining volume changes with each warming/cooling cycle to maintain confining pressure on the sample and likely due to volume change of the sample with methane converting to gas within the sample.

**Table 2.2. Volume changes (mL) of methane during each warming and cooling cycle.**

	Cycle 1	Cycle 2	Cycle 3	Cycle 4	Cycle 5
Cold	179	122	145	148	145
Warm	na	107	130	140	143
Confining vol	na	5.0	4.6	5.0	4.9

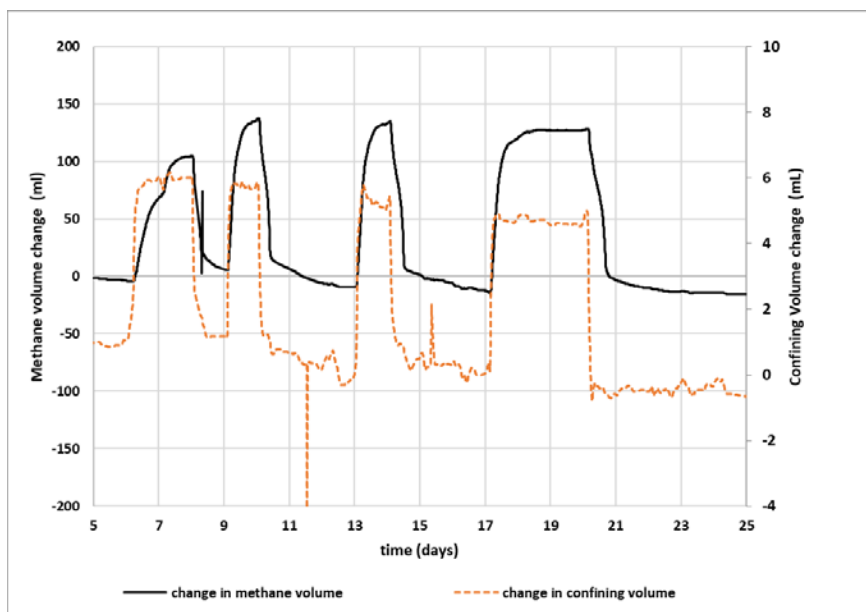


**Fig.2.25. Confining and methane volume change during heating and warming cycles. When warmed, methane volume increases in the pump (positive change on graph) and when cooled, methane volume leaves pump and flows into sample (negative change on graph). This is also reflected in the confining volume, which shows an increase in volume in pump (larger sample size) when under warm conditions and decrease in volume when cooling (smaller sample size). Overall decrease in confining volume over time is likely due to leaks in the system.**

Methane gas should appear as lower density areas within X-ray CT scan. To visualize, CT images from the cold sample were subtracted from CT images in the warm cycle. Results of the image subtraction (warm minus cold) from Cycle 2 are shown in Fig.2.26. The dark areas in this image indicate increasing density with cooling and are located near the interface between the heated and non-heated zones and near the endcap (right of the sample). Z-axis profiles of average density along the sample for the heated zone only also show these density variations Fig. 2.27.

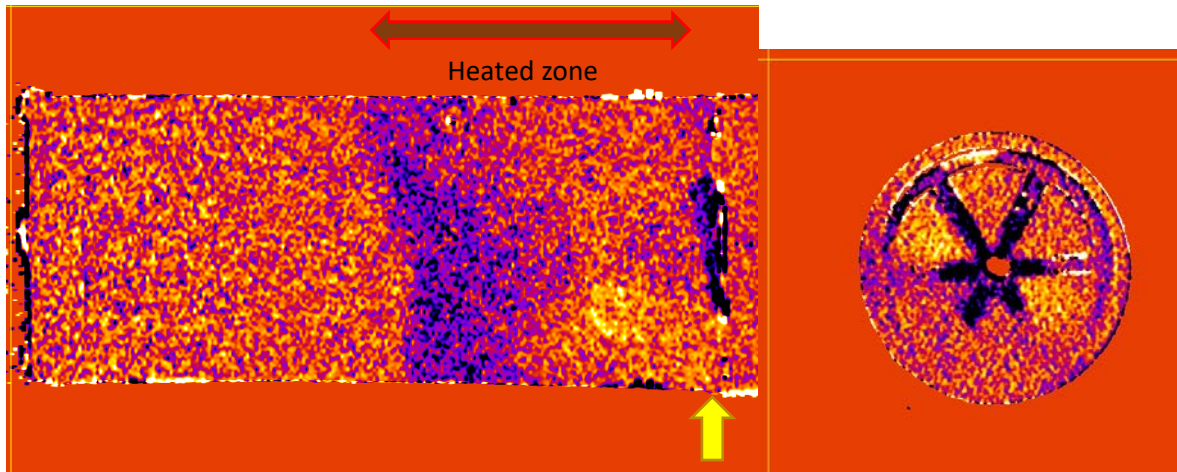


Fig.2.26. Difference between warm sample and cold sample for cycle 2. Darker color (purple and black) indicated areas were density increases on cooling. Area near the outlet endcap to the right of the sample also shown in cross section (location indicated by arrow) shows the accumulation of low density fluid which may be methane in gas form.

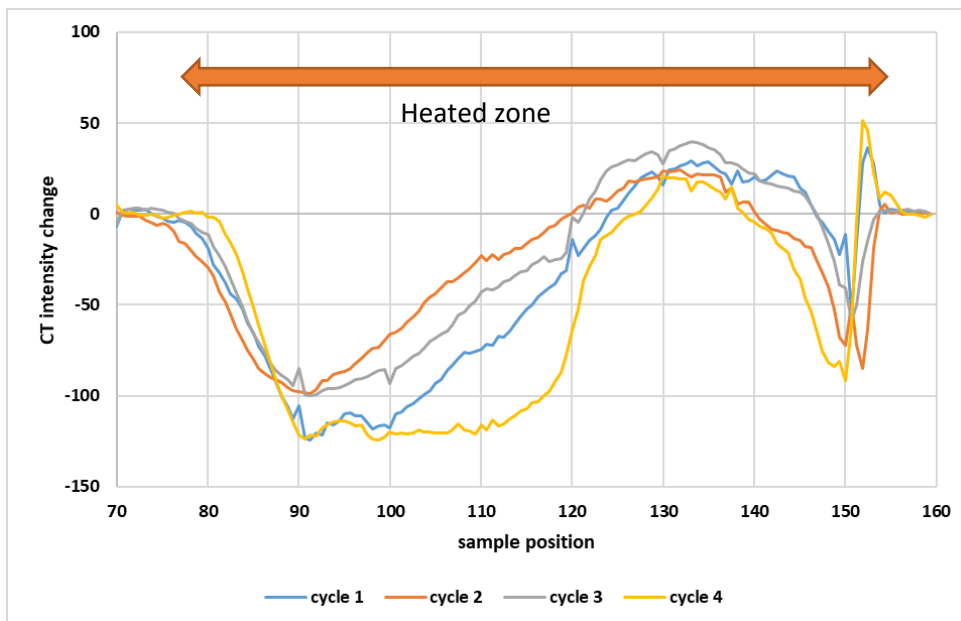


Fig.2.27. Profile of the average density difference along the z-axis between the warm and cold samples, showing the heated zone only. Most density changes were on the sample half closer to the cold zone, and also near the outlet of the sample.

## 2.6 Conclusions

Many experiments were performed over the course of this project. In viewing geomechanical changes, conclusions can be summarized as:

1. Sand control is critical. No samples catastrophically failed when sand was controlled.
2. Muds will compact upon the increase of effective stress. Our samples were not large enough to show significant failure, but compaction was obvious. In our tests, we may not have waited a sufficient duration prior to starting the large effective stress changes to clearly quantify this for the specific effective stress change but it was easy to visualize.
3. Sample size increased slightly upon hydrate formation. This is in contrast to earlier observations (Kneafsey et al., 2007; Moridis et al., 2005). This was not always easy to detect however. Direct observation by CT is only sensitive over large volumes, or can not detect significant sample changes over small volumes.
4. In experiments performed here, erosion of the mud layer was not significant.
5. A number of unique capabilities were developed in this project. These include the ability to quantify capillary pressure during hydrate formation and hydrate-related processes. Another important capability whose development continued was the application of a temperature gradient to carefully control the location of hydrate formation and dissociation and observe related processes. These new capabilities allow teasing out the effect of different processes.

### **3. Relative Permeability in Presence of Hydrate and Identification of Hysteresis in Hydrate Stability (Task 3-Subtask 3.4, Subtask 3.5 by Adams J., Akkutlu, I.Y., Moridis, G.J.)**

#### **3.1. Construction of the Relative Permeability Data in Presence of Hydrate (Subtask 3.4)**

##### **3.1.1. Introduction**

In reservoir simulation technologies, it is a common practice to capture multi-phase flow dynamics using relative permeability curves. However, the nature of these curves is not well established for the simulation of methane flow and production from the hydrate bearing formations. The current relative permeability curves are based on correlations developed in the absence of hydrates and they may not be suitable for the representation of the flow. In Subtask 3.4, apart from the work on geo-mechanics, we plan to perform multi-phase flow studies at varying levels of hydrate saturation in order to construct relative permeability curves that are suitable for the methane production method of depressurization.

Methane hydrate will be formed in a sand pack in the laboratory in stages, ranging from no hydrate to the level of hydrate saturation when the porous medium is no longer permeable. Both mass balance and x-ray computed tomography (CT) will be used to predict the average saturations in the sand pack. Effective permeability and relative permeability to gas will be measured at each stage.

Relative permeability data is one of three key issues on producing from hydrate bearing resources; the other is hydrate reformation during the depressurization, and the structural stability of the reservoir during production. Hydrate re-formation and the associated hysteresis will be addressed in Subtask 3.5; the other two are geomechanics coupled to flow is at the heart of this project. To better understand the relative permeability to gas in the presence of methane hydrate, a series of flow experiments are conducted at Lawrence Berkeley National Laboratory (LBNL). The setup includes a pressure vessel transparent to x-rays so that a CT scanner can be used to image the system while the tests are being conducted. Four tests are conducted to measure the effective permeability of packed sand for gas. The relative gas permeability is predicted using the gas permeability data. The relative permeability to water has large fluctuations, we therefore show only the gas permeability data.

Current methods in literature for conducting relative permeability measurements in hydrate vary, from natural hydrate samples and CT scanning (Delli et.al., 2014; Johnson et.al.,2011) to measure capillary pressure in a sand pack (Delli et.al., 2014, Pini et.al., 2013), to using CT scanning in a horizontal vessel and measuring the saturations and differential pressures (Seol et.al., 2011 , Kneafsey et.al., 2010), but all have the same trends controlling hydrate saturations and mitigating its formation during testing. Natural hydrate samples are challenging to perform any experiment on, especially the flow and permeability experiments (Johnson et.al., 2011). The flow measurements suffer from non-homogeneous saturations, which creates uncertainties in the permeability calculations since the basic assumptions are that the saturations are uniform (Honarpour et. Al., 1988). To get around this problem, the use of uniform sand packs is considered. The sand is packed in such a way that its density variations are not too large so that, when hydrate is formed, its porosity and permeability are uniform. When the hydrate saturation is as uniform as possible, the permeability experiments can be conducted for gas effective permeability. The flowing gas needs to be colder than the equilibrium temperature of hydrate formation. When relative permeability is needed, however, a few additional effects occur: hydrate start to form or melt during the

flow if the pressure changes rapidly, and the trick is to keep the hydrate formation rate as slow as possible thus mitigating the effects, though this is easier said than done (Rees et. al., 2011). Hydrate when forming causes pore volume to decrease thus increasing the capillary pressure of the sand pack, this is not done uniformly, but is driven by the local saturations and flow characteristics (Rees et. al., 2011). The capillary pressure developing due to the hydrate formation, creates a drive, which forces water in the sand pack to the hydrate rich zones. This causes a no-flow zone for gas by having low-permeability regions that are saturated with hydrate and water. Consequently, the low water saturation or “dry” and high-permeability regions are what is measured during the flow experiments. This does not mean that hydrate relative permeability experiments cannot be done, it just means that new ways of mitigating these local effects need to be found.

### **3.1.2. Laboratory Setup**

Previous studies have shown that injection of the inert gases causes dissociation of the hydrate during the flow measurements and influence the average saturations at which the relative permeability is measured. To predict the relative permeability in the presence of hydrate, the hydrate saturation must stay the same for all the ratios of the volumes of the flowing phases. Therefore, one important consideration for the measurements is the requirement to have a stable hydrate saturation during the flow measurement stage. To accomplish this the pressure of the system needs to be just below the dissociation pressure, or right at it, thus preventing the formation of new hydrate.

The excess gas method (more gas stoichiometrically than water) is used in the sand pack so that all water is converted to hydrate. The pore volume is estimated from a spread sheet using the grain size distribution. The grain size distribution of the sand used is as follows: 49.4% 60 mesh, 43.2% 70 mesh, 4.1% 80 mesh, 3.1% 50 mesh, 0.1% 80. The sand is weighed, and water is added to the desired level using an accurate scale. The sand and water are mixed thoroughly and left to sit overnight in a plastic bag. Next a sleeve 2 inches diameter by 8 inches in length is chosen. The endcaps for the sleeve are chosen and the inlet side is coated with silicon high vacuum grease, to prevent the leaks. A stainless wire is then wrapped around the sleeve at the end cap. The inlet, and outlet of the end caps is filled with steel wool to act as a filter and not let sand into the auxiliary lines and pumps. Then the sleeve is filled with the sand, this is done by taking a spoonful of sand and tamping it down. There are 60 tamps per spoonful. This is repeated until the sleeve is filled with six inches of sand. Next the outlet end cap is installed in the same manner as the inlet end cap. The filled sleeve is attached to the head of the pressure vessel and a high-pressure plastic tube is routed from the outlet to the head. Next, the inside of the pressure vessel is coated with the same high vacuum silicon grease to prevent corrosion. Once completed, the vessel head is installed with the sleeve attached.

There are 4 different main lines that are installed to the vessel head, the gas inlet, the gas outlet, the water inlet, and the confining pressure, see Fig. 3.1. Transducers and valves are placed on each line, and a manifold between the gas inlet and the gas outlet is joined by a differential Azbil pressure transmitter. The water injection is placed after the differential pressure transmitter measurement point. On the outlet side, a volume 3/8-inch T fitting (the splitter, which is oriented vertically) is used to prevent two-phase flow effects from affecting the differential pressure transmitter. The inlet gas and the inlet water lines are routed through a heat exchanger to chill the injected fluids so that hydrate dissociation does not occur.

The vessel has a sleeve filled with a ratio of 1:1 propylene glycol water mixture to flow through so that the temperature of the sand pack can be controlled.

Fig. 3.1 shows the layout of the experimental apparatus used for the study. All the connecting lines are 1/8-inch stainless steel Swagelok 5,000-psi-rated lines. The setup is built on a general electric medical CT scanner, and the sample is scanned initially and scanned each time a change in the saturations is expected to take place due to flow or hydrate formation.

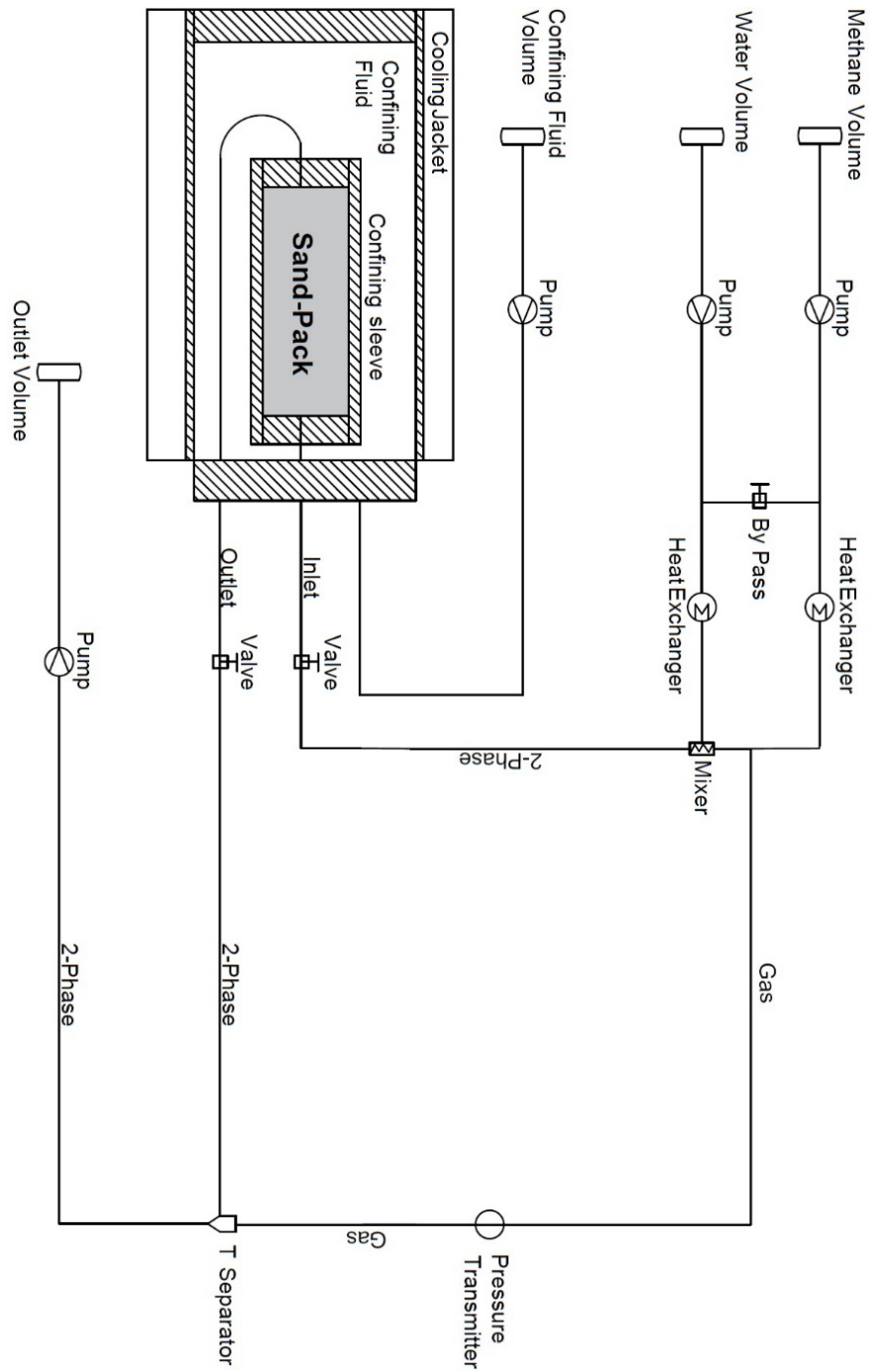


**Fig. 3.1: Diagram showing the laboratory setup of the sand pack and the auxiliary units including the syringe pumps, differential pressure transmitter, gas-water mixer, and the splitter.**

In Fig. 3.1 the separator used is a T fitting between the differential pressure transmitter and the outlet. The gas phase rises to the top and the water is separated downwards toward the volume of the outlet pump. While the separator works reasonably well, it can cause pressure build up in the gas phase during the flow measurements. This can cause complications in pressure response. This type of setup, when the T separator is vertical, can create a Trompe (a type of air compressor without any moving parts). This contributes to the pressure oscillations that are seen in Fig. 3.2 (Azzi et. al., 2010). While this buildup will affect the system, due to the low volumes and low head pressure on the sand pack, its magnitude is expected to be low relative to the pressure values measured during the experiment.

### 3.1.3. Experimental Procedure

The experimental procedure involves steady-state flow measurements and has three main parts: (i) single-phase (gas) flow measurements at room temperature in the absence of hydrates, (ii) gas flow measurements at low temperatures with hydrates, and (iii) multi-phase flow measurements where a fixed ratio of gas and water flow rates is injected. Each part includes measurement of effective gas permeability, followed by the relative gas permeability.

For all the flow experiments the initial steps are as follows:

1. First step is to check the assembly for leaks by pressurizing the lines to 100 psi initially. To test the lines at higher pressure, the sand pack is isolated from the other lines at the inlet and outlets of the vessel. Then, each line and fitting are checked with soapy water at the operating pressure of 500psi, where a leaky component produces bubbles. If leaks are found, they are dealt with by tightening the fittings. Then the system is returned to atmospheric pressure and a vacuum is placed on the system. Next, the system is pressurized with low pressure carbon dioxide to flush the nitrogen out of the system, and any nitrogen out of solution, since CO<sub>2</sub> is preferentially dissolved and displaces nitrogen molecules in water. Next, another vacuum is placed on the system and the system is flushed with methane gas. The vacuum and methane injection thus remove the CO<sub>2</sub> gas and provide an environment for pure methane hydrate formation to occur.
2. The sand pack is next needed to be pressurized to operating conditions at 500 psi pore pressure and 600 psi confining pressure. A pressure difference of 100 psi is kept for the sand pack. The pore pressure and confining pressure are increased by 50 psi increments. The confining pressure is controlled manually so that the fluctuations are kept in the 25-45 psi range during pressurization.
3. Once the sample is pressurized the system is left to equilibrate for a few hours, this allows the stress field in the sand pack to stabilize. Once the setup is ready, the initial CT scan is performed, and the corresponding images are saved.

Now, we perform the first part of the flow experiments, i.e., the steady-state single phase (gas) flow experiment. This test is performed at room temperature.

4. Prior to begin the gas flow, the zero differential pressure point needs to be established, so the differential pressure transmitter is closed in at the manifold and the data recorded for a few minutes, this is to provide a zero of the system. Then, the transmitter is opened to the system, and the upstream and downstream bypass valve is closed. The inlet and outlet pumps are set to constant flow, inlet injecting at constant rate, and outlet drawing at a constant rate.

5. Steady-state flow measurements are performed. The applied gas flow rates in ml/min are as follows: 20, 25, 40, 45, all the while the pressure difference, delta P, is measured. After the gas flow is completed at these rates, the sand pack is scanned, and the images saved.
6. Once the pressure and flow rate data are collected, the permeability of the sand pack is estimated using Darcy's equation of flow for ideal gases:

$$\frac{Q}{A} = \frac{k}{\mu} \left( \frac{p_1^2 - p_2^2}{2 * L * p_2} \right) \quad (3.1)$$

Eq. 3.1 is used in graphical format as a straight line. When  $q/A$  versus  $(p_1^2 - p_2^2)/(2p_2L)$  is plotted, the slope is equal to  $k/\mu$  and it can be used to solve for the permeability, if the methane viscosity at the room temperature is known.

7. Next step is to repeat the flow measurements at different rates when the sand pack is cooled so that the methane hydrate crystals form in the sand pack. To form hydrate, we perform the following steps: at the operating pressure of 500 psi the system is cooled down to 2 degrees Celsius to initiate the hydrate crystallization. The cooling process is observed by keeping track of the temperature change in the system. When the cooling is complete, in order to determine if the hydrate is finished forming, gas volume is recorded. If there is no change in the inlet volume of the pump, then hydrate formation is considered complete, or at the least, the crystallization is occurring at very low rate. Following the hydrate formation, the flow is considered at a fixed rate, as we did in Step 5 in the absence of hydrate. Finally, the sand pack is scanned again.
8. Steps 5-6 are repeated with the sand pack in the presence of hydrates.

The above section outlines the steps for single-phase (gas) flow at a fixed saturation of water and methane hydrate. In order to see the impact of hydrates on the flow, the hydrate saturation needs to be increased, but this must be done in the sand pack in a uniform fashion. We ensure this with the following steps:

9. Water and gas were simultaneously injected at the equal and constant rate of 6 ml/minute. Co-injection continued until 3 pore volumes of water were filtrated through the sand pack. At the end of co-injection, the data is collected for the effective gas permeability. Step 9 was repeated twice, and these two steps produced intermediate hydrate saturation. When there is hydrate present in the sand pack, the rates measured ranged in between 0.25 ml/min to 6 ml/min. The procedure continues until the water injection and hydrate formation resulted in no flow. This final stage will be the case when hydrate saturation reached to no-flow conditions, thus the measurements were stopped for the single phase (gas) flow.
10. Finally, the steady-state multi-phase flow experiments were conducted at 20 degrees Celsius when a total (water + gas) flow rate of 12 ml/min was flowed through the sand pack. The gas/water flow rate ratios applied during the experiments were 8/4, 6/6, and 4/8 ml/min. Three pore volumes of water were injected to ensure that steady state was reached. Fig. 3.2 shows the

flow rates applied and the differential pressure values measured in time during the steady-state multi-phase flow experiments.

There are oscillations in pressure that are quite large, this is due to two phenomena. Firstly, the tubes that injected the fluids are 1.45 mm in diameter, and for the two-phase flow, this results in capillary tube effects, thus causing fluctuation. Secondly, the outlet has the two phases flow out into a T-junction, which was shown as the fluid separator in Fig. 3.1. A T-type separator can act as trompe. A trompe is a device that separates gas and water due to buoyancy, causing the gas to build pressure in the gas only region if there is no outlet, where the gas pressure limit is the pressure head of the water. Historically this device was used as a water compressor in mines and thus was useful, but here it produces oscillations in the pressure transducer response.

The selected data points in Fig. 3.2 shows the smooth data (shown in green) near the middle to the end of each flow rate, this allows for equilibration of the saturations thus the pressure drop. Taking this data, the relative permeability can be calculated using Darcy's law. Next, we measure the effective gas permeability in the presence of hydrate and compared to the effective permeability with no hydrate, as discussed earlier in Figures 3.7 and 3.8.

At the end of the injection period for each ratio the sand pack was scanned, and the images saved. The resulting data is then used to calculate the effective gas permeability at different saturations.

11. Next, the relative gas permeability is calculated from the effective gas permeability data. The gas relative permeability at saturation  $S_w$  is defined in our study as the effective permeability  $k_g$  at that saturation divided by the permeability at the irreducible water saturation  $k_g @_{S_{w,irr}}$  :

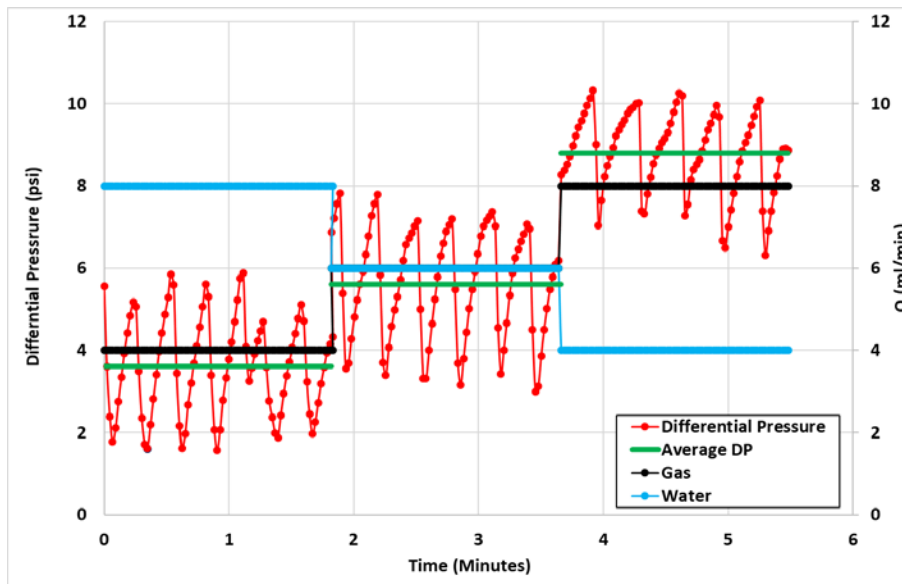


**Fig. 3.2:** Differential pressure versus time when the steady-state flow is reached. The secondary y-axis showing the flow rates of the gas and water is on the right. The green line represents the data used for the gas relative permeability estimation using the Darcy's law.

$$k_{rg} = \frac{k_g}{k_g @ S_{w,irr}} \quad (3.2)$$

We perform the relative permeability calculations using Eq. 3.2 for each flow experiments separately such that there will be separate curves for the single phase and multi-phase flow measurements and in the presence of hydrate.

### 3.1.3.1 Estimation of the Saturations using X-ray CT Scanning

CT scan data can be converted to density by using a calibration curve that relates the Hounsfield units to density in  $g/cm^3$  thus allowing different calculations, such as saturations of water, hydrate, or porosity. To determine the water saturation in the sand pack from a CT image, the image is calibrated to a standard that relates densities of different materials to that of Hounsfield's units. Once this is done, the image is a map of density in  $g/cm^3$  and a mass balance can be conducted. Eq. 3.3 shows the mass balance in the absence of the methane hydrate phase.

$$\rho_{vox} = \frac{m_{vox}}{V_{vox}} = \frac{\rho_{sand} * V_{sand} + \rho_{Water} * V_p * S_w + \rho_{CH_4} * V_p * S_{CH_4}}{V_{vox}} \quad (3.3)$$

where  $\rho$  is the mass density and  $V_p$  is the pore volume of the sand pack. Eq. 3.3 can be changed to a mass base by multiplying both sides by the voxel volume,  $V_{vox}$ . Eq. 3.3 can then be reduced by eliminating the methane portion. This is possible due to the density of methane being relatively very low. The value for methane is near zero on the CT image. Thus, when the methane term drops out, Eq. 3.4 is the resulting mass balance:

$$\rho_{vox} = \frac{m_{vox}}{V_{vox}} = \rho_{sand} * V_{sand} + \rho_{Water} * V_p * S_w \quad (3.4)$$

Eq. 3.4 is then solved for the water saturation  $S_{w1}$  in the absence of hydrate:

$$S_{w1} = \frac{V_{vox} \rho_{vox} - \rho_{sand} * V_{sand}}{\rho_{Water} * V_p} \quad (3.5)$$

In the presence of hydrate:

$$\rho_{vox} = \frac{m_{vox}}{V_{vox}} = \frac{\rho_{sand} * V_{sand} + \rho_{Water} * V_p * S_{w2} + \rho_h * V_p * S_H}{V_{vox}} \quad (3.6)$$

Here,  $S_{w2}$  is the water saturation in the sand pack presence of hydrate. Taking the difference of Eq. 3.6 and Eq. 3.3 results in Eq. 3.7:

$$(\rho_{vox2} - \rho_{vox1}) V_{vox} = (m_{w2} - m_{w1}) + m_H \quad (3.7)$$

The difference in the masses of the two water saturations is the water content of the hydrate. It can be shown that the ratio of the molecular weights of the hydrate and the water is as in Eq. 3.8:

$$m_W = \frac{M_W}{M_H} = \frac{1}{1.1469 m_W} \quad (3.8)$$

**Table 3.1: Parameters used for the estimation of saturations using x-ray CT**

$V_{vox}$ (cm <sup>3</sup> )	$V_p$ (cm <sup>3</sup> )	$\rho_h$ g/cm <sup>3</sup>	$\rho_w$ g/cm <sup>3</sup>
2.384e-5	8.583e-6	0.95	1.00

In the voxel we have:

$$(m_{w2} - m_{w1}) = m_H \quad (3.9)$$

Taking Eq. 3.9 and substituting into Eq. 3.7 results in Eq. 3.10:

$$m_H = \frac{\Delta\rho_{vox}V_{vox}}{1.87194} \quad (3.10)$$

Then, the hydrate saturation can be determined from the CT scan as:

$$S_H = \frac{V_{vox}*\Delta\rho_{vox}}{1.87194\rho_H*V_p} \quad (3.11)$$

Once the hydrate saturation is determined, the free water content in the sand pack can be calculated too. With some algebra Eq. 3.12 can be obtained for the water saturation in the presence of hydrate:

$$S_{w2} = \frac{1.1469m_{w1} - m_H}{1.1469\rho_{Water}*V_p} \quad (3.12)$$

Eq. 3.5 is used to map the water saturations. Eq. 3.11 represents the hydrate saturation, the densities of the sand-pack before and after the hydrate formation are subtracted from each other, i.e., with the hydrate minus no hydrate. This results in a positive value for hydrate and zero or negative for no hydrate. The mass of hydrate then is solved by assuming the hydration number is 6, and the residual water is calculated by Eq. 3.12, by which this residual water will be used in the relative permeability measurements. Table 3.1 shows the constants used for the calculations above.

The average water and hydrate saturations in the sand pack are calculated by summing all the voxel saturation together and dividing it by the total number of voxels. Once the hydrate saturation is found, the water content not in the hydrate can be calculated too, and with some algebra Eq. 3.13 can be given for the water saturation in the presence hydrate.

### 3.1.4. Experimental Results:

#### 3.1.4.1. Steady-state Single-phase (Gas) Flow Experiments

Now, we discuss the steady-state single-phase (gas) flow experiments for the sand pack. First is the gas flow in the absence of hydrate. Fig. 3.3 shows the graphical representation of Darcy's equation as a straight line with the slope equal to 5.9757e-8. The y-axis is the fluid flow rate divided by the cross-sectional area of the sand pack perpendicular to the flow, and the x-axis is the pressure-square difference divided by the length of the sand pack. The slope is then the mobility ( $k/\mu$ ) of the sand-pack. Taking the viscosity of methane at 18C equal to 10.6x10<sup>-6</sup> Pascal-second, the permeability of the sand pack without

hydrate was measured as 0.660 Darcy. Fig. 3.3 (bottom) shows the water saturation distribution in the sand pack with no hydrate after the gas flow experiment was completed. (In the CT images presented in this report, the inlet of flow is on the left and the outlet is on the right.)

The water saturation in the sand pack can be considered uniform; the only exception is the high-water saturation area to the right of the center, shown as the origin of the coordinate system in yellow. The sand pack is estimated to have an average 58% water saturation. This leaves a 42% gas saturation for the circulation at different rates during the permeability estimation.

Fig. 3.4 includes the steady-state single-phase (gas) flow and permeability measurements for the sand pack in the presence of methane hydrate. This experiment belongs to the scanned sand in Fig. 3.3. Using the same approach, the permeability is now estimated to be 0.064 Darcy, which indicated a one-order magnitude reduction in the permeability of the sand pack. Indeed, the hydrate formation causes a significant reduction in permeability.

The data includes only four flow rates due to limitations on the cooling rate of the injecting fluid heat exchanger. Fig. 3.4 (middle) shows the hydrate saturation once the sand pack was cooled and hydrate crystallization took place. Here, the bright orange and white colored areas are hydrate rich regions and the blue and red are dryer areas. The formation of hydrate causes a change in the pore network filled with water and gas. This leads to increases in the capillary pressure and draws the water to the hydrate rich regions, thus causing a non-uniform saturation profile. The average hydrate saturation in the sand pack is 2.5 percent.

In order to see the impact of higher hydrate saturation on the flow, we increased the water saturation in the sand pack. Fig. 3.5 Top shows the sand pack now with an average 18% hydrate saturation. The gas flow experiment at this hydrate saturation showed that the sand pack was no longer permeable. This resulted from injecting a significant volume of water into the system and increasing the average water saturation and forming hydrate to such an extent that the flow system became impermeable to gas. Fig. 3.5 Middle shows the high levels of water saturation ( $S_{w2}$ ) in the sand pack. Fig. 3.5 Bottom shows the transient nature of the differential pressure measured during the gas injection. Clearly, the pressure is not stabilized and kept increasing during the flow measurement, which is indicating the lack of filtration in the sand pack.

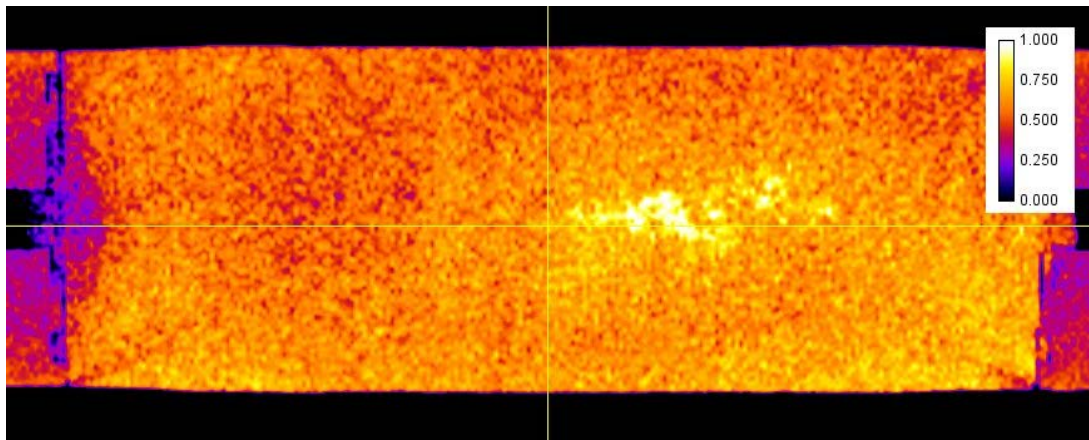
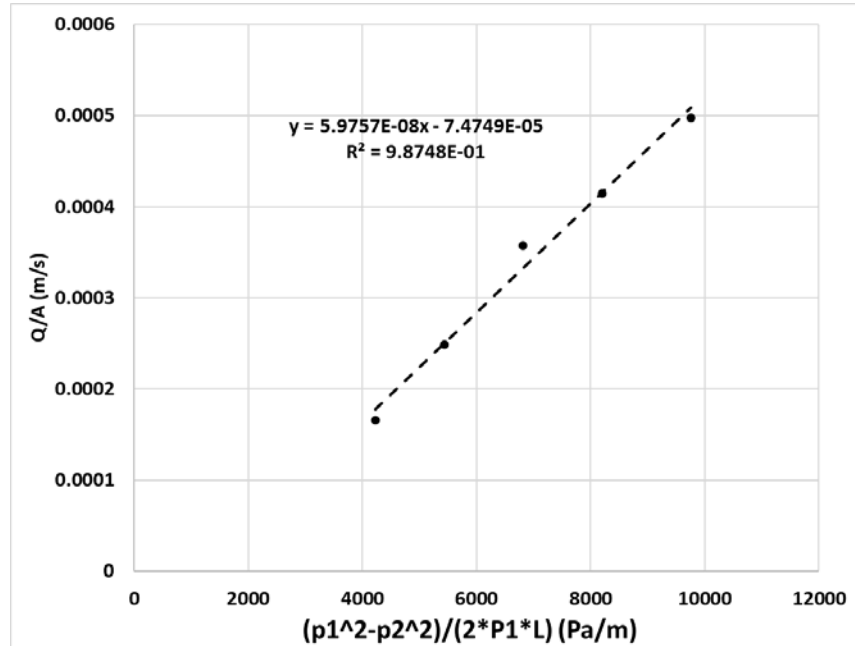


**Fig. 3.3: TOP: Rate versus applied pressure drop during the steady-state single-phase (gas) flow without hydrate in the sand pack. The slope is the mobility and used to estimate the absolute permeability of the sand. BOTTOM: Water saturation distribution in the sand pack at the end of the gas flow experiment.**

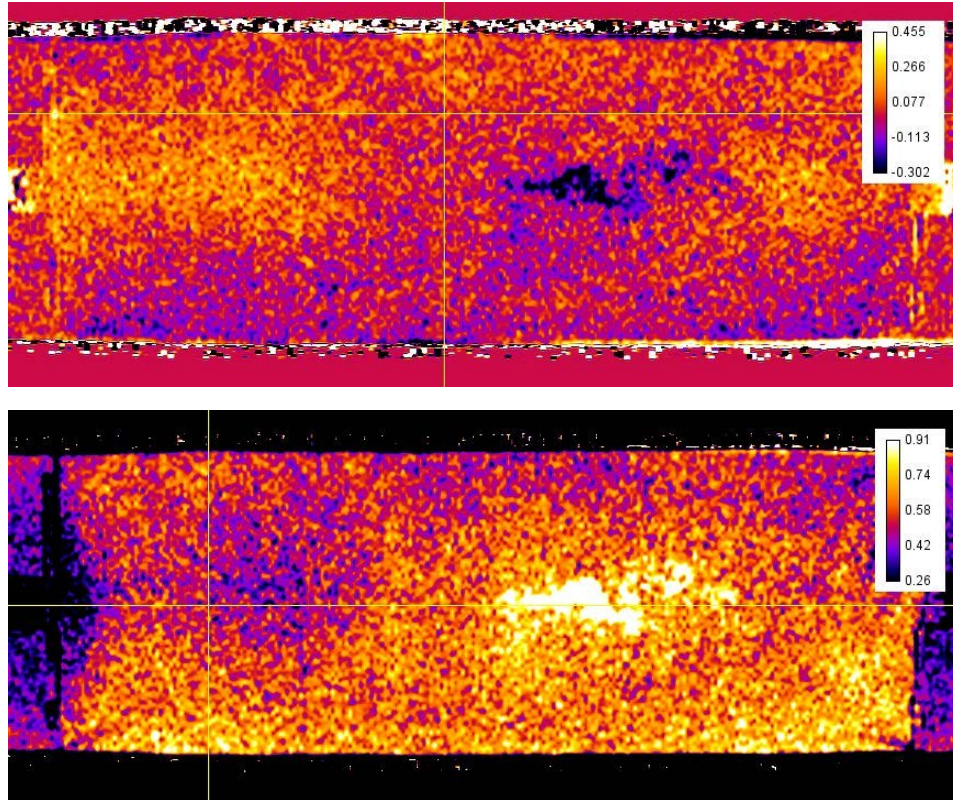
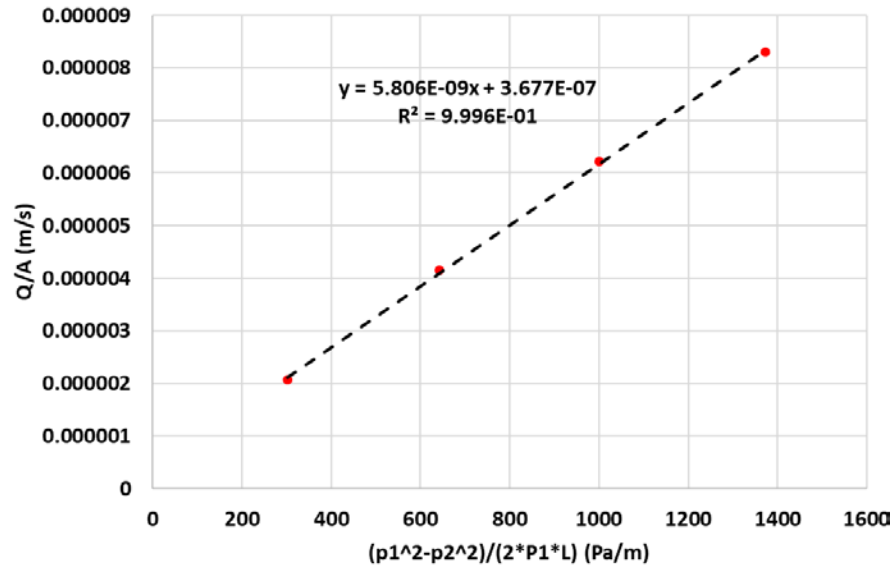
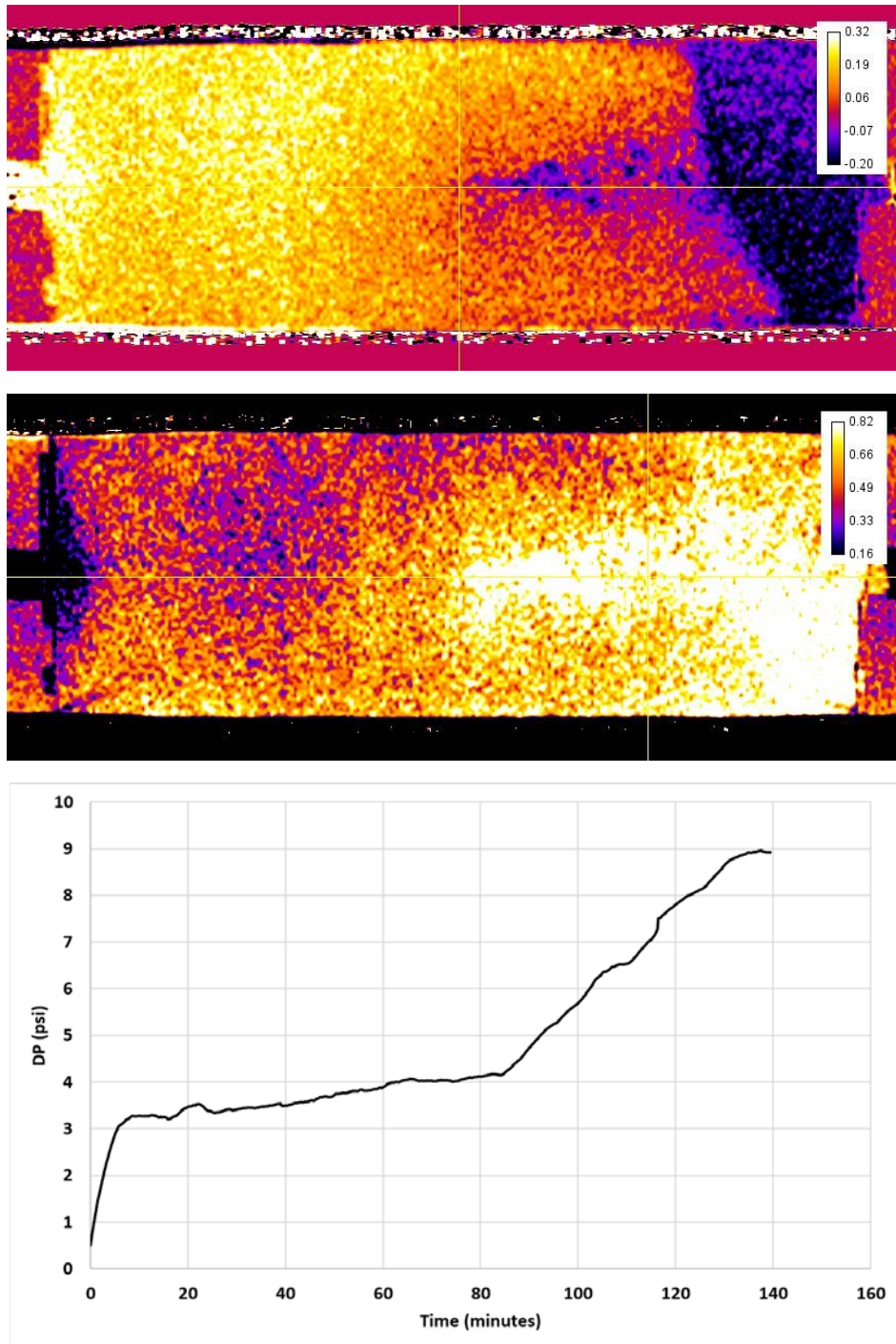


Fig. 3.4: TOP: Rate versus applied pressure drop during the steady-state single-phase (gas) flow with hydrate in the same sand pack in Fig. 3.2. Again, slope is used to determine the permeability of the sand. MIDDLE: Saturation of hydrate in the sand pack after the hydrate formation. Hydrate forms at higher water saturations. Dark region near the center has less hydrate saturation due to low gas availability, therein the water saturation is near 100%. BOTTOM: Residual water saturation in the sand pack after the hydrate formation. This shows a lowered water value when compared to (a).



**Fig. 3.5: (TOP) Hydrate saturation in the sand pack after one pore volume of water is injected into the sand pack. Line between light and dark is a dissociation front caused by the pressure drop at the outlet of the sand pack. (MIDDLE) Residual water saturation in the same sand pack, showing at the downstream region on the right the melted hydrate area with high water saturation, while hydrate bearing upstream region on the left has lower water saturation. (BOTTOM) Differential pressure response during the single-phase (gas) flow. This shows that the system was blocked by the hydrates completely and no flow through the sand pack was occurring.**

The hydrate in the sand pack is melted, and the system is returned to the 20C and 500 psi to perform the flow measurements at various water saturation levels in the absence of methane hydrate. First, we measure the effective gas permeability as a function of the water saturation. The following discusses the construction of the relative gas permeability curve.

Fig. 3.6 shows the measured effective gas permeability values as a function of the water saturation. Since the sand was sifted the permeability variations are expected to be low due to packing. As expected, the results showed a linear relationship between the effective gas permeability and the gas saturation. When the gas saturation in the sand pack was increased, the effective gas permeability improved. We suggest formulating this relationship using a linear regression as follows:

$$k_g = 7.8 * S_g - 2.53 \quad (3.13)$$

To estimate the relative permeability values, a reference effective gas permeability value was needed, which is often the effective gas permeability at the irreducible water saturation. 10% water saturation was chosen as the irreducible water saturation of the sand pack from the literature (Naar et. al., 1962) due to constraints in time and scope of the experiment. Using Eq. 3.13, the resulting gas effective permeability at the irreducible water saturation is predicted 4.49 Darcy.

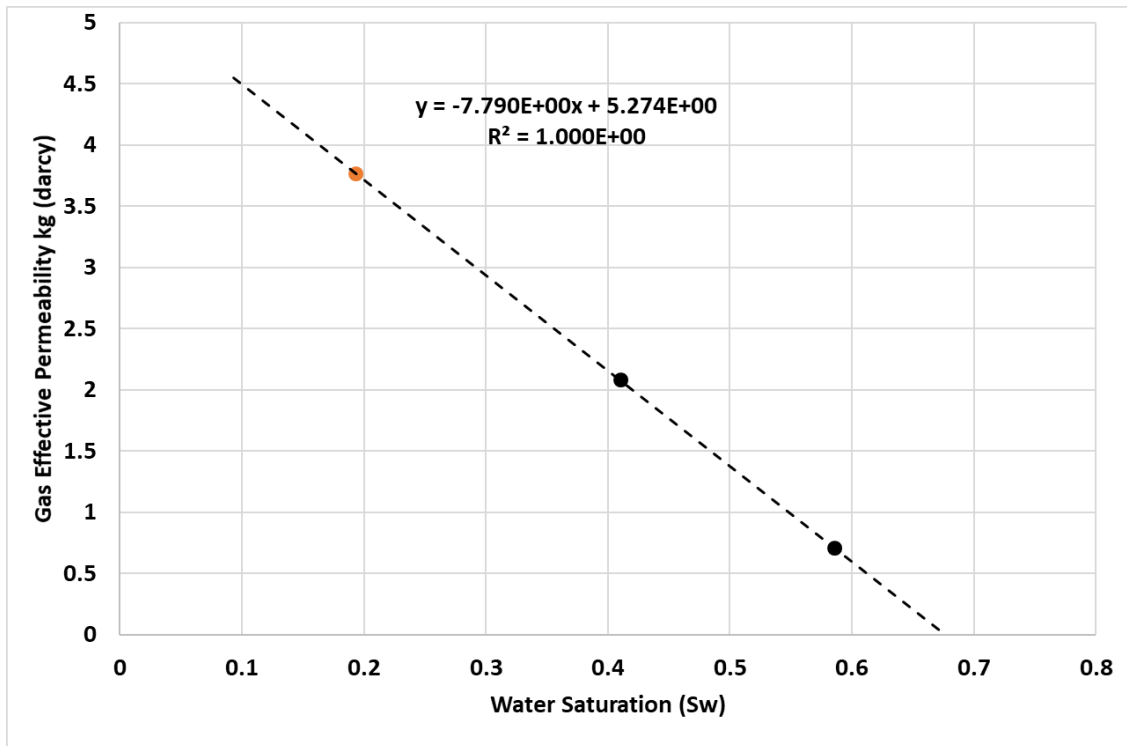


**Fig. 3.6: Effective gas permeability versus water saturation using single phase flow experiments. Orange data point is a different sand pack than the black points, thus a different packing. The results show that the packing has negligible impact on the effective gas permeability estimation.**

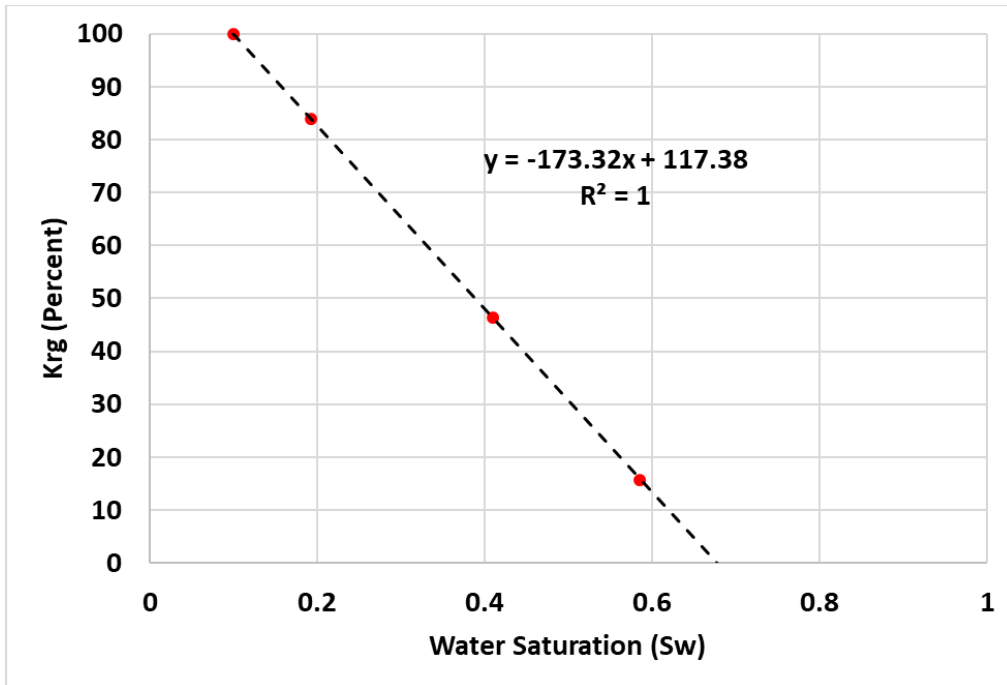


Fig. 3.7: Relative permeability to gas in the sand pack in the absence of hydrates using single-phase flow experiments. Critical gas saturation is predicted 67%.

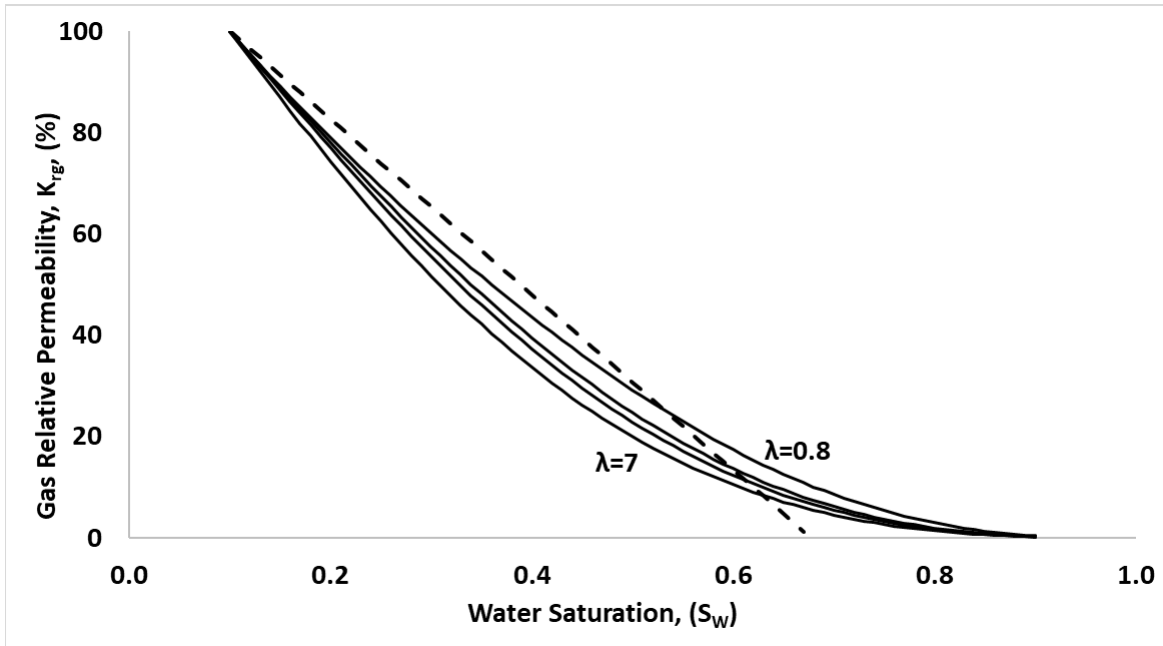


Fig. 3.8: Comparison of the laboratory measured single-phase (gas) flow data to Brooks and Corey model curves with varying pore size distribution index values  $\lambda=0.8, 2, 3,$  and  $7$ .

At this point, the relative permeability is defined as the effective permeability divided by the permeability at irreducible water saturation:

$$k_{rg} = \frac{k_g}{k_{g@S_{w,irr}}} = \frac{k_g}{4.49} \quad (3.14)$$

Fig. 3.7 shows the gas relative permeability in the sand pack in the absence of methane hydrates using the steady-state single phase (gas) flow experiment.

When the gas relative permeability of the sand pack in the absence of hydrate is compared to the Brooks and Corey equation (shown below as Eq. 3.15),

$$k_{rg} = \left( \frac{1-S_w}{1-S_{w,irr}} \right)^2 \left[ 1 - \left( \frac{S_w - S_{w,irr}}{1-S_{w,irr}} \right)^{\frac{2+\lambda}{\lambda}} \right] \quad (3.15)$$

we found out that the shape of the experimental relative permeability curve (which is linear) is not the same as the model curves, see Fig. 3.7. The experimental values, shown as black dashed line, appears to be a straight-line approximation to the Brooks and Corey model. Varying pore size distribution index ( $\lambda$ ) values are used for comparison. Clearly, the model does not match the relative gas permeability behavior of the sand pack reasonably. We will re-visit the model comparison later, while we discuss the multi-phase flow experiment results.

Fig. 3.16 shows the effective gas permeability as a function of the hydrate saturation. Severe drop in effective permeability is observed at relatively low values of hydrate saturation during the gas flow experiments.

$$k_g = k_{g@S_H=0} \times \left[ 1 + \operatorname{erf} \left( -\frac{a}{b} * S_H \right) \right] \quad (3.16)$$

Here  $a/b=57.7$  and has the units of (pore volume)/ (hydrate volume).

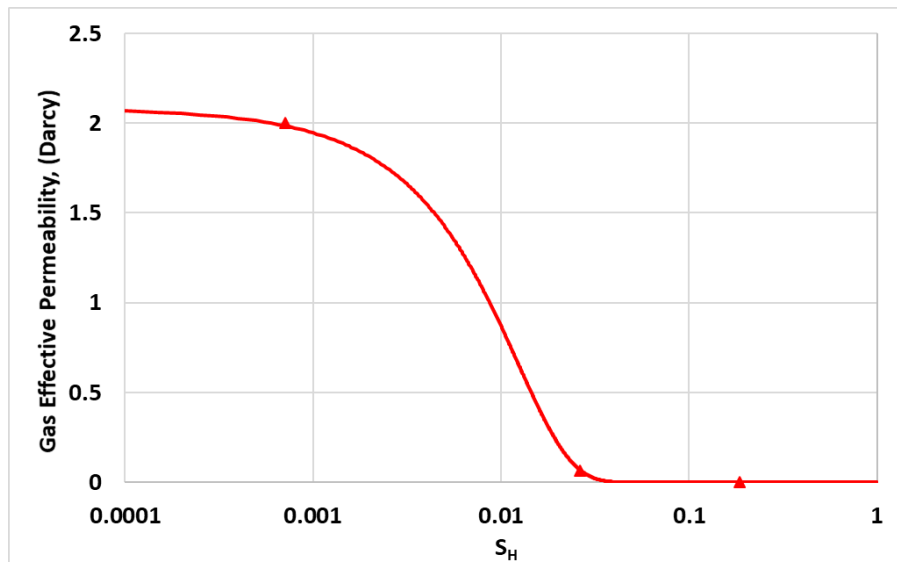


**Fig. 3.9: Effective gas permeability versus hydrate saturation based on the steady-state single phase (gas) flow experiments.**

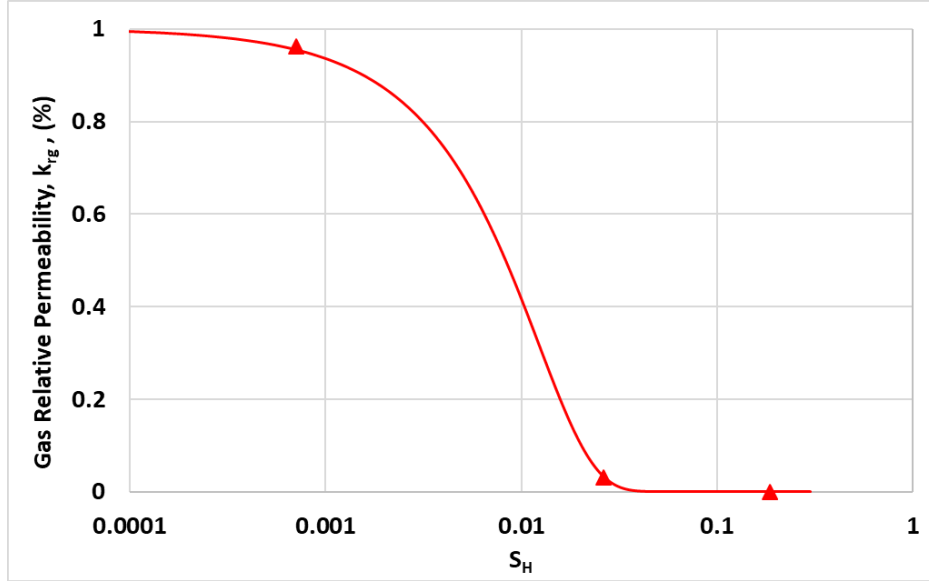


**Fig. 3.10: Relative gas permeability versus hydrate saturation at different average water saturation in the sand pack. From left to right, relative permeability goes from 100% permeability at  $S_w = 41\%$  to 1.42% permeability at  $S_w = 57\%$ , 0% permeability at  $S_w = 43\%$ .**

In Fig. 3.9, the effective permeability at  $S_H = 0$  is equal to 2.0072 Darcy at the corresponding water saturation  $S_{w1}=S_{w2}=41\%$ . This value is the effective gas permeability obtained using Eq. 3.13 (or Fig. 3.6).

Fig. 3.10 shows the relative permeability to gas versus hydrate saturation in the presence of hydrate using the single-phase flow experiments. The best fit for this data is the following exponential decline:

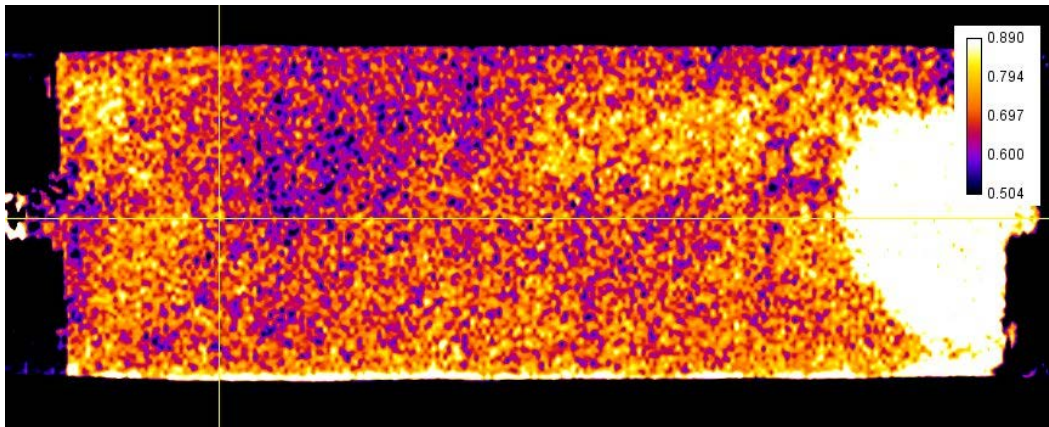
$$k_{rg} = \left( \frac{k_{g@S_H=0}}{k_{g@S_H=0, S_{wirr}}} \right) \left[ 1 + erf \left( \frac{a}{b} * S_H \right) \right] \quad (3.17)$$

Thus, it can be concluded here that the hydrate has a significant effect on the relative permeability of the system, but as the hydrate is removed, the system returns to the relative permeability in the absence of hydrate. Next, we will discuss the results for the steady-state multi-phase flow experiments.

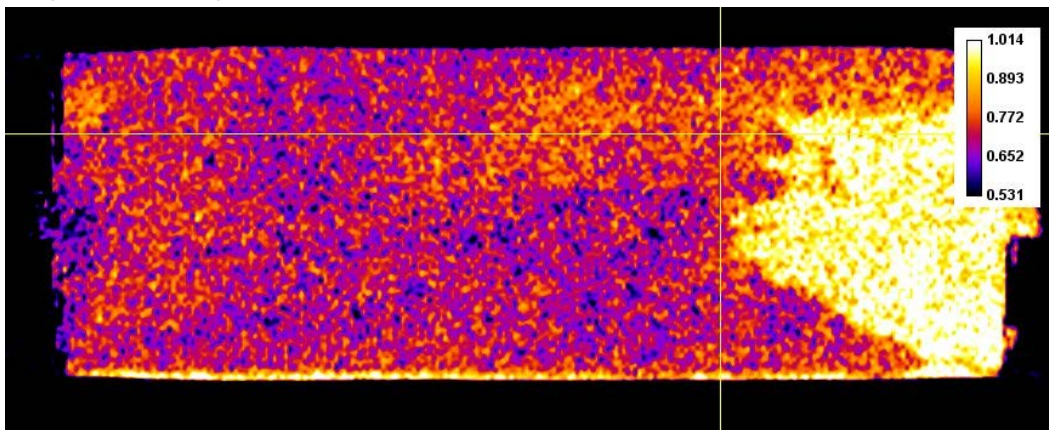
### 3.1.4.2. Steady-state Multi-phase (Gas/Water) Flow Experiments

Now we shall discuss the steady-state multi- phase flow experiment results. Fig. 3.11 shows the water saturation distribution of the sand pack at the end of the three separate stages of flow experiments where different rates of water and gas are injected. Fig. 3.11A shows the saturation distribution after 3 pore volumes of fluids were injected at the flow rates of 8 ml/min methane to 4 ml/min of water. The water saturation in the sand pack ranges from 89 % with the white voxel to about 55 percent with the blue voxel. This also shows that the saturation profile is not uniform; the bright spot is seen to be coalescing water phase preferentially exiting through the center of the sand pack. Fig. 3.11B shows the case when water and gas phases are injected at the same rate, both at 6 ml/min. See how the overall saturations change, there are fewer blue voxels and, more orange voxels indicating a global saturation increase. The bright

8ml/min Gas-4ml/min Water



A. 6ml/min Gas-6ml/min Water.



C. 4ml/min Gas-8ml/min Water

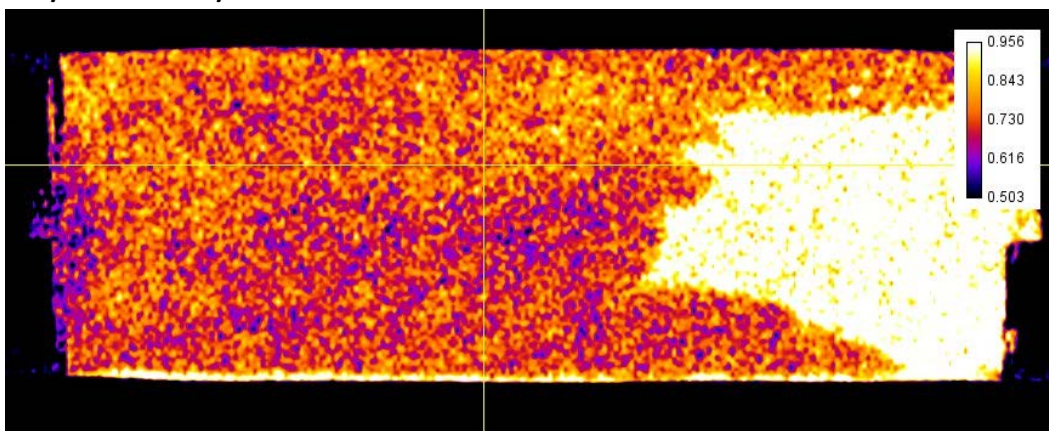


Fig. 3.11: Water saturation distribution at the end of three stages of steady-state two-phase simultaneous gas/water flow experiments at room temperature, in the absence of methane hydrate.

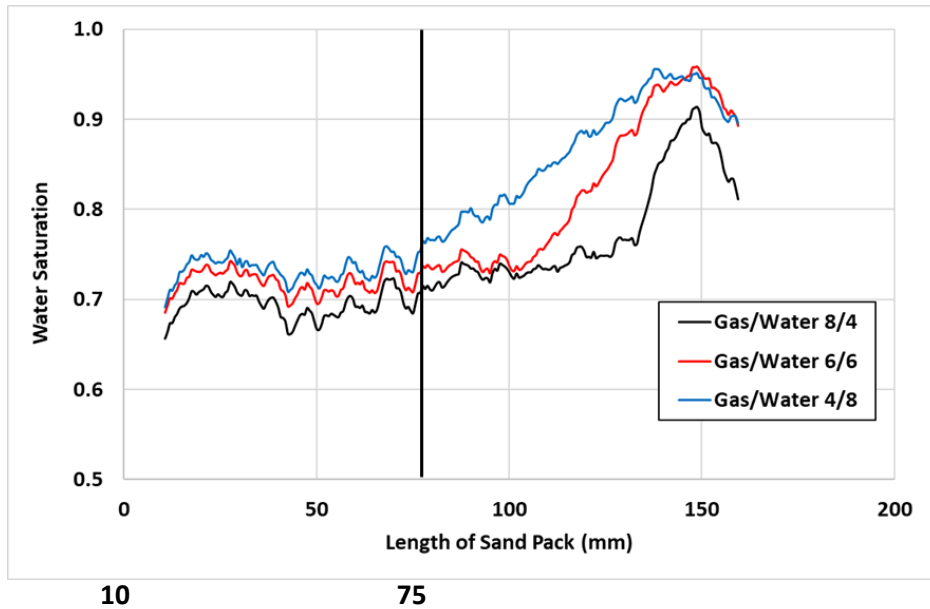


Fig. 3.12: Average water saturation profile along the main direction of flow during the relative permeability tests that were performed at three different rates at room temperature. Only values left of the 75 mm line will be used due to non-realistic water saturations near the outlet (left).

Table 3.2: Average Water saturation values used in the Permeability Analysis

Injection Rates as Ratio, $Q_g/Q_w$	8ml/min Gas, 4ml/min Water	6ml/min Gas, 6ml/min Water	4ml/min Gas, 8ml/min Water
Average Water Saturation, %	74	78	81

cone near the outlet is also increasing in length, thus indicating that this phenomenon could be linked to the flow ratio at the inlet, not to the total amount of water injected. Increasing water injection rate causes the water flowing through new flow paths (new saturation branches) to merge and the average water saturation to increase. Fig. 3.11C shows the impact of further increasing water rate on the water saturation field. Note that the water cone on the right is getting larger.

Fig. 3.12 shows an increase in water saturation near the outlet of the sand pack. The end cap of the sand pack at the outlet is on the axis of the sand pack, thus, causes the water to merge close to the exit. This causes an increase in the saturation and the marked increase in differential pressure. Since the development of the water cone is associated with the outlet boundary, the values of saturation that can be used during the multi-phase flow experiments will only contain the values in the absence of the cone, including the saturation within 10mm-75mm portion of the sand pack. This separation is indicated in Fig. 3.12 with a vertical line. Table 3.2 shows the average water saturation values corresponding to that portion of the sand pack where the saturation varies somewhat more uniformly, but in the presence of some fluctuations.

Fig. 3.13 shows the effective gas permeability in the absence of hydrate using the multi-phase flow experiment. Note that the domain of water saturation is very narrow and in near 70% water saturation. The three points at different injection rates of gas and water give a perfect straight line for the effective permeability. Extrapolating to 10% irreducible water saturation, gives the gas permeability equal to 0.07 Darcy. This value is significantly lower than that using the single-phase gas flow experiment data. We use this value for the calculation of the relative permeability values. The result is shown in Fig. 3.14.

Fig. 3.15 shows the gas relative permeability of the sand pack versus water saturation compared to the Brooks and Corey model. Clearly, the model matches the relative permeability in the absence of hydrates reasonably for  $\lambda$  value close to 7, which corresponds to unconsolidated sand.

$$k_g = -0.1022S_w + 0.0759 \quad (3.18)$$

$$k_{rg} = -136.22S_w + 101.26 \quad (3.19)$$

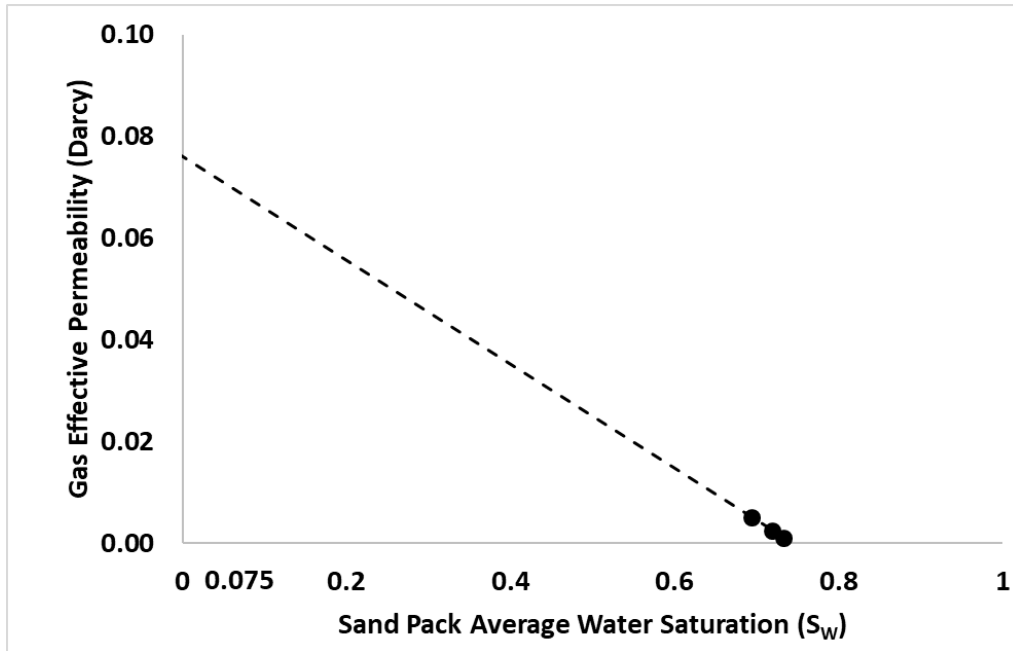


Fig. 3.13: Gas effective permeability with no hydrate obtained using multi-phase flow experiments.

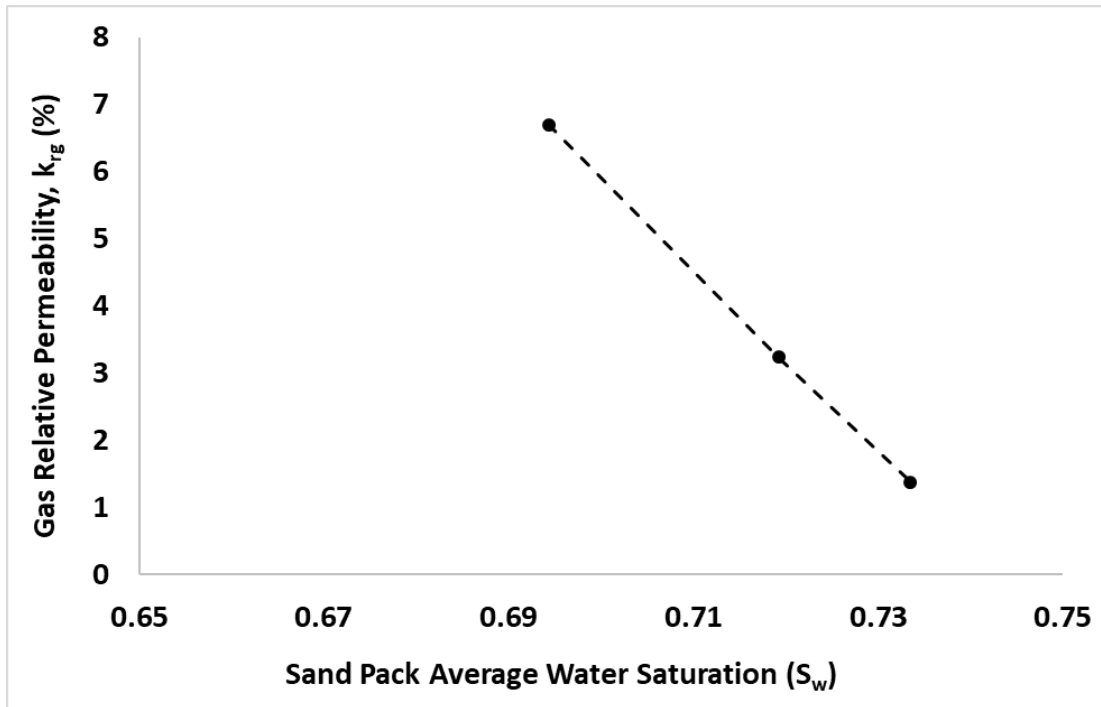


Fig. 3.14: Relative permeability to gas in the sand pack in the absence of hydrates using multi-phase flow experiments.

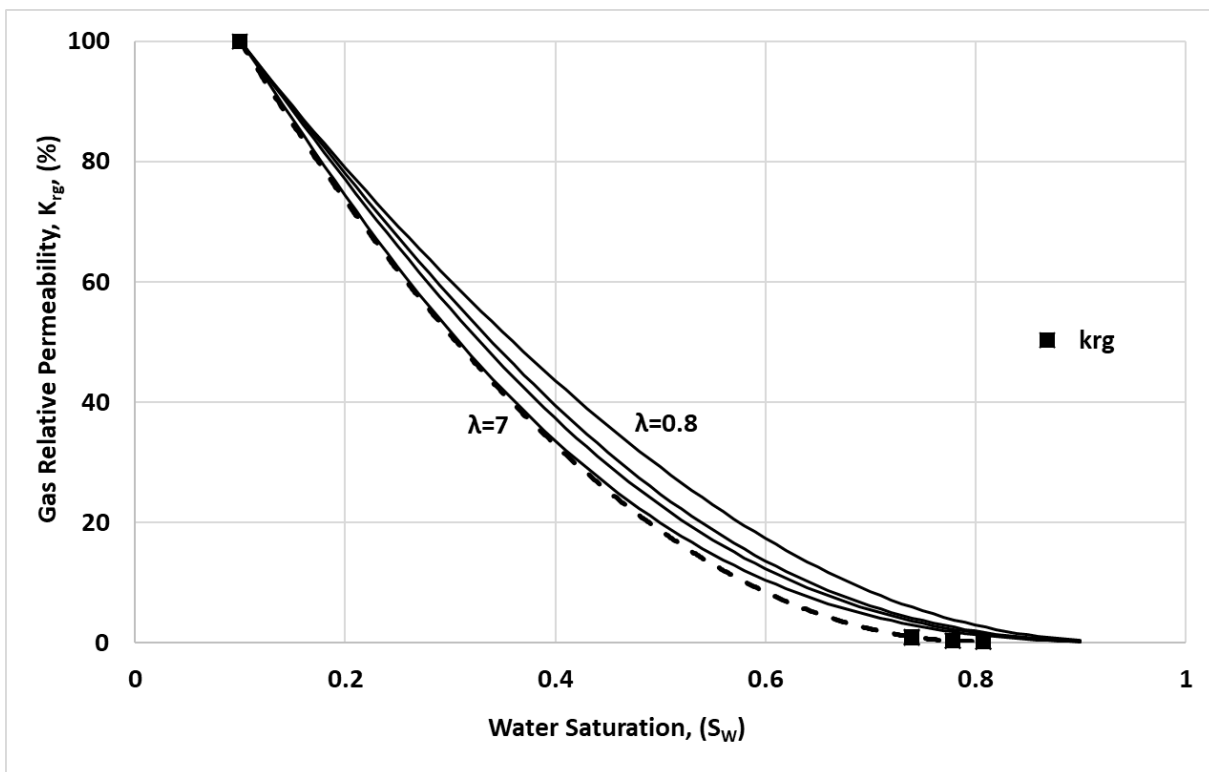


Fig. 3.15: Comparison of the laboratory measured relative permeability data in the absence of hydrate to Brooks and Corey model type curves with varying pore size distribution index values  $\lambda=7, 3, 2, 0.8$ .

$$k_{rg} = 202.75S_W^2 - 325.02S_W + 130.47 \quad (3.20)$$

Based on the experimental results the following final discussions can be made. Of the two different methods that are described in Sections 3.1.4.2 and 3.1.4.1, Section 3.1.4.1 (single phase steady-state flow) experiments are recommended due to direct measurement of the effective and relative permeabilities in the presence of hydrate. The steady-state multi-phase (gas/water) flow experiments work well with no hydrate present, but when hydrate is present the two components either form new hydrate, or the hydrate present dissociates. These develop locally in the sand pack and are due to either a chemical imbalance or temperature differences. In our experiments they have led to erratic saturations when the relative permeabilities cannot be measured in the presence of hydrates. So, this paper recommends using the method laid out in section 3.1.4.1.

For a sand pack with similar characteristics the following equations can be used to determine the effective and relative permeability:

In the absence of hydrate:

$$k_g(S_W) = -0.1022S_W + 0.0759 \quad (3.21)$$

$$k_{rg}(S_W) = -136.22S_W + 101.26 \quad (3.22)$$

In the presence of hydrate:

$$k_g(S_H) = k_{g@S_H=0} \times \left[ 1 + \operatorname{erf} \left( -\frac{a}{b} * S_H \right) \right] \quad (3.23)$$

$$k_{rg}(S_H) = \left( \frac{k_{g@S_H=0}}{k_{g@S_H=0, S_{wirr}}} \right) \left[ 1 + \operatorname{erf} \left( \frac{a}{b} * S_H \right) \right] \quad (3.24)$$

To use Eq. 3.23 and 3.24, it is important to first determine the effective and relative permeabilities as in Equations 3.21 and 3.22. Equations 3.23 and 3.24 are used for the hydrate effective and relative permeabilities, and the value at zero hydrate saturation needs to be on the same line as in Equations 3.21 and 3.22, this ensures that the values are consistent and representative of the system.

### 3.1.5. Conclusion

In conclusion, hydrates restrict the flow of water and gas when in a single phase or in 2 phases. The complex interaction that arises from 2-phase flow in a hydrate bearing sand pack adds challenges to the measurements of relative permeability and effective permeability due to the temperature and pressure requirements. Furthermore, capillary pressure can cause water to travel to the high hydrate regions causing non-uniform hydrate saturations, but if the hydrate is formed in layers, this effect is mitigated. Hydrate restricts the flow of gas by 10 times when there is an increase of hydrate from zero to 2.5 percent average. The low hydrate saturation indicates that it forms in the pore throats rather than pore body filling. Variation in hydrate saturation follows the initial water saturation, and any water saturation changes are due to injection of water. Hydrate at 18 percent stops all flow, and pressure on the outlet side decreased to below the equilibrium pressure and start dissociation. The use of single-phase gas flow in the measurement of gas relative permeability is recommended due to the complex formation and dissociation effects has when injecting both water and methane. Furthermore, the water gas interaction

as a two-phase flow in the auxiliary pipes cloud the results of the sand pack, thus again the single gas phase measurements are the clear winner here.

## **3.2. Phase Equilibria Studies in Pore-Space: Identification of Hysteresis (Subtask 3.5)**

### **3.2.1. Introduction**

The need to understand the basic physics of formation and dissociation in the hydrate-bearing formations is paramount to the natural gas production. In the past few years, test wells have been drilled in hydrate bearing formations, and their production were monitored (Moridis et al., 2009). During the production, however, sand was produced along with the gas, which indicated the unconsolidated nature of the formation (Yamamoto et al., 2014). Another issue is the cooling effect that results when producing hydrate using the depressurization method. While not observed directly in the field, laboratory results exist corroborating this effect (McGuire, 1981; Moridis et. al., 2007; Oyama et. al., 2009; Seol et. al., 2011). This result is an effect of the nature of methane hydrates--they generate heat when forming, and absorb heat when melting; thus, the temperature in the formation near the well decreases during the production. This cooling can even freeze water and re-form methane hydrate (McGuire, 1981). The purpose of our research in this section of the report is to describe this cooling effect and how hydrates behave after melting initially--and if once the re-formed hydrate is melted again, how that, too, is affected. This cycle can repeat, and it is of interest to see whether the hydrate is becoming easier to form, or whether the re-formation conditions stay the same; and if it is forming easier, then what controls this change in behavior. In bulk hydrate formation, an effect has previously been observed in which the formation of the hydrate is easier than that of the initial formation; this is called hysteresis (Lekvam et. al., 1997). But current scientific knowledge in the case of hydrate formation in porous medium is limited (Kim et. al., 2017).

Hysteresis of methane hydrate has been studied in bulk samples extensively (Buchanan et al., 2005; Lee, Susilo et. al., 2005; Ohmura et. al., 2003; Rees et. al., 2011; Rodger, 2000). In most of the cases, the study was completed in a stirred reactor so that the crystallization and melting develop homogeneously, and the heat transfer does not affect the system behavior. The experiments targeting the hysteresis were also seen in systems that have compounds other than methane, thus showing that hysteresis has been observed in many clathrate systems, thus strengthening the idea (Ohmura et al., 2003). And another study has used a large time-scale molecular dynamics simulation to describe hysteresis (Rodger, 2000). Thus, hysteresis is an important feature to capture when there are multiple hydrate forming and melting cycles, as is the case in this report.

A hypothetical example is that the hydrate begins forming in a container, say in 10 minutes, but if one were to melt that same hydrate and form it again under the same cooling rate, the hydrate forms in 8 minutes instead of 10. This means there is a mechanic that reduces the barrier to the hydrate formation. There are two theories on what this mechanic is: one is the memory effect of the water, which is thought to be in the form of partially-melted hydrate cages that form microscopic nucleation sites; the other is more gas availability in the form of dissolved gas in water near the nucleation sites. Either of these can be used to explain the behavior. This report presents an experimental approach that forms and melts methane hydrates in a sand pack under similar cooling rates. The objective is to determine where in the porous medium and when the hydrate forms; and determine if the cooling rate influences the formation time. If there is a difference in the formation time due to cooling rate, and there is a difference in formation time

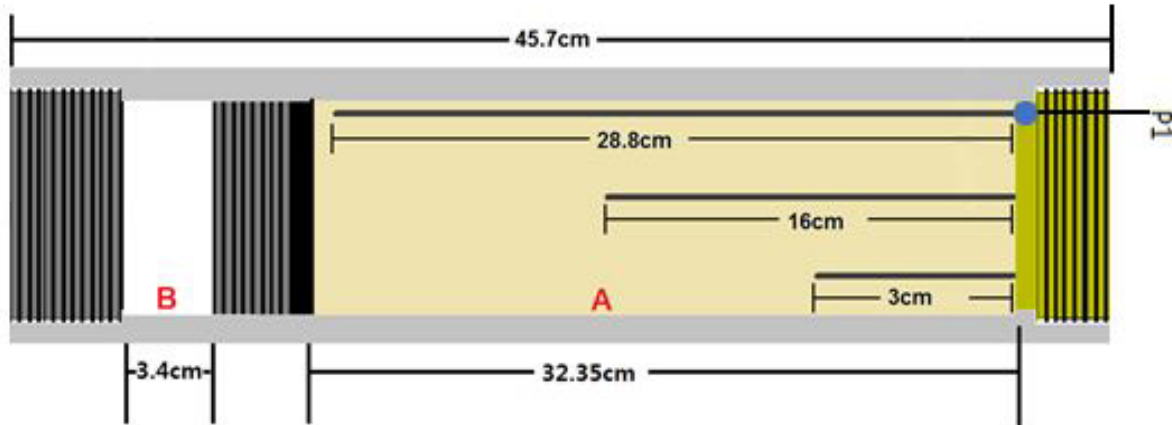


**Fig. 3.16:** The diagram of the cell used in the study of methane hydrate formation. (A) Sand pack including a pressure transducer and three thermocouples: Short, Medium, and Long; (B) Hydraulic cylinder used for the compaction of the sand. Cell stands vertically in a thermally insulated refrigerator during the measurements such that the pressure transducer and the thermocouples are located at the top.

under similar cooling rates, then there are two mechanics that help form hydrates: the mechanics of hysteresis, and the mechanics of cooling rates. We will focus to the former case; further study will be needed in the latter case. In the final part of the paper we propose a reaction modeling approach including the hysteresis during the reservoir-scale simulation of hydrate gas production. Due to limited space, the simulation work will be presented in a separate paper.

### 3.2.2. Experimental Set Up and Laboratory Procedure

In Fig. 3.16, a diagram of the hydrate cell used in the laboratory is shown. The cell is made of stainless steel and has a maximum working pressure of 10,000 psi. The sand is in volume A in the cell. In this region the cell has three thermocouples and one pressure transducer that records the pressure, P1. Volume B is filled with water which is used to apply a uniform force to a steel piston (seen as grey and black) to keep the sand compressed. The upper side of the cell in Fig. 3.16 is made of copper and is used to promote a heat transfer that is similar to the walls. While the copper has much larger thermal conductivity, the thickness is much greater than the walls, so the copper provides a similar heat flow as the steel walls. At the bottom, the plug is stainless steel and is much thinner than its copper counterpart. Not shown are the lines that provide the water and methane gas to the system, and there is a vacuum line that can be added to the system as well.

The first step in running the experiment is to have the ingredients: dry sand that is oven baked, distilled water, and pure methane. 1,100 ml of the sand is added to volume A in the cylinder from the top, in which the thermocouples are added as well. The thermocouples run through the copper plug into the sand pack as shown in Fig. 3.16, in Volume A. They are placed at different locations in the sand pack. A short thermocouple reaches 3 cm into the sand pack and is 1 cm from the edge of the sand pack. The next thermocouple is in the center of the pack, 16 cm from the copper plug, nearly exactly halfway between the sand pack and the steel piston and is labeled the “medium” thermocouple. The last thermocouple is located 180 degrees opposite to the short thermocouple and is 1 cm from the wall and 28.8 cm from the copper top and is labeled as the “long” thermocouple. The final component before sealing the system is a tube that runs down the sand pack (1 cm from the edge of the sand pack) past the long thermocouple and is used to add the water to the system. With these in place, the copper top is screwed on and the cell



long thermocouples along with the pressure for the transducer are recorded at one-second intervals. After the five cycles are complete, the system is taken apart, the sand is dried, and the experiment is repeated from the beginning. The experiment is repeated twice more for a number of 3 experiments. Although it was time consuming, the repetition was necessary to re-produce the results and quantify the error in the pressure and temperature measurements.

### 3.2.3. Theoretical Basis for the Experiment

The reason for this approach with multiple cycles of heating and cooling is to determine the effect known as hysteresis. Hysteresis describes a path-dependent phenomenon in the form of a time series. This effect is seen during methane hydrate formation as differences in the initial formation times, and at different locations on the pressure-temperature phase diagram, i.e., the difference in sub-cooling, and the difference in equilibrium pressure and current pressure. The cycles connect the physical phenomena by creating a continuous data set in which the mass and volume of the system stay constant. This provides an environment where the only independent variable is the temperature, and any observed differences in hydrate formation behavior are either due to a change in cooling rate or due to hysteresis.

The objective is to find hysteresis in porous medium, and thus a discovery of a dependence on thermal rate was secondary to this objective. The determining factor of hysteresis is *when hydrate starts to form*, and especially *when significant formation occurs*. In bulk hydrate formation, the only importance is the initial formation time, due to the nucleation event being singular. But in porous medium, the nucleation process is spatially distributed and can be countless. Thus, the need appears for including the location at which significant formation is observed. In the case of initial formation, the formation data is based on the phase diagram, and equilibrium conditions are assumed because no simulation work is used to calculate a deviation from the equilibrium. Point of significant hydrate formation is determined by the recorded temperature data. Hydrate has a heat of enthalpy of 438 J/g. The cooling of a system produces a monotonously decreasing temperature profile, unless there is internal heating in the system, in which there can be an increase in the local temperature of the system. A temperature increase in the time series indicates rapid hydrate formation, and the inflection point is the point when the hydrate heat generation rate is equal to the cooling rate of the system. The determination of significant hydrate formation is then the time that the heat generated is equal to the heat loss of the system. This point can be observed easily on the recorded temperature time series, and on the recorded pressure versus temperature plots as an inverse of the slope. All these features will be shown in the following sections accompanied by a detailed explanation of each cycle. Further, a quantitative approach will be introduced to consistently determine the initial hydrate formation time.

### 3.2.4. Analysis of Experimental Results

#### 3.2.4.1. Time Series of Temperature

In the corresponding analysis, the time series for the short and medium thermocouples are shown; there is a long thermocouple, which will be briefly described--but since no significant amount of hydrate can form in its surrounding, it is not mentioned hereafter.

Fig. 3.18 shows the measured temperature history of the short and medium thermocouples during each cycle. For the first 24 hours the system is in thermal equilibrium, and the temperature at the very beginning is higher than the room temperature because the sand had not been out of the oven for very long. After a day, the temperature readings settled within a degree and a half of each other. During the cooling phase, starting around 24th hour, the temperature profiles for each thermocouple are given.

Clearly, there is a distinct behavior that is observed at hour 18.3, when the temperature increases, rather than decrease, during the cooling. This is due to hydrate formation. At this time, the refrigerator temperature is roughly 1.5 C and the only heat source is the crystallization. Given that the heat generation for hydrate is 438 J/g, and the average specific heat capacity of the surroundings is around 2,000 J/kg-C, the amount of hydrate formed is significant (Gupta, Lachance, Sloan, & Koh, 2008). There is at least 1 C increase for the middle thermocouple, and a half degree increase for the short thermocouple. Based on this information only, one can make an estimation of what the water saturation distribution in the sand pack looks like. Since the water was added from the bottom of the sand using the tube, and the sand being unconsolidated, the saturation transition zone in between the water and gas phases is short. Hence, the water should be mostly localized to the long thermocouple, and the medium thermocouple. This means that the short thermocouple at the upper portion of the sand receives much less water, the medium has more. Focusing on the medium thermocouple, now there are obvious thermal effects in **Fig. 3.18** due to the hydrate formation. There are responses in the temperature that both fluctuate and linger longer than that of the short or long thermocouples. This is important later when determining the initial hydrate formation times.

Continuing to Cycle 2, Fig. 3.18 shows the same type of graph, and sheds light on what happens when the hydrate formed is only melted to 17 C. A note here is that the thermal gradient Cycle 2 experiences is uniquely different than the other cycles, which can be seen clearly in the analysis section of the pressure versus temperature profiles. It is stated here since the medium thermocouple is also quite unique with four major temperature peaks--one being earlier than the short thermocouple, and another three peaks in rapid succession. These peaks, rather spikes, make the analysis of this cycle more complicated, and it is most likely a feedback response to the generated heat. The hydrate cell is in a thermally insulated system, where the hydrate-generated heat can increase the overall temperature of the system. This has previously been reported in other publications as well, and in one particular work (Linga, et. al., 2009), it was shown that the magnitude of the temperature spike is proportional to

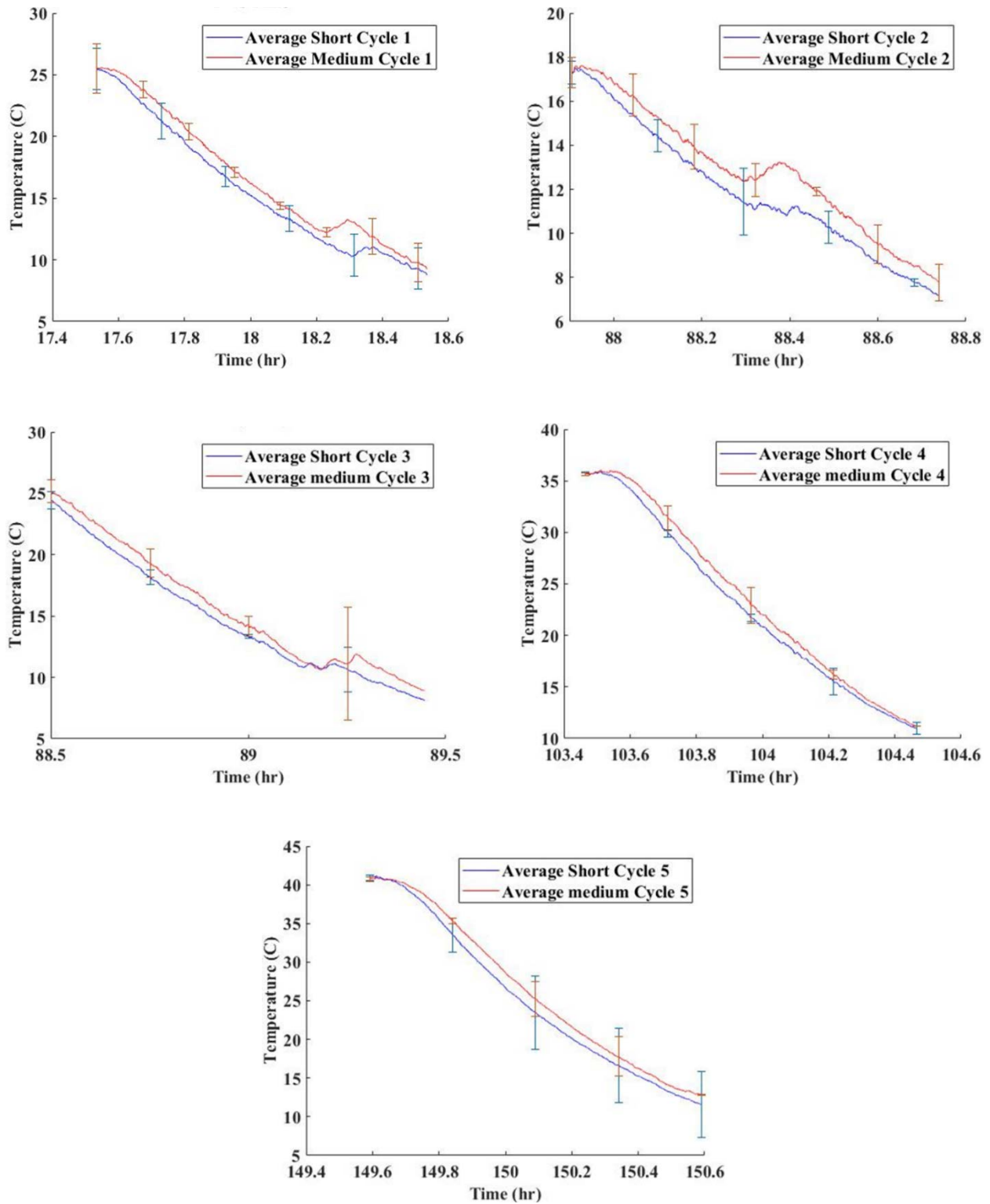


Fig. 3.18: The recorded temperature history of the short (blue) and medium (red) thermocouples during cycles. bars are 90% confidence bounds

how thermally-insulated the system was. This makes for an interesting experiment, since most natural hydrates are not in a thermally conductive system, while many laboratory setups are. The referenced experiment also demonstrated that there can be a feedback loop in the system. While in this case the amount of hydrate in the sand is not enough to melt the hydrate, in a natural system it is foreseeable that this type of situation can occur. Having enough to melt the hydrate, in a natural system it is foreseeable that this type of situation can occur. Having completed the discussion of cooling, looking at the heating side for Cycles 1 and 2 in Fig. 3.18, there is a significant temperature drop near the hydrate melting temperature of 15 C, (roughly the melting temperature for the pressure in this particular system) which has the effect of re-forming hydrate, even ice, if enough hydrate is melted. This is due to the system being thermally confined.

One of the major reasons that this experiment was designed to begin with is to be able to determine if hydrates became easier to form when repeated cycles of melting and forming are conducted. Based on the experimental data, it certainly seems that this is true. The temperature spikes in Cycles 2 and 3 show that they are more aggressive than in the first cycle. These aggressive temperature spikes are indicative of earlier hydrate formation, i.e., a faster hydrate formation rate. Cycle 3 temperature behavior includes the same trend during the cooling. Furthermore, as the cycles continue, the short thermocouple has only one peak and is similar in size to the other peak for the small thermocouple. The long thermocouple shows a reduced trend, and only a small increase in temperature at the same time as the large second peak of the medium thermocouple--indicating that it is the heat transfer, not hydrate formation.

A reduced magnitude of the medium thermocouple temperature spikes is shown for Cycle 4, and is prolonged over an hour, rather than being sharp as in Cycles 2 and 3. This indicates that there was a reduction in the hydrate formation rate. One of the ideas in hysteresis is that there are partially melted clusters of clathrates that form nucleation sites for the subsequent cycle to form hydrate easier, but these nucleation sites can be destroyed when the temperature in the sand rises above a certain point. In this case, the temperature for the start of the relaxing effect was 35 C.

This effect associated with the removal of the nucleation sites is seen even more clearly as the magnitude, and the general shape of the medium thermocouple reading, resembles the first cycle. From a temperature point of view, the analysis should be focused on the short thermocouple. Based on the analysis, we conclude that during any calculations and predictions, the limited hydrate formation in the short thermocouple will provide smoother and more predictable response. A side note on bulk hydrate formation is that it is highly random in its nature. [This has previously shown by Bagherzadeh et al. where the rates were measured using a magnetic resonance imaging method (Bagherzadeh et. al., 2011)]. Randomness means that even when all conditions are kept the same, the hydrate formation rates are not constant. In the sand pack, which includes added complexities, the hydrate formation could experience larger variance in the formation rates. Due to this issue and the fact that hydrate produces heat when generated, the short thermocouple is the main focus of the analysis. This is for two reasons, as just stated--the hydrate formation rate has a random aspect, but also the heat transfer is radial in this section due to it being near the edge of the sand pack. The long thermocouple is in a mostly water environment; thus, hydrate formation is minimal. The medium thermocouple is in the center of the sand pack; thus, it is affected by heat transfer from all directions, and is more insulated to the surroundings. Therefore, hydrate formation will produce complicated thermal profiles, such that under analysis of experimental data only, it will be unclear as to which the major contributors are. Therefore, the short thermocouple is used to further analyze the system and define hysteresis.

### 3.2.4.2. Time Series of Pressure

Fig. 3.19 shows the pressure response related to hydrate formation during the cycles. The black dashed line is a reference to a linear line to help us visually identify the severity of the deviations

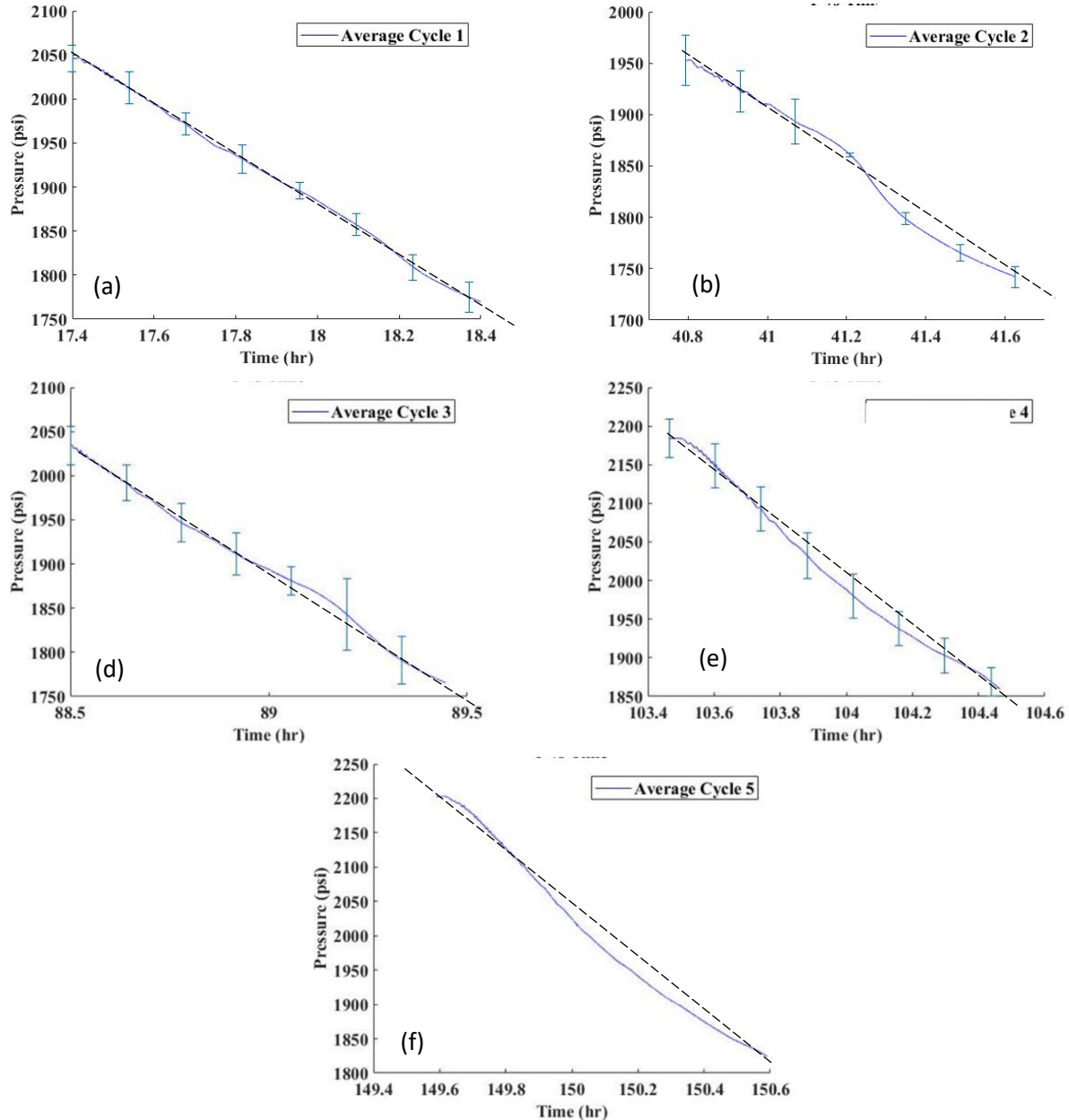


**Fig. 3.19: The recorded pressure history during the cycles of cooling and heating.**

in the pressure profile. While it looks minor, any observed deviation from linearity due to temperature drop indicates the hydrate formation. Remember, the hydrate formation started at the 18th hour, and there is a change in slope here confirming the hydrate formation.

Fig. 3.19 clearly shows an inflection point in all of parts a-f. The pattern (looking from left to right) for cycle 2 was as follows: the pressure drop was concave to just before 41 hours, convex for a short amount

of time, concave for a good period and then back to convex, where it turns to a linear function to the end of the cycle. The hydrate formation rate increases when the slope steepens, then slows down when the pressure levels off. The change in slope continues to vary, and thus the hydrate formation rate varies.

Cycle 3 has almost the identical thermal gradient as that of the first cycle, but it has a drastically different pressure profile. There exists four inflection points on the pressure profile, and these points line up with the temperature spikes. The pattern for Cycle 3 increases in frequency and has a combination of linear parts and highly nonlinear parts as well. This is due to hydrate formation during Cycle 3. Pressure response to a temperature change is rapid and linear.

Cycle 4 is the cycle where we expect that the response should have reverted back to the original shape, and indeed it does so for the most part; the complexity of the previous cycle has been all but eliminated, with only slight oscillations, and one bump. This indicates a direct link between the temperature spikes and the pressure nonlinearities.

Cycle 5 shows a similar response with a pressure profile very similar to Cycle 4. The repeated melting and cooling can affect the saturations of the water and gas in the system and thus change the initial conditions; thus, the difference between Cycle 1 and Cycle 5 can be explained. In conclusion, the relaxation of the memory effect has occurred, and that there are small differences in saturation that prevent the exact return to the initial conditions.

### 3.2.4.3. Pressure versus Temperature Data and the Phase Diagram

To make a fair comparison of different thermal cycles, a clear basis for comparison is needed. There are a few obvious choices: pressure vs time, temperature vs time, or a set time from the initial cooling. These choices, however, do not represent a clear measure, which ensures that all the cycles are compared equally. What is needed in the investigation is a reference, and one that considers both the temperature and pressure so that there can be a standard measure. This reference is the equilibrium phase line in the pressure versus temperature plot. All cycles will be compared to starting from a certain distance from the line, using the pressure difference.

In Fig. 3.20, a location shown as blue circles represents an experimental value for a pressure and temperature in time. The difference in pressure from the experimental and the equilibrium line could be either *positive*, which means that the system can form hydrates, or *negative*, meaning that under equilibrium conditions there is no hydrate formation. Eq. 3.25 is the phase equilibrium curve shown in Fig. 3.20. The data for the curve is obtained from the Tough+Hydrate simulation software.

$$P_{eq} = a_1 T^5 + a_2 T^4 + a_3 T^3 + a_4 T^2 + a_5 T + a_6; \quad (3.25)$$

The coefficients  $a_1$ - $a_6$  are given in **Table 3.3**.

Knowing these coefficients, Eq. 3.26 can be used to predict the pressure difference, or the delta-pressure:

$$\Delta p = P - P_{eq}; \quad (3.26)$$

The recorded temperature and pressure values of the experiment used to calculate the delta-pressure values behave as they should: they yield negative delta-pressure when they are below the equilibrium line, and positive when they are above the line. This is done for each cycle. The smallest common starting value observed is used for the reference point of all cycles. In this case, it is Cycle 2 which has the lowest starting temperature of 17 C, and thus the smallest delta-

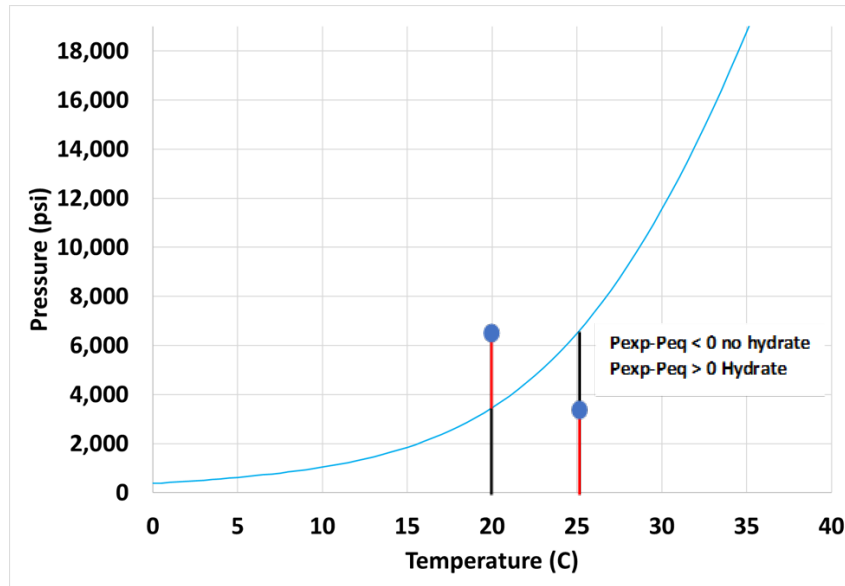


Fig. 3.20: Pressure-temperature phase diagram for methane hydrate showing delta-pressure and delta-temperature.

Table 3.3 The coefficients and their values used in Eq. 3.25

Coefficient	Value
$a_1$	-0.00056
$a_2$	0.05147
$a_3$	-1.025
$a_4$	11.93
$a_5$	2.282
$a_6$	406.6

pressure at the start of any cycle. The value is -572 psi. The next step was to find this value (or as close as possible) in all the other cycles and to zero out the time when all cycles are equal to this value. This means that all the cycles start the same delta-pressure away from the equilibrium line, thus considering both temperature and pressure. One other factor to ensure that all cycles can be equally compared is to look at the driving force during the hydrate formation, which was the temperature difference between thermocouple and the outside refrigerator. To fairly compare each cycle, this temperature difference needs to be very close for the different cycles; if they were not close, that cycle should be set aside in the discussion of hysteresis. As we show in Fig. 3.21, there exists a large difference in delta-temperature between Cycle 2 and the other cycles; this is due to how close the starting temperature was to the hydrate

formation line. There was not enough time for refrigerator temperature to equalize and produce a consistent result, so Cycle 2 will not be considered in the analysis of the hysteresis.

Another feature of the delta-pressure is that it mirrors the temperature profile, so a peak such as the ones observed in the temperature profiles will produce a valley, and a valley in temperature will produce a peak in the delta-pressure plot. This is also important because the trends of formation and melting can be easily observed. To find hysteresis, the values near zero delta-pressure are important, because a value of zero will determine when hydrate start forming.

Fig. 3.22 shows the delta- temperature, which is on the left, and the delta-pressure on the right. Clearly, the thermal gradient shows some variance but is very close for cycles 1, 3, 4, and 5--but Cycle 2 is very different, and since the cooling is slower, the initial formation time will be different.

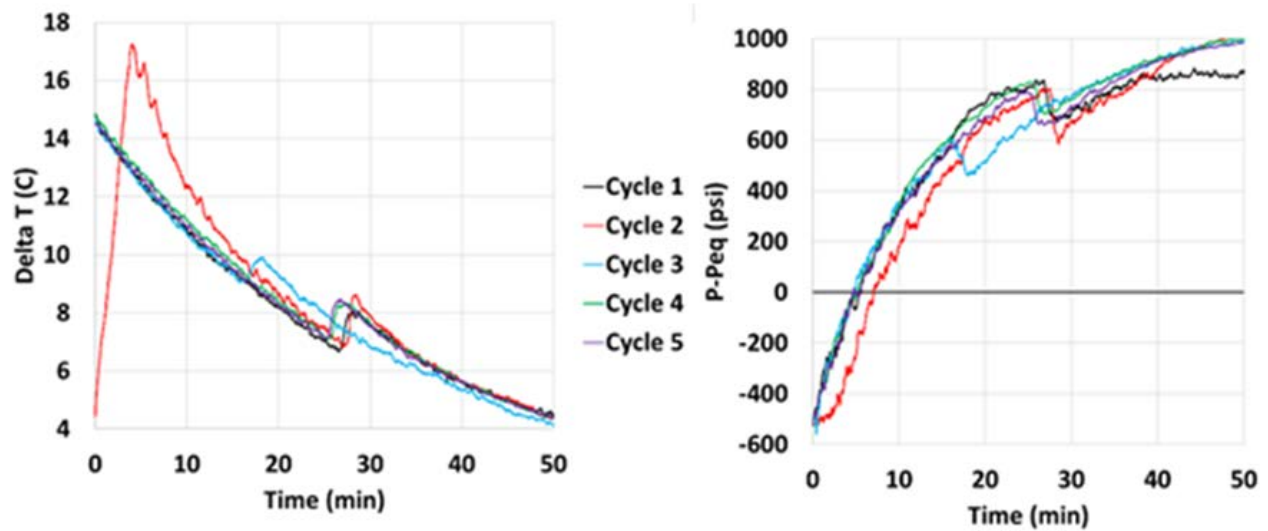
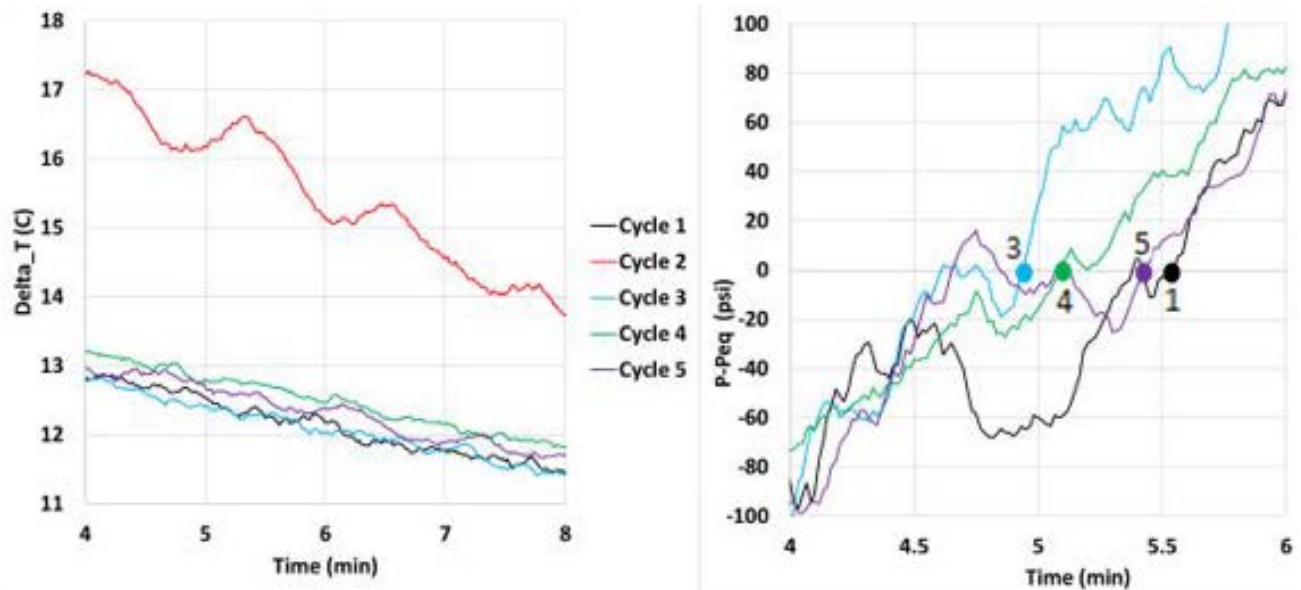


Fig. 3.21: Delta-temperature and delta-pressure time-series of the cycles



**Fig. 3.22: Close-up view of the Delta-pressure near zero.**

Thus, the analysis of cycles 1, 3, 4 and 5 can focus on hysteresis rather than the thermal issues. The idea of hysteresis is that hydrate forms easier when there are repeated melting and cooling cycles. This is thought to be caused by a memory effect of the water, so that the hydrate forms faster and easier the next time the temperature is near or at its freezing point. So logically, the hydrate should form easier as we proceed with the cycles. To test whether the melting temperature would influence the memory effect, the later cycles (Cycles 4 and 5) are designed so that the sand pack is heated to a much higher temperature than that of the first cycle.

The idea is that the higher melting temperature would erase the memory of water, hence the hydrate formation characteristics of the cycle should be similar to the first cycle. With this understanding, now we visit Fig. 3.22, and observe that this pattern clearly exists on the right figure --Cycle 1 forms the slowest, then Cycle 5, then 4, then 3, with 3 being the fastest. Again, Cycle 2 should not be added to the discussion here due to its inconsistent thermal difference. As seen in Table 3.4, a clear correlation exists in between the maximum melting temperature of the cycle and the hydrate formation time. The time difference between cycles 1 and 3 is 30 seconds, which does not sound like much, but it is significant when one considers the small difference in thermal gradients in between the cycles. 10 percent difference in the gradients would only account for 15 seconds in the initial formation time. Clearly the experimentally observed differences are much larger than that.

Before continuing the discussion of the hysteresis, the thermal difference in Cycle 2 shows that the thermal distance to the outside temperature is important to the formation rate, the temperature and pressure profiles. In Fig. 3.22, the temperature difference for Cycle 2 is 4 degrees larger than that of the other cycles; thus, the formation time is longer by 1 minute and a half. The percent difference in the thermal distance is -31 percent and the difference in formation time for Cycle 2, when compared to cycle 1, is -27 percent; thus, there is nearly a one-to-one relation between the differences in thermal distance to the formation time. Accordingly,

**Table 3.4: Recorded maximum temperature and hydrate formation time for the cycles 1-5**

Cycle	1	3	4	5
Max. Temperature (C)	25	25	35	40
Formation Time (s)	332	296	305	325

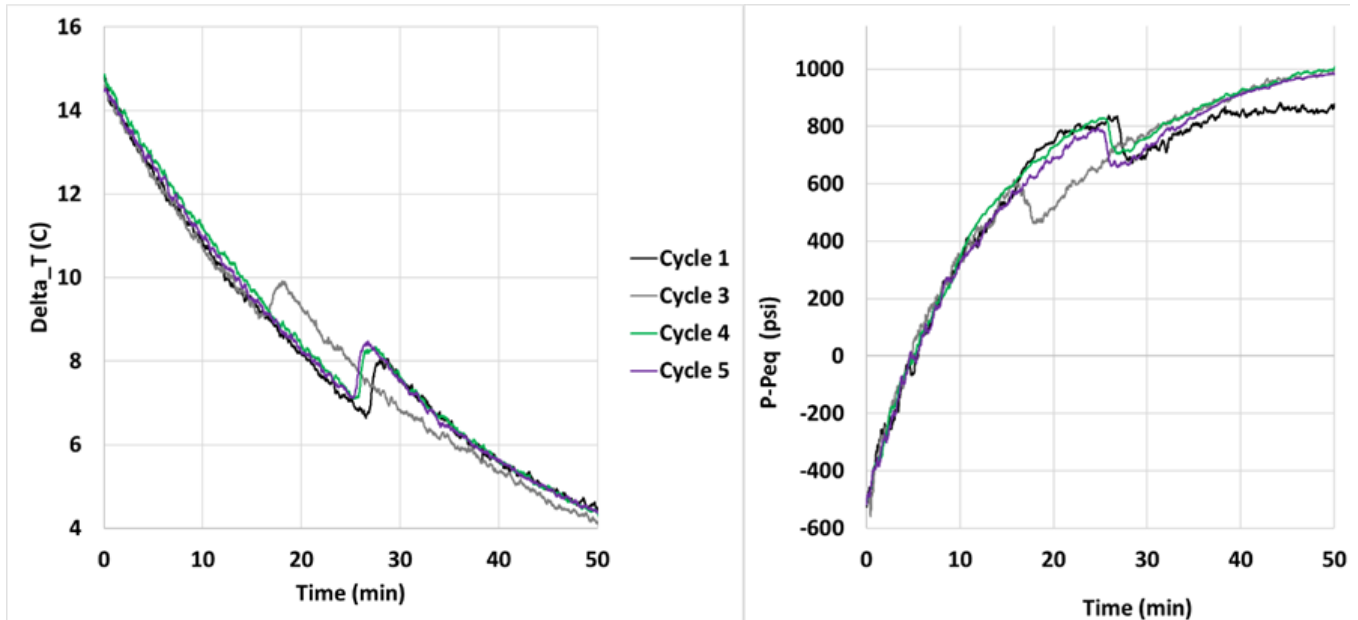


**Fig. 3.23: Delta-pressure and delta-temperature history at large timescale.**

the difference between the cycle 1 and 3 temperature distances should produce a similar result in the formation times of the cycles 1 and 3. However, the formation time of the first cycle and the third cycle is larger than the difference caused by the temperature difference. Thus, hydrate hysteresis is clearly observed.

But this is only a small timeframe, so let's look at the larger picture and see what unfolds. In Fig. 3.23, large-scale differences in delta-pressure are shown as the time progresses. The valleys in the profiles are places where heating occurs due to hydrate formation. The heat causes the system to advance towards the hydrate equilibrium line -- the zero line. If the system is near the line to begin with, it is foreseeable that heat generated by hydrate formation can cause the hydrate to melt. While not encountered in this work, it is an issue to be aware of. The locations of the valleys are indication of when significant hydrate is formed; heat generation is proportional to the amount of hydrate, and since there are valleys in the delta-pressure profile indicating a temperature spike in the time series, there has to be hydrate generated. Looking at the thermal difference can give more insight; the locations of the valleys in the delta-pressure and peaks in delta-temperature, show a change in the slope from cooling to heating-- meaning that there is more heat being generated than that taken away by cooling meaning that there is more heat being generated than that taken away by cooling. This is another indicator of hysteresis; not only does the initial formation time vary, and becomes easier for the Cycle 3, it also forms hydrate faster than the other cycles

by 10 minutes. This means that there is a significant difference in times and clearly shows the hysteresis. Further, the return to the first cycle indicates that there is a loss of the memory effect in cycle 4 and cycle 5, thus corroborating that hysteresis exists in a sand pack and that there is a temperature range at which it occurs.

In Fig. 3.24, the strong correlation between the temperature peaks and the hydrate consumption is shown. The time rate change of pressure is proportional to the hydrate formation because thermal effects are linear, and under a cooling environment, the pressure change should not increase, but should be proportional to the cooling rate of the system. However, in Fig. 3.24 a pressure change is not constant, nor is it just proportional to the cooling rate of the system. In Fig. 3.24, *A* is the location of the first major change in pressure rate and precedes the temperature peak by a small amount. It is seen that the pressure corresponds with all the thermocouples and not just one thermocouple. Thus, pressure represents the whole system, while the analysis of the temperature is restrained to the local area. Continuing to point *B*, the start of the lowest value of the pressure rate is observed. This corresponds with the medium thermocouple and recalling that the medium thermocouple is in the center of the sand pack and takes the longest to be affected by the thermal gradients, it makes sense that its temperature peak is later than the others. By the time point *C* is observed, the initial hydrate formation has leveled off and there is an increasing pressure rate change until about 117.6 hours, when a large increase in the medium thermocouple temperature is observed. Point *D* is the starting point of a drastic change in pressure rate, thus indicating large hydrate formation. At point *E*, the second temperature peak indicates further hydrate formation. At point *F*, the formation rate has subsided, and the pressure rate increases again.

### **3.2.5. Estimation of Hydrate Formation Rate and Amount**

Thus, hydrate formation is observed at the temperature peaks, and the time of the temperature peaks corresponds with the onset of significant hydrate formation. Therefore, these times can be used to indicate hysteresis. The time derivative of pressure is not linear; thus, the hydrate formation is nonlinear. This indicates that the system cannot be described by singular activation energy, nor can it be described with fixed reaction rate constants. A possible change in theory of hydrate formation would be not to use reaction rate equations associated with the hydrate formation and melting; an approach that uses Gibbs free energy (surface and bulk energy), may be a better approach to hydrate formation than the kinetic rate equations, due to the nature of hydrates being closer to a mixture than a stoichiometric compound.

Knowing that the hydrate forms, the next question is how much has formed. To answer this question, two fundamental information is needed, an equation of state for methane gas that takes the gas compressibility into account and predicts the gas pressure in the sand pack from the temperature data, and pressure data from the experiment when hydrates form. The difference between the real gas law and the experimental pressure should be related to the hydrate formation. Redlich-Kwong equation of state (eq. 3.27) is used for the study. To determine accurately the initial moles of gas and the volume of methane used,

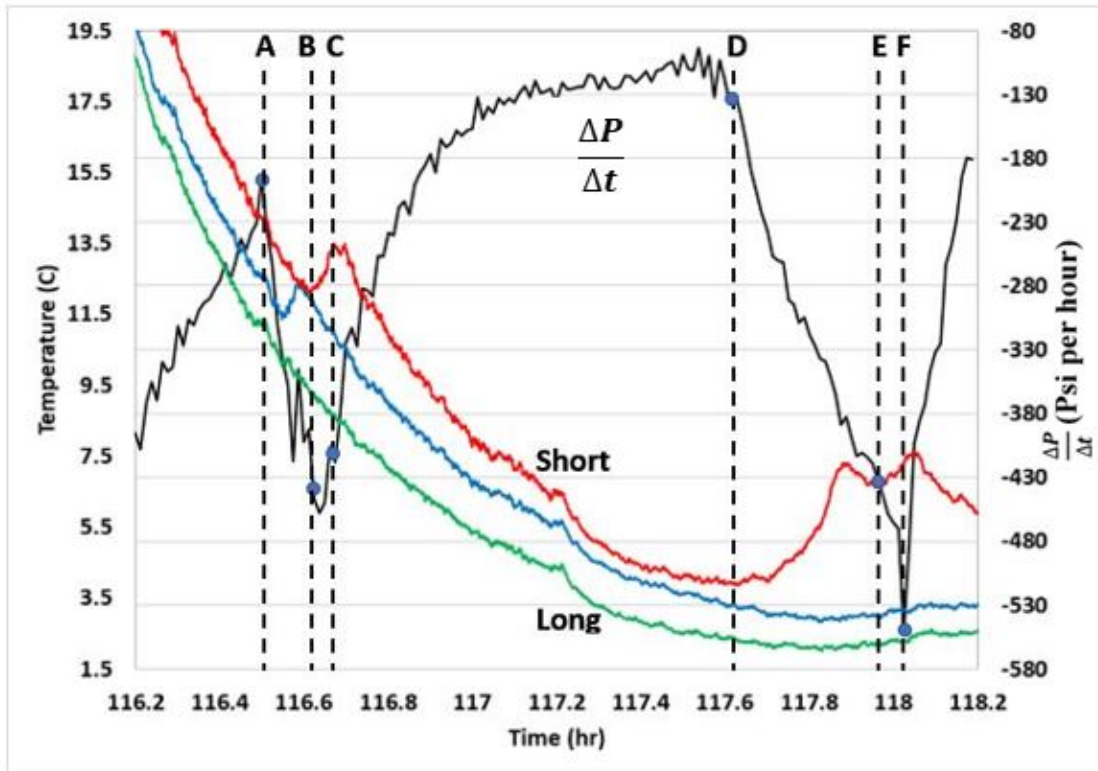


**Fig. 3.24: Recorded histories of the temperature and time rate of pressure. Red, blue and green are the temperature profiles recorded by the three thermocouples, and yellow is time rate of pressure.**

the pressure and temperature data between 25 C and 16 C. The values for the constants (a and b) are also fitted due to there being water in the system. This gives table 3.5, which show the parameters that are used to predict the pressure.

$$\left(P + \frac{a}{\sqrt{TV}(\bar{V}+b)}\right)(\bar{V} - b) = RT \quad (3.27)$$

To predict the amount of consumed methane, Newton-Raphson iteration is used to solve for the number of moles at each experimental temperature and pressure. This means that only one variable is unknown and that for each set of temperatures the moles of methane can be predicted. However, if this equation is solved by using the experimental values during the temperature spikes of the medium and short thermocouples, erroneous results will be seen. What is seen is that the number of moles of methane will increase due to the higher temperature, but it is known that the moles of gas are going down due to pressure decrease, therefore only the end of each cycle (when hydrate formation is almost zero) will the hydrate mass be calculated.

To calculate how much hydrate has formed all that is needed is the relationship between moles of water and methane, which, assuming 100 percent hydration is  $(CH_4) 5.75(H_2O)$ , making the molecular mass of hydrate at 119.629 g/mole. From this data, the average hydrate formation rate can be calculated. The time period in between the time when hydrate begins to form and

**Table 3.5 Initial conditions and coefficient for Redlich-Kwong equation.**

a	b	V (L)	n (mol)	$R \frac{\text{L}\cdot\text{psi}}{\text{K}\cdot\text{mol}}$
467.2337	0.02957	0.301	2.06	1.2059

**Table 3.6: The estimated hydrate amount formed and the rate of hydrate formation during at each cycle**

Cycle	Hydrate Amount (g)	Hydrate Formation Rate (g/hr)	Cycle Period (Hrs)
1	61.19	3.59	17.01
2	61.74	2.60	23.68
3	41.09	1.76	23.30
4	61.74	2.64	23.38
5	62.30	4.06	15.36

**Table 3.7: The estimated water consumption**

Cycle	Mass (g)	Percent Water Consumed
1	52.93	53.46
2	53.41	53.94
3	35.55	35.90
4	53.9	54.44
5	51.89	52.41

the end of the experiment represents the time of hydrate formation, and the total mass calculated at the end of the period divided by the period gives the average rate. Table 3.6 shows the total mass of hydrate produced and the average rates. Note that the values vary, this is due to the period of time spent forming, which is different for each cycle.

Important as well is the mass of the water. Given that there is 99ml of water, or 99 grams of water in the system, the total conversion percentage can be calculated. From this data, which is table 3.7, a picture of what the water saturation profile can be deduced.

This means that the potential to form hydrate is double of what was produced. So, this means that half of the water was not in contact with methane and validates the assumption that most of the water was at the bottom quarter of the sand pack with only a small amount in the upper section. Knowing the porosity, and the cross-sectional area, the portion of 100 percent saturated sand can be calculated to be

2.8 cm from the bottom of the sand pack, and the diagram can be seen in Fig. 3.25. The distribution of the other water is unknown.

### 3.2.6. Reaction Model in the Presence of Hysteresis

In Table 3.4 the measured values of the initial hydrate formation time values for the cycles are presented. In this part of the article we propose to develop a simple predictive tool for the initial hydrate formation time as a function of the melting temperature. For this, we first normalize the recorded times in the presence of hysteresis by subtracting the initial time in the absence of hysteresis,  $\Delta t_{init}$ , which is the time that belongs to cycle 1. Following using the normalized initial times for Cycles 3, 4, and 5 and their corresponding melting temperatures to plot Fig. 3.25 and then linear fit the data points to predict the initial formation time based on the melting temperature as a straight-line relation.

In Fig. 3.25, the equation for  $\Delta t_{init}$  shows a clear trend the melting temperature has on the system. While the model, (Eq. 3.28) is simple, it shows that the higher the melting temperature is the closer the system behavior to the first cycle in the absence of hysteresis, ( $\Delta t_{init} = 0$ ). This develops at 46.4 C. On the other hand, when the melting temperature is lower, the initial hydrate formation develops sooner in the next cycle. This is true for melting temperatures, so the minimum temperature can only be the temperature just outside of the phase diagram,  $T_{phase}$ , which is dependent on what pressure is used.

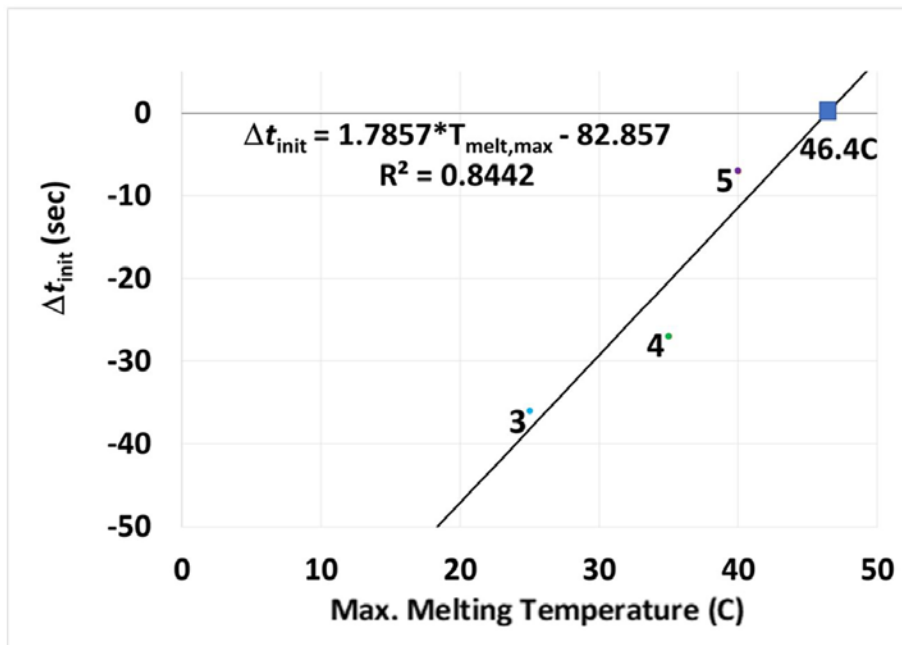


Fig. 3.25: Normalized initial formation time versus the maximum melting temperature for Cycles 3, 4, and 5.

$$\Delta t_{init} = 1.7857 * T_{max,melt} - 82.857; T_{max,melt} > T_{Phase} \quad (3.28)$$

The 36 second head start that cycle 3 has over cycle 1 results in a 534 second head start in significant hydrate formation. The significant formation time is important because it signifies the start of the major

thermal effects that hydrate has on the whole system. These thermal effects are what need to be understood so that a procedure to mitigate these effects can be developed and implemented.

Fig. 3.26 shows how the equilibrium pressure changes in the presence of the hysteresis. The higher the melting temperature is, the harder it is for the system initially form hydrates while at lower melting temperatures the easier it is. The quadratic equation fits the data perfectly and is valid for temperatures from  $T_{Phase}$  up to 46.4C. Fig. 3.26 also shows the temperature at which hydrate forms when the hysteresis is present. As with the pressure the same trend is seen, the higher the melting temperature is, the harder it is for hydrate to form while the lower melting temperature the easier it is. Therefore, in order to implement the hysteresis, a shift in the pressure-temperature phase diagram is needed. This is done in equations 3.29a and 3.295b. To determine the change in the initial hydrate formation time that the hysteresis causes, the shift in the diagram is estimated in equations 3.29a and 3.29b.

$$T_{shift\ melt} = T_{eq} - (-6.57E^{-4}T_{melt}^2 + 3.31E^{-2}T_{melt} + 14.7) \quad (3.29a)$$

$$P_{shift\ melt} = P_{eq} - (-1.67E^{-1}T_{melt}^2 + 8.39T_{melt} + 1770) \quad (3.29b)$$

$$T_{eq}^* = T_{shift\ melt} + T_{eq} \quad (3.30a)$$

$$P_{eq}^* = P_{shift\ melt} + P_{eq} \quad (3.30b)$$

$T_{eq}^*$  and  $P_{eq}^*$ , the modified equilibrium temperature and the modified equilibrium pressure, respectively, are then estimated using equations 3.30a and 3.30b. This represents a shift in the phase diagram to the right.

In Fig. 3.27 the flow chart for hydrate formation in the presence of hysteresis is illustrated. For the chart, we considered the hydrate formation algorithm of the Tough+Hydrate simulator as the basis. This simulator directly computes the kinetic rate of formation. The necessary modification to the existing algorithm for the presence of the hysteresis is shown in red. The kinetic rate of hydrate formation is computed using the following formulation:

$$\frac{DQ}{dt} = k_o e^{-E_A/RT} A_s (P_{eq} \phi_{eq} - P_{CH_4} \phi) y_{CH_4} \quad (3.31)$$

In Eq. 3.31 the hysteresis comes into play through the driving force which is represented by the parenthesis term. The drive basically represents the tendency of the water-gas system to form hydrate and in this case, it is measured as the difference in the fugacity values of methane in the cages at equilibrium and the methane in the bulk gas. In Eq. 3.31 these fugacity values

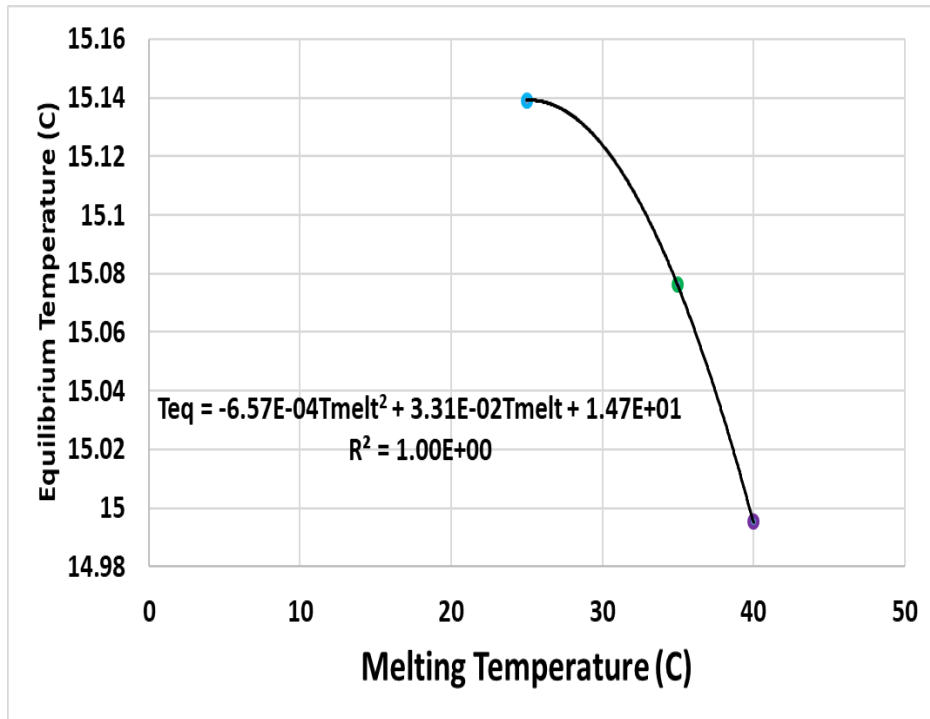
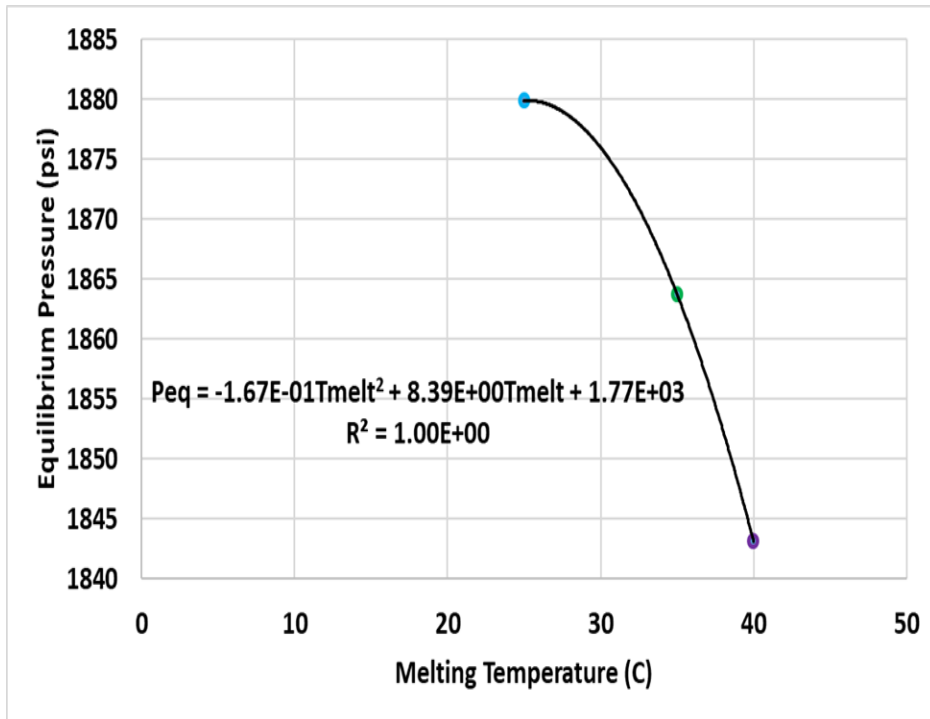


Fig. 3.26: Equilibrium pressure and temperature versus maximum melting temperature in presence of hysteresis

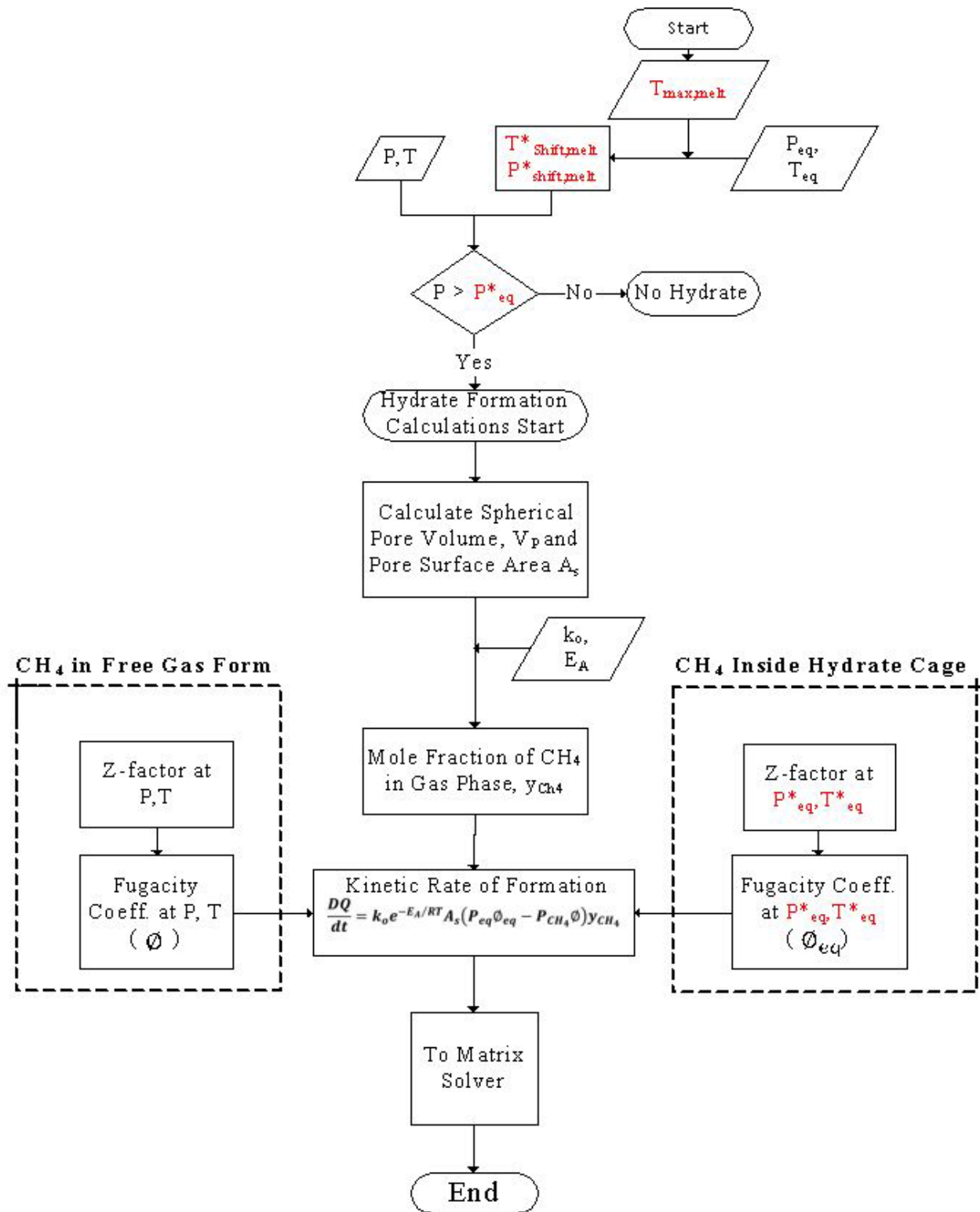


Fig. 3.27: Flow chart for Implementing Hysteresis into Tough+Hydrate. Necessary changes in the algorithm due to the presence of hysteresis is shown in red.

are represented by the fugacity coefficients multiplied by their respective pressures, (equilibrium pressure, and partial pressure for methane). The hysteresis should change the equilibrium fugacity of methane in the cages based on the shift in the equilibrium pressure and temperature.

### 3.2.8. Conclusions

In this article the presence of hysteresis during hydrate formation in porous media is shown using an experimental approach. The measured pressure and temperature time series are dependent on the past runs, which is, by definition, a hysteresis. Furthermore, the change in the temperature and pressure profiles are dependent on the hydrate formation rate. Further corroborating the existence of hydrate formation at the temperature peaks are the time derivative of the pressure, in which the decrease in pressure drop corresponds with the increase in temperature, and increases when the temperature decreases; thus, the hydrate rate has a direct effect on the pressure change. Therefore, any equations formulated need to have second order effects to capture this dependence. Thermal effects come into play that are not present in the bulk experiments. Thermal confinement was a major factor of the temperature peaks that were observed, which indicates when the hydrate is forming rather rapidly. Furthermore, these temperature peaks are at a location of a valley in the temperature profile. Thus, a perfectly insulated system would produce a greater thermal peak than one that is not insulated. This feature could be used as a metric of when hydrates are forming or when they are not forming significantly. Melting temperatures clearly matter, and the closer the system is to the equilibrium line, the more pronounced the thermal effects become; conversely, the further away the starting point is, the more important the hysteresis effects are. As a certain point (35 C) was reached for the melting temperature, most effects of the hysteresis were eliminated, and by only 40 C there was negligible difference in between the runs. This means that for thermally dissociated media, the system has to be heated quite high to eliminate secondary hydrate formation.

Hydrate mass was estimated by solving for the number of moles of bound gas in the system from the Redlich-Kwong equation of state at the observed pressure and temperature, and then using the stoichiometric relation for methane hydrate. Furthermore, it was found that most runs produced the same mass, indicating that there was not a large water saturation difference between the runs. There was a small region (around 2.8 cm) that was 100 percent saturated with water, thus preventing the entirety of the available water from forming into hydrate.

A simple predictive model was developed and shown to follow the trends of the experimental data. The model results are important because initial hydrate formation time is proportional to the significant hydrate formation, which is when the forming hydrate starts affecting the system thermally. Correlations of melting temperature versus equilibrium pressure and melting temperature versus equilibrium temperature are shown so that the phase diagram can be modified to account for hysteresis by shifting the values of the phase diagram by the shifted values. This relation is then implemented into the logic of kinetic rate of formation in the simulation software Tough+Hydrate. Future work could be to study hysteresis under constant temperature, while varying pressure to form and dissociate the hydrate; and to investigate the dissolved gas amount during and after hydrate formation. Also, to increase the number of maximum melting temperatures, for example, 17-45 C, would make a finer grid (more cycles) of the melting temperatures to the formation times (both initial and significant formation).

## Nomenclature

$a_i$	Coefficients for equilibrium pressure polynomial
$a, b$	Coefficients of Redlich-Kwong equation of state
$A_s$	Surface Area of hydrate particles ( $m^2$ )
$\Delta T$	Internal temperature minus external temperature; (C)
$DP/Dt$	Derivative of measured pressure with respect to time (psi/hr)
$DQ/Dt$	Hydrate Formation Rate (kg/sec)
$E_A$	Activation Energy (J/mole)
$k_o$	Intrinsic reaction rate constant (Mole/(m sec))
$P$	Measured pressure (psi)
$P_{CH_4}$	Partial pressure of methane in the gas phase (psi)
$P_{eq}$	Pressure shift of $P_{Phase}$ (psi)
$P_{shift, melt}$	Shift in $P_{eq}$ ; (psi)
$P_{eq}^*$	New equilibrium pressure; (psi)
$R$	Universal gas constant, L.psi / K.mol
$T$	Temperature; (C)
$T_{max, melt}$	Maximum melting temperature; (C)
$T_{Phase}$	Equilibrium phase line temperature; (C)
$T_{shift, melt}$	Temperature shift of $T_{Phase}$ ; (C)
$T_{eq}^*$	New Equilibrium Temperature; (C)
$\bar{V}$	Molar volume; (L/mole)
$\Delta p$	Pressure difference between experimental and equilibrium values: (psi)
$\Delta t_{init}$	Cycle 1 formation time minus Cycle $i$ formation time; (sec)
$\phi_{eq}$	Fugacity coefficient inside hydrate cage
$\phi$	Fugacity coefficient of free gas

#### 4. Advanced numerical simulation of coupled flow and geomechanics (Task 4-Subtask 4.2, Task 5-Subtask 5.1, Subtask 5.3, Subtask 5.4 by Ahn, T.W., Guo, X., Killough, J., Kim, J., Lee, J.Y., Yoon H.C., Zhou, P.)

We describe advanced modules for rigorous numerical simulation of coupled flow and geomechanics of gas hydrate deposits, which have already been or will be published in several journals (eg, Kim, 2018a; Kim, 2018b; Yoon and Kim, 2018; Yoon et al., 2019; Yoon et al., 2020). The papers are supported by this project. We condense the research outcomes in this section.

##### 4.1 Large deformation in poromechanics (Subtask 5.1, Subtask 5.3)

We propose a new numerically stable sequential implicit method for coupled flow and finite-strain multiplicative elastoplastic geomechanics. We show the rigorous mathematical statement of coupled nonisothermal flow and largely deformable geomechanics based on the total Lagrangian approach. We employ the Piola transformation to obtain the equivalent permeability, thermal conductivity, and velocity, not changing the initial grid system. Here, we employ the finite volume method for flow, and the finite element method for geomechanics, and then develop an integrated in-house simulator, by taking a variant of the fixed-stress sequential method that can provide numerical stability. Because the sequential method can make use of the existing simulators, we also describe in detail the algorithm of the fixed-stress method, how the two individual simulators can be integrated. We then take synthetic production scenarios of largely deformable gas hydrate problems, and test the simulator.

###### 4.1.1 Mathematical description

We introduce two domains of reference and current states to use the total Lagrangian approach shown in Fig. 4.1.

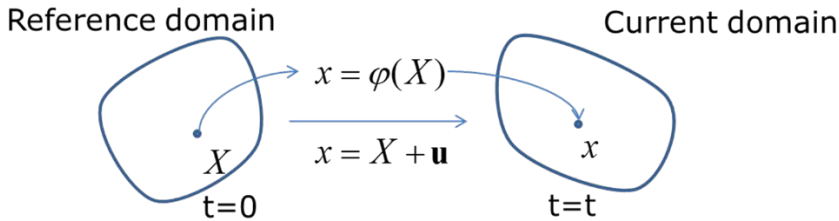


**Fig. 4.1 Lagrangian description of motion. The physical quantities in the current domain are pulled back to the reference domain or those in the reference domain are pushed forward to the current domain.**

Let us define the following deformation gradient.

$$F_{aA} = \mathbf{F} = \mathbf{GRAD}(\varphi(\mathbf{X})) = \frac{\partial x}{\partial X} = \frac{\partial(\mathbf{X}+\mathbf{u})}{\partial \mathbf{X}} = \mathbf{1} + \frac{\partial \mathbf{u}}{\partial \mathbf{X}} \left( = \delta_{aA} + \frac{\partial u_a}{\partial X_A} \right), \quad (4.1)$$

where  $\mathbf{x}$  and  $\mathbf{X}$  are the coordinates of the current and initial configurations, respectively.  $\mathbf{1}$  is the rank-2 identity tensor.  $\mathbf{u}$  is the displacement vector. Gradient and Divergence operators in the reference domain are written as

$$\mathbf{GRAD}(\cdot) = \frac{\partial(\cdot)}{\partial \mathbf{X}}, \mathbf{DIV} \cdot (\cdot) = \frac{\partial}{\partial \mathbf{X}} \cdot (\cdot). \quad (4.2)$$

The governing equation for quasi-static geomechanics is written as

$$\mathbf{div} \cdot \boldsymbol{\sigma}^t + \rho_b^t \mathbf{g} = \mathbf{0} , \quad (4.3)$$

where  $\boldsymbol{\sigma}^t$ ,  $\rho_b^t$ ,  $\mathbf{g}$  are the total stress tensor, bulk density, and gravity vectors, respectively.  $\mathbf{div}$  is the divergence operator at the current domain. The superscript  $t$  indicates the current domain. Eq. 4.3 can be rewritten in a weak form as follows.

$$\int \boldsymbol{\sigma}^t : \delta \boldsymbol{\varepsilon}^t(\mathbf{u}) d\Omega^t = \int \rho_b^t \mathbf{g} \cdot \delta \mathbf{u} d\Omega^t + \int \bar{\mathbf{t}}^t \cdot \delta \mathbf{u} d\Gamma^t , \quad (4.4)$$

where  $\Omega^t$  and  $\Gamma^t$  are the current domain and its boundary, respectively.  $\boldsymbol{\varepsilon}^t(\mathbf{u})$  and  $\bar{\mathbf{t}}^t$  are the Cauchy total strain tensor and traction at the boundary. Eqs. 4.3 and 4.4 can be mapped on the reference domain, respectively, written as

$$\mathbf{DIV} \cdot \mathbf{P} + \rho_b^0 \mathbf{g} = \mathbf{0} , \quad (4.5)$$

$$\int \mathbf{S} : \delta \mathbf{E}(\mathbf{u}) d\Omega^0 = \int \rho_b^0 \mathbf{g} \cdot \delta \mathbf{u} d\Omega^0 + \int \bar{\mathbf{t}}^0 \cdot \delta \mathbf{u} d\Gamma^0 , \quad \rho_b^0 = J \rho_b^t, \quad J = \det(\mathbf{F}), \quad (4.6)$$

where  $\mathbf{P}$  and  $\mathbf{S}$  are the first and second Piola Kirchoff total stresses, respectively. The superscript 0 stands for the reference domain.  $\mathbf{E}$  is the Green-Lagrange total strain, expressed as

$$\mathbf{E}(\mathbf{u}) = \frac{1}{2} (\mathbf{GRAD}(\mathbf{u}) + \mathbf{GRAD}^T(\mathbf{u}) + \mathbf{GRAD}(\mathbf{u}) \cdot \mathbf{GRAD}^T(\mathbf{u})), \quad (4.7)$$

where the superscript  $T$  is the transposed of the rank-2 tensor or matrix.

The governing equation for fluid flow can be obtained from mass balance, as

$$\frac{d}{dt} \int m^k d\Omega^t + \int \mathbf{div} \cdot \boldsymbol{\omega}^k d\Omega^t + \int q^k d\Omega^t = 0 , \quad (4.8)$$

where the superscript  $k$  indicates fluid component. In this section, we only consider two components, water and methane ( $k=w, m$ ).  $m$ ,  $\boldsymbol{\omega}$ ,  $q$  are the fluid mass, mass flux, and an external sink term of component  $k$ , respectively.  $m$  and  $\boldsymbol{\omega}$  are expressed as

$$m^k = \sum_{J=A,G,H,I} (\phi S_J \rho_J^t X_J^k) , \quad \boldsymbol{\omega}^k = \sum_J (X_J \rho_J^t \mathbf{v}_J + S_J \rho_J^t \mathbf{u}_J^k) , \quad (4.9)$$

where we consider aqueous, gas, hydrate, ice phases ( $J=A,G,H,I$ ).  $\phi$  is the true porosity, defined as the ratio of the pore volume to the bulk volume in the deformed configuration.  $S_J$ ,  $\rho_J^t$ , and  $X_J^k$  are saturation and density of phase  $J$ , and the mass fraction of component  $k$  in phase  $J$ , respectively.  $\mathbf{v}_J$  and  $\mathbf{u}_J^k$  are the convective and diffusive flow, written as,

$$\mathbf{v}_J = -\frac{\mathbf{k}^t k_{rJ}}{\mu_J} (\mathbf{grad}(p_J) - \rho_J^t \mathbf{g}) , \quad \mathbf{u}_J^k = -\phi \tau_G \mathbf{d}_J^t \mathbf{grad}(X_J^k), \quad (4.10)$$

where  $\mathbf{k}^t$  is the absolute permeability tensor.  $\mu_J$ ,  $k_{rJ}$ ,  $p_J$  are the viscosity, relative permeability, and pressure of the fluid phase  $J$ , respectively.  $\tau_G$  and  $\mathbf{d}_J^t$  are the gas tortuosity and hydrodynamic dispersion tensor.

When Eqs. 4.8, 4.9, and 4.10 are pulled back to the reference domain, we have respectively

$$\frac{d}{dt} \int M^k d\Omega^0 + \int \mathbf{DIV} \cdot \mathbf{W}^k d\Omega^0 + \int Q^k d\Omega^0 = 0 , \quad (4.11)$$

$$\mathbf{W}^k = \sum_J (X_J \rho_J^t \mathbf{V}_J + S_J \rho_J^t \mathbf{U}_J^k), \quad (4.12)$$

$$\mathbf{V}_J = -\frac{\mathbf{K}^0 k_{rJ}}{\mu_J} (\mathbf{GRAD}(p_J) - \rho_J^0 \mathbf{F}^T \mathbf{g}), \quad \mathbf{U}_J^k = -\phi \tau_G \mathbf{D}_J^0 \mathbf{GRAD}(X_J), \quad (4.13)$$

where  $M^k$ ,  $\mathbf{W}^k$ ,  $\mathbf{V}_J$ ,  $\mathbf{U}_J^k$  are the physical quantities in the reference domain that correspond to  $m^k$ ,  $\boldsymbol{\omega}^k$ ,  $\mathbf{v}_J$ ,  $\mathbf{u}_J^k$  in the current domain. The permeability ( $\mathbf{K}^0$ ) and diffusion ( $\mathbf{D}_J^0$ ) tensors in the reference domain are

$$\mathbf{K}^0 = J \mathbf{F}^{-1} \mathbf{k}^t \mathbf{F}^{-T}, \quad \mathbf{D}_J^0 = J \mathbf{F}^{-1} \mathbf{d}_J^t \mathbf{F}^{-T}. \quad (4.14)$$

Similar to the mass balance of fluid flow, the energy equation can be obtained from conservation of energy as follows.

$$\frac{d}{dt} \int m^\theta d\Omega^t + \int \mathbf{div} \cdot \boldsymbol{\omega}^\theta d\Omega^t + \int q^\theta d\Omega^t = 0, \quad (4.15)$$

where  $m^\theta$ ,  $\boldsymbol{\omega}^\theta$ ,  $q^\theta$  are the heat, heat flux, and external sink of heat respectively. The superscript  $\theta$  means heat component. The heat flux can be written as

$$\boldsymbol{\omega}^\theta = -\mathbf{k}_\theta^t \mathbf{grad} T + \sum_J (h_J \rho_J^t \mathbf{v}_J), \quad (4.16)$$

where  $\mathbf{k}_\theta^t$  is the heat conductivity tensor in the current domain.  $T$  and  $h_J$  are temperature and enthalpy of phase  $J$ . When Eqs. 4.15 and 4.16 are pulled back to the reference domain, we have respectively,

$$\frac{d}{dt} \int M^\theta d\Omega^0 + \int \mathbf{DIV} \cdot \mathbf{W}^\theta d\Omega^0 + \int Q^\theta d\Omega^0 = 0, \quad (4.17)$$

$$\mathbf{W}^\theta = -\mathbf{K}_\theta^0 \mathbf{grad} T + \sum_J (h_J \rho_J^t \mathbf{V}_J), \quad \mathbf{K}_\theta^0 = J \mathbf{F}^{-1} \mathbf{k}_\theta^t \mathbf{F}^{-T}, \quad (4.18)$$

where  $M^\theta$ ,  $\mathbf{W}^\theta$ ,  $Q^\theta$  are the heat, heat flux, and external sink of heat, respectively.  $\mathbf{K}_\theta^0$  is the heat conductivity rank-2 tensor in the reference domain.

The constitutive relations of thermoporoelasticity are given as

$$\delta \mathbf{S} = \underbrace{\mathbf{C}^0 : \delta \mathbf{E}(\mathbf{u})}_{\mathbf{S}'}, \quad -b_B \sum_J S_J \delta p_J \mathbf{F}^{-1} \mathbf{F}^{-T} - 3\alpha_T K_{dr} \delta T \mathbf{F}^{-1} \mathbf{F}^{-T}, \quad (4.19)$$

$$\frac{\delta M_J^0}{\rho_J^0} = b_B S_J \mathbf{1} : \delta \mathbf{E}(\mathbf{u}) + \mathbf{N}_B \delta p_J + \alpha_{m,J} \delta T, \quad (4.20)$$

$$\delta \bar{S}_m - \sum_J \bar{s}_{m,J}^0 \delta M_J^0 = \alpha_T \mathbf{1} : \delta \mathbf{E}(\mathbf{u}) + 3 \sum_J \alpha_{m,J} \delta T + \frac{C_T}{T} \delta T, \quad (4.21)$$

where  $\mathbf{S}'$  is the second Piola Kirchhoff effective stress.  $K_{dr}$ ,  $b_B$  and  $\mathbf{N}_B$  is the drained bulk modulus, Biot's coefficient, and the inverse matrix of the Biot modulus in multiphase flow.  $\alpha_T$  and  $\alpha_{m,J}$  are the thermal dilation coefficients of volumetric skeleton and fluid, respectively.  $\bar{S}_m$ ,  $\bar{s}_m$ ,  $C_T$  are the total entropy, specific entropy of phase  $J$ , and total volumetric heat capacity, respectively.

We consider two-way coupling between fluid flow and geomechanics while taking one-way coupling from heat to geomechanics in this study, not from geomechanics to heat flow. For the case that all-way coupling is needed, we can take the extended algorithms developed in Kim (2018b).

Then, we can rewrite Eq. 4.20 in terms of reservoir porosity  $\Phi$ , also called Lagrange porosity, as follows.

$$\delta\Phi = \left( \frac{b_B - \Phi_0}{K_s^0} + \frac{b_B^2}{K_{dr}^0} \right) \sum_J S_J \delta p_J + 3\alpha_T b_B \delta T - \frac{b_B}{K_{dr}^0} \mathbf{1} : \delta \mathbf{S}, \quad (4.22)$$

where  $\Phi$  is defined as the ratio of the pore volume to the bulk volume in the reference (initial) configuration.

#### 4.1.2 Space and time discretization

We employ the finite-volume method for flow in space discretization, while using the nodal-based finite-element method for geomechanics. For flow, the pressure is located at the cell center, taking the piecewise constant interpolation function. For geomechanics, the displacement vector is located at the vertices of an element, having the piecewise linear interpolation. This mixed space discretization provides a relatively stable pressure field for early-time behavior of poromechanics, whereas the finite-element methods for both flow and mechanics can cause spurious pressure oscillations at early times if equal-order approximations of pressure and displacement are used. We take the backward Euler method for time discretization. In the subsection of numerical examples, we will show superiority of this mixed finite element method with the following sequential method (ie, fixed-stress sequential method).

Note that we have full-tensors of permeability and heat conductivity. In this case, multipoint flux approximation (MPFA) can eliminate the grid-orientation effect that two-point flux approximation (TPFA) may cause. Although MPFA provides accuracy better than TPFA, the resulting matrix might be indefinite for full tensor permeability. In particular, strong anisotropy causes an ill-conditioned linear system of flow. Thus, a strong linear solver for the ill-conditioned matrix is required. At this point, we take TPFA in flow simulation, not changing the flow simulator.

#### 4.1.3 Formulation for sequential modeling

We take sequential approach to solve coupled flow-geomechanics problems. The fixed-stress sequential method or its variants are well-known for unconditional stability and outstanding accuracy. The fixed-stress sequential method solves flow first, fixing the total stress field locally, and solves geomechanics at the next step with the solutions of flow (Kim et al., 2012). The fixed-stress method has turned out to be unconditionally stable and convergent in time. It facilitates the use of existing individual flow and geomechanics codes, only by implementing the interface code. The fixed-stress method has been applied to many engineering problems that exhibit small deformation. In this study, we extend the fixed-stress sequential method to the case of large deformation in coupled flow and geomechanics.

Specifically, we have three different stress measures: Cauchy stress, first Piola-Kirchhoff stress, and second Piola-Kirchhoff stress. From a-priori stability analysis, the fixed first Piola stress method provides unconditional stability while the fixed second Piola stress method also show good stability practically, shown in the subsection of numerical examples. The formulation becomes

$$\Phi^{n+1} - \Phi^n = \left( \frac{b_B - \Phi_0}{K_s^0} + \frac{b_B^2}{K_{dr}^0} \right) \sum_J S_J^{n+1} \delta(p_J^{n+1} - p_J^n) + 3\alpha_T b_B (T^{n+1} - T^n) - \Delta\Phi, \quad (4.23)$$

$$\Delta\Phi = \left( \frac{b_B - \Phi_0}{K_s^0} + \frac{b_B^2}{K_{dr}^0} \right) \sum_J S_J^n \delta(p_J^n - p_J^{n-1}) + 3\alpha_T b_B (T^n - T^{n-1}) - b_B (J^n - J^{n-1}), \quad (4.24)$$

where the fixed first and second Piola stress methods have different  $K_{dr}^0$ 's ( $K_{dr}^0 = K_{dr}^{PK1}, K_{dr}^0 K_{dr}^{PK2}$ , respectively) as follows.

$$K_{dr}^{PK2} = \frac{1}{9} \mathbf{1} : \mathbf{c}^t : \mathbf{1} , \quad K_{dr}^{PK1} = K_{dr}^{PK2} + \frac{1}{3} \frac{P:\dot{F}}{j/J} , \quad (4.25)$$

where the  $(\dot{\cdot})$  means time derivatives.

Using the fixed first or second Piola stress method, we can straightforwardly extend a coupled simulator of infinitesimal assumption to that of finite-strain geomechanics for large deformation. Specifically, we extend the capability of T+M (a coupled simulator of TOUGH+Hydrate and ROCMECH for flow and geomechanics, respectively), currently used in solving many geosciences problems. The original T+M was designed on the basis of infinitesimal transformation. In this study, we enhance T+M for large deformation. The current version of TOUGH+Hydrate stands on the basis of two-point flux approximation (TPFA) for the full tensor permeability.

#### 4.1.4 Numerical examples

##### 4.1.4.1 Stability and convergence of the fixed-stress method in space discretization

We first investigate spatial stability with various numerical discretizations in displacement and pressure fields for poroelasticity. We study two sources of the early time instability: discontinuity of pressure and violation of the inf-sup condition. We consider an incompressible fluid by employing the monolithic, stabilized monolithic, and fixed-stress sequential methods. Four different spatial discretization schemes are used: Q1Q1, Q2Q1, Q1P0, and Q2P0 (Fig. 4.2). The number of Q/P indicates the order of the basis (shape) function (e.g., Q2, Q1, and P0 for piecewise biquadratic, piecewise bilinear, piecewise constant interpolations, respectively). Thus, Q1P0 is the discretization method we are focusing in this study. From mathematic analysis and numerical tests, the piecewise constant finite volume method for flow provides stability at the early time for the case of the pressure discontinuity. On the other hand, a piecewise-continuous (or higher-order) interpolation of pressure shows spatial oscillation, having lower limits of time step size, although lower approximations of pressure than displacement can alleviate the oscillation. On the other hand, Q2Q1 can be better than Q1P0, because Q1P0 might not satisfy the inf-sup condition. However, regardless of fluid compressibility and the pressure discontinuity, the fixed-stress method can effectively stabilize the oscillation without an artificial stabilizer. Even when Q1P0 and Q1Q1 with the monolithic method cannot satisfy the inf-sup condition, the fixed-stress method can yield the full-rank linear system, providing stability. Thus, the fixed-stress method with Q1P0 can effectively circumvent numerical instability. We show these findings in the following numerical tests.

For numerical experiments, we consider two cases: 1D Terzaghi's and 2D McNamee-Gibson's problems (Fig. 4.3). For the Terzaghi's problem (1D consolidation problem), the domain is discretized with 20 grids, where each grid has a size  $(\Delta x \times \Delta z)$  of 1 m  $\times$  0.25 m, being 5min depth and 1m in width (Fig. 4.3). For geomechanics, 2.125 MPa of traction is applied to the top, whereas a no-vertical displacement boundary is placed at the bottom, and a no-horizontal displacement boundary is applied to both sides. Flow has a drainage boundary at the top, where pressure is zero, and a no-flow boundary at the bottom. The initial pressure and total stress are also both zero (ie, zero excessive pore-pressure). Then, before the traction is applied, the system is mechanically in equilibrium. The simulation results are obtained after 1 time step with  $\Delta t = 0.01$  s, ( $t_d = c_v t / h^2 = 1.9378 \times 10^{-6}$ ). The main properties of fluid and geomechanics are shown in Table 4.1.

Fig. 4.4 shows numerical results at early times for the 1D consolidation problem. For Q1Q1, the oscillation becomes severer because of violation of the inf-sup condition as well as discontinuity of pressure at the drainage boundary. However, the fixed-stress sequential method yields much more stable and accurate results than the monolithic methods, although it still shows very tiny oscillation at the drainage boundary. STAB can reduce the oscillation up to the same intensity as the fixed-stress method. Although no oscillation can be found in FPL, it causes the same level of errors as STAB does, inducing artificial pressure diffusion for stabilization near the drainage boundary.

On the other hand, for Q1P0, we find different results from the Q1P0 pair, as contrasted with Q1Q1. We do not observe instability at the drainage boundary at the top, because the pressure field is interpolated piecewise constant, facilitating discontinuous pressure distribution. Also, Q1P0 is known to be more stable than Q1Q1, although it does not satisfy the inf-sup condition in general. Both the monolithic and fixed-stress methods do not cause oscillation in pressure, being accurate and not violating the inf-sup condition. Q2Q1 can satisfy the inf-sup condition for an incompressible fluid while the pressure discontinuity causes pressure oscillation at the boundary. Q2P0 exhibits the same numerical behaviors as Q1P0.

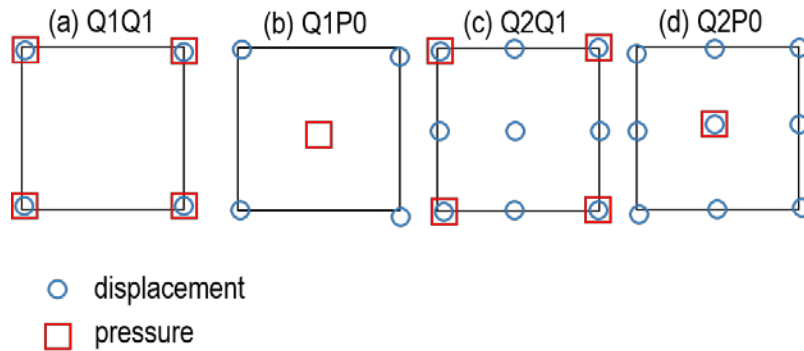


**Fig. 4.2 Four space discretization methods of flow and geomechanics.** Q1Q1: bilinear interpolation of both displacement and pressure within an element. Q1P0: bilinear interpolation of displacement and constant interpolation of pressure. Q2Q1: biquadratic interpolation of displacement and bilinear interpolation of pressure. Q2P0: biquadratic interpolation of displacement and constant interpolation of pressure

**Table 4.1 Main input data**

Property	Value	Unit
Young's modulus	100	MPa
Poisson ratio	0	-
Biot's coefficient	1.0	-
porosity	0.3	-
permeability	50	mD
fluid density	1000	kg m <sup>-3</sup>
fluid viscosity	1	cp
fluid compressibility	4.0 × 10 <sup>-9</sup> or 0	Pa <sup>-1</sup>

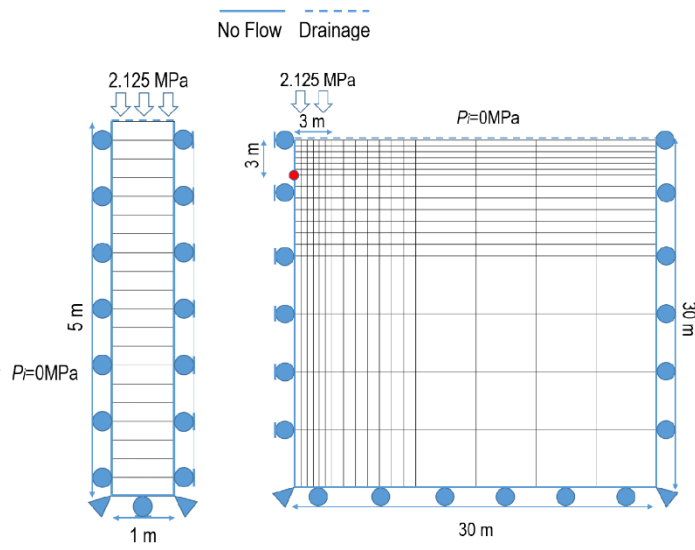


Fig. 4.3 Left: A 1D consolidation problem (ie, Terzaghi's problem). Right: A 2-dimensional (2D) plane strain strip-footing consolidation problem (ie, McNamee-Gibson's problem).

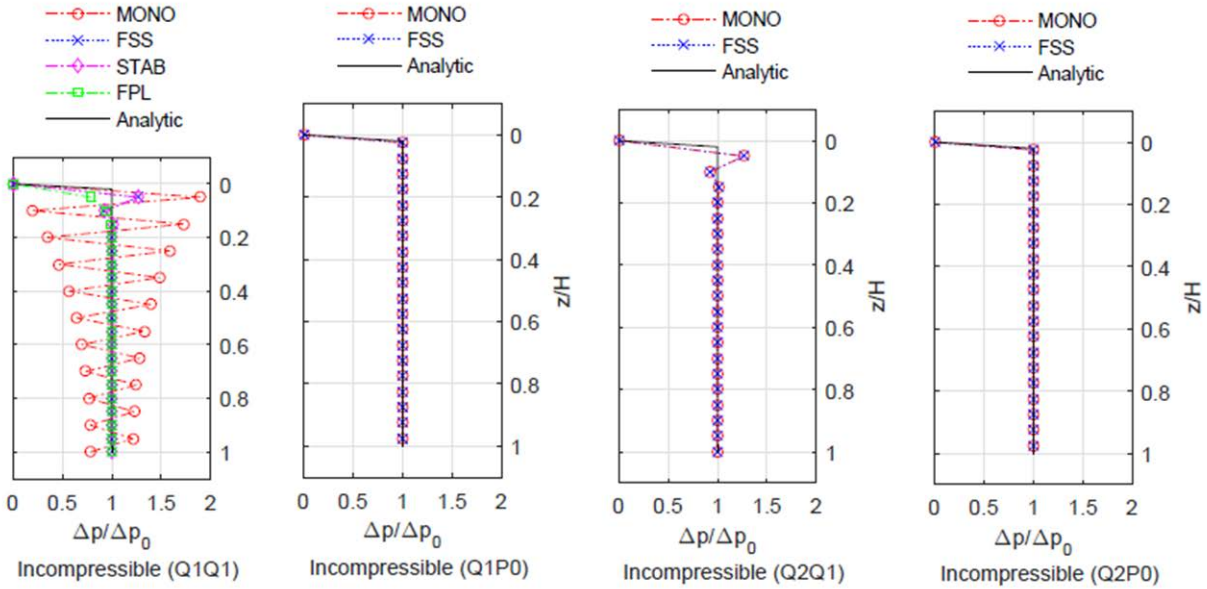
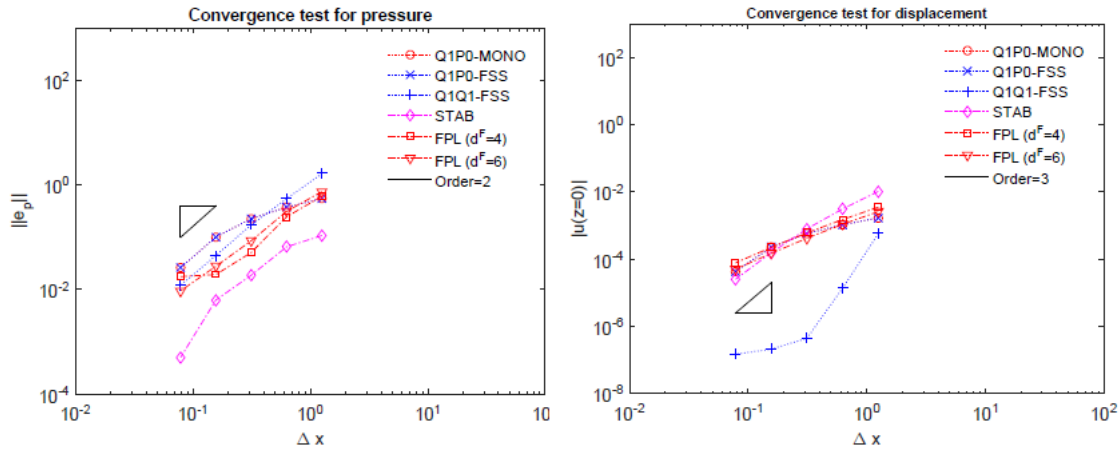


Fig. 4.4 Pressure distributions for an incompressible fluid. “MONO” and “FSS” indicate the solutions of the monolithic and the fixed-stress sequential methods, respectively. STAB and FPL are the stabilized monolithic method and fluid pressure Laplacian stabilized method, respectively. For Q1Q1, the monolithic method shows severe oscillations.

We also study the behavior of convergence, called h-convergence for the monolithic, stabilized monolithic, and fixed-stress methods (Fig. 4.5). We take 4, 8, 16, 32, and 64 gridblocks, which yield  $\Delta z$  of 1.25, 0.625,

0.3125, 0.15625, and 0.078125 m, respectively. In order to eliminate the error of time discretization, we take a very tiny time step size of  $\Delta t = 5 \times 10^{-4}$  s, having the total simulation time of  $t = 1.0$  s. From Fig. 4.5, we find that the fixed-stress method shows good convergence, having the same order of the monolithic method and STAB. In addition, we identify that the FPL method also shows good rates of convergence.



**Fig. 4.5 Convergence study for the monolithic, stabilized-monolithic, and fixed-stress methods with various space discretization. The fixed stress method shows good convergence, having the same order of the monolithic method.**

For the 2D problem (the right figure of Fig. 4.3), we employ a typical 2D plane strain problem with a strip-footing, known as the McNamee and Gibson problem. For the boundary condition of geomechanics, we apply no horizontal displacement to the left and right boundaries and no vertical displacement at the bottom. The overburden of 2.125 MPa is applied to the left 3mat the top. For flow, we have no-flow boundary along the both sides and at the bottom, while the drainage boundary is applied at the top. For the time step size, it begins with  $\Delta t = 10^{-8}$  s, and it is doubled until it reaches  $\Delta t=1.0$ s.

From Figs. 4.6-4.8, we identify the same numerical behavior as shown in the 1D consolidation problem. Q1Q1 with the monolithic method is unstable, having severe oscillation. The fixed-stress method can remove the oscillation effectively. On the other hand, all the solutions from the other pairs (Q1P0, Q2Q1, Q2P0) are stable and accurate.

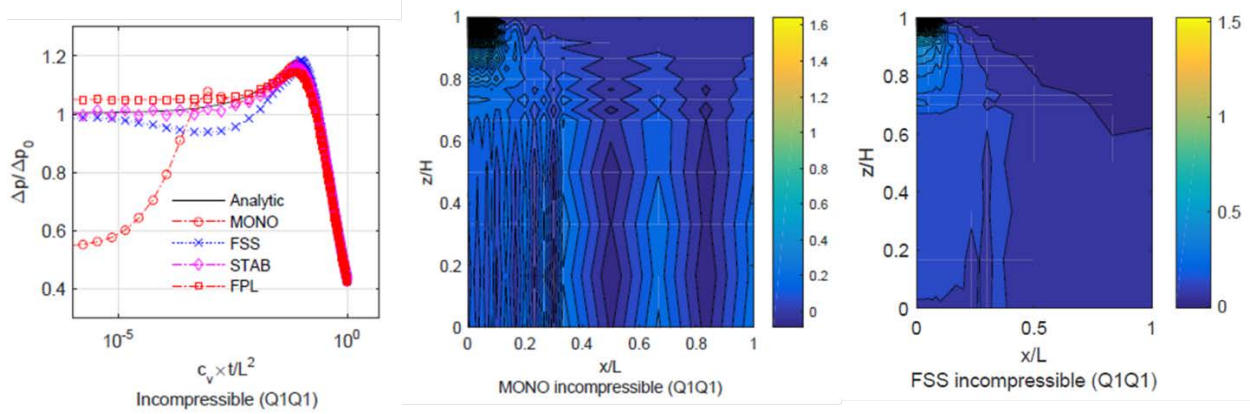


**Fig. 4.6** For Q1Q1, inaccuracy at early times becomes severer because of the violation of the inf-sup condition. Pressure distributions with Q1Q1 at the early time ( $t = 0.1023$  s) by using the monolithic method. Pressure is normalized by the initial overburden of 2.125 MPa.

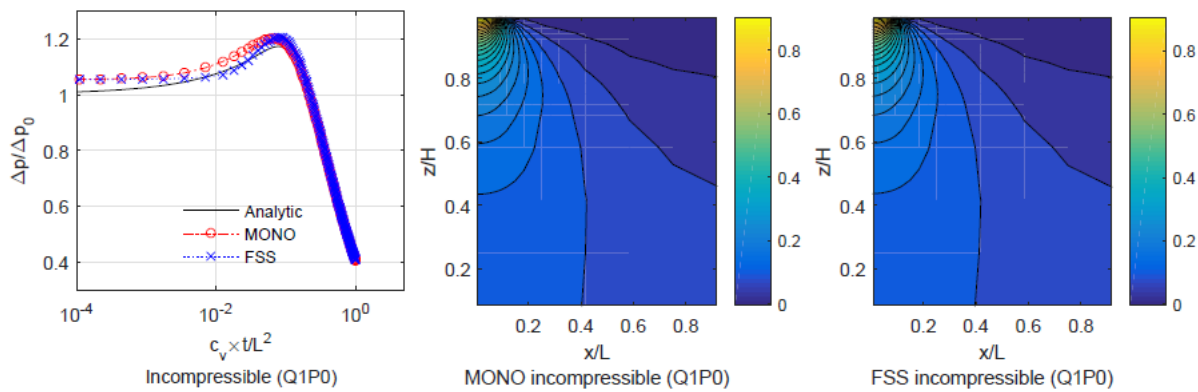


**Fig. 4.7** For Q1P0 Evolutions of pressure at the monitoring point (left), and pressure distributions of the monolithic method (center) and the fixed-stress method (right) at the early time ( $t = 0.1023$  s) with Q1P0. All the solutions are stable and accurate.

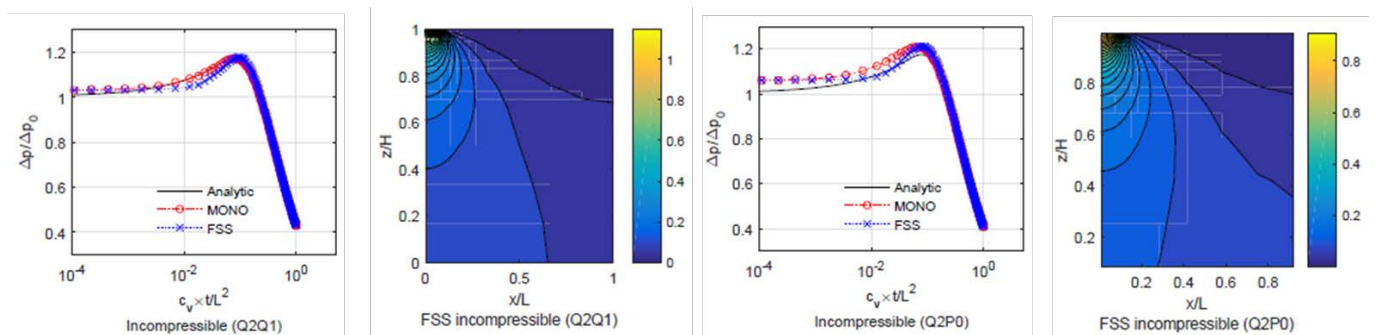


**Fig. 4.8** Just like Q1P0, all the solutions of Q2Q1 and Q2P0 are stable and accurate.

#### 4.1.4.2 Stability of the fixed stress method extended in largely deformable coupled geomechanics and flow.

We take the McNamee and Gibson problem while taking different overburden conditions (the left of Fig. 4.9). There is the overburden to the left 5 m at the top ( $\bar{\sigma}_f = 2 \times 10.0 \text{MPa}$  for small overburden and  $\bar{\sigma}_f = 11 \times 10.0 \text{MPa}$  for large overburden), while taking the overburden of 10.0 MPa for the rest area at the top boundary. Small overburden is used for verification the developed simulator for coupled largely deformable geomechanics and flow. The right of Fig.4.9 shows that the simulator is verified with the analytical solution.

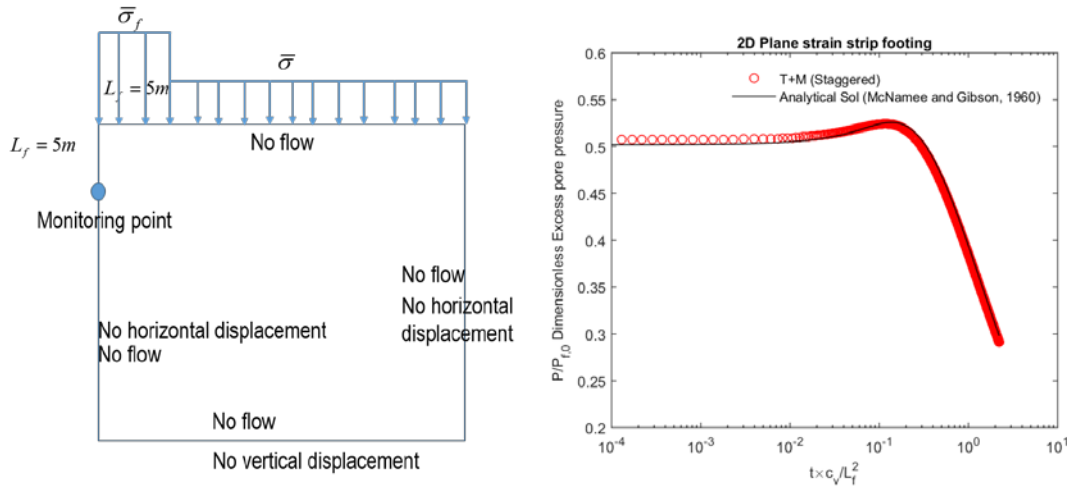


**Fig. 4.9 All the solutions are stable and accurate. Verification of coupled flow and geomechanics.  $\bar{\sigma}_f$  is geomechanical loading.  $t_d = t \times c_v / L_f^2$ . The numerical solution matches the analytical solution of the McNamee and Gibson problem, capturing the Mandel–Cryer effect.**

Then, we increase overburden at the left-top domain (i.e. large overburden). Shown in the left of Fig. 4. 10, the results of pressure and displacement from 'PK1' and 'PK2' are almost identical. We also find significant difference in pressure at early times between the total Lagrangian and the infinitesimal transformation approaches. At late times, even though the pressure difference decreases, the difference in subsidence increases considerably, (not shown here but in Kim (2018a)). We identify larger subsidence from the total Lagrangian method than that from the infinitesimal transformation approach. From the right of Fig. 4.10, for large overburden, we identify enormous changes of the reservoir configuration as well as huge compaction particularly near the loading area, where the assumption of infinitesimal transformation is not valid.

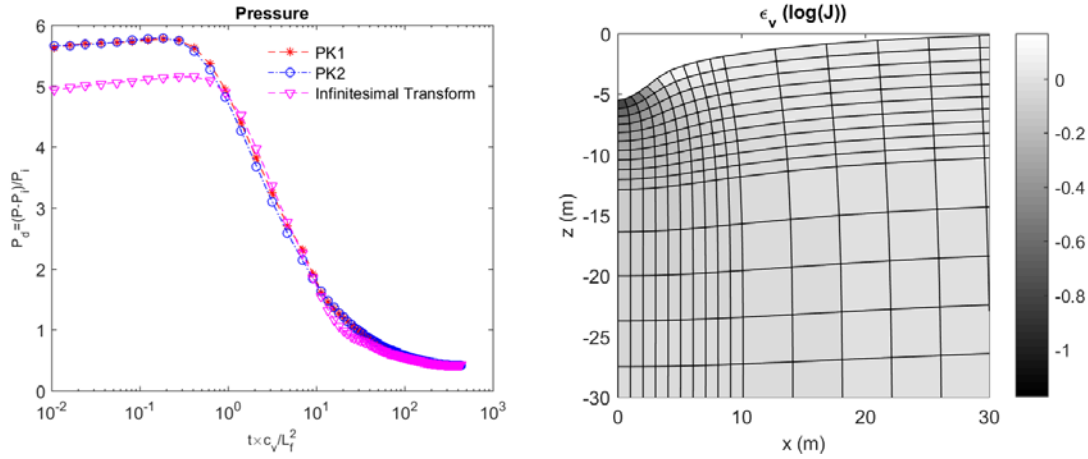


**Fig. 4.10 Left: Evolution of pressure at the monitoring point. There are substantial differences between finite-strain and infinitesimal geomechanics. Right: Distribution of  $\epsilon_v$  at  $t_d = 71.1$  with the corresponding deformation. We identify large subsidence and significant compaction around the loading zone.**

#### 4.1.4.3 Stability of the fixed stress method extended in largely deformable coupled geomechanics and flow.

The left of Fig. 4.11 shows a 2D production problem in a heterogeneous domain, similar to the previous largely deformable elastic geomechanics coupled with flow (Fig. 4.9), but we consider two different formations. The flow and geomechanics properties of Formation 1 are the same as the domain in Fig. 4.9. The Young modulus and Poisson's ratio of Formation 2 are  $E = 160.0$  MPa and  $\nu = 0.0$ , respectively. The permeability of Formation 2 is  $k_{xx} = k_{zz} = 6.6 \times 10^{-2}$  mD,  $k_{xz} = k_{zx} = 0$  mD. We produce fluid with a constant rate of  $2.0 \times 10^{-4}$  kg/s at ( $x = 0$  m,  $z = -6.5$  m). The other input data are the same as those in Fig. 4.9. In order to test numerical stability for elastoplasticity, we first employ the J2 plasticity theory with isotropic hardening, described in Simo and Hughes (1998), where we take  $K_H = 600$  MPa (the hardening modulus) and  $\sigma'_Y = 6.0$  MPa (yield stress) for both Formations 1 and 2.

Figs. 14–17 show numerical results of plasticity, pressure, displacement, and reservoir compaction by using the total Lagrangian methods of 'PK1' and 'PK2'. In Figs. 4.11 and 4.12, we observe that 'PK1' and 'PK2' yield similar trends of pressure and failure area but that slight differences between the two methods exist unlike the previous case. Plastic deformation first occurs at the top edge of Formation 1 where shear deformation is severe (Fig. 4.12 (a)). Then, plasticity caused by shear deformation also occurs near the left-bottom boundary between Formations 1 and 2 due to the different elasticity moduli, and it propagates upward to the other areas of Formation 1 (Fig. 4.12 (b)–(d)).

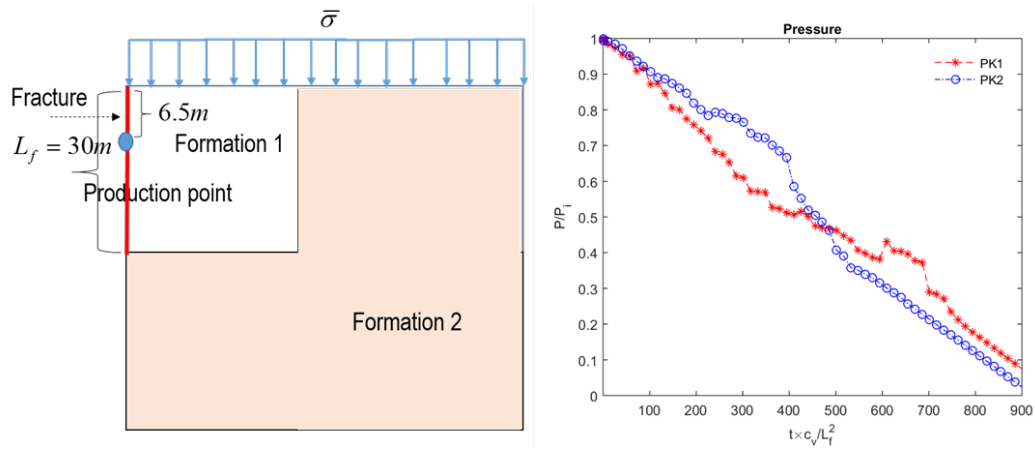


**Fig. 4.11** Left: A production scenario. Right: Comparisons between ‘PK1’ and ‘PK2’ for Case 4. Evolution of pressure at the monitoring point. The two sequential methods cause some differences unlike the previous cases.

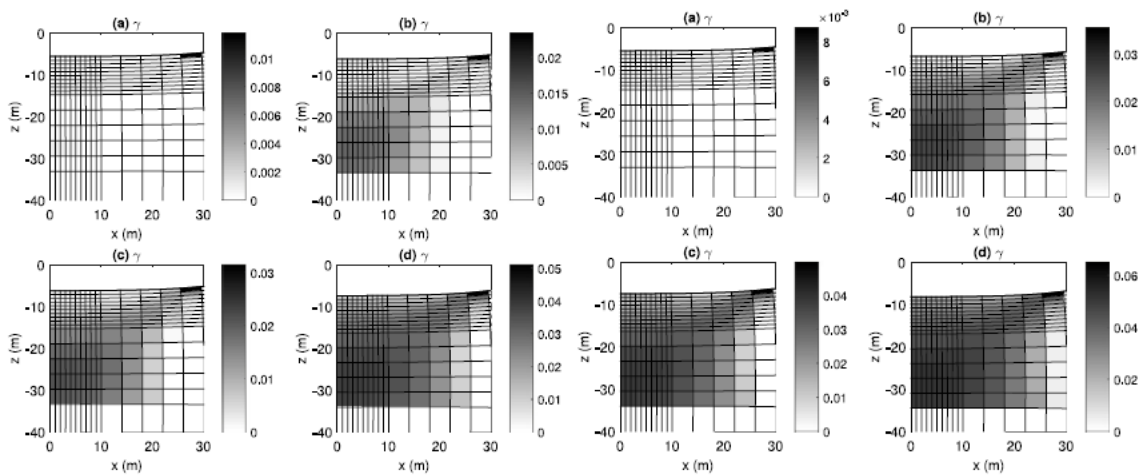


**Fig. 4.12** Distributions of the plasticity consistency parameter (measure of plasticity) at different times for Case 4 when ‘PK1’ (left) and ‘PK2’ (right) are employed. (a)  $t_d = 3.61 \times 10^2$ . (b)  $t_d = 4.38 \times 10^2$ . (c)  $t_d = 5.15 \times 10^2$ . (d)  $t_d = 5.91 \times 10^2$ . Severe plastic deformation occurs at late times.

#### 4.1.4.4 Verification of hydrate simulation for largely deformable coupled geomechanics and flow.

Then, we have been implementing the geomechanics module of large deformation in TOUGH+Hydrate, coupling two simulators. After implementation, we tested the enhanced simulator of T+M, comparing it with the previous study, Kim and Moridis (2012). Specifically, we introduce a 2D reservoir with the plane strain geomechanics, placing a horizontal well located in the first hydrate layer at the left corner, shown in Fig. 4.13. We set the depth of the top zero (i.e.,  $z=0$ ). We take a scenario where a vertical fracture is created from the well down to the top of the underlying zone (i.e.,  $-32 \sim -48\text{m}$  in depth at  $x=0.25\text{m}$ ). The

hydrate and mud layers are located between -32m and -48 m in depth. Both layers have 0.25m thickness, being placed alternatively, and there are 64 layers in total.

We have no flow at the boundaries for the flow problem. The initial pressure at the top layer is 20 MPa, and distributed with the hydrostatic pressure gradient. The initial aqueous and hydrate saturation  $s$  are 0.5, and the initial temperature is 12.5°C. The initial porosities for the overlying, hydrate, mud, and underlying zones are 0.3, 0.6, 0.5, and 0.3, respectively. The porosities of the fracture zones take the same porosities of the hydrate and mud zones, assuming very small pore volume to be taken by the fracture. The intrinsic permeabilities for the hydrate, mud, overlying, underlying, and fracture zones are  $5.0 \times 10^{-14} \text{ m}^2$ ,  $5.5 \times 10^{-18} \text{ m}^2$ ,  $5.5 \times 10^{-18} \text{ m}^2$ ,  $5.5 \times 10^{-18} \text{ m}^2$ , and  $5.5 \times 10^{-8} \text{ m}^2$ , respectively, where 1 Darcy is  $9.87 \times 10^{-13} \text{ m}^2$ . Since the intrinsic fracture permeability is high enough for pressure to be hydrostatic, numerical results are not sensitive to different permeability models for the fracture. The medium heat capacities, wet and dry thermal conductivities for all layers are 1000 J/kg/°C, 3.1 W/m/°C, 0.5 W/m/°C, respectively. No capillarity is considered. We apply a constant total fluid production,  $Q_p = 4.0 \text{ kg/s}$ .

For the geomechanics problem, we have no horizontal displacement at both sides, no displacement at the bottom, and the normal traction of 20 MPa at the top. Drained bulk moduli at zero solid saturation (ie,  $S_s (=S_H + S_l) = 0.0$ ) for the hydrate, mud, overlying and underlying zones are 61.67 MPa, 54.79 MPa, 54.79MPa, and 54.79MPa, respectively, and those at  $S_s = 1.0$  are 616.67MPa, 547.86MPa, 547.86MPa, and 547.86MPa, respectively. Shear moduli for the zones at  $S_s = 0.0$  are 92.5 MPa, 57.75 MPa, 57.75 MPa, and 57.75MPa, and those at  $S_s = 1.0$  are 925 MPa, 577.5 MPa, 577.5 MPa, and 577.5 MPa. The vertical initial principal total stresses at the top are -20.0 MPa, and increased by the loading from gravity, where the bulk density is 2200 kg/m<sup>3</sup>, and the horizontal and vertical stresses are the same.

The previous code is restricted to small deformation because it is based on infinitesimal transformation (eg, linearized strain tensor), while the current enhanced code is applicable not only to small deformation but also to large deformation. Thus, the results from the two simulators should be almost the same when a physical problem exhibits small deformation while they do not have to be for the cases of large deformation. From Fig. 4.13, we identified that the results between the previous and currently enhanced codes are identical, when deformation is small. This implies that the implementation of the enhanced codes is successful.

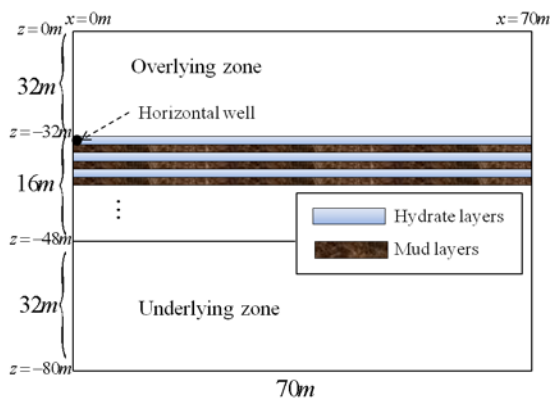


Fig. 4.13 2D problem of gas production from the hydrate deposits by depressurization.

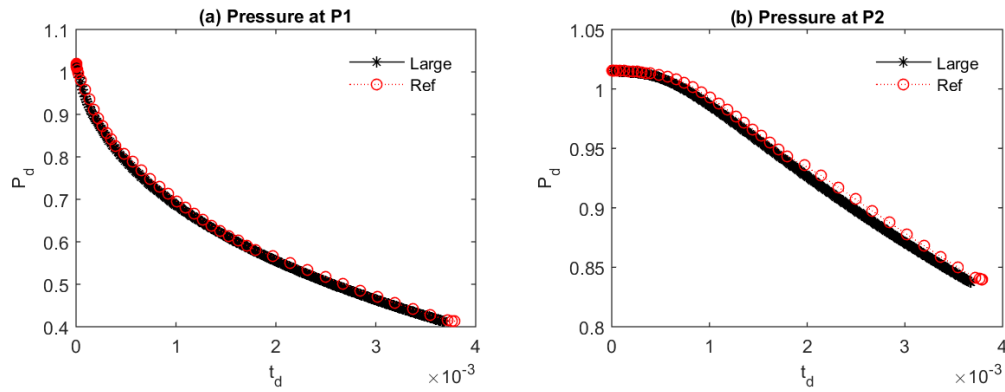


Fig. 4.14 Evolution of pressure at two monitoring point of P1 at the well (0.25m, -32.125m) and P2 at (12m, -32.125m), located at the first hydrate layer. ‘Ref’ indicates the previous study based on assumption of small deformation, and ‘Large’ indicates the current enhanced simulator that can account for large deformation.

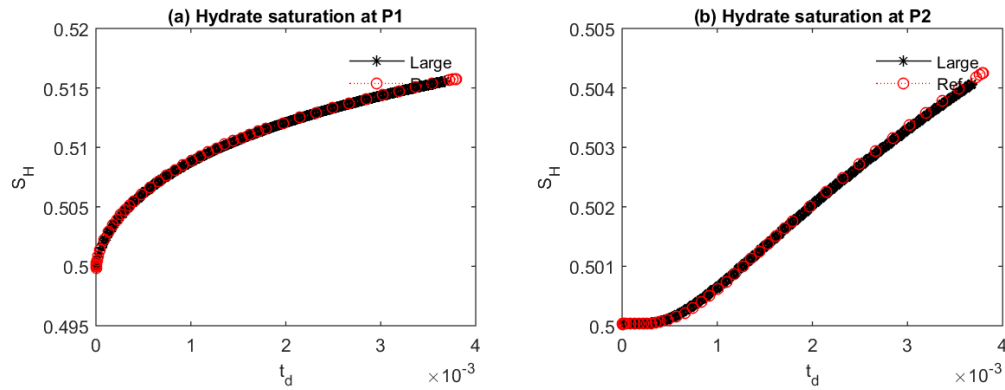


Fig. 4.15 Evolution of hydrate saturation at the two monitoring point of P1 at the well (0.25m, -32.125m) and P2 at (12m, -32.125m), located at the first hydrate layer.

## 4.2 Parallel Simulation of coupled flow and geomechanics (Subtask 5.3)

We develop a parallel code for coupled non-isothermal flow and elastoplastic geomechanics. We mainly focus on flexible and pragmatic parallel code development and its scalability. Specifically, beginning with uncoupled individual serial codes of non-isothermal flow and geomechanics, we primarily implement MPI (Message Passing Interface) for matrix assembly and parallel solvers, particularly using the PETSc library codes while using OpenMP (Open Multi-Processing) for other miscellaneous subroutines to prevent significant overheads. We consider various matrix decomposition schemes for preconditioning parallel solvers as well as assigning computation loads to different CPU cores. For the coupled simulation, we take the fixed-stress sequential method, which allows the coupling between two simulators with least efforts of code development. As a result, the parallel code can easily be developed within a short period of time.

In numerical experiments, we take more than one million cells to investigate parallel performance. For both flow and geomechanics, the parallelization largely reduces the overall simulation execution time with scalable speedups. The matrix decomposition methods have effects on execution time and solver performance, which implies that appropriate matrix decomposition is important for computational efficiency and scalability. We also find that the scalability of the parallel coupled simulator by the sequential method can honor the scalability of individual parallel simulators. Still, plasticity can cause imbalance in the parallel environment of geomechanics simulation.

#### **4.2.1 Development of parallel simulators**

The parallel method in this study is based on a mixed distributed and shared memory architecture on a Linux cluster, ADA supercomputer at Texas A&M University. The compute nodes for this study are IBM NeXtScale nx360 M4 dual-socket servers based on Intel Xeon 2.5GHz E5-2670 v2 10-core processors. In each 10-core processor, each core (CPU) has its own on-chip L1 and L2 caches. L3 cache is within each processor. Each processor has its own DDR3 memory.

The distributed memory is important for the efficiency for solving large scale problems while the shared memory can reduce overheads. We then use MPI and a MPI-based parallel solver for the distributed memory architecture, while taking OpenMP for the shared memory architecture. The parallel scheme aims to largely enhance the efficiency for solving the linear system in order to speed up the array assembly, reducing communication costs. It typically takes more time to solve the geomechanics problem than the time to solve the flow problem due to more unknown to be solved and/or a larger domain of geomechanics in order to reduce the boundary effect.

This large computational cost caused by the geomechanics problem for large scale simulation requires using parallel linear solvers, such as PETSc as well as parallelizing other subroutines such as the matrix-vector array assembly. PETSc, the parallel solver utilized in this study, is an open source software package from Argonne National Laboratory based on the MPI standard. It has many features including parallel matrix operations and preconditioned parallel solvers. In this study, PETSc replaces the serial linear solvers used in the serial codes. PETSc provides the parallel matrix array assembly subroutines and parallel solvers for the parallel scheme of this study.

Fig. 4.16 shows the parallel scheme of this study when the two individual codes are coupled sequentially. We first parallelize the serial codes mainly in the matrix assembly subroutines and linear solvers. The parallel assembly scheme reduces the complexity of implementing scalable parallelization for the matrix assembly. The parallel matrix assembly scheme is applied to the Jacobian matrix, taking compressed row storage (CRS) format for the sparse matrix. The main job to utilize the PETSc solver is to assign values to the linear system in parallel. It is worth noting that the array operations largely increase the matrix assembly efficiency and the sparse matrix format yields the optimum efficiency.

On the other hand, when values are assigned to the arrays by iteration through each element, the efficiency might considerably decrease, causing deficient parallelization. Furthermore, miscellaneous subroutines do not take long execution time. If distributed memory-based parallelization is used for these subroutines, the cost of parallel communication can be significant which might limit parallel efficiency. Instead, OpenMP parallelization is used for these miscellaneous subroutines. Specifically, miscellaneous subroutines are processed only on one core, and OpenMP is used to speed up the local iteration using the shared memory threads.

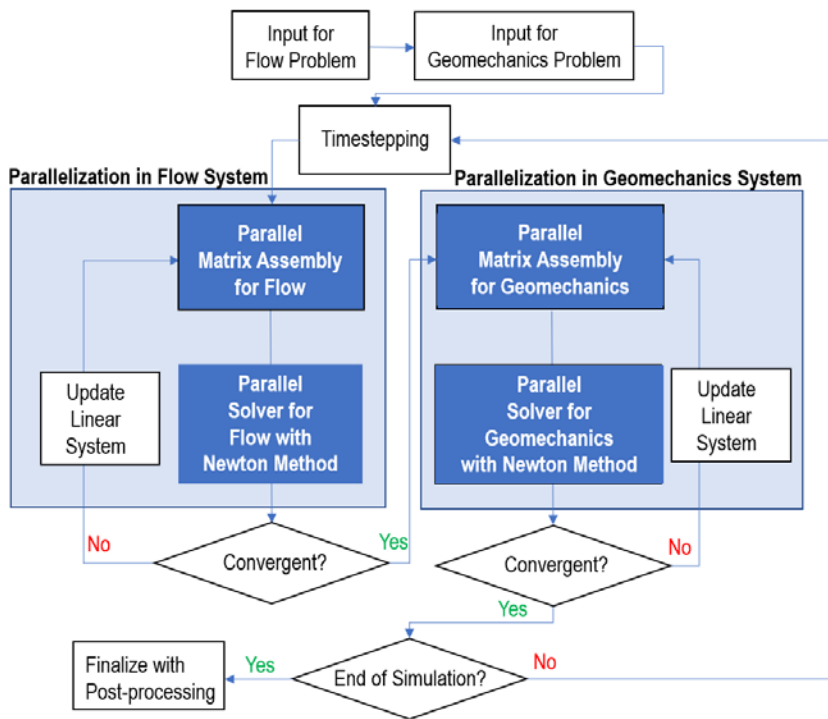


**Fig. 4.16 Framework of the parallel scheme with the sequential method.**

#### 4.2.3 Numerical experiments

##### 4.2.3.1 Coupled non-isothermal single-phase flow and elastic geomechanics

We introduce a three dimensional synthetic reservoir model to test the performance of the parallel codes (Fig. 4.17). We consider injection of single-phase fluid with a fixed specific enthalpy as well as the same fluid production in the reservoir. Elastic geomechanics is considered in this case. We take a uniform grid system with more than million grid blocks (i.e.,  $320 \times 320 \times 10$ ) and the grid size of  $5\text{m} \times 5\text{m} \times 5\text{m}$  in the x, y, z directions. We inject a fluid at the first grid block (1, 1, 1) with a rate of  $0.5\text{kg/s}$  and a specific enthalpy of  $2.263 \times 10^{-5} \text{ J/kg}$ . We also produce the fluid at the last grid block, (320, 320, 10), with a rate of  $0.5\text{kg/s}$ . For the flow problem, the initial pressure and temperature are  $30\text{MPa}$  and  $30^\circ\text{C}$ , respectively, and no-flow boundary is imposed. The geomechanics problem has overburden of  $30\text{MPa}$  and no displacement normal to the sides and bottom.

The initial horizontal and vertical total stresses are both  $-30\text{MPa}$ , from which we initially have zero effective stress. We consider a type of fluid that can exist in oil reservoirs. Specifically, we take dead oil (i.e., single phase n-decane oil) with the density function that follows the Yaws law as well as the constant viscosity. The other main input data are listed in Table 4.2. The simulation time is 1 year.

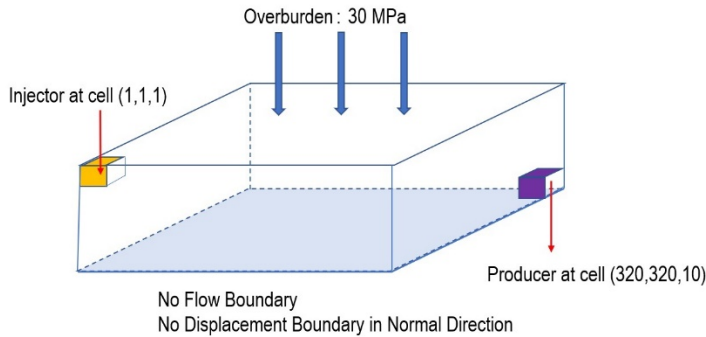


**Fig. 4.17 Schematics of a coupled non-isothermal single-phase flow and elastic geomechanics problem**

**Table 4.2: Input data for the problem in Fig. 17.**

Property	Value/Specification
<b>Reservoir</b>	
Porosity	0.15
Bulk density	$2600 \text{ kg/m}^3$
Saturated Heat Conductivity	$3.1 \text{ W/(m.K)}$
Desaturated Heat Conductivity	$0.5 \text{ W/(m.K)}$
Specific Heat	$1000 \text{ J/kg/K}$
Permeability	$1.5 \times 10^{-13} \text{ m}^2$ (152 mD)
Young's Modulus	600 MPa
Shear Modulus	300 MPa
Thermal Dilation Coefficient ( $\alpha_T$ )	$4.5 \times 10^{-5} \text{ K}^{-1}$
Biot's Coefficient ( $\alpha_f$ )	1.0
<b>Fluid</b>	
Reference Density	$728.3 \text{ kg/m}^3$
Compressibility	$1.0 \times 10^{-9} \text{ Pa}^{-1}$
Reference Pressure	0.1 MPa
Reference Temperature	$25 \text{ }^\circ\text{C}$
Reference Viscosity	$8.632 \times 10^{-4} \text{ Pa} \cdot \text{s}$
Reference Heat Conductivity	$0.1322 \text{ W/(m.K)}$
Reference Specific Heat	$313.72 \text{ J/kg/K}$
Mole Weight	$0.1423 \text{ kg/mol}$

Due to the nonlinearity of fluid-heat flow, several Newton-Raphson iterations of the flow problem are required at each time step. On the other hand, the geomechanics problem of this case requires only one Newton-Raphson iteration because of linear elasticity. This implies that, even though the size of the linear system of flow is smaller than the geomechanics linear system, efficient solution of the flow problem is still important due to the multiple iterations. The solver specification is GMRES with restart of 30. We take a preconditioner of ILU(0) for a single processor, while the block Jacobi method is used for multiple

processors. Note that block Jacobi methods limit the parallel performance as the ratio of processor-unknowns to total-unknowns decreases, and other preconditioning strategies such as the domain decomposition preconditioners or the multigrid methods might yield better performance. The simulation specifications are listed in Table 4.3.

**Table 4.3: Numerical parameters for the problem in Fig. 17**

Numerical Parameter	Value
Convergence Criterion for Newton-Raphson Method	$10^{-9}$
Geomechanical Total Degree of Freedom	3283188
Number of Flow Problems Primary Variables	2048000
L2-Norm of Residual	$10^{-50}$
Decrease of L2-norm of Residual / L2-norm of Residual	$10^{-5}$

Fig. 4.18 shows pressure distribution at the bottom and top layers as well as the temperature distribution around the injection well. Fig. 4.19 shows the evolution of volumetric strain at the injection and production wells.

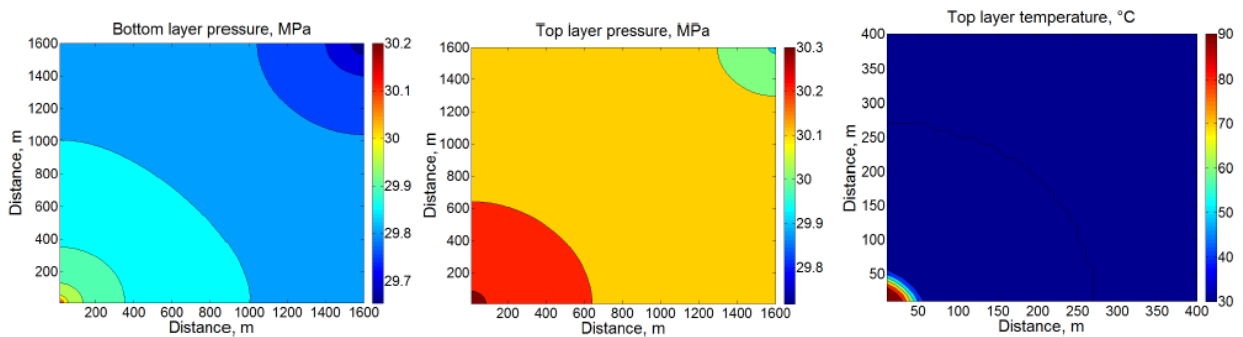


**Fig. 4.18 Distributions of pressure and temperature after 1 year.**

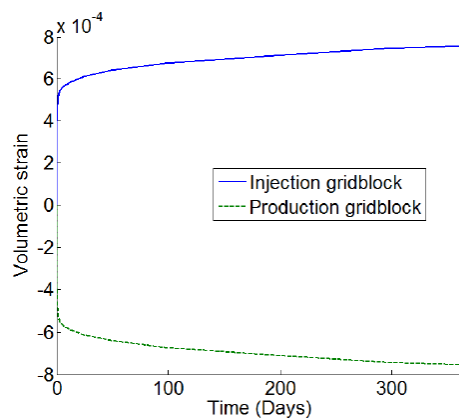


**Fig. 4.19 Evolution of volumetric strain at the injection and production wells.**

Pressure increases near the injection well while pressure decreases near the production well. The pressure at the center of the reservoir model does not experience significant changes due to symmetry. We also observe that pressure diffusion is much faster than the temperature propagation because of high permeability. Only certain areas close to the injection well show significant changes in temperature with the highest temperature of 90°C. Volumetric strain increases at the injection well (i.e., dilation) while it decreases at the production well (i.e., compaction), because pore-pressure increases and decreases, respectively.

We exclude the reading time of the input data for flow simulation in the parallel performance profiling, because the subroutines for reading the input data in TOUGH have not been parallelized yet, while we have parallelized the input subroutines for geomechanics simulation. The input for the flow problem requires a one-time reading of gridblocks and element connection data, which might take long time for large scale problems.

Figs. 4.20-4.22 show the parallel performance (i.e., execution time) and speedup for the geomechanics-only, flow-only, and coupled flow-geomechanics problems. For the geomechanics-only problem, from the figures, we find that the parallel performance reaches the optimum at 32 processes. The 64-process parallel simulation has a slightly longer execution time than the optimum 32-process simulation, which indicates that the efficiency of the 64-process simulation decreases significantly. From Fig. 4.21, the speedup of the parallel solver significantly increases as the processes increase, and this trend increases monotonically. We obtain good scalability of the parallel solver until it reaches 32 processes with significant reduction of computational cost for matrix solution. As the overhead grows, the speedup from the parallel solver decreases slightly due to limitation of the data communication for non-solver parts. Fig. 4.20 shows that parallel performance for the non-solver parts does not become improved very much after 32 processes. For the geomechanics simulation, the overall optimum speedup is 24.7 with 32 processes (right of Fig. 4.21 and 4.22). Also, from Figs. 4.20 and 4.21, the optimum assembly speedup is 16.9 at 32 processes and the optimum parallel solver speedup reaches 28.4 at 32 processes.

For the flow-only problem, while the optimum parallel solver speedup is 24.8 at the 64 processes, the optimum speedup of flow is 10.9 at 32 processes, as shown in Figs. 4.21 and 4.22. Fig. 4.21 shows that the computational efficiency is not obtained at 64 processes just like the geomechanics simulation.

Figs. 4.21 and 4.22 show the overall parallel performance of the coupled simulator, based on the parallelization of both flow and geomechanics. The optimum overall parallel implementation is achieved by 32 processes with a speedup of 14.8. For both flow and geomechanics, when the process number exceeds 32, we obtain very limited increase of parallel performance, which causes significant reduction in parallel efficiency, while more massive parallelization could provide more efficiency. This little improvement between 32 and 64 can be explained by the well-known Amdahl's law which describes the limit of achievable speedup and efficiency relating to the serial part of the program as follows.

$$S_{up} = \frac{1}{(r_s + r_p/N_p)}, \quad (4.26)$$

where  $S_{up}$  and  $N_p$  are the speedup and number of processes, respectively.  $r_s$  and  $r_p$  represent the ratios of the sequential and parallel portions in one program, respectively, and  $r_s + r_p = 1$ . From Eq. 4.26, as the number of processes increases, the speedup of parallelization decreases significantly. At the same time, aforementioned, the communication time between processes becomes less parallelized as the processes

increase, which lessens the parallelized portion. As a result, even though many processes are introduced, the speedup cannot be improved significantly or might decrease at a certain number of processes.

The scalability of the parallel coupled flow and geomechanics simulator is close to the ideal scalability with up to 16 cores. This indicates that the parallel implementation with 8 or 16 processes has relatively high scalability, being cost-effective. Thus, when the parallel environment is limited, the 8-or 16-process implementation can achieve practical speedups.

Considering the observation of speedup, in this study, we find that the parallel scheme achieves better overall scalability for the geomechanics simulation than that for the flow simulation. The parallel solver scalability of the geomechanics simulation is also better than that of the flow simulation. This might be due to linear elasticity while the non-isothermal flow problem is nonlinear.

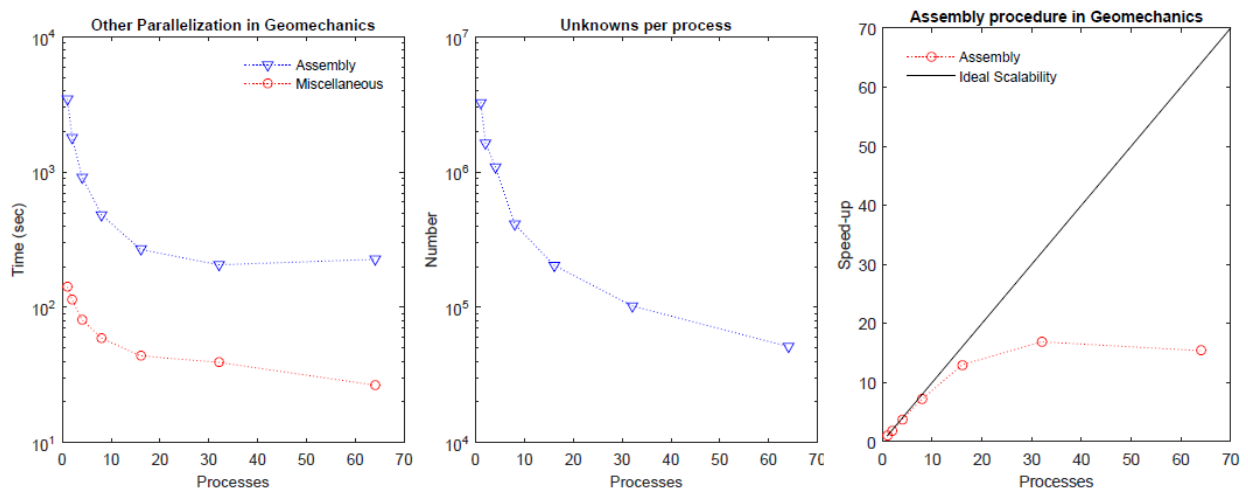
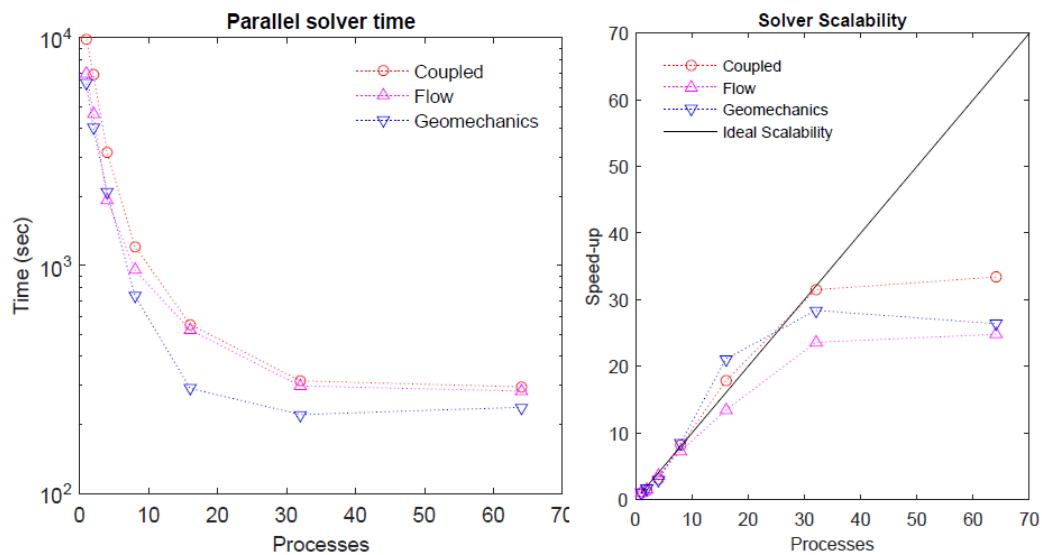
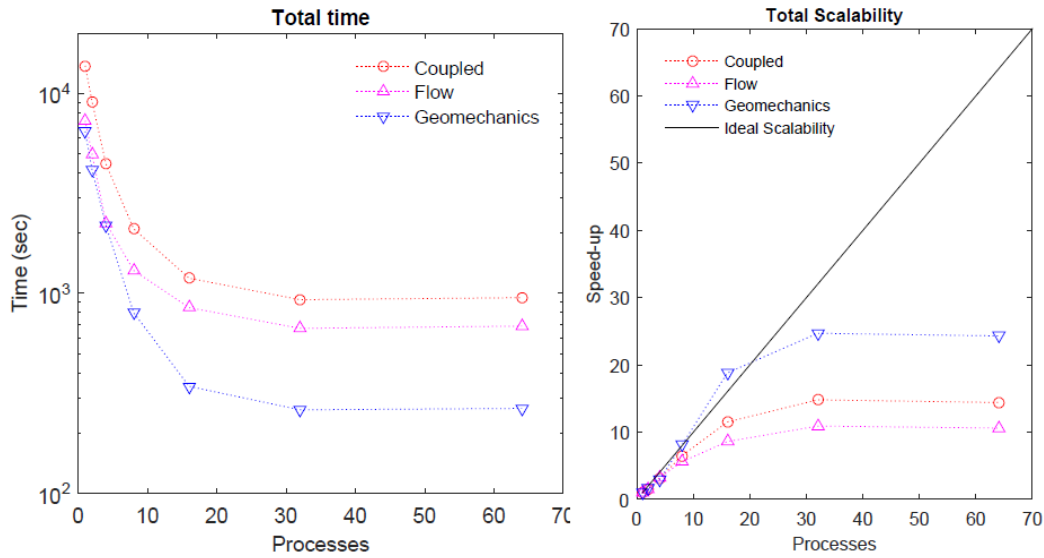


Fig. 4.20 Parallel performance for the geomechanics-only simulation



**Fig. 4.21 Parallel solver performance and speedup**



**Fig. 4.22 Total simulation performance and speedup.**

**4.2.3.2 Coupled elastoplastic geomechanics and flow**

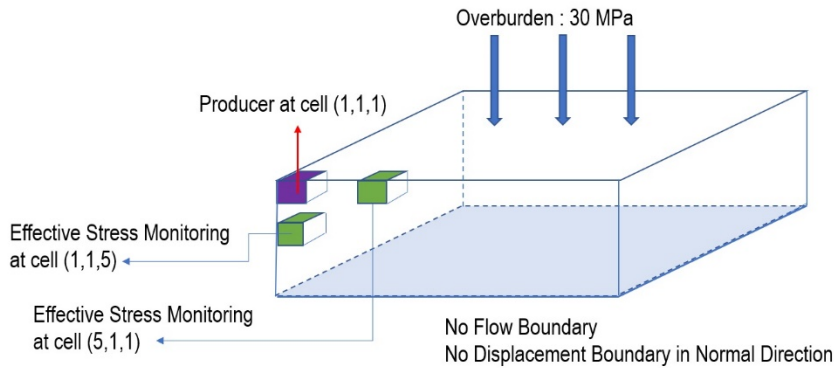


**Fig. 4.23 Schematics of a coupled single-phase flow and elastoplastic geomechanics problem.**

We take the same domain, material properties, and discretization, as used in the previous case, while taking a single production well, shown in Fig. 4.23, with a rate of 8 kg/s and the simulation time of 1095 days. The cohesion is 3 MPa, and the friction Fig. 4.23 and dilation angles are both 30°.

Fig. 4.24 shows evolution of the effective stresses at two gridblocks near the production well. The effective stresses start from the origin and propagate to the upper-left direction. Pore pressure decreases due to production, inducing the changes of effective stress. The effective stress is located a little bit higher than the failure line, because we add some tolerance to ensure that the effective stress is in the plastic region.

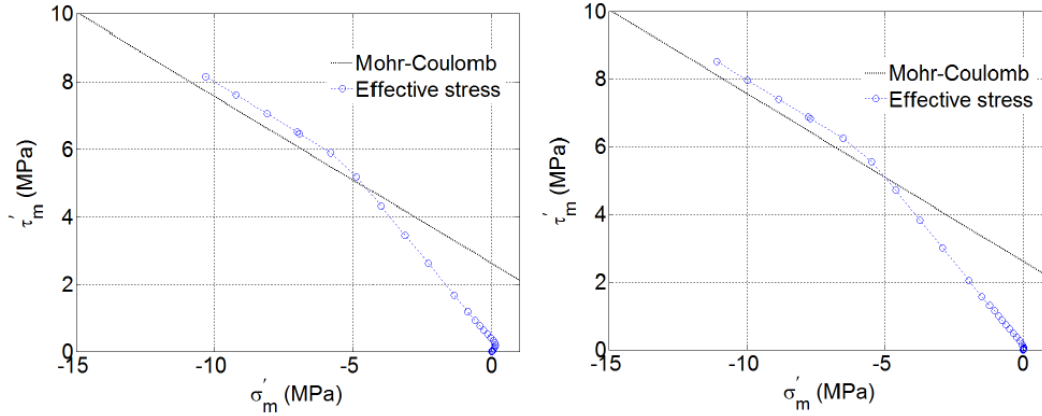


**Fig. 4.24 Evolution of effective stress at near-well gridblocks (i.e., (5,1,1) (left) and (1,1,5) (right)).**

The plasticity algorithm (i.e., return mapping) in the parallel environment is highly local and no communication between neighboring grid blocks is required. Some processes are assigned to the gridblocks of elasticity, while other processes are assigned to plasticity. As a result, the processes that face plasticity have higher workload, because the plasticity computation takes additional local iterative loops to solve the nonlinearity of plasticity.

For the load assignment, we distribute the equal amount of continuous gridblocks to each process. In order to measure the imbalance caused by plasticity, we introduce an idle-time ratio  $r_{id}$ , as

$$r_{id} = \frac{t_{max} - t_{min}}{t_{max}}, \quad (4.27)$$

where  $t_{max}$  is the longest execution time taken by a process for the return mapping, and  $t_{min}$  is the shortest execution time. The desirable case is  $r_{id} = 0$ , which implies that all processes are occupied fully and equally, and no process needs to wait for others to finish the return mapping computation. On the other hand, when  $r_{id} > 0$ , the workload is assigned to processes unequally.

Fig. 4.25 shows the idle-time ratios at the first time step when no plasticity occurs, and the idle time ratio at 395 days when plasticity occurs near the production well. The execution time used to calculate the idle time ratio does not include the time for message passing, and the results shown in the figure directly indicate the workload assigned to processors. At the initial time, the workload is balanced well. As the processor number becomes larger, the ratio increases. However, the execution time on each process becomes a few seconds as the processor number becomes large, and even small difference of execution time can make the idle-time ratio significantly grow (eg, 0.14 for 64 processes). On the other hand, at 395 days, the computational load for plasticity increases overall, resulting in the increment of idle-time ratios: some processors take elasticity predominantly while the other processors experience plasticity. At 395 days, 44864 gridblocks take computation of plasticity.

This is a well-known issue due to the localized nature just as previously studied in compositional reservoir simulation where the load imbalance caused by calculation of equations of state is similar to elastoplastic calculation. Static load balancers used in this study might not be effective because the areas experiencing plasticity cannot be accurately predicted before running the simulation. Load balancers might be a possible way to enhance more computational efficiency. The use of dynamic load balancers with more massive parallelization can be a method to adaptively modify partitions during time stepping and to assign less gridblocks to a core if the gridblocks have heavy plasticity computation.

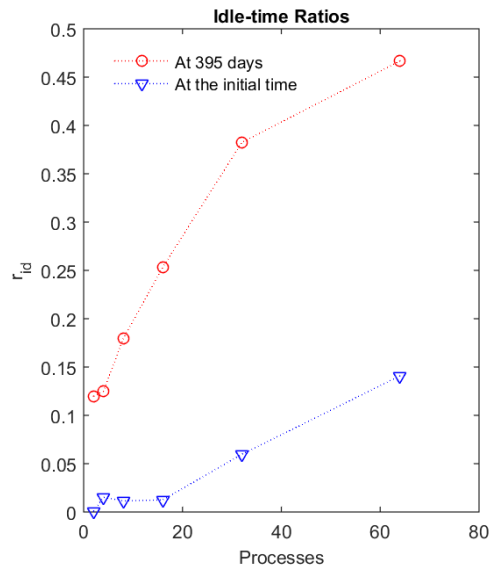


**Fig. 4.25 Imbalance caused by the return mapping process**

#### 4.2.3.3 Investigation of matrix decomposition

We investigate the parallel solver performance related to matrix decomposition. In the parallel environment, the decomposition strategy can be considered as a preconditioning method, which affects iteration and computational time of iterative matrix solvers. A proper decomposition strategy can improve the parallel solver performance and consequently improve the efficiency of the entire parallel implementation. Specifically, we here focus on the stiffness matrix of the geomechanics problem, considering many non-zero elements in the sparse matrix, compared to the flow problem. Because we consider structured hexahedral grids (linear 3D hexahedral) in this study, the maximum number of non-zero elements a row contains is up to 81. Fig. 4.26 shows a typical example of the structure of a sparse stiffness matrix with 204 degrees of freedom and 6658 non-zero elements. The number of non-zero elements and total degrees of freedom of the large stiffness matrix investigated in this case are 246,224,568 and 3,283,188, respectively.

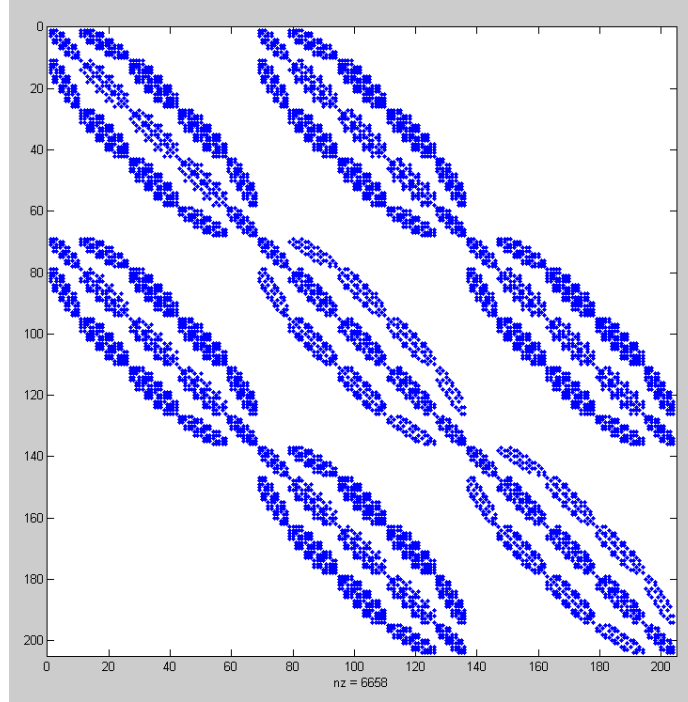


**Fig. 4.26 Non-zero elements of a stiffness matrix with a degree of freedom of 204.**

The default decomposition method of the parallel solver in this case is decomposition of the stiffness matrix into subdomains that consist of continuous rows. Thus, each subdomain has the same number of rows, being assigned to a certain process. When the number of rows of the stiffness matrix is not divisible by the number of processes, the number of rows assigned to processes will be as close as possible to each other, with a maximum difference of row numbers of one. Since each row does not necessarily contain the same number of non-zero elements, the default decomposition strategy assigns different numbers of non-zero elements to processes, which can result in the load imbalance.

In this study, we propose a new decomposition strategy that can assign the same number of nonzero elements to processes. Thus, each process might take different numbers of consecutive rows but very similar numbers of non-zero elements. When the number of total non-zero elements is not divisible by the number of processes, numbers of non-zero elements received by processes are kept as close as possible. We introduce a parameter to describe the difference of numbers of non-zero elements between the heaviest workload ( $N_{max}^{nz}$ ) and lightest workload ( $N_{min}^{nz}$ ), defined as

$$N_d^{nz} = N_{max}^{nz} - N_{min}^{nz}. \quad (4.28)$$

**Table 4.4: Comparison of decomposition results for 4-Processes**

Processes	Default Decomposition		New Decomposition	
	Local Row Number	Local Non-zero Number	Local Row Number	Local Non-zero Number
0	820797	57888006	866200	61556145
1	820797	66125799	764237	61556121
2	820797	66168834	763456	61556148
3	820797	56041929	889295	61556154

Table 4.4 shows the difference between the new decomposition strategy and the default strategy for the 4-process case. Specifically,  $N^{nz}_d$  from the new decomposition method is 33 between Process 1 and Process 3 ( $61556154 - 61556121 = 33$ ) while  $N^{nz}_d$  from the default decomposition strategy is 10,126,905 between Process 2 and Process 3 ( $66168834 - 56041929 = 10126905$ ). We identify that  $N^{nz}_d$  of the new decomposition strategy is significantly lower than that of the default decomposition strategy, meaning that the workload such as multiplication operation can be more evenly distributed by the new strategy.

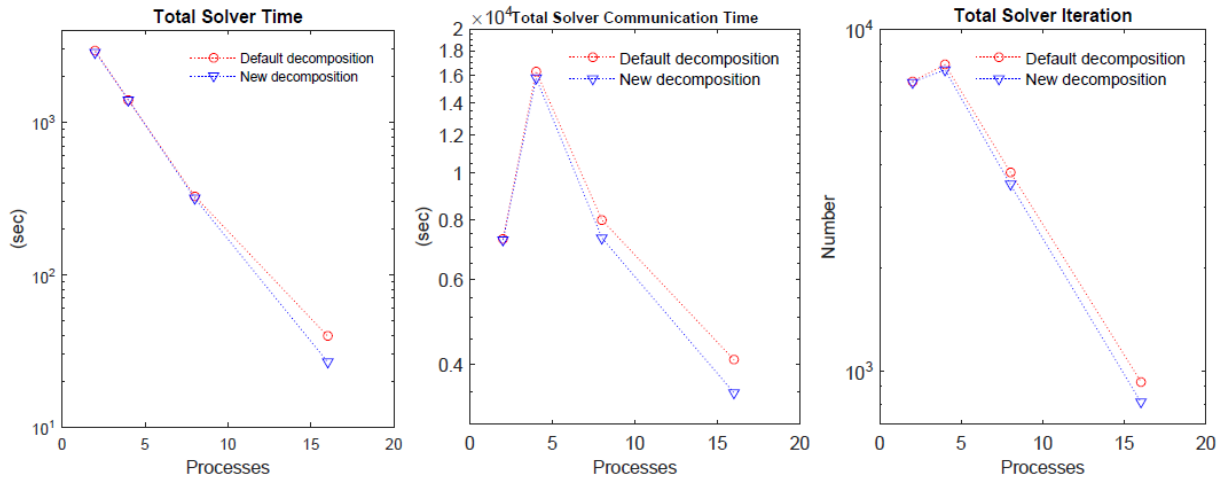


**Fig. 4.27 Comparison of geomechanics solver profiling for the two different decomposition methods of geomechanics simulation**

We take 4 parallel cases in order to further investigate the difference between the two decomposition methods: 2-process, 4-process, 8-process, and 16-process. Each case is simulated twice: the default and new decomposition methods. In order to obtain the solver profiling accurately, the specifications of the parallel environment are kept constant in the parallel simulations.

Fig. 4.27 shows the geomechanics-only parallel solver performance. The batch job is used to assign certain nodes to the simulation runs in order to reduce the impact of load variability on the supercomputer on the performance profiling. From the comparison, the new decomposition method reduces the number of parallel solver iterations. The new method also decreases the MPI communication time in the parallel solver. The MPI communication time for this test is calculated by the sum of timings from all involved processes, and thus it might be longer than the total run time reported by the master process. The total solver time is only the time spent on solving the matrix systems.

The results also indicate that the new decomposition strategy generally reduces the solver time with the only exception found in the 4-process case, where the new strategy results in 6.8 more seconds of solver time than the default method.

It is also worth noting that, for parallel simulation scenarios involving a large number of processes, the local calculation on each individual process becomes small while the communication cost between the processes becomes significantly high. In this case the effort to balance the workload might become less effective while the effort to reduce inter-process communication based on degree of freedom and mesh geometry (eg, graph partitioners) can improve the parallel performance.

#### **4.2.4 Summary of parallel code implementation**

We have developed a parallel sequentially coupled flow-geomechanics simulator for nonisothermal poroelastoplasticity from individual serial codes of flow and geomechanics, which can straightforwardly be applied to T+M<sup>AM</sup> for parallel simulation of gas hydrate deposits. The parallelization is based on both distributed memory architecture of MPI and shared memory architecture of OpenMP. We used PETSc as a parallel linear solver and enhanced the scalable solution of linear systems for flow and geomechanics. The scalable parallelizations for array assembly, updating variables, and return mapping have also been achieved, as they are local, not requiring data communication. The parallel scheme in this study is portable and it can easily be applied to other sequentially coupled simulators, preserving the original structure of individual codes: the flow and geomechanics simulators. The scheme also minimizes re-coding efforts. We summarize the findings from this study as follow.

- The test results showed good scalability and efficiency up to 32 CPUs of parallel solver performance for both flow and geomechanics. This also implies that parallel simulation can effectively be performed with a multicore desktop that has about 40 CPUs.
- Geomechanics shows better parallel performance than flow. But this finding is still restricted to the parallel scheme used in this study.
- It is worth noting that, when the flow and geomechanics simulators are sequentially coupled, the scalability of the parallel flow-geomechanics simulator can still be honored.
- Plasticity can lead to imbalance in the parallel environment. Smart assignment of processes should be incorporated in the future studies to consider plasticity more efficiently.
- Matrix decomposition methods affect the parallel solver performance in terms of convergence rate and solver computational time.

#### **4.3 Thermodynamically consistent modeling of hysteresis in capillary pressure and relative permeability (Subtask 4.2, Subtask 5.3, Subtask 5.4)**

We investigate a robust and systematic modeling approach for hysteretic capillary pressure and relative permeability in porous media by using the theory of plasticity, considering that plasticity and hysteresis exhibit both irreversible physical processes.

Focusing on the immiscible two-phase flow of methane gas and water, closely related to flow in gas hydrate deposits, we investigate stability analysis and find that the method based on the plasticity can yield wellposedness (contractivity) and algorithmic stability (B-stability). This modeling approach can track and compute history-dependent flow properties such as residual saturation. In numerical simulation, we apply the algorithm of the 1D isotropic/kinematic hardening plasticity to reservoir simulation of gas-water flow. For weak and strong capillarity, the modeling yields strong numerical stability even for several drainage-imbibition processes. We also identify differences between with and without hysteresis, showing the importance of hysteretic capillary pressure and relative permeability. Thus, the hysteresis modeling based on the theory of plasticity is promising for robust numerical simulation of strong hysteresis. We describe these findings as follows, summarizing the paper by Yoon et al. (2019), part of outcomes from this project.

#### 4.3.1 Capillary hysteresis and plasticity

We can find fundamental similarity between capillary hysteresis and plasticity in geomechanics. Theory of plasticity relates stress to elastic (recoverable) strain and plastic (irrecoverable) strain. For example, the left of Fig. 4. 28 shows an elastoplastic volumetric stress-strain relation under loading (From Points A to C) and unloading (From Points C to D) processes. After the yielding point (Point B), plastic strain occurs during loading (From Points B to C) and does not disappear even after unloading of stress. We can find the similarity in capillary hysteresis, as shown in the right of Figure 1. During the drainage process (from Points P to R), the irreversible process occurs from Points Q to R, causing residual (irrecoverable/irreducible) saturation, while the process from Point P to Q is reversible. Then, during the imbibition process from Points R to S, we identify residual saturation. It is worth noting that plastic strain or residual saturation can only be observed during the unloading or imbibition process, respectively.

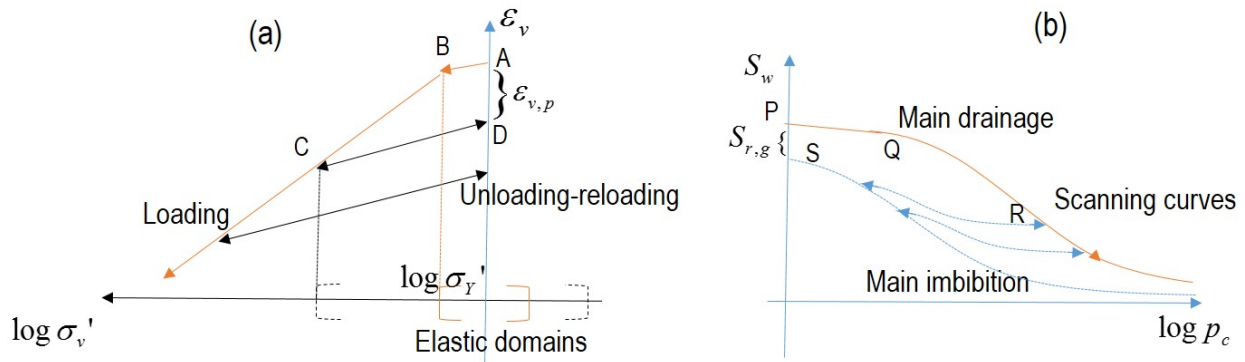


**Fig. 4. 28 Return-mapping is a numerical approach for modeling plasticity. Specifically, for an example of the gas water system, the theory of plasticity allows us to have the following equations for modeling capillary hysteresis.**

Yoon et al. (2019) showed that the new algorithm used in the project for capillary hysteresis is mathematically sound and numerically stable. Specifically, consider the following norm.

$$\|\mathcal{X}\|_T^2 = \frac{1}{2} \int (p_g M_g^{-1} p_g + p_w M_w^{-1} p_w + \sigma_c \phi E_h^{-1} \sigma_c + \kappa \phi H_h^{-1} \kappa) d\Omega$$

$$T := \left\{ \chi := (p_g, p_w, \sigma_c, \kappa) \in R \times R \times R \times R : p_g, p_w, \sigma_c, \kappa \in L^2(\Omega) \right\} ,$$

where  $\sigma_c = -p_c$  to have positive correlation between  $\sigma_c$  and  $S_w^t$ . Thus,  $E_h$  and  $H_h$  are positive, characterizing a capillary pressure curve. Then, the new algorithm provides

$$\frac{d}{dt} \left\| {}^d \chi \right\|_T^2 \leq 0, \quad \left\| {}^d \chi \right\|_T^{n+1} \leq \left\| {}^d \chi \right\|_T^n,$$

which implies unconditional numerical stability (i.e., B-stability) when we take implicit time stepping method.

#### 4.3.2 Hysteresis Modeling of Capillary Pressure and Relative Permeability

In this study, we employ a hysteresis model for capillary pressure used in Nuth and Laloui (2008), based on application of one dimensional plasticity with kinematic hardening, focusing on the two phase flow system (e.g., gas and water). We specifically have a yield function of

$$f_Y = |\log p_c - \log q + \sigma_Y| - \sigma_Y \leq 0, \quad (4.29)$$

$$\sigma_Y = \frac{1}{2} (\log q_0 - \log p_{eH}), \quad (4.30)$$

where the elastic modulus, hardening relation and plastic flow followed by the plastic multiplier are given respectively as

$$E_H = K_H \frac{p_c}{p_{eH}}, \quad \dot{q} = \gamma \frac{\partial f_Y}{\partial q}, \quad \dot{S}_w^p = \gamma \frac{\partial f_Y}{\partial p_c}, \quad \gamma = \frac{\dot{p}_c}{B_H} \text{sign}(\log p_c - \log q + \sigma_Y) \quad (4.31)$$

Note that the plastic water saturation to correspond to the residual gas saturation in the capillary pressure curve, as shown in Fig. 4.28. For the modeling of relative permeability, we assume that the residual saturation of gas can be related to plastic water saturation, as follows.

$$k_g(S_g^t, S_{rg}) , S_{rg} = \psi S_w^p, \quad (4.32)$$

where  $\psi$  is a factor that indicates the difference between capillary pressure and relative permeability for the residual saturation. From Pruess et al. (1999),  $\psi$  is less than unity. We use the modified version of Stone's relative permeability model, written as

$$k_{rg} = \max \left\{ 0, \min \left\{ \left( \frac{S_g^t - S_{rg}}{1 - S_{rw}} \right)^{n_g}, 1 \right\} \right\}, \quad k_{rw} = \max \left\{ 0, \min \left\{ \left( \frac{S_w^t - S_{rw}}{1 - S_{rw}} \right)^{n_g}, 1 \right\} \right\}, \quad (4.33)$$

where we take  $n_g=4$  and  $\psi = 1.0$  unless noted otherwise.

Then, return mapping algorithm is applied to model the drainage and imbibition process with the details given in Table 4.4. For particular ranges of capillary pressure and saturation, within the saturated state ( $p_c$

$< p_{eH}$ ) on the one hand and the residual saturation state ( $S_w = S_{rw}$ ) on the other hand, the elastic increment remains null, and the degree of saturation equals either  $1 - S_{rg}$  or  $S_{rw}$ , respectively.

When the fully implicit method is taken with the Newton-Raphson method,  $p_c^{n+1}$  is updated every iteration. As a result, the return mapping is invoked every iteration, too. The algorithm of Table 4.5 is based on the given capillary pressure field (e.g., the case where the flow problem takes the primary variables of  $p_g$  and  $p_w$ ). When the saturation field is given (e.g., the case where the primary variables are  $p_g$  and  $S_w^t$ ), we can easily modify the procedure of the return mapping, shown in Table 4.6, which corresponds to the 1D isotropic/kinematic hardening in Simo and Hughes (1998) after taking the logarithms of  $p_c$  and  $q$ .

In this study, the reservoir is initially saturated mostly with water, assuming the constant maximum residual water saturation. This return algorithm can straightforwardly be applied to the opposite case where the reservoir is initially saturated mostly with gas, assuming the constant maximum residual gas saturation and calculating dynamic residual water saturation. One might also be able to extend this algorithm to the case for both dynamic residual gas and water saturations, which will be part of the future study. Also, without significant modification, the return mapping algorithm of 1D isotropic/kinematic hardening can potentially be applied to Brooks-Corey and van Genuchten models, although the elastic and elastoplastic moduli are not constant but calculated from capillary pressure at the previous step due to nonlinearity.

Fig. 4.29 and 4.30 show the numerical results of capillary pressure and relative permeability for the cyclic drainage-imbibition processes by arbitrarily changing the capillary pressure (Algorithm I) and the total gas saturation (Algorithm II), respectively. In this test case we have  $p_{eH} = 1.2\text{kPa}$ ,  $q_0 = 2.0\text{kPa}$ ,  $K_h = 4.8\text{kPa}$ , and  $B_h = 1.0\text{Pa}$ . We take constant residual water saturation,  $S_{rw} = 0.1$ . Even though the drainage and imbibition processes are changed repeatedly and significantly, we identify that the numerical algorithms based on the plasticity theory are stable for the hysteretic modeling.

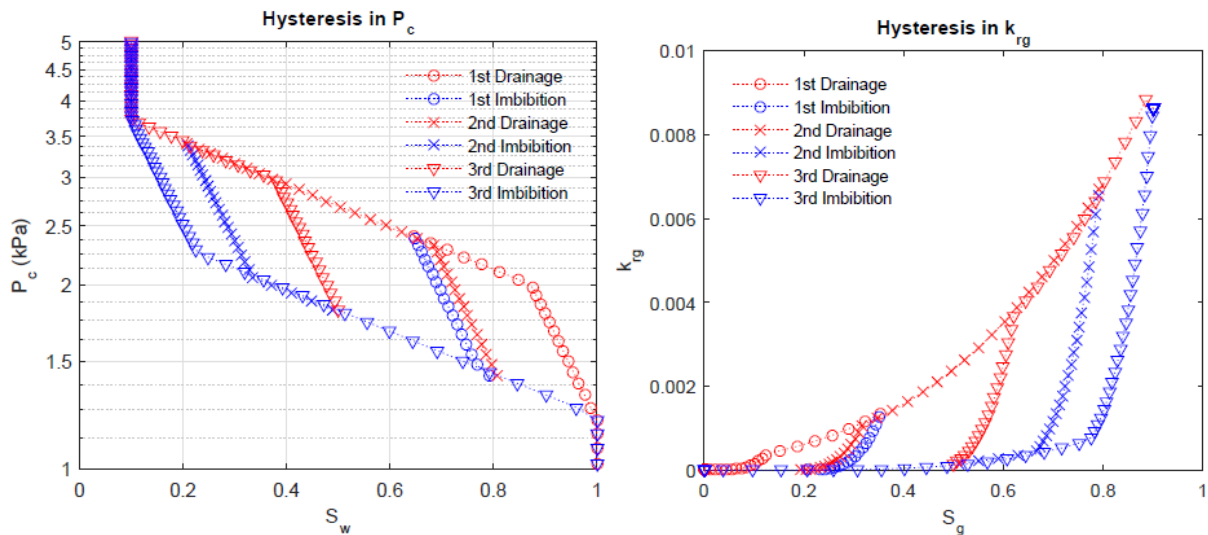


**Fig. 4. 29 Hysteresis by the drainage-imbibition process in a single gridblock by arbitrarily changing the capillary pressure (Algorithm I). Left: capillary pressure. Right: relative permeability of gas. The algorithm provides numerical stability.**

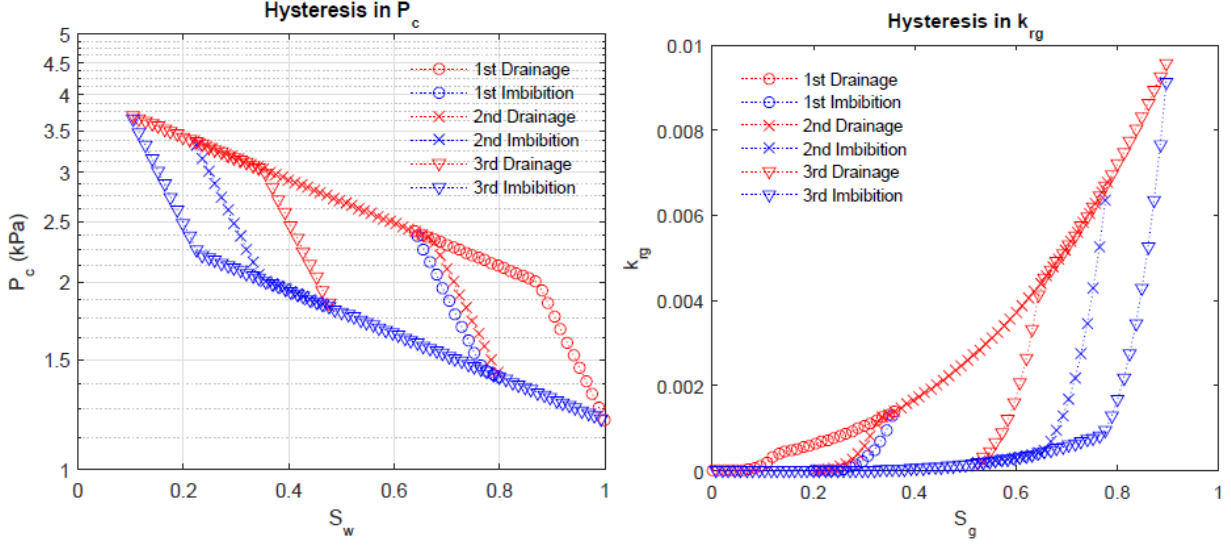


**Fig. 4.30 Hysteresis by the drainage-imbibition process in a single gridblock by arbitrarily changing the total gas saturation (Algorithm II). Left: capillary pressure. Right: relative permeability of gas. The algorithm provides numerical stability.**

**Table 4.5 Algorithm I when capillary pressure is given**

Algorithm I of the return mapping for hysteretic capillary pressure and relative permeability

1. Given the capillary pressure field at the  $n+1$  time step:  $p_c^{n+1} = p_c^n + \Delta p_c^n$ ,
2. Compute  $f_Y^{trial} = |\log p_c^{n+1} - \log q^n + \sigma_Y| - \sigma_Y$ ,

$$S_w^{trial} = S_w^n - \frac{\Delta p_c^n}{K_h(p_c^{n+1}/p_{eH})}.$$

3. If  $f_Y^{trial} \leq 0$ , then

$$\text{Elastic step: } S_w^{n+1} = S_w^{trial}, S_w^{p,n+1} = S_w^{p,n}, q^{n+1} = q^n.$$

Else

Plastic step: proceed to Step 4.

4. Return mapping

$$S_w^{n+1} = S_w^{trial} - \frac{\Delta p_c^n}{B_H p_c^{n+1}},$$

$$S_w^{p,n+1} = S_w^{p,n} + \frac{\Delta p_c^n}{B_H p_c^{n+1}},$$

$$q^{n+1} = q_0 \cdot \exp(B_H S_w^{p,n+1}).$$

5. Update relative permeability:  $k_{rg}^{n+1}(S_g^{t,n+1}, S_{rg}^{n+1}), S_{rg}^{n+1} = \psi S_w^{p,n+1}$ .

**Table 4.6 Algorithm II when total water saturation is given**

#### Algorithm II of the return mapping for hysteretic capillary pressure and relative permeability

1. Given the saturation field at the  $n+1$  time step:  $S_w^{t,n+1} = S_w^{t,n+1} + \Delta S_w^{t,n}$ ,

2. Compute the trial variables:

$$\log p_c^{trial} = \log p_c^n - \frac{K_h}{p_{eH}} \Delta S_w^{t,n},$$

$$\log q^{trial} = \log q^n,$$

$$\zeta^{trial} = \log p_c^{trial} - \log q^{trial},$$

$$f_Y^{trial} = |\zeta^{trial} + \sigma_Y| - \sigma_Y.$$

3. If  $f_Y^{trial} \leq 0$ , then

$$\text{Elastic step: } \log p_c^{n+1} = \log p_c^{trial}, q^{n+1} = q^{trial}, S_w^{p,n+1} = S_w^{p,n}.$$

Else

Plastic step: proceed to Step 4.

4. Return mapping

$$\log p_c^{n+1} = \log p_c^{trial} - \frac{f_Y^{trial}}{\frac{K_h}{p_{eH}} + B_H} \frac{K_h}{p_{eH}} \text{sign}(\zeta^{trial}),$$

$$\log q^{n+1} = \log q^{trial} + \frac{f_Y^{trial}}{\frac{K_h}{p_{eH}} + B_H} B_H \text{sign}(\zeta^{trial}),$$

$$S_w^{p,n+1} = S_w^{p,n} + \frac{f_Y^{trial}}{\frac{K_h}{p_{eH}} + B_H} \text{sign}(\zeta^{trial}),$$

5. Update relative permeability:  $k_{rg}^{n+1}(S_g^{t,n+1}, S_{rg}^{n+1})$ ,  $S_{rg}^{n+1} = \psi S_w^{p,n+1}$ .

---

### 4.3.3 Numerical Examples

We perform several numerical experiments in order to investigate stability and robustness of the proposed hysteresis modeling method. We consider an isothermal flow problem in a 1D horizontal reservoir to show the hysteresis effect in capillary pressure and relative permeability on multiphase flow. We take the finite volume method for space discretization. The domain is uniformly discretized with 60 gridblocks, where the gridblock sizes are uniform, ( $\Delta x = 4\text{m}$ ,  $\Delta y = 10\text{m}$ ,  $\Delta z = 10\text{m}$ ) and the length of the domain is  $L_x = 240\text{m}$ . We take no-flow boundary conditions at both sides, as shown in Fig. 4.31. The permeability and porosity are  $3.0 \times 10^{-15} \text{ m}^2$  and 0.1, respectively. We take the backward Euler method. We use the Peng-Robinson equation to solve the equation of state for gas, which determines gas properties such as viscosity and compressibility. We take the properties of water defined at given reservoir pressure and temperature.

Methane gas ( $\text{CH}_4$ ) and liquid water are injected continuously and successively into the reservoir in order to model the drainage and imbibition processes. The simulation time is 70 days. Initial saturations of gas and water are  $S_g = 0.1$  and  $S_w = 0.9$ , respectively. We take initial gas pressure of  $p_g = 10\text{MPa}$  and

temperature of  $T = 20^{\circ}\text{C}$ , respectively. We take a monitoring point located at  $x = 182\text{m}$  to observe variation of the saturation and capillary pressure. The entire simulation is divided into six steps (Fig. 4.31) as follows:

1. A first  $\text{CH}_4$  injection ( $0.3\text{kg/s}$  for 2 days) in the element at ( $x = 182\text{m}$ ) for the first drainage
2. A first  $\text{H}_2\text{O}$  injection ( $0.02\text{kg/s}$  for 23 days) in the element ( $x = 194\text{m}$ ) for the first imbibition
3. A second  $\text{CH}_4$  injection ( $0.05\text{kg/s}$  for 10 days) in the element at ( $x = 206\text{m}$ ) for the second drainage
4. A second  $\text{H}_2\text{O}$  injection ( $0.01\text{kg/s}$  for 20 days) in the element ( $x = 218\text{m}$ ) for the second imbibition
5. A third  $\text{CH}_4$  injection ( $0.02\text{kg/s}$  for 10 days) in the element at ( $x = 230\text{m}$ ) for the third drainage
6. A third  $\text{H}_2\text{O}$  injection ( $0.01\text{kg/s}$  for 5 days) in the element ( $x = 238\text{m}$ ) for the third imbibition

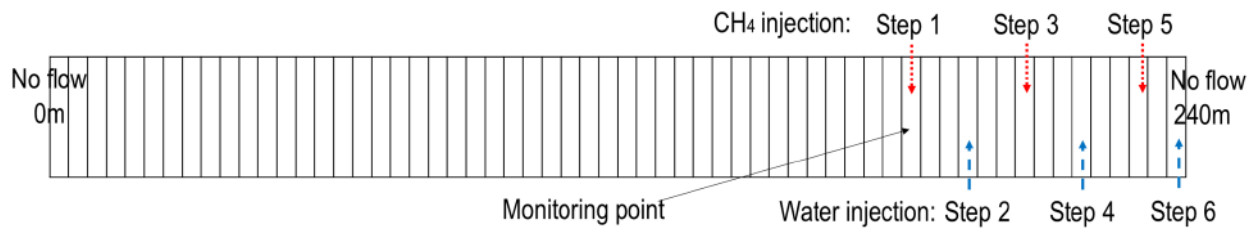


**Fig. 4.31 Illustration of the 1D reservoir, boundary conditions, source, and monitoring point locations.**

With the drainage and imbibition cycles of the six steps, we investigate the effects of hysteresis in capillary pressure and relative permeability with 6 different test cases, considering weak and strong capillarity. Cases 1, 2, 3, and 6 have weak capillarity while Cases 4 and 5 have strong capillarity (See Table 4.7).

Specifically, Cases 1, 2, 3, and 6 take  $p_{eH} = 1.5\text{kPa}$ ,  $q_0 = 4.0\text{kPa}$ ,  $E_H = 15.0\text{kPa}$ , and  $B_H = 1.0\text{Pa}$ , while Cases 4 and 5 have  $p_{eH} = 1.5\text{MPa}$ ,  $q_0 = 4.0\text{kPa}$ ,  $E_H = 15.0\text{MPa}$ , and  $B_H = 1.0\text{Pa}$ . Initial residual saturations of gas and water are  $S_{rg} = 0.0$  and  $S_{rw} = 0.15$ , respectively. The specific values of the parameters of  $p_{eH}$ ,  $E_H$ , and  $q_0$  are summarized in Table 4.7.

Those cases are separated by the different scenarios in hysteresis. For example, we consider hysteresis effects in both capillary pressure and relative permeability for Case 1, while only hysteresis in capillary pressure is considered for Case 2. Case 3 takes neither hysteretic capillary pressure nor relative permeability. Only Case 6 takes  $n_g = 2$  for Equation 40, while all the other cases take  $n_g = 4$ . We take Case 1 as a reference case. Table 4.8 summarizes the six different scenarios.

**Table 4.7 Parameters of capillary pressure.**

	Case 1	Case 2	Case 3	Case 6	Case 4	Case 5
Parameters	Weak capillarity				Strong capillarity	
$p_{eH}$	1.5 kPa				1.5 MPa	
$E_H$	15.0 kPa				15.0 MPa	
$q_0$	4.0 kPa				4.0 MPa	

**Table 4.8 Six different scenarios. O: Hysteresis, X: No hysteresis.**

<b>Six different scenarios. O: Hysteresis, X: No hysteresis</b>		
	Capillary Pressure	Relative Permeability
Case 1	O	O
Case 2	O	X
Case 3	X	X
Case 4	O	O
Case 5	O	X
Case 6	O	O

#### 4.3.3.1 Hysteresis in capillary pressure and relative permeability

Figs. 4.32 and 4.33 show dynamic capillary pressure and relative permeability at the monitoring point for Cases 1 (reference case), 2, and 3. For those cases, we identify cyclic drainage and imbibition processes from Step 1 through Step 6. For the reference case, we find that the modelings of hysteretic capillary pressure and relative permeability are stable even for the complex drainage and imbibition processes.

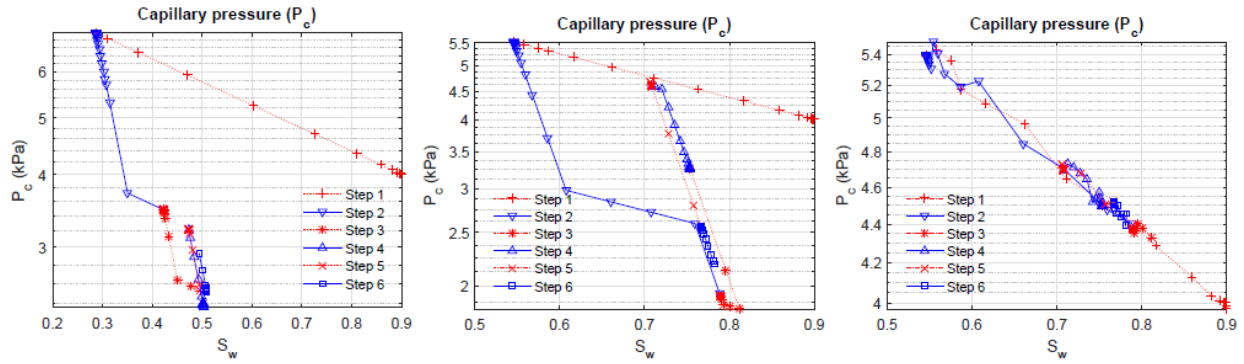


Fig. 4.32 Evolution of capillary pressure for the reference case (left), Case 2 (center), and Case 3 (right).

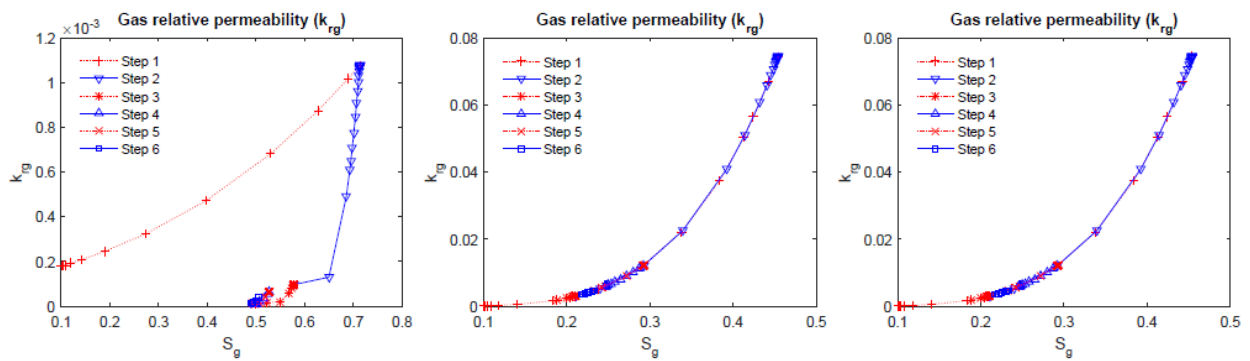
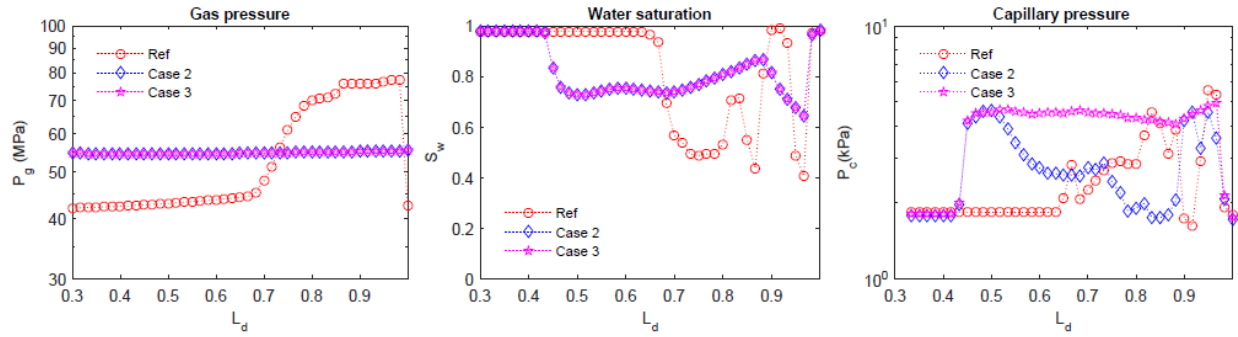


Fig. 4.33 Evolution of gas relative permeability for the reference case (left), Case 2 (center), and Case 3 (right).

Even when the relative permeability of gas is zero, the residual saturation of gas can decrease (the left of Fig. 4.33) due to mass influx of water into the gridblock. For Case 2, the behavior of capillary pressure is different from that of the reference case, because only hysteretic capillary pressure is considered, not hysteretic relative permeability.

The relative permeability significantly affects the flow regime. From Fig. 4.34 and Fig. 4.35, we identify the considerable differences in gas pressure and water saturation between the reference case and Case 2, while the results of gas pressure and water saturation between Cases 2 and 3 are almost identical. This implies an important role of  $k_{rg}$  of relative permeability in multiphase flow. For capillary pressure, we find different distributions and evolutions for all three cases.



**Fig. 4.34** Distribution of gas pressure (left), water saturation (center), and capillary pressure (right) after Step 6 for the reference case, Cases 2 and 3. 'Ref' indicates the reference case.  $L_d = x/L_x$  is a normalized distance.

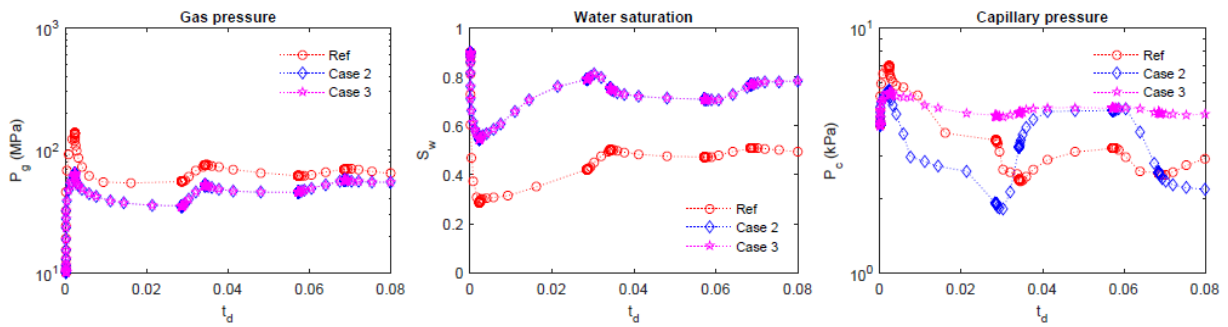


**Fig. 4.35** Evolution of gas pressure (left), water saturation (center), and capillary pressure (right) at the monitoring point for the reference case, Case 2, and Case 3.  $t_d = Q_f/M_t t$  is a normalized time, where  $Q_f$  and  $M_t$  are the average mass rate of injection and the original total mass of fluid in the reservoir, respectively.

#### 4.3.3.2 Effect of strong capillarity

We further investigate the modeling capability of hysteresis for strong capillarity. In Cases 4 and 5, from Fig. 4.36, we find numerical stability of strong hysteretic capillary pressure, where the capillary pressure increases up to 10 MPa. Fig. 4.37 shows evolutions with and without hysteresis in gas relative permeability when the hysteresis of strong capillary pressure is considered, which corresponds to Fig. 4.36. These results show numerical stability in the relative permeability field, too.

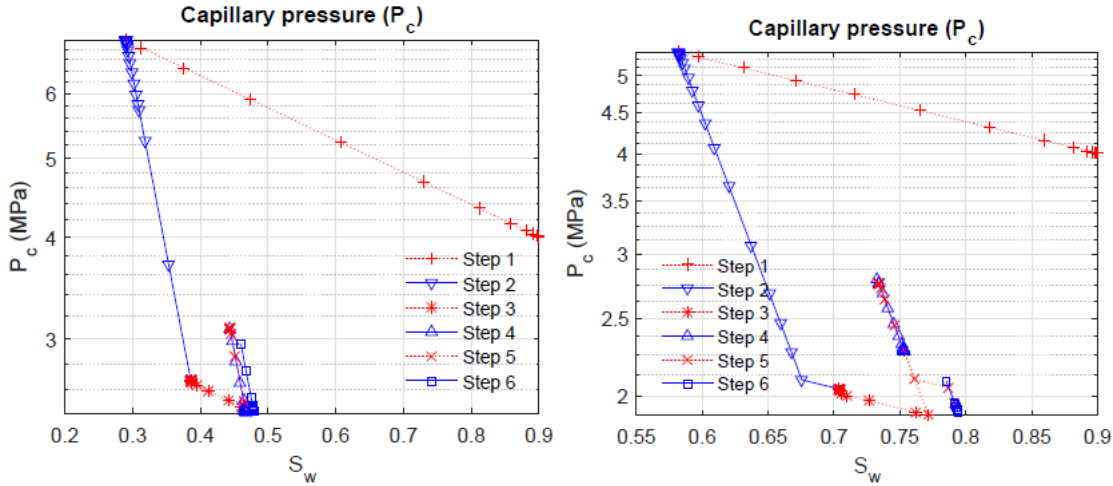


Fig. 4.36 Evolution of strong capillary pressure for Case 4 (left) and Case 5 (right).

Fig. 4.38 shows spatial distributions of gas pressure, water saturation, and capillary pressure after Step 6 for Cases 4 and 5 as well as the reference case. The behavior of relative permeability in Case 4 (the left of Fig. 4.37) is almost identical to that in the reference case. Thus, the distributions of gas pressure and water saturation of Case 4 are almost same as those of the reference case, although the distribution of the capillary pressure is different. Similarly, shown in Fig. 4.39, evolutions of gas pressure and water saturation at the monitoring point between Case 4 and the reference case are almost identical, while those of capillary pressure are different. From the results of both weak and strong capillarity cases, the capillary hysteresis changes residual gas saturation dynamically. When the dynamic residual saturation is reflected in relative permeability, it alters the flow regime significantly, affecting the fields of pressure and saturation.

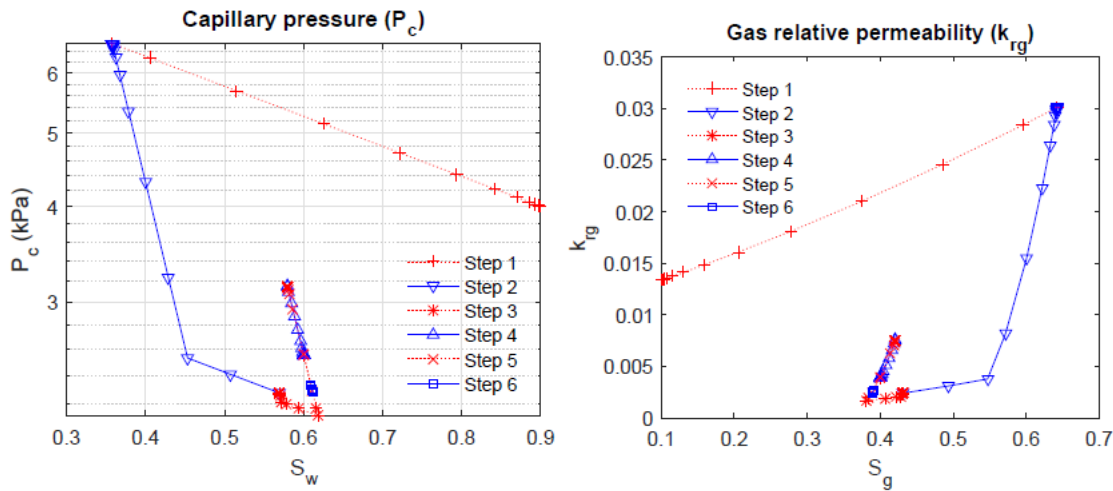
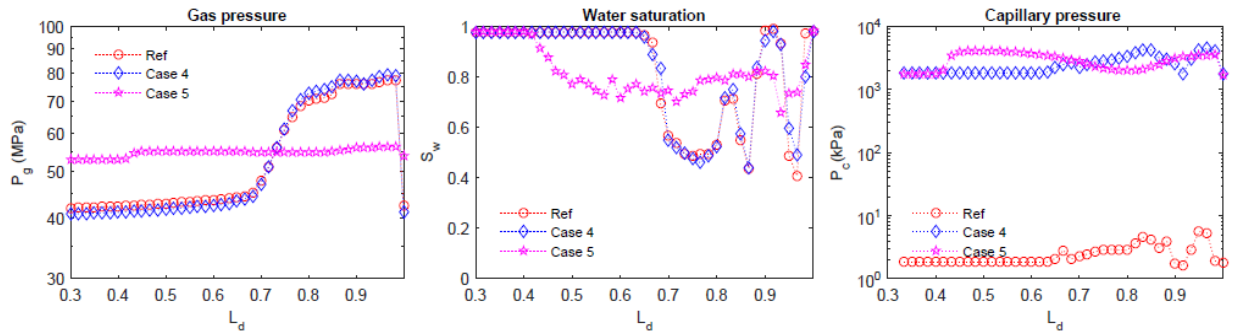
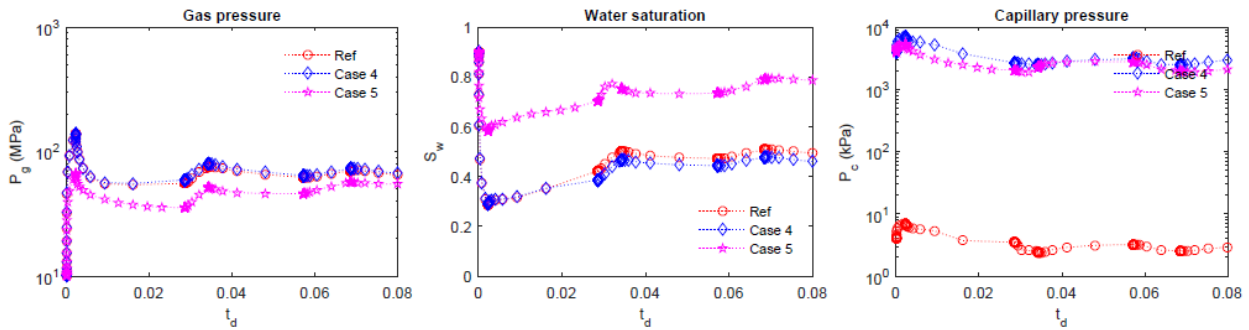


Fig. 4.37 Evolution of gas relative permeability for Case 4 (left) and Case 5 (right), which corresponds to Fig. 4.36.



**Fig. 4.38** Distribution of gas pressure (left), water saturation (center), and capillary pressure (right) after Step 6 for the reference case, Cases 4 and 5.



**Fig. 4.39** Evolution of gas pressure (left), water saturation (center), and capillary pressure (right) at the monitoring point for Cases 4 and 5.

#### 4.3.3.3 Effect of relative permeability

We take a different model of gas relative permeability while keeping the same model of capillary pressure (i.e., Case 6). In this case, we still obtain numerically stable results of hysteretic capillary pressure and relative permeability for cyclic drainage and imbibition processes, as shown in Fig. 4.40. In particular, the relative permeability of Case 6 is mostly higher than that of the reference case. As a result, as shown in the center of Fig. 4.41, water movement in this case is faster than that of the reference case. From Fig. 4.41, we find the different distributions of water saturation and capillary pressure between Case 6 and the reference case. At the monitoring point, the two different models of relative permeability also yield different evolutions of gas pressure, water saturation, and capillary pressure (Fig. 4.42).

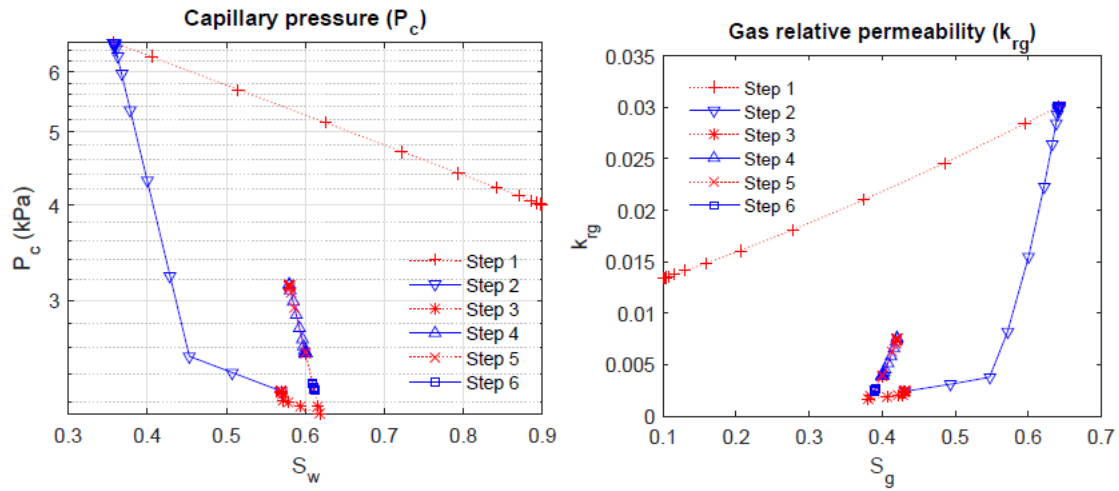


Fig. 4.40 Evolution of capillary pressure (left) and gas relative permeability (right) for Case 6.

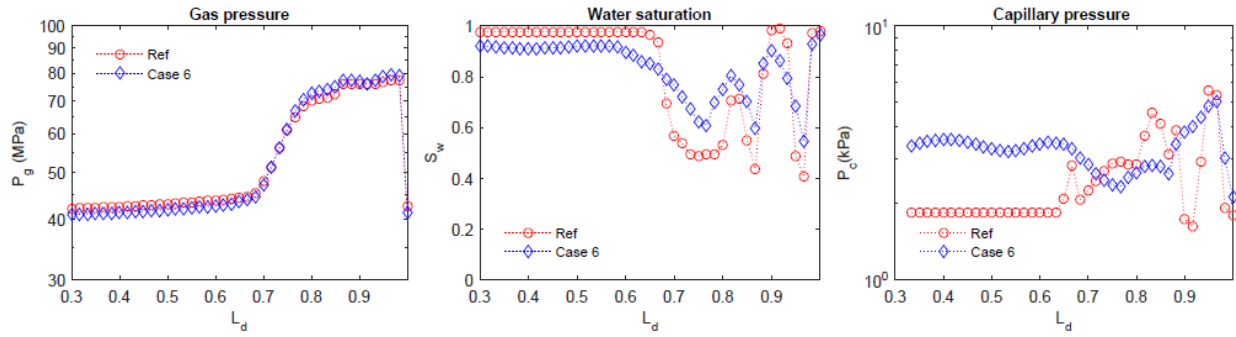


Fig. 4.41 Distribution of gas pressure (left), water saturation (center), and capillary pressure (right) after Step 6 for Case 6.

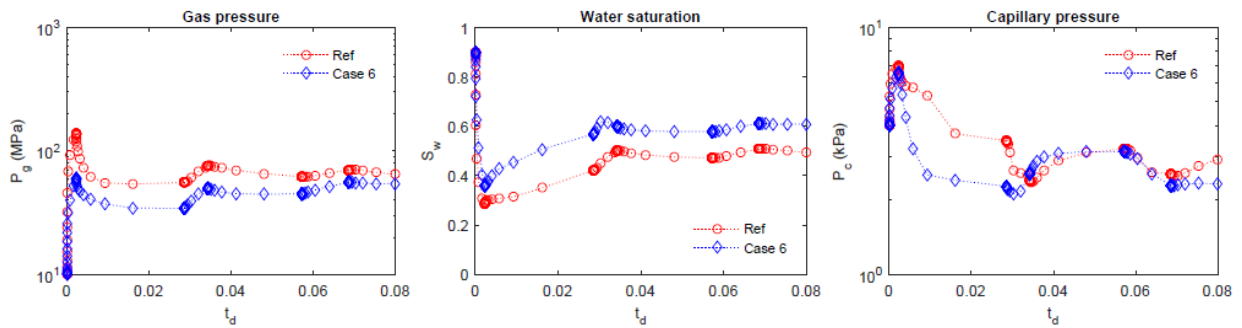


Fig. 4.42 Distribution of gas pressure (left), water saturation (center), and capillary pressure (right) after Step 6 for Case 6.

#### 4.3.3.4 Computational performance

We compare computational costs of the test cases in terms of the total number of Newton’s iteration during simulation, shown in Table 4.9. We define the convergence criterion based on the relative error, or  $\epsilon_r = r^k/m^k$ , where  $r^k$  and  $m^k$  are the residual and mass of phase J at the  $k^{\text{th}}$  iteration, respectively. We then take tolerance of  $10^{-5}$  for all test cases in this study, and convergence for the Newton-Raphson method is achieved every time step when  $|\epsilon_r| \leq 10^{-5}$  each gridblock. No significant difference of iteration was found among the cases except Case 6, where  $n_g=2$  while  $n_g=4$  for the other cases. It is natural that different exponents of the relative permeability model (Case 1 and Case 6) induce different computational costs. In particular, the iteration number of Case 1 is lower than that of Case 3, which implies that the hysteresis modeling of this study does not cause significant extra computational cost. It is worth noting that the return mapping algorithm used in this study is linear. Thus, computational efforts between with and without hysteresis are almost the same.

**Table 4.9 Total number of Newton’s iteration during simulation.**

	Case 1	Case 2	Case 3	Case 4	Case 5	Case 6
Iteration	413	430	431	413	442	347

#### 4.3.4 Summary of hysteresis modeling

We analyzed applicability of the plasticity theory to the modeling for hysteretic capillarity and relative permeability in the two-phase flow system. This modeling approach is generic, not being restricted to a specific type of equations for capillary pressure and relative permeability. We can also make use of systematic algorithms and mathematical rigorouslyness previously developed in computational plasticity. We performed mathematic analysis and found that the plasticity-based modeling provides contractivity and B-stability. This implies that the modeling scheme is numerically stable even for many cyclic drainage-imbibition processes. The numerical experiments supported the mathematic analysis, showing that the proposed modeling approach is robust and rigorous, which can track residual saturation dynamically. We identified the importance of hysteresis modeling from numerical results, which showed substantial differences between with and without hysteresis modeling for strong hysteretic capillary pressure and relative permeability.

## 5. Validation and field application of T+M<sup>AM</sup> (Task 4-Subtask 4.1, Subtask 4.3, Task 5-Subtask 5.2, Subtask 5.4, Subtask 5.5, Subtask 5.6 by Ahn T.W., Kim, J., Lee, J.Y., Yoon, H.C., Yoon, S.)

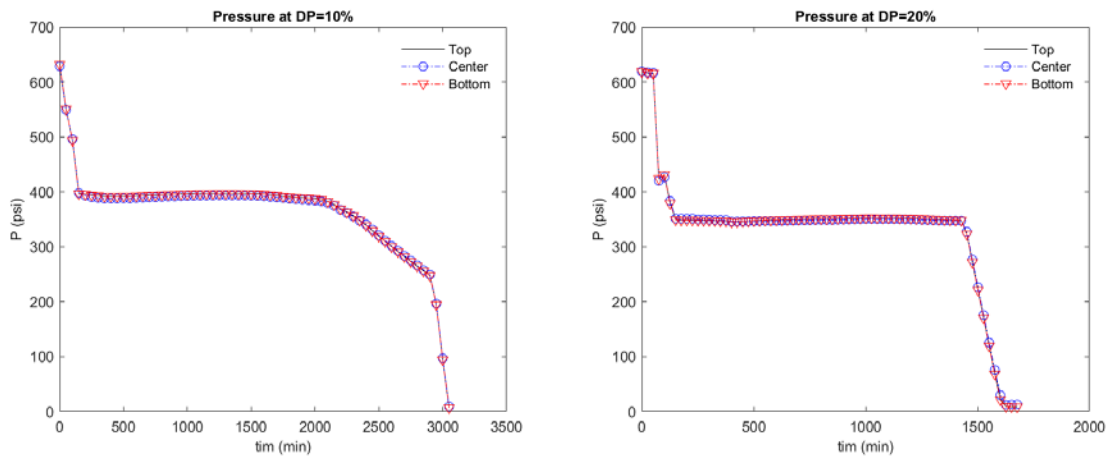
We further validate the developed simulator described in the previous section with the experimental data in Section 1. Then, we perform field scale simulation for the two fields located in Ulleung Basin, South Korea, and in Alaska, United States.

### 5. 1 Validation of T+M<sup>AM</sup> with experimental data (Subtask 4.1, Subtask 5.2)

#### 5. 1.1 Data processing for the 1D-1m experiment

We process the data from Section 1 for numerical simulation. From the experimental data, we identify non-uniform distribution of temperature (Fig. 5.2) during gas production while the pressure is almost constant except for the case of DP=40% (Figure 5.1), where DP stands for the level of depressurization. Also, comparing the results between DP=30% and DP=40%, the two cumulative production are similar (Fig 5.3) while the vertical displacements are significantly different each other. We have these complex physical behavior due to different time scales as well as strong coupling among fluid flow, heat transfer, and geomechanics.

To prepare for the input data of numerical simulation, pressure (particularly for the cases of DP=10%, DP =20%, DP =30%) can be taken as a minimum bottom hole pressure condition. Then, we can compare these experimental data with the numerical results of vertical displacement for validation of T+M<sup>AM</sup>.



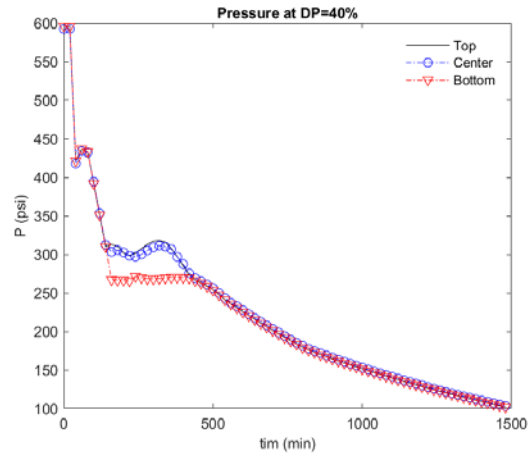
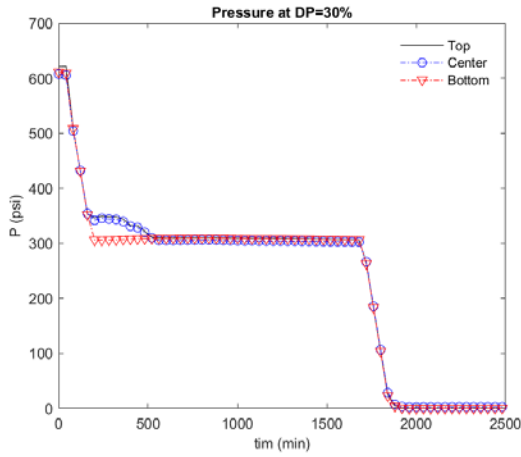


**Fig. 5.1 Evolution of pressure at the top, center, and bottom locations for different levels of depressurization (DP=10%, DP=20%, DP=30%, DP=40%).**

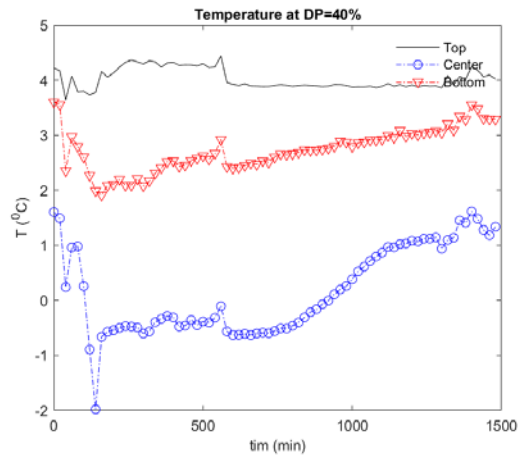
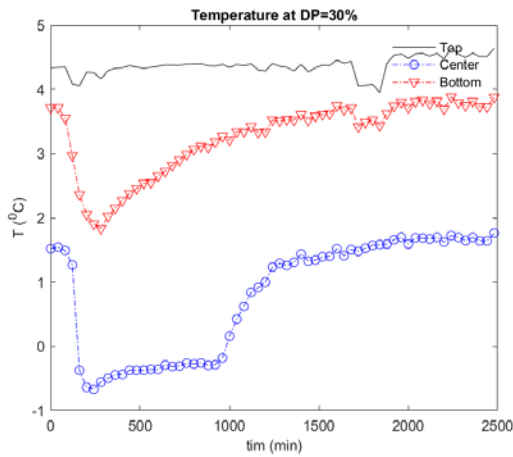
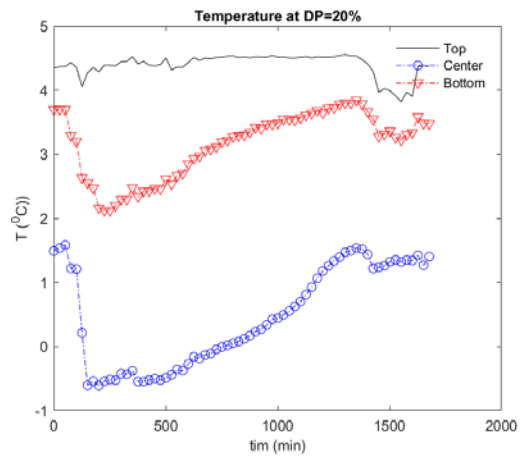
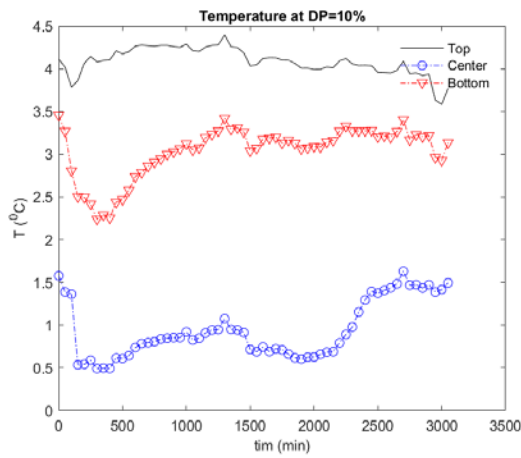


**Fig. 5.2 Evolution of temperature at the top, center, and bottom locations for different levels of depressurization (DP=10%, DP=20%, DP=30%, DP=40%).**

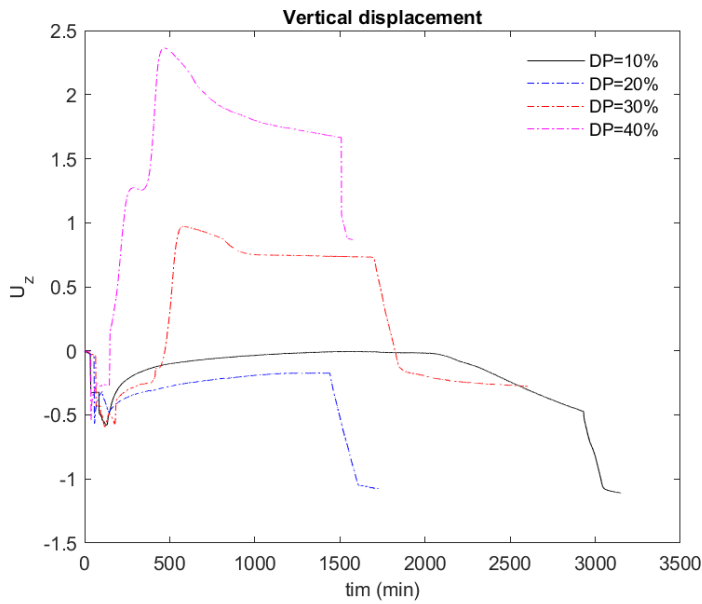


**Fig. 5.3 Measured vertical displacement at the top for different levels of depressurization (DP=10%, DP=20%, DP=30%, DP=40%).**

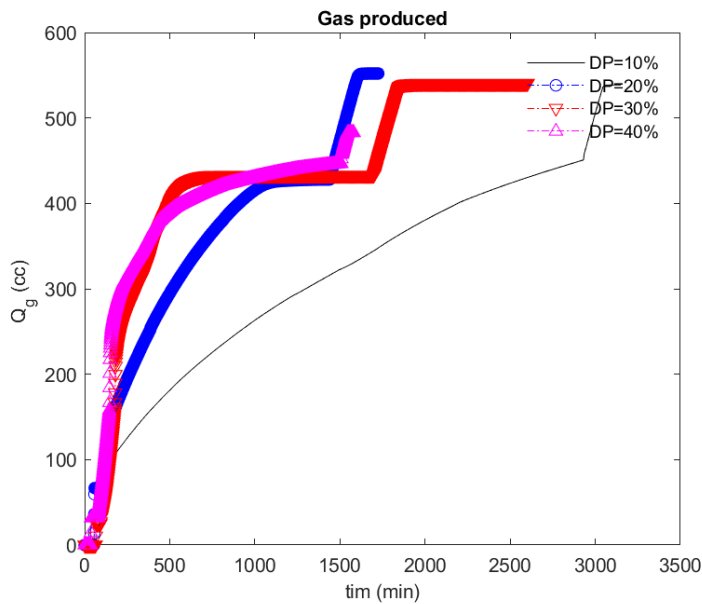


**Fig. 5.4 Evolution of gas production from different levels of depressurization (DP=10%, DP=20%, DP=30%, DP=40%).**

**5.1.2 Validation of T+M<sup>AM</sup> with the 1D-1m experiment**

We extract the data of pressure and displacement when the depressurization is 20% (DP=20%), along with the data of DP 30%. Then, we validate T+M<sup>AM</sup> (TOUGH+ROCMECH), matching parameters of geomechanics and flow by using the data of the single sand-layer system and taking 1D simulation domain. We impose the constant pressure at the bottom boundary (instantaneous pressure drop), as the depressurization was applied at the bottom in the experiment. Figs. 5.5 and 5.6 are the experimental results used for validation. Note that the same sample was used in the experiments of the different levels of depressurization. This implies we can take the same intrinsic permeability and initial porosity although there might be slight changes when the sample was reused.

For validation, we first consider the following uncertain parameters: initial hydrate saturation, intrinsic permeability, drained elastic geomechanics moduli at  $S_H=0\%$  and  $100\%$ . We use the linear interpolation when estimating the geomechanics moduli at a certain hydrate saturation. Fig. 5.7 shows that the numerical results are good agreement with the experimental results, validating T+M<sup>AM</sup>. If we consider the pressure constraint more accurately, particularly at early times for DP=20% or take a nonlinear relation between geomechanics moduli and hydrate saturation already built in T+M<sup>AM</sup>, we can obtain better agreement between numerical and experimental results.

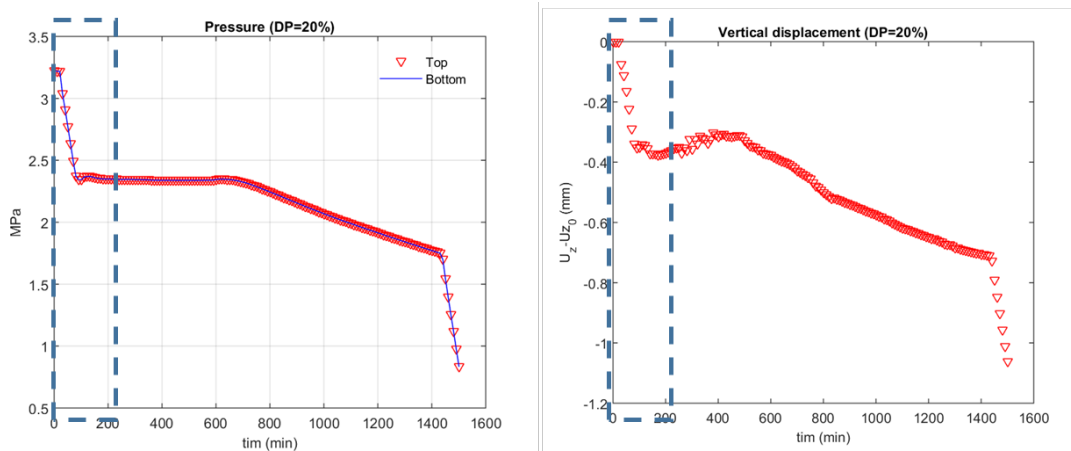


**Fig. 5.5 Experimental results of Subtask 1 (DP=20%): Pressure (left) and displacement (right). The blue dotted area means the interval used for validation of T+M.**

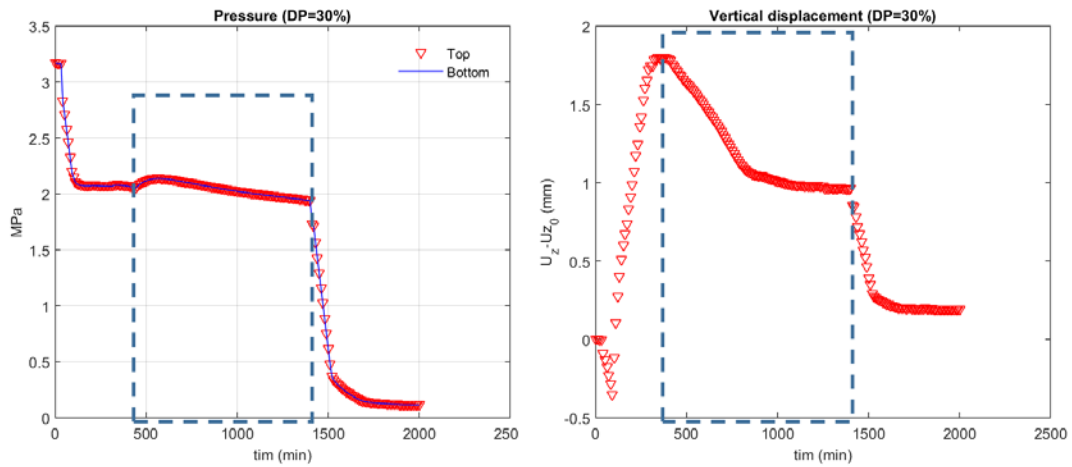


Fig. 5.6 Experimental results of Subtask 1 (DP=30%): Pressure (left) and displacement (right).

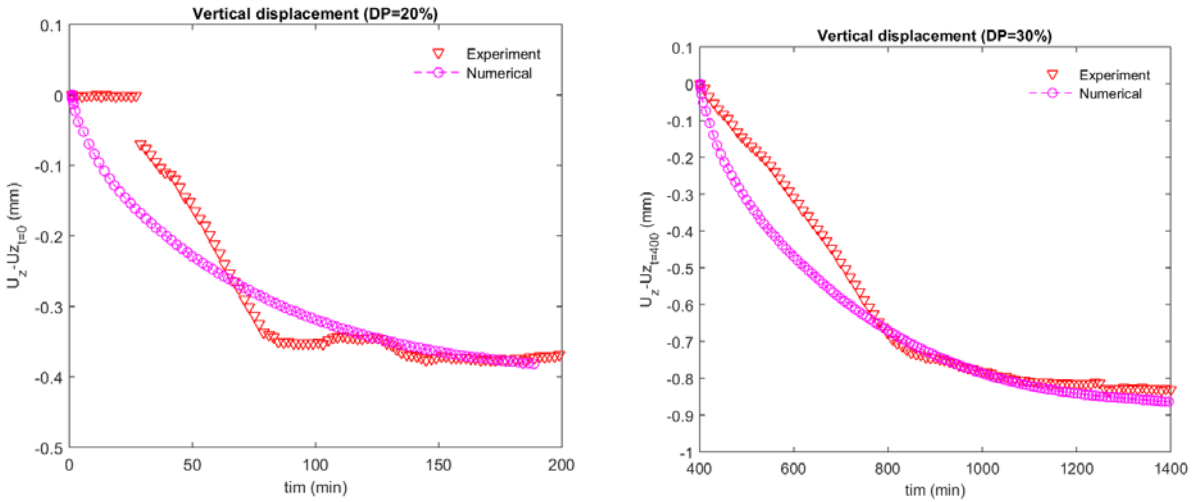
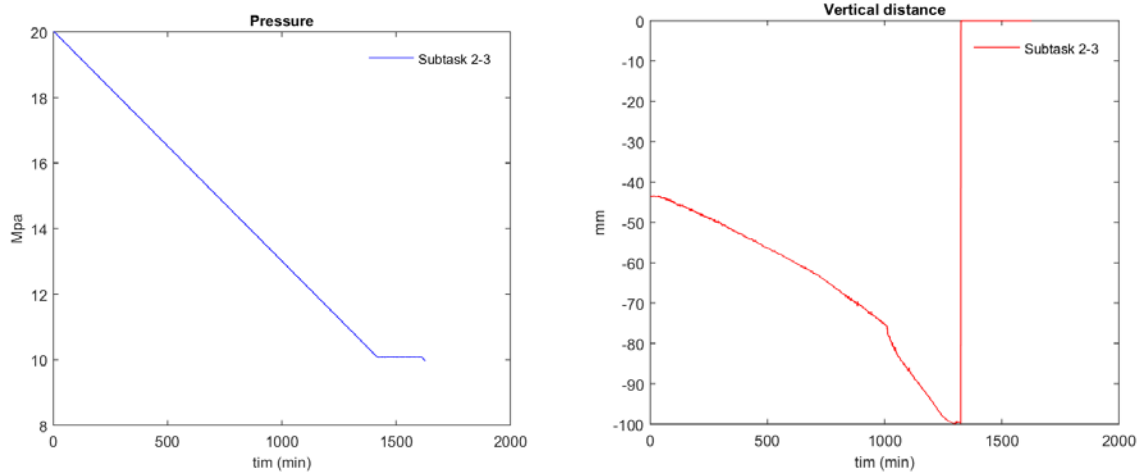


Fig. 5.7 Comparison between numerical and experimental results. Left: DP=20%. Right: DP=30%.

### 5.1.3 Data processing for the 3D-1.5m experiment

We analyze the data of the 3D-1.5m experiment, where displacement after around 1300 min was not measured (Fig. 5.8). The bottom hole pressure decreased linearly, but it did not reach the constant pressure unlike the previous 1D experiment. Then, we again compare these experimental data with the numerical results of vertical displacement for validation of  $T+M^{AM}$ .



**Fig. 5.8 Experimental results of 3D-1.5m experiment (Subtask 2.3): Pressure (left) and displacement (right).**

#### 5.1.4 Validation of T+M<sup>AM</sup> with the 3D-1.5m experiment

We validate T+M<sup>AM</sup> by matching parameters of geomechanics and flow with the data of the sand-mud alternating layer system of the 3D-1.5m experiment. In numerical simulation we constrain the linear pressure drop at the vertical production well, same as the experiment. The 2D axisymmetric geomechanics simulation newly developed in this project is employed in this numerical validation. Just like the previous 1D case, we use the linear interpolation when estimating the geomechanics moduli. We mainly consider the following uncertain parameters: initial hydrate saturation, permeability, drained elastic geomechanics moduli at  $S_H=0\%$  and  $100\%$ . Figs. 5.9 and 5.10 show the schematics of numerical simulation and results for validation, respectively.

From Fig. 5.10 we find that numerical simulation results match the pressure data exactly as well as the vertical displacement well. From the right of Fig. 5.10, the numerical result is in good agreement with the experimental results, validating T+M<sup>AM</sup>. There is some misfit at the early and late times. The misfit at the early time is possibly due to numerical simulation without initialization (i.e., the initial condition did not exactly satisfy the mechanical and thermodynamic equilibriums.). The misfit at the late time might be due to nonlinear relation between hydrate saturation and geomechanics moduli. We can further calibrate the numerical model by tuning initial condition and other flow and geomechanics properties.

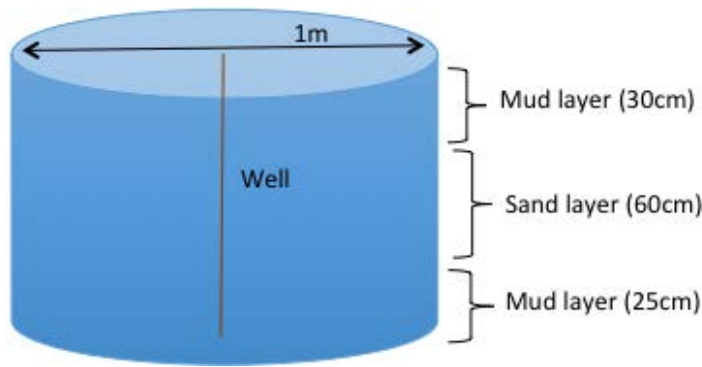


**Fig. 5.9** A schematic of numerical simulation related to the 3D-1.5m experiment. The well was perforated almost through the sand layer.

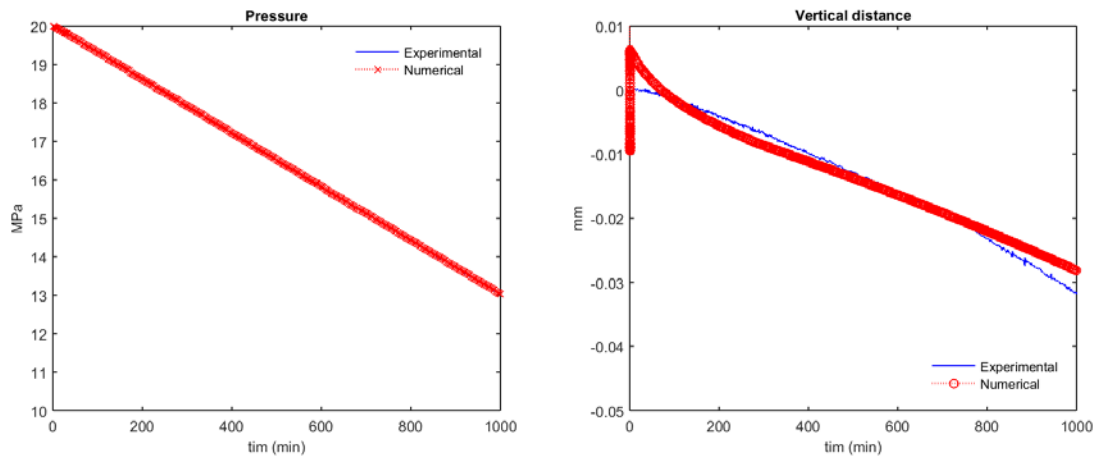


**Fig. 5.10** Comparison between experimental and numerical results: Pressure (left) and displacement (right).

## 5.2 Field wide simulation for a field located in Ulleung Basin (UBGH2-6), South Korea (Subtask 4.3, Subtask 5.6)

We employ the axisymmetric domain of simulation, considering gas production with a vertical well. In this study, we take the exact formulation of 2D axisymmetric geomechanics in order to have more accurate results. Precisely, we take the cylindrical coordinate system of stress and momentum balance to calculate deformation and stress near the wellbore appropriately. We use an in-house simulator of coupled flow and geomechanics (TOUGH+Hydrate-ROCMECH). From numerical results shown below, for long production of depressurization, we identify small subsidence at the surface but significant vertical displacement above the hydrate zones. Thus, as found in the previous study, careful consideration for wellbore stability is required.

### 5.2.1 A gas hydrate deposit located in the Ulleung Basin (UBGH2-6)

The site of UBGH2-6 is located near the sea floor in the East Sea, South Korea, having significant overburden in the deep sea (Fig. 5.11). The hydrate zone consists of alternating hydrate-bearing sand and mud layers. As shown in the right of Fig. 5.11, we take the domain of 250m by 220m for numerical simulation, which has irregular sizes of grid blocks (160 by 140). In particular, we have small gridlocks near the vertical well and the hydrate zone.

The initial pressures at the top and bottom are 23.1MPa and 24.59MPa, respectively, and the initial temperatures at the top and bottom are 6.366 °C and 18.633 °C, respectively. They are distributed linearly from top to bottom. The initial hydrate saturation at the hydrate zone is 0.65, while it is zero at the other zones. The initial vertical and horizontal stresses are -23.1MPa and -3.47 MPa, respectively, and they are distributed vertically with the gradients of -25.0kPa/m and -3.47 kPa/m. Tensile stress is positive. Table 5.1 shows main properties of flow and geomechanics simulation. We produce gas by depressurization, applying the constant bottom hole pressure of 9MPa.

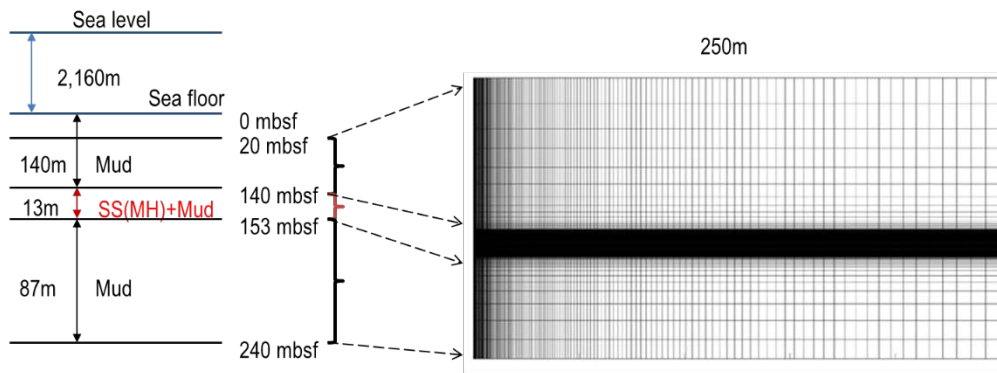


**Fig. 5.11 Left: geological information of UBGH2-6 Right: discretized domain for flow**

**Table 5.1. Material properties for flow and geomechanics**

Property	Overburden	Hydrate layer	Mud-Interlayer	Underburden
Drained bulk modulus, SH=0%	15.55 MPa	27 MPa	20 MPa	22 MPa
Drained shear modulus, SH=0%	5.185 MPa	16 MPa	6.667 MPa	7.407 MPa
Drained bulk modulus, SH=100%	285 MPa	933.33 MPa	285 MPa	285 MPa
Drained shear modulus, SH=100%	99.75 MPa	560 MPa	99.75 MPa	99.75 MPa
Permeability, SH=0%	0.02 mD	500 mD	0.14mD	0.02 mD
Initial porosity	0.76	0.45	0.67	0.0

## 5.2.2 Numerical simulation for comparison study between short term and long term production

Figs. 5.12 and 5.13 show distributions of pressure, gas saturation, temperature, and hydrate saturation after 14day and 100day productions, respectively. Depressurization induces dissociation of gas hydrates, which produces gas, shown in Figs. 5.12 and 5.13 (a), (b), and (d). Also, dissociation of gas hydrate is endothermic reaction, and thus temperature decreases (Figs. 5.12 and 5.13(c)).

In Fig. 5.14, we identify changes in pressure, gas and hydrate saturations at the two different monitoring points (mud and sand layers, respectively) near the wellbore. Pressure drops fast (Fig. 5.14 (a)), which can dissociate gas hydrate (Fig. 5.14 (d)), and thus gas is produced (Fig. 5.14 (b)). Also, from Fig. 5.14 (c), we find small vertical displacement away from the well at the hydrate zone.

However, as shown in Fig. 5.15, significant vertical displacement can be found near the well and above the hydrate zone after 100 days, where the vertical displacement ranges up to 1m, although the vertical displacement after 14 days at the same location is about 0.3m. On the other hand, the surface subsidence does not look critical, having the vertical displacement of 0.05m after 100 days and -0.02m (uplift) after 14 days. Fig. 5.16 shows distribution of volumetric strain after 100days. We identify significant compaction near the wellbore (particularly just above the perforation area).

Figs. 5.17-5.19 show the distributions of effective stress after 100 days. The changes of effective stress correspond to the depressurized area. Specifically, the compressive volumetric mean effective stress shown in Fig. 5.19 induces large compaction in Fig. 5.16, followed by the aforementioned substantial vertical displacement.

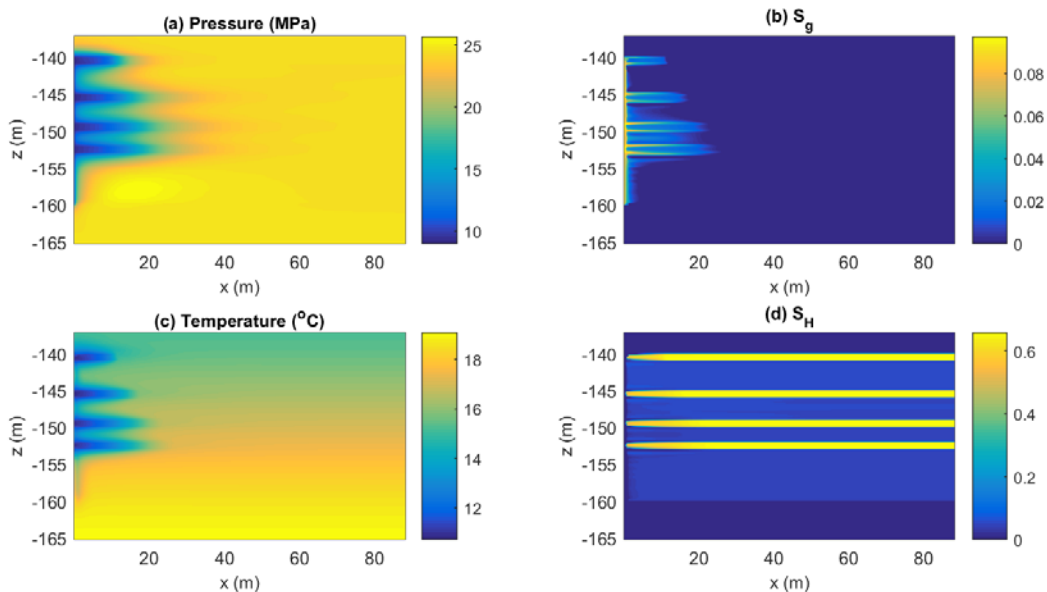


**Fig. 5.12 Distributions of pressure (a), gas saturation (b), temperature (c), and hydrate saturation (d) after 14 day production.**

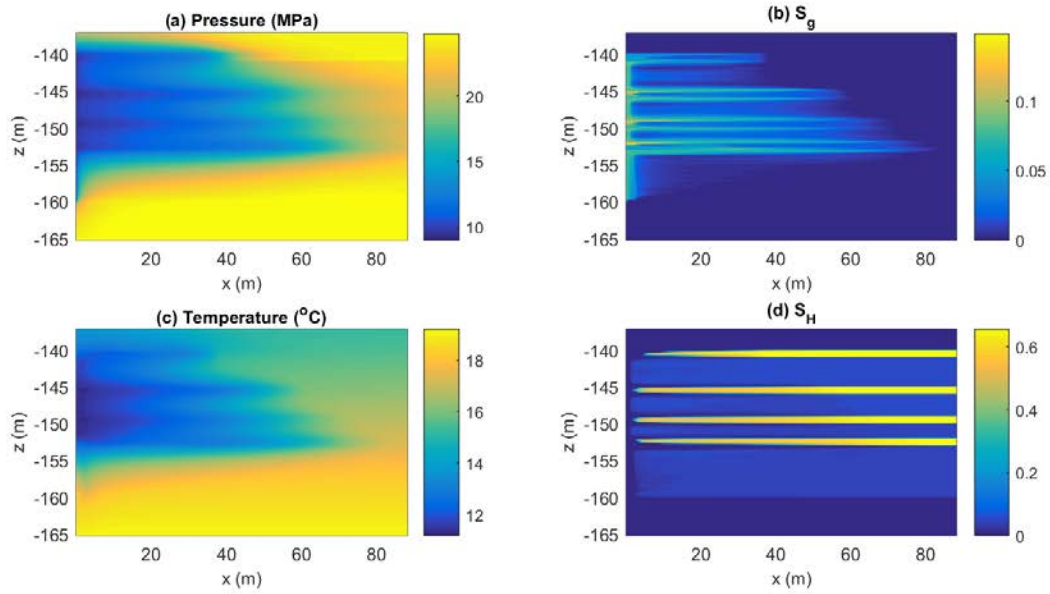


**Fig. 5.13** Distributions of pressure (a), gas saturation (b), temperature (c), and hydrate saturation (d) after 100 day production.

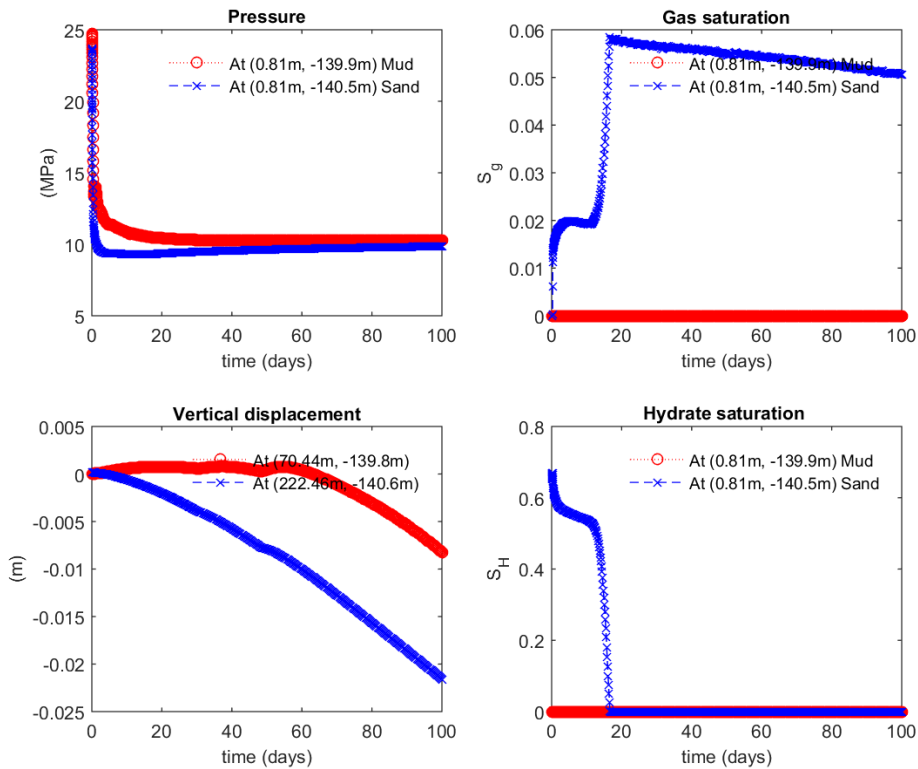


**Fig.5.14.** Evolutions of pressure (a), gas saturation (b), vertical displacement (c), and hydrate saturation (d) at two different locations.

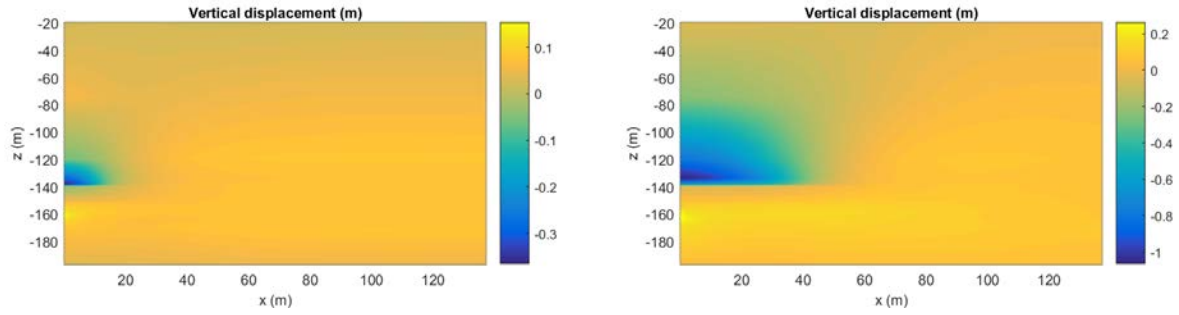


Fig. 5.15 Distribution of vertical displacement. Left: 14 day production. Right: 100 day production.

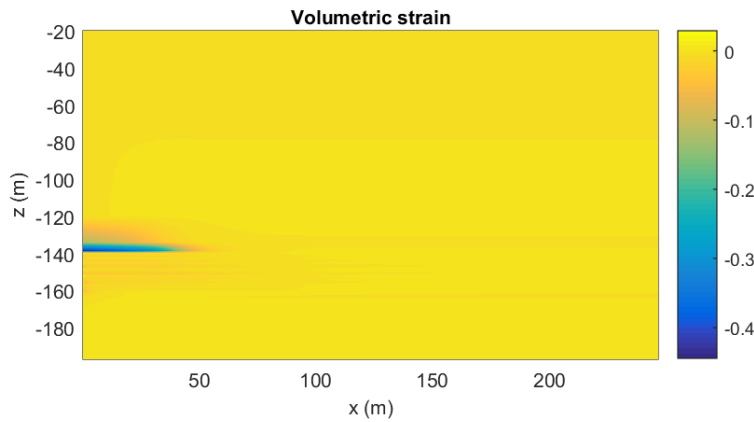


Fig. 5.16 Distribution of volumetric strain ( $\epsilon_v$ ) after 100 days.

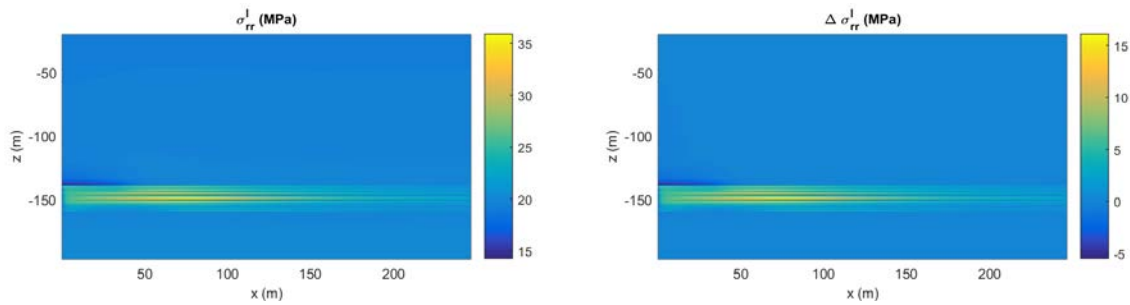
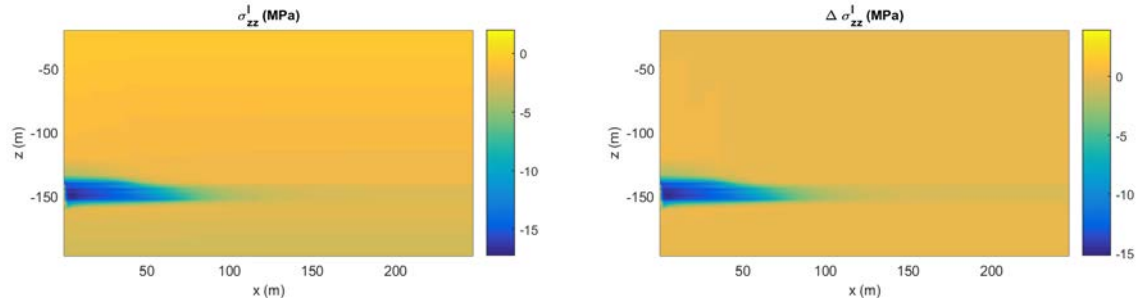
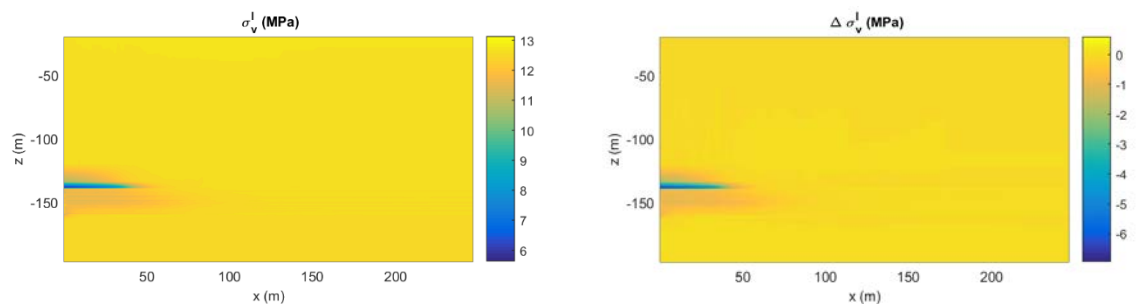


Fig. 5.17 Left: Distribution of radial effective stress ( $\sigma'_{rr}$ ) after 100 days. Right: Distribution of change of radial effective stress ( $\Delta \sigma'_{rr}$ ) from the initial state after 100 days.



**Fig. 5.18 Left: Distribution of vertical effective stress ( $\sigma'_{zz}$ ) after 100 days. Right: Distribution of change of vertical effective stress ( $\Delta\sigma'_{zz}$ ) from the initial state after 100 days.**



**Fig. 5.19 Left: Distribution of volumetric mean effective stress ( $\sigma'_v$ ) after 100 days. Right: Distribution of change of volumetric mean effective stress ( $\Delta\sigma'_v$ ) from the initial state after 100 days.**

We have successfully simulated the behavior of coupled flow and geomechanics at UBGH2-6. Considering more accurate axisymmetric formulation, we obtained the same conclusion in the previous study that the wellbore might not be stable, which can suffer from significant vertical slip. Thus, careful consideration of geomechanics behavior is required. Currently, more simulation with various production scenarios and further in-depth analysis are ongoing in order to investigate geomechanical behavior such as subsidence, evolution of effective stress, and any potential of geological failure including wellbore collapse. In what follows, we study various scenarios for 30 day production to minimize geomechanical risks as well as to maximize productivity.

### 5.2.3. Numerical simulation for productivity and geomechanical analyses with various production scenarios

We study productivity of gas as well as geomechanical responses subsidence by taking 4 different cases shown in Table 5.2 when considering 30 day production. The simulation is based on the geological model developed in 2014 just as done in the previous section while we take different initial horizontal total stress of -23.1MPa, same as the vertical stress, for conservative stress analysis. Also, the two different horizontal stress conditions do not make differences, shown in Kim and Lee (2019). Here, the brief summary of the simulation results is as follows.

Figs. 5.20 and 5.21 including Tables 5.3 and 5.4 show production of gas and water for the four cases. Overall, for all cases, gas production is much higher than water production. When BHP (bottom hole pressure) is low (i.e., Case 1), we can get higher production of gas and water while larger subsidence is obtained. For Case 2, where BHP (bottom hole pressure) drops linearly rather than instantaneously, the numerical results of production are still almost same as those of the reference case, where BHP is 9MPa. For Case 3, where periodic BHP's of 9MPa and 14MPa are applied, we can have almost same results as those of reference case. On the other hand, from Fig. 5.22, the subsidence of Case 3 is the lowest among the four cases, which shows that this case is one of the promising scenarios for UBGH2-6 field test production. From the effective stress distribution for Case 3 shown in Fig. 5.23, we also find that changes in effective stress are not very significant when we take the periodic production scenario (Case 3).

**Table 5.2 Four production scenarios for 30 day production by depressurization with a vertical well.**

	Reference Case	Case 1	Case 2	Case 3
Scenarios	Instant BHP drop, 9MPa	Instant BHP drop, 5MPa	BHP, 9MPa with 0.5MPa/hr	1. 9MPa; 8days 2. 14MPa: 2days 3. 9MPa: 8days 4. 14MPa:2days 5. 9MPa: 10days

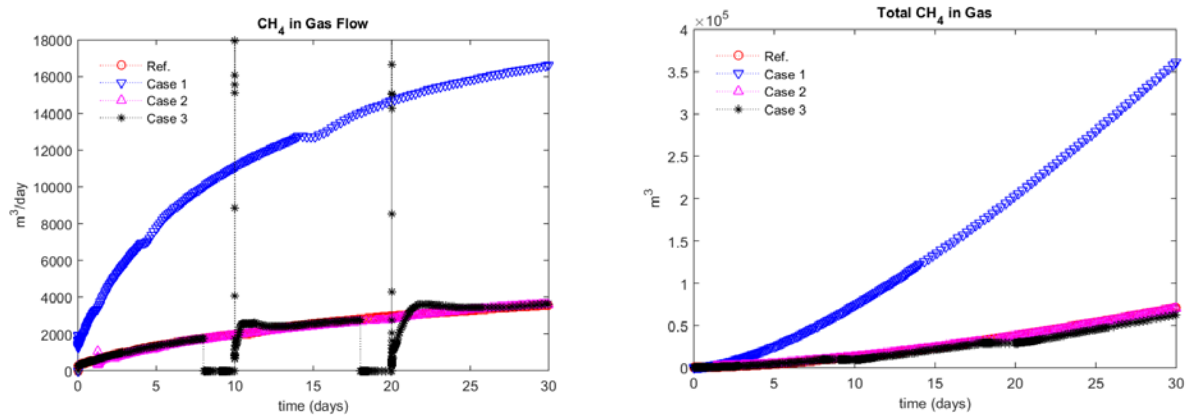


**Fig. 5.20 Left: methane gas flow rate. Right: cumulative production of gas phase methane.**

**Table 5.3 Total gas production for the four cases.**

	Reference Case	Case 1	Case 2	Case 3
Total Gas CH4 volume (m³)	70,818	361,270	69,677	62,733

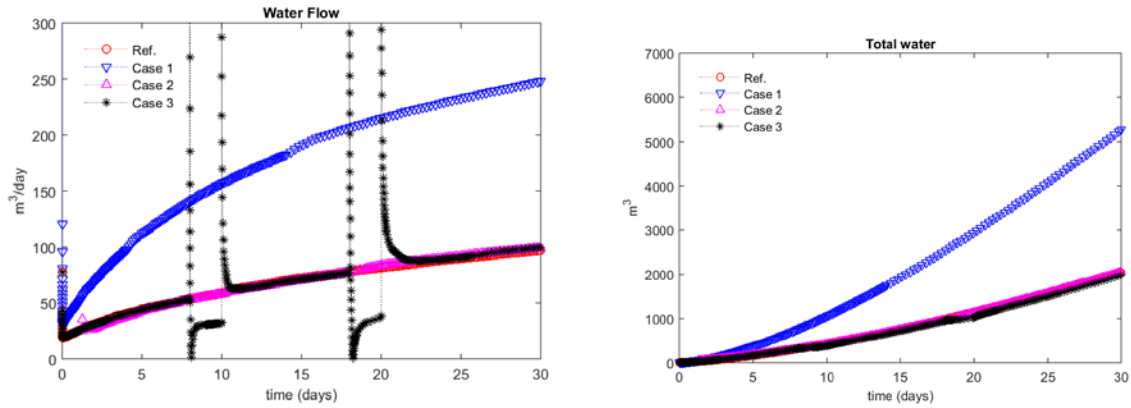
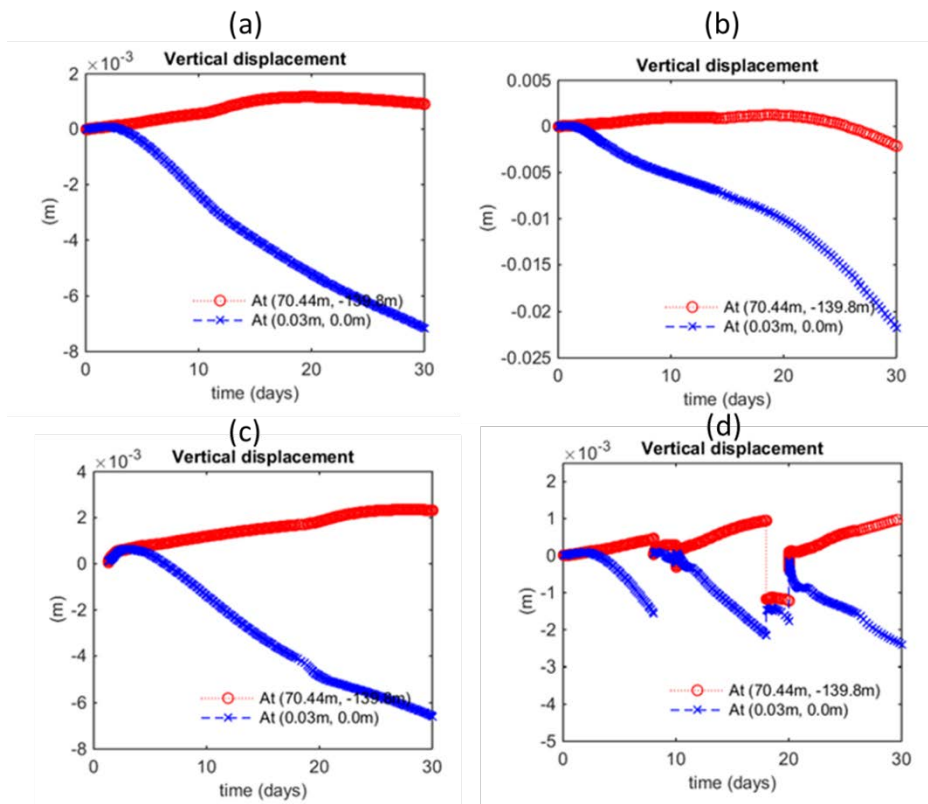


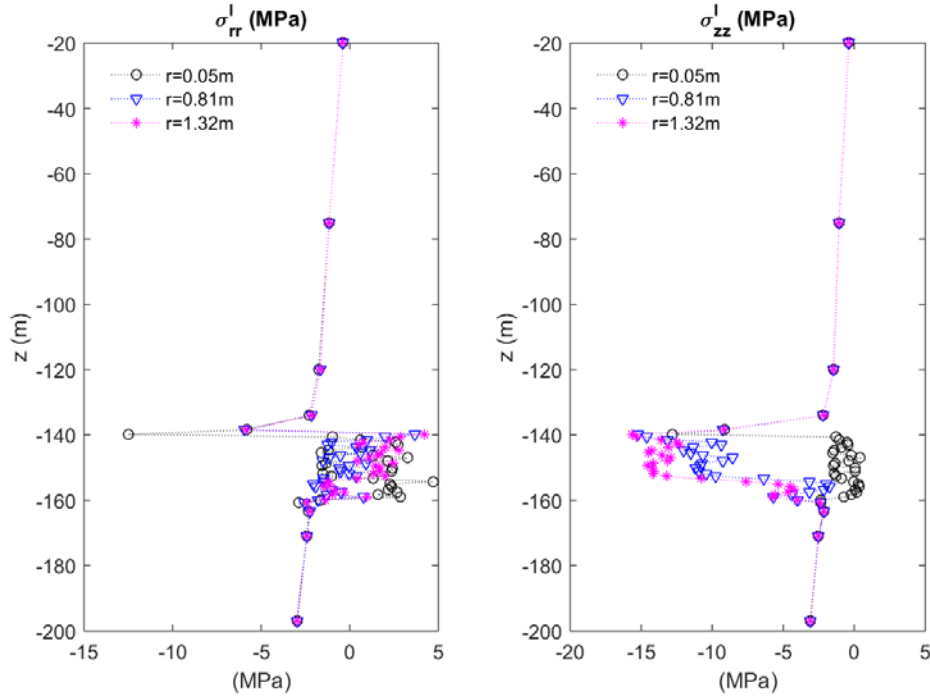
Fig. 5.21 Left: water flow rate. Right: cumulative production of water.

Table 5.4 Total water production for the four cases.

	Reference Case	Case 1	Case 2	Case 3
Total water volume ( $m^3$ )	2,041	5,280	2,053	1,977



**Fig. 5.22 Vertical displacements near and away from the well for all four cases. Overall, subsidence is not significant during 30 day production.**



**Fig. 5.23 Effective stress distribution along the vertical direction at the formation near the well for Case 3. Left: Radial effective stress. Right: Vertical effective stress.**

### 5. 3 Slip fracturing and wellbore stability analysis for a field located in Ulleung Basin (UBGH2-6), South Korea (Subtask 4.3, Subtask 5.4, Subtask 5.6)

In this section, we employ the most up-to-date model (2017 model) with axisymmetric domain of simulation. Compared to 2014 model, 2017 model contains more gas hydrate layers and different hydrate saturation values among the layers as shown in Fig 5.24. We use a simulator of coupled flow and geomechanics (TOUGH+Hydrate-FLAC3D). Continuing to the previous section, we perform more in-depth mechanical analysis near the wellbore or along the pipe. We test various cases with realistic interface properties to assess potential impacts on the wellbore and pipe, which can provide useful information for the field test in the future.

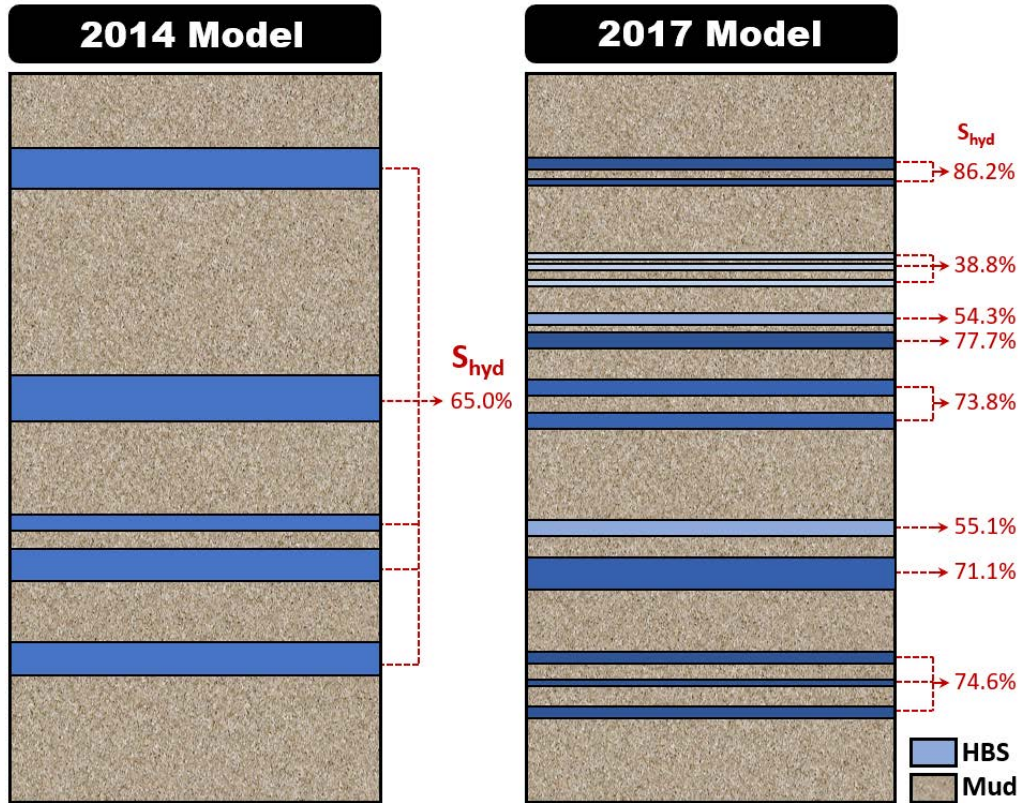
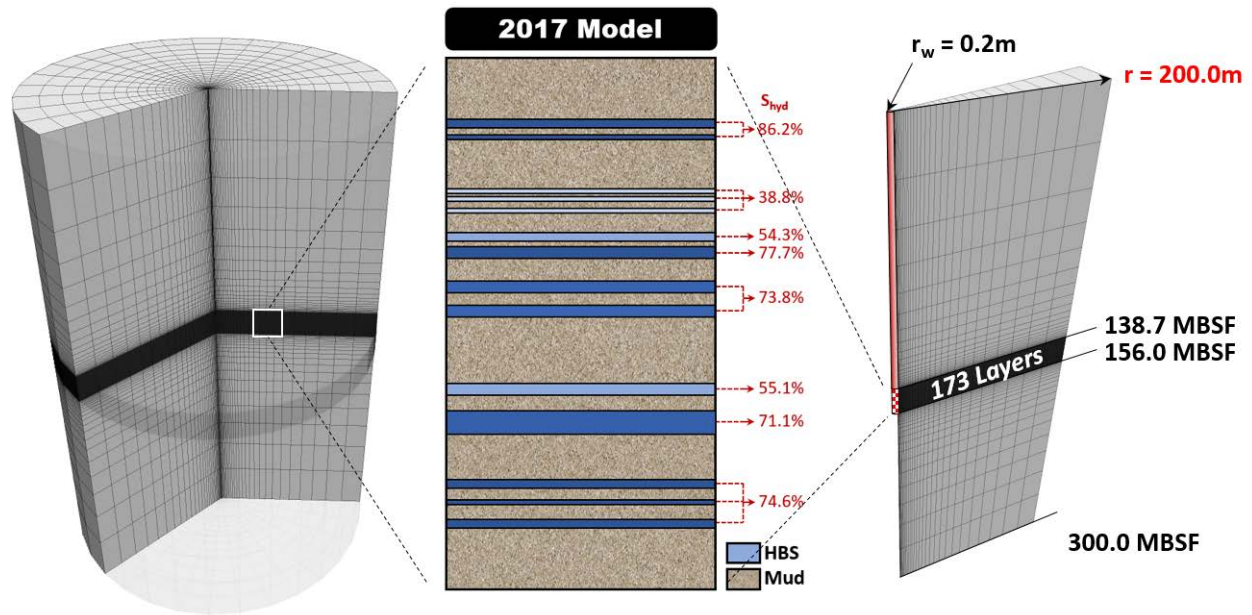


Fig. 5.24 Schematics of Hydrate Bearing Sediments and mud layers UBGH2-6. Left: 2014 model. Right: 2017 model.

### 5.3.1 A gas hydrate deposit located in the Ulleung Basin (UBGH2-6)

As shown in the Fig. 5.25, we take two different domains for the geomechanics (left) and the flow (right), where the flow domain is included in the geomechanics domain to reduce computational cost. The total domain size of 2017 model is 300m×200m for the numerical simulation in the radial and vertical directions, taking axisymmetric geomechanics simulation, respectively, which has non-uniform gridblocks (216 and 30 including the pipe element). In particular, we have smaller gridblocks near the wellbore and gas hydrate zone. The thickness of the hydrate layer is  $\Delta z = 0.1$  m.

The initial pressure at the top and bottom of the domain are 22.90MPa and 24.57Mpa, respectively, and the initial temperature is 15°C. The pressure is distributed linearly from top to bottom while the temperature is constant over the domain. The initial hydrate saturation at the hydrate zones are various layer by layer from 33.8% to 86.2% as can be seen in Fig. 5.25. The initial vertical total stress starts from -23.1MPa at the top layer because it represents the sea floor, distributed with the gradients of -25.0kPa/m along the depth. In this study, we assume the vertical and horizontal stress to be the same. Here, compression stress is negative. We produce gas by depressurization, applying the constant bottom-hole pressure of 9MPa. In addition, we assume fully completion from 138.7m to 156.0m rather than partial completion scenario, which only targets hydrate bearing zones. We use the same main properties of flow and geomechanics simulation except initial hydrate saturation as shown in Table 5.1.



**Fig. 5.25 Simulation domains for geomechanics (left) and flow (right) for the 2017 model at UBGH2-6.**

### 5.3.2 Results of numerical simulation for a field located in Ulleung Basin (UBGH2-6)

In this section, we do not employ the interface element around the pipe. After running the two-way coupling numerical simulation without interface elements, we use the simulation results to perform sensitivity analysis of wellbore cement fracturing by changing interface properties so that we can investigate the impact of interface on wellbore stability. Figs. 5.26 shows distributions of pressure, temperature, gas saturation, and hydrate saturation after 14 days. The pressure tends to decrease mostly with production. However, there are some layers showing substantial pressure increase due to the compaction and undrained condition at the above and below gas hydrate layers. Compared to 2014 model from Section 5.2, dissociation of gas hydrates occurs at the layers that have low hydrate saturation at the initial time. As a result, we obtain much larger production of gas and water, as shown in Figs. 5.27.

Fig. 5.28 shows distributions of vertical displacement, volumetric strain, radial effective stress, and vertical effective stress after 14 days. In the figure, significant vertical displacement can be found locally near the hydrate bearing zone even after 14 day production, where the vertical displacement ranges between -1.0m to 0.8m. The vertical displacement at the sea bottom of 0.1m after 14 days.

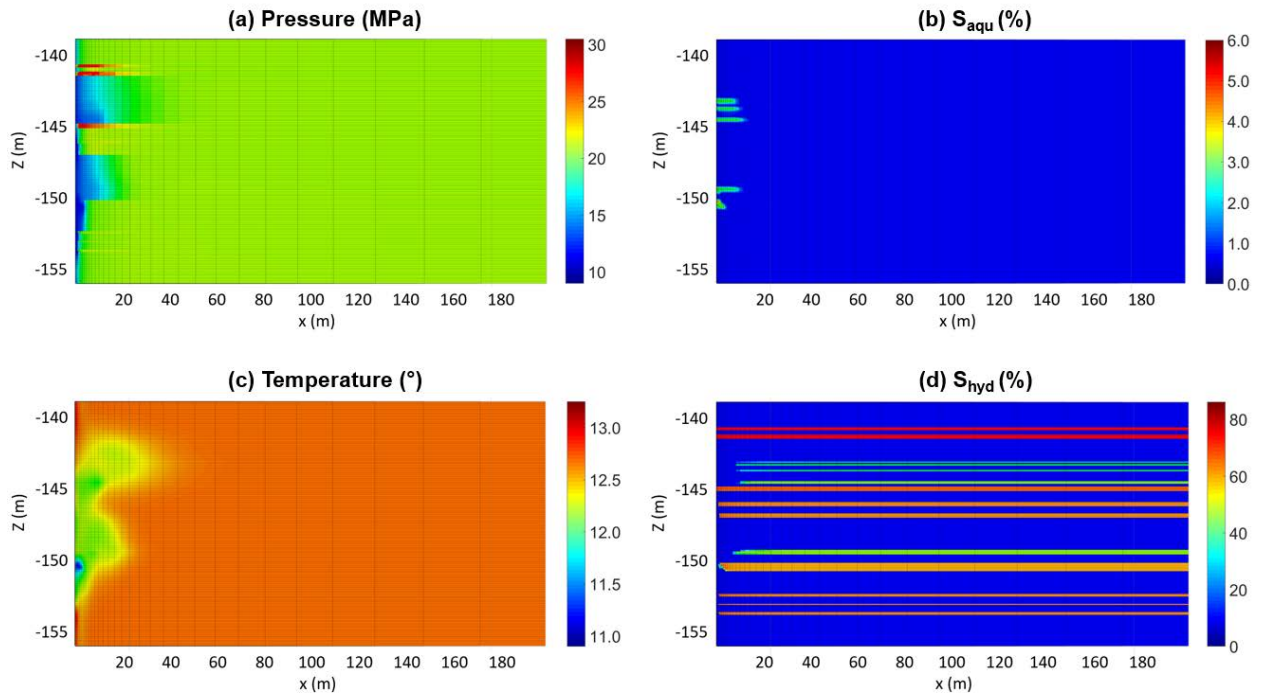


Fig. 5.26 Distributions of pressure (a), gas saturation (b), temperature (c), and hydrate saturation (d) after 14 day production.

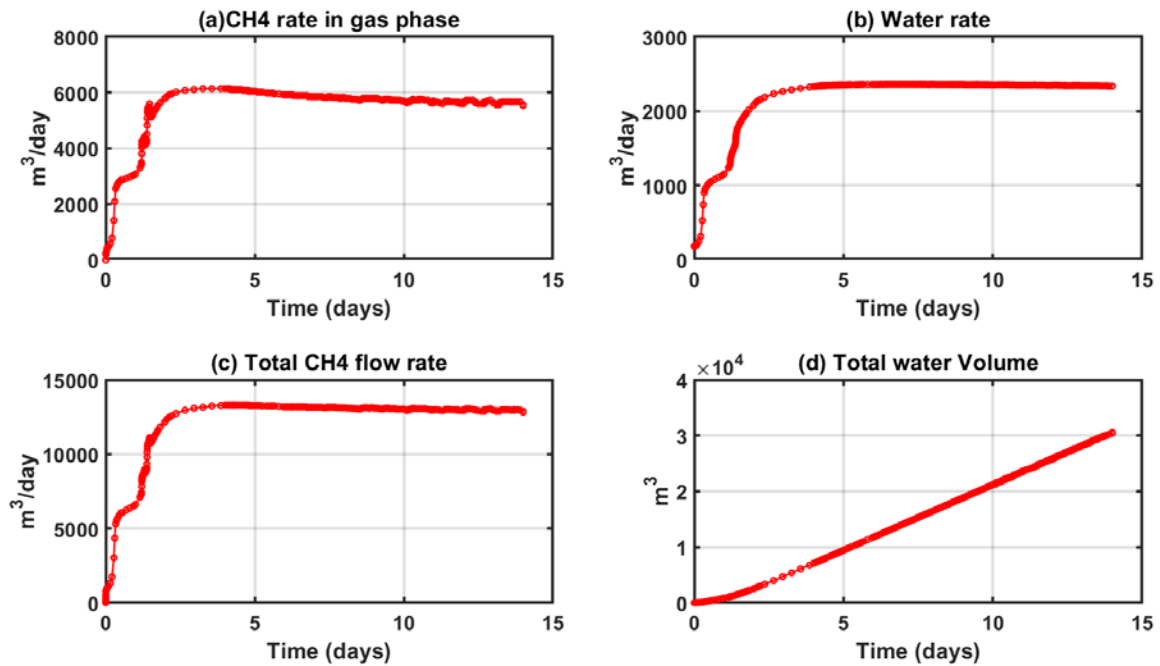
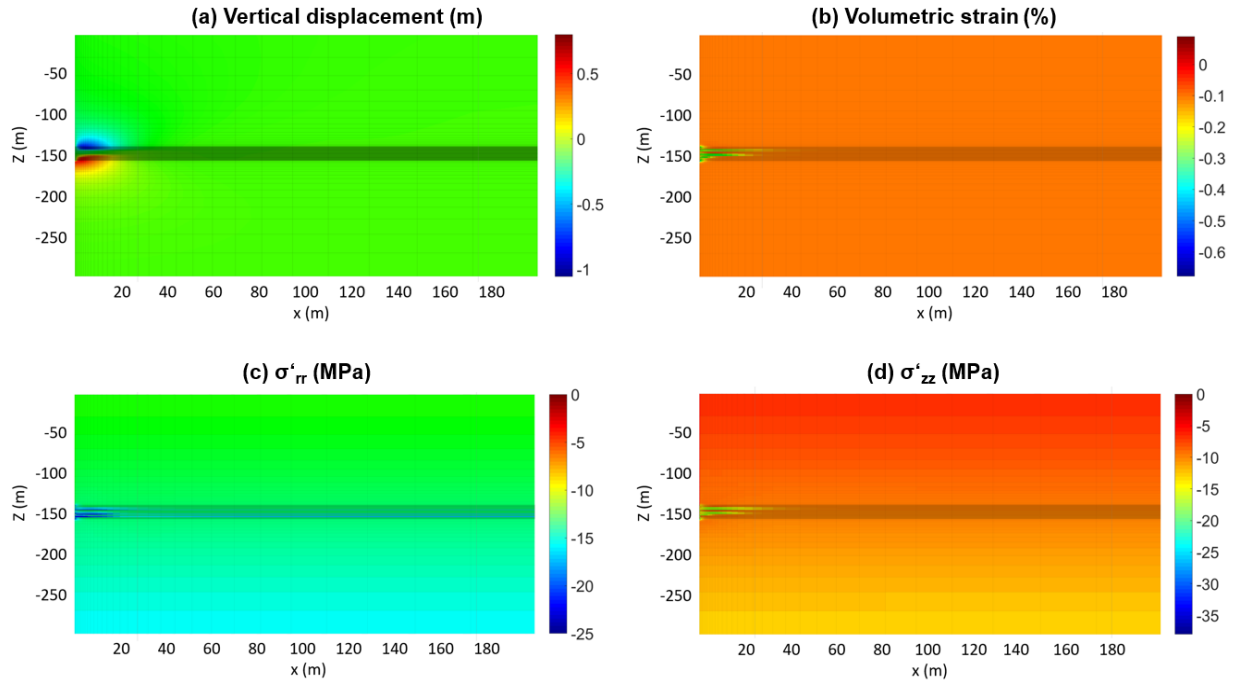


Fig. 5.27 Methane gas flow rate (a), water flow rate (b), Total methane flow rate (c), and cumulative production of water (d) after 14 day production.



**Fig. 5.28 Distributions of displacement (a), volumetric strain (b), radial effective stress (c), and vertical effective stress (d) after 14 day production.**

### 5.3.3 Numerical simulation for comparison study with various interface properties for a field located in Ulleung Basin (UBGH2-6)

We take 5 test cases with different realistic interface mechanical properties shown in Table 5.5 to conduct the wellbore stability analysis. The interface elements are implemented between the pipe and the reservoir formation, where we assume that it is possible to have shear and normal-slip depending on the initial bonding force, as shown in in Fig. 5.29. Fig 5.30 shows the normal failure along the vertical well by using the Mohr–Coulomb failure model for all 5 cases. It is worth noting that all the cases show shear failure and each displacement in the vertical direction is shown in Fig 5.31.

Case 1 is based on the properties from the laboratory test, the reference case (Kim et al, 2019). For uncertainty analysis, we vary the normal stiffness, shear stiffness, tensile strength, and cohesion values. For all the 5 cases, we find that the vertical stress in the pipe ranges from -150 MPa to 120 MPa. This implies that it can be safe with the current scenario if we use 9 5/8” production casing. The strength of the intact casing is 758MPa. We use 454.8 MPa for yield strength because the casing is perforated by 60%.

**Table 5.5. Interface properties for wellbore stability**

Property	Case 1	Case 2	Case 3	Case 4	Case 5
Normal stiffness	57.41 MPa	5.741 MPa	57.41 MPa	57.41 MPa	57.41 MPa
Shear stiffness	26.11 MPa	26.11 MPa	2.611 MPa	26.11 MPa	26.11 MPa
Tensile stress	1.74 MPa	1.74 MPa	1.74 MPa	3.48 MPa	1.74 MPa

Cohesion	17.39 MPa	17.39 MPa	17.39 MPa	17.39 MPa	1.739 MPa
Friction Angle	30°	30°	30°	30°	30°

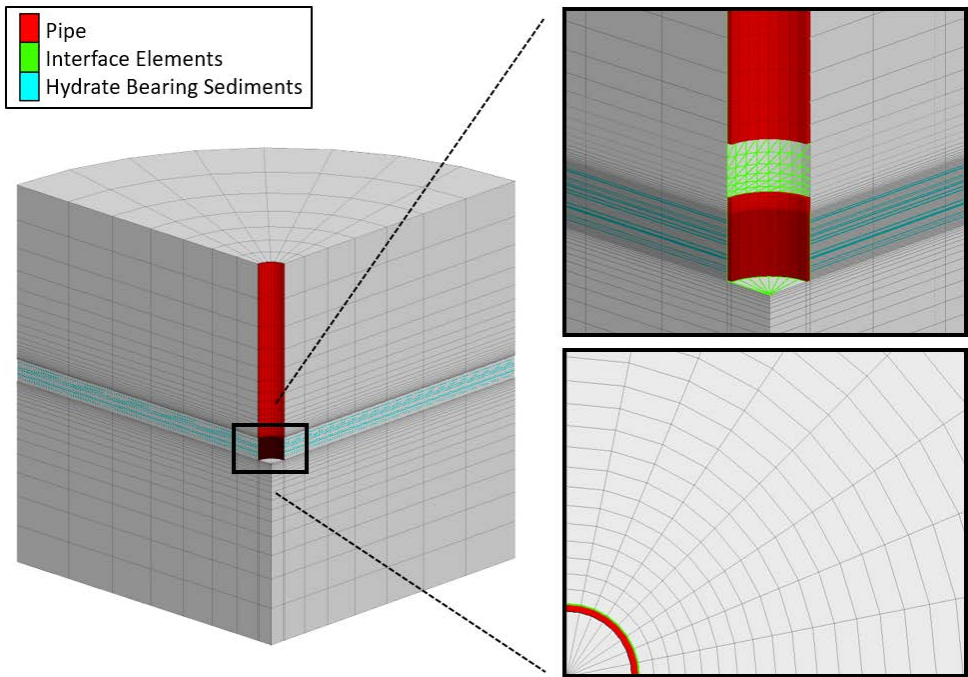


Fig. 5.29 Description of simulation domain with pipe and interface elements.

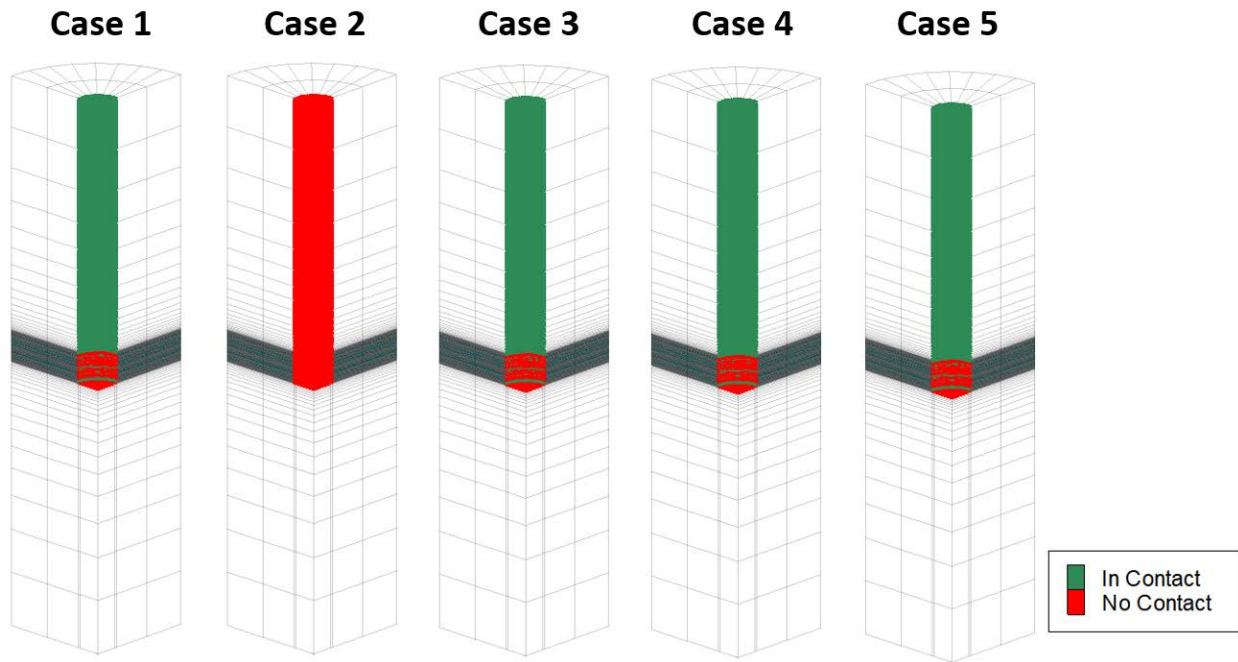


Fig. 5.30 Normal Slip on the interface elements between the pipe and the formation after 25 day production.

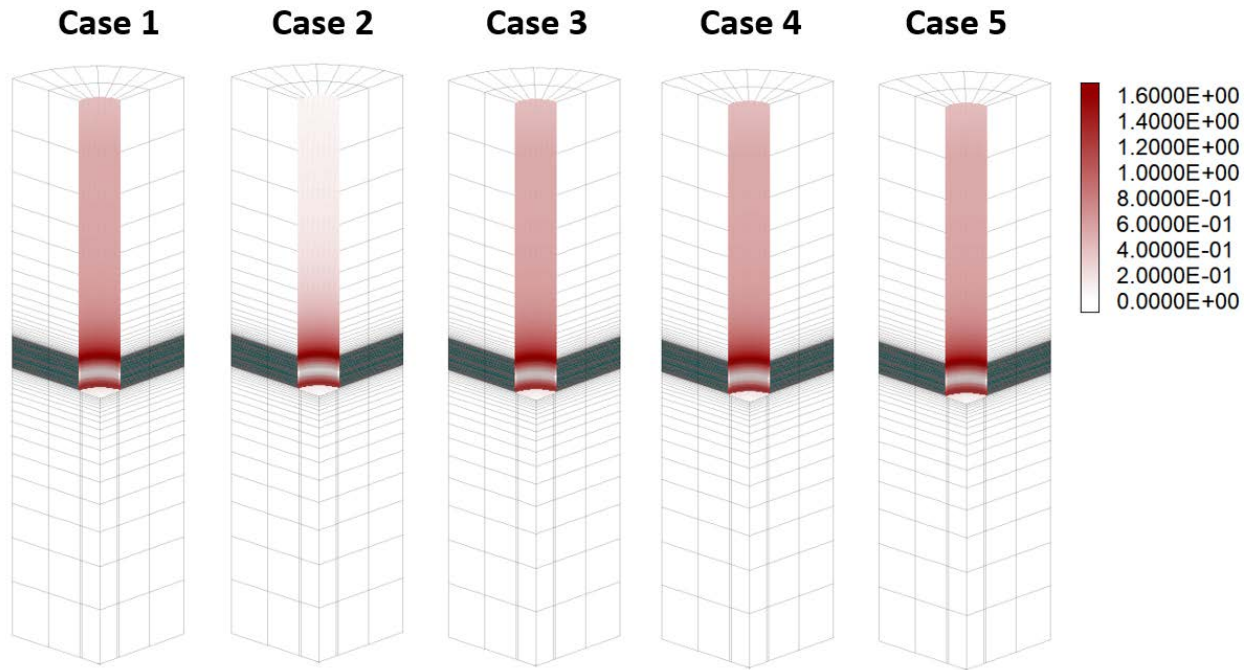


Fig. 5.31 Shear slip displacement (m) along the interface elements for 5 test cases after 25 day production.

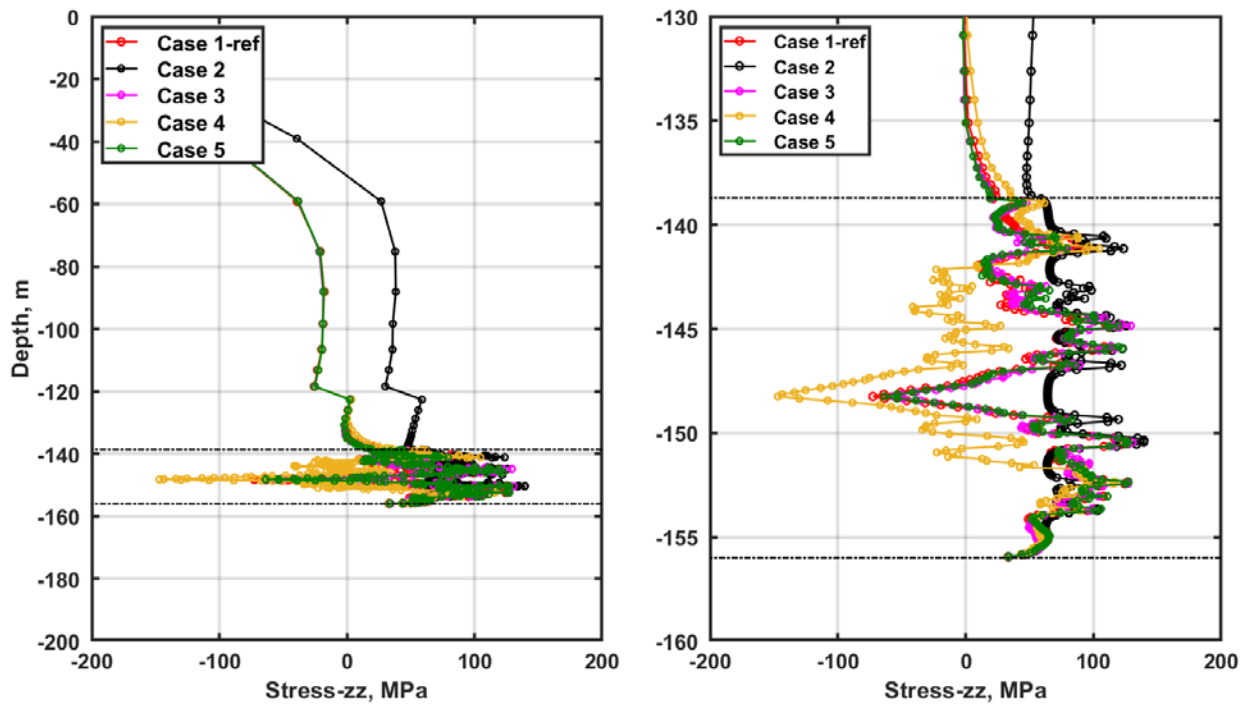


Fig. 5.32 Vertical stress distribution along the vertical direction at the pipe.

#### 5. 4. Slip fracturing and wellbore stability analysis for a field located in the vicinity of Prudhoe Bay Unit L-Pad on the North Slope (PBU-L106), Alaska (Subtask 4.3, Subtask 5.4, Subtask 5.5)

Kim et al. (2012) investigated the flow performance and geomechanical response of vertical well production at Unit C of PBU-L 106 site with constant pressure conditions of the depressurization method. We revisit the previous study to investigate for the wellbore stability analysis, as we did in the previous subsection. From numerical results shown below, we can find a full range of different stresses applied in the pipe elements with different bonding scenarios between the pipe and the reservoir formation.

##### 5.4.1 A gas hydrate deposit located in the Prudhoe Bay area on the North Slope (PBU-L106)

The PBU-L-106 site is located on the North Slope in Alaska. The geology of the gas hydrate deposits in North Slope of Alaska have been described in Moridis et al. (2010) and Kim et al. (2012). We slightly modify a smaller domain for the flow simulation, 500mX105.2m, while taking a larger domain for the geomechanics, 1000m by 800m in the radial and vertical directions, respectively. Here, we make the grids become smaller near the wellbore and hydrate bearing sediments (Fig. 5.33). We create 4270 grids (i.e., 61 X 70 in radial r and vertical z directions) for the flow problem and 182,528 grids (i.e., 62 X 32 X 92 in radial r, azimuthal  $\theta$ , and vertical z directions) including the pipe grids for the geomechanics problem.

Liquid water and hydrate saturations in C1 and C2 are 0.25 and 0.75 with porosity of 0.4, respectively, while shale layers contain only water with porosity of 0.05. Here, we assume no capillary effect. Initial pressure distributes from 7.3 MPa (top layer of C2) to 7.7MPa (bottom layer of C1). The initial total stresses are distributed from the surface (0 MPa) with the vertical gradient of -19.62 kPa/m and the horizontal gradient of -15 kPa/m. For the other properties, refer to Moridis et al. (2010), Kim et al. (2012), and in Table 5.6.

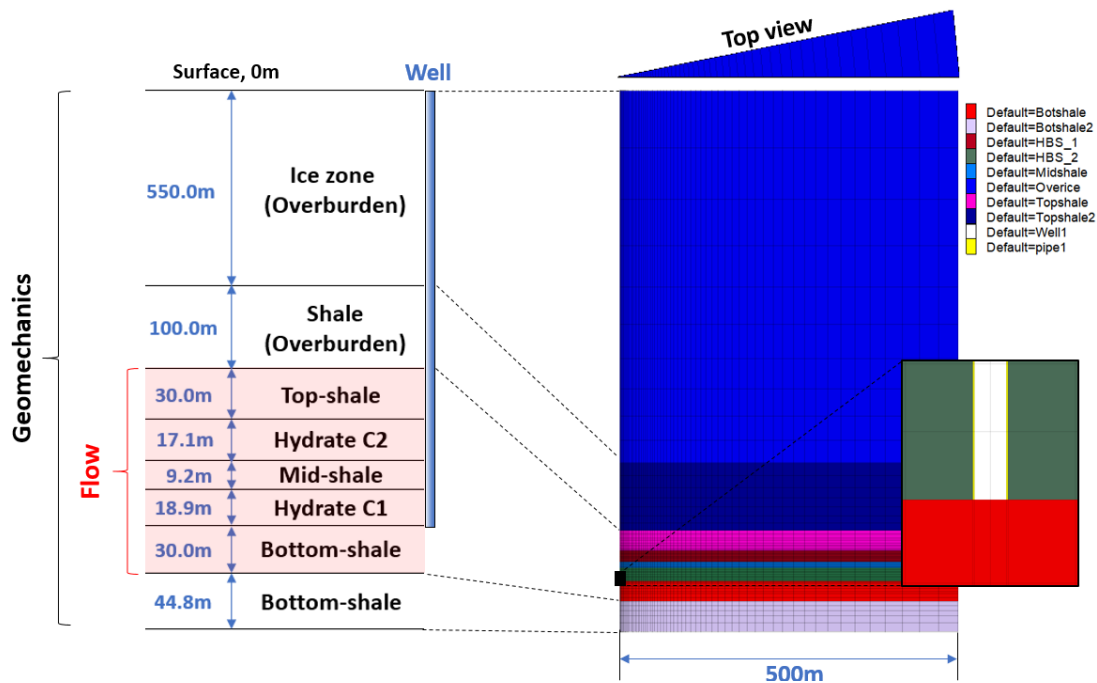


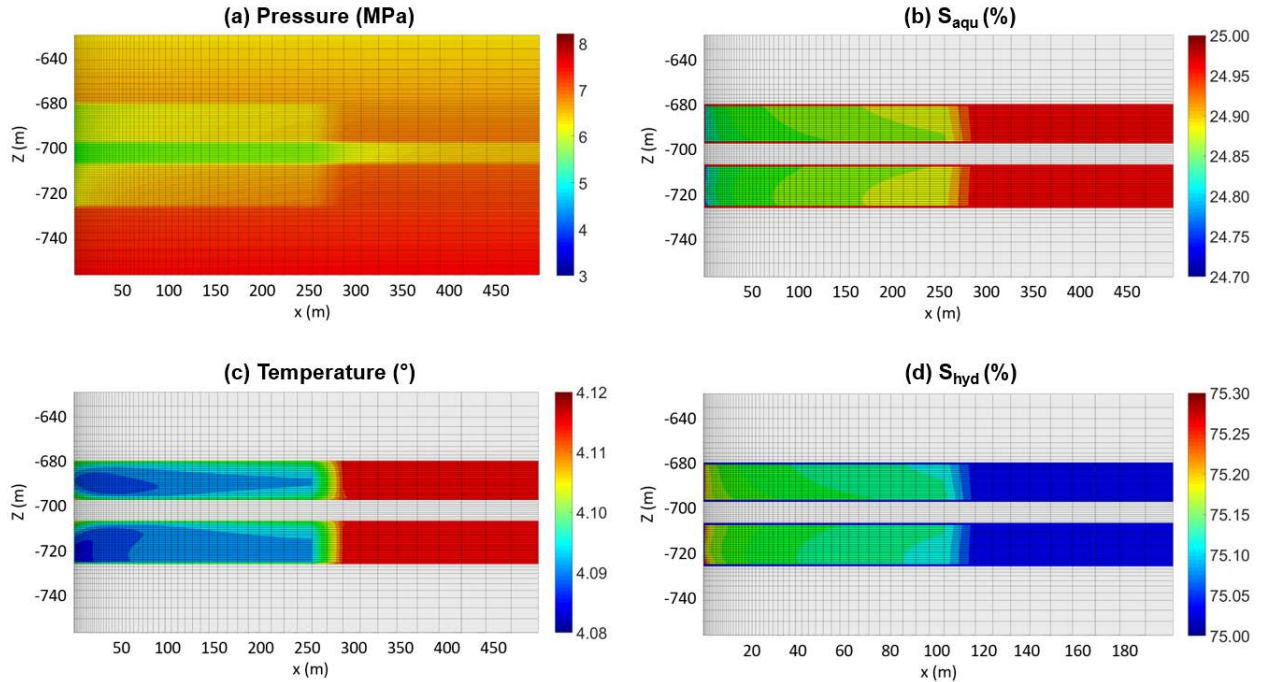
Fig. 5.33 Left: Geological information of PBU-L106. Right: Discretized domain for flow and geomechanics

Table 5.6. Material properties for flow and geomechanics

Property	Overburden	Hydrate layer	Mud-Interlayer	Underburden
Drained bulk modulus, SH=0%	95 MPa	95 MPa	95 MPa	95 MPa
Drained shear modulus, SH=0%	87 MPa	87 MPa	87 MPa	87 MPa
Drained bulk modulus, SH=100%	N/A	670 MPa	285 MPa	N/A
Drained shear modulus, SH=100%	N/A	612 MPa	99.75 MPa	N/A
Permeability, SH=0%	0 m <sup>2</sup>	1.00E-12 m <sup>2</sup>	5.00E-15 m <sup>2</sup>	0 m <sup>2</sup>
Initial porosity	0.05	0.4	0.05	0.05

#### 5.4.2 Results of numerical simulation for a field located in the Prudhoe Bay area on the North Slope (PBU-L106)

Figs. 5.34 shows distributions of pressure, water saturation, temperature, and hydrate saturation after 1 year production. In this particular scenario of depressurization, there is little dissociation of gas hydrates while there is some increase in hydrate saturation because of the pore volume reduction shown in Fig. 5.35. As shown in Fig. 5.35, noticeable changes of vertical displacement can be observed near the well and above the hydrate zone after 1 year, where the vertical displacement ranges up to -0.02m. Fig. 5.35 also shows distribution of volumetric strain, radial effective stress, and vertical effective stress. We identify significant local compaction near the wellbore. Because of low gas hydrate dissociation and low gas productivity from this production scenario, numerical simulation for different production scenarios might need to be further performed in the future for economically feasible development of gas hydrate deposits. Here, we focus on investigation of geomechanical responses and wellbore stability as follows.



**Fig. 5.34 Distributions of pressure (a), gas saturation (b), temperature (c), and hydrate saturation (d) after 1 year production.**

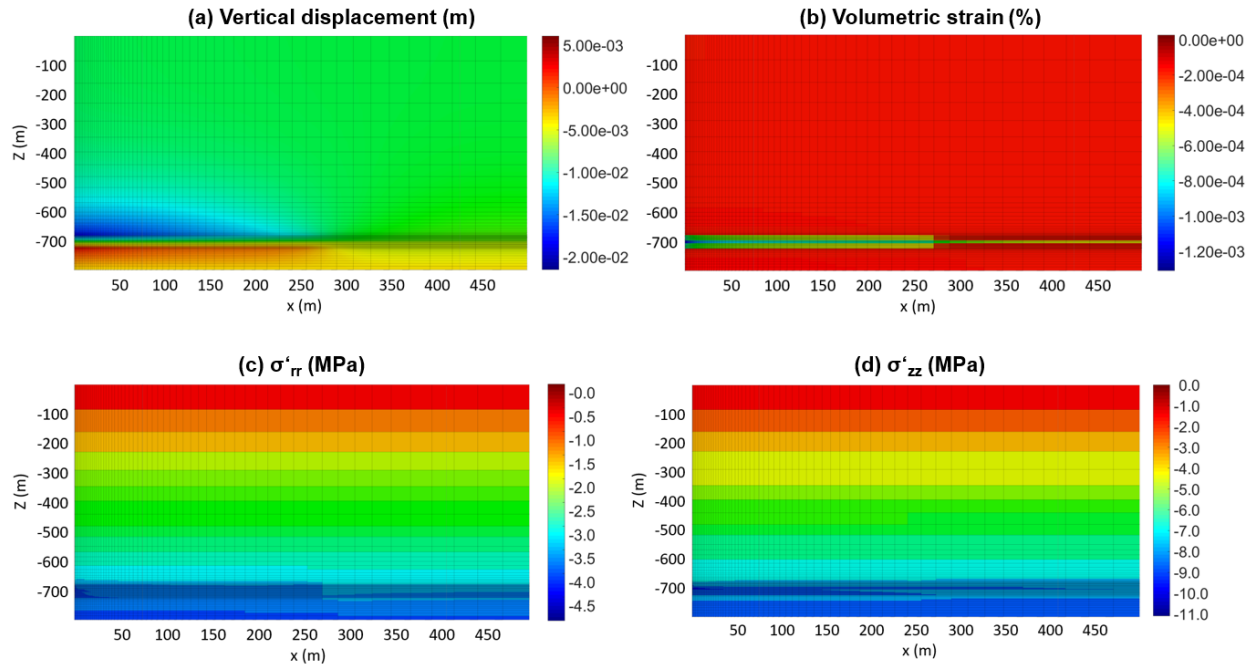


**Fig. 5.35 Distributions of displacement (a), volumetric strain (b), radial effective stress (c), and vertical effective stress (d) after 1 year production.**

### 5.4.3 Numerical simulation for comparison study with various interface properties for a field located in Prudhoe Bay on the North Slope (PBU-L106)

As mentioned in the previous subsection, we study wellbore stability by taking 5 different cases shown in Table 5.7, considering different properties of interface elements. The interface elements are located between the pipe and the reservoir formation shown in Fig. 5.36. We have a full 3D domain of numerical simulation in geomechanics to investigate the shear/normal slip and displacement shown in Fig 5.37 and Fig. 5.38, respectively. We show one figure only as a representative of all 5 cases for the slip status because those show almost the same trends in shear and normal slip. In Fig. 5.39, we compare the vertical stress along the pipe with the 5 test cases. Compared to the Ullung Basin study, there is much less changes in vertical stress along the casing due to smaller depressurization. Here, we take the interface properties used in the previous subsection, reliable values from the laboratory test. Considering that the vertical stress is within the range of yield strength of the previous perforated 9 5/8" casing (454.8 MPa), we can anticipate that the wellbore assembly would be stable for this specific production scenario although more various scenarios of depressurization with uncertainty analysis need to be tested in the future.

**Table 5.7. Interface properties for wellbore stability**

Property	Case 1	Case 2	Case 3	Case 4	Case 5
Normal stiffness	57.41 MPa	5.741 MPa	57.41 MPa	57.41 MPa	57.41 MPa
Shear stiffness	26.11 MPa	26.11 MPa	2.611 MPa	26.11 MPa	26.11 MPa
Tensile stress	1.74 MPa	1.74 MPa	1.74 MPa	3.48 MPa	1.74 MPa
Cohesion	17.39 MPa	17.39 MPa	17.39 MPa	17.39 MPa	1.739 MPa
Friction Angle	30°	30°	30°	30°	30°

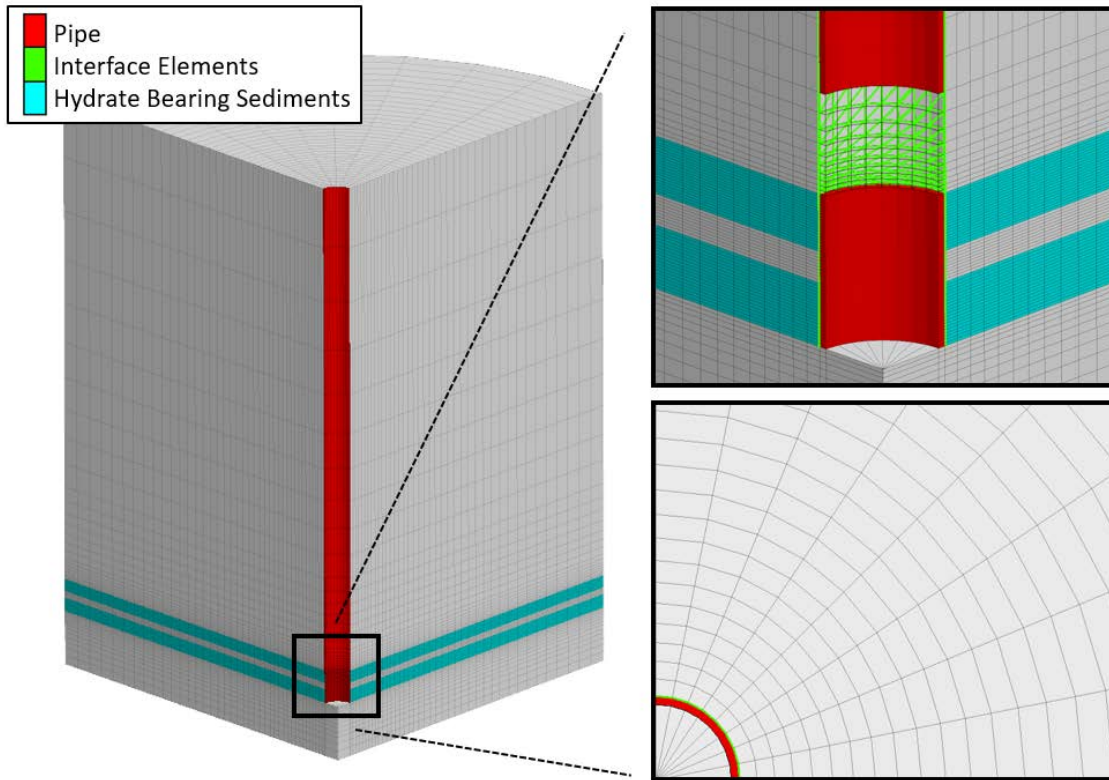


Fig. 5.36 Description of simulation domain with the pipe and interface elements.

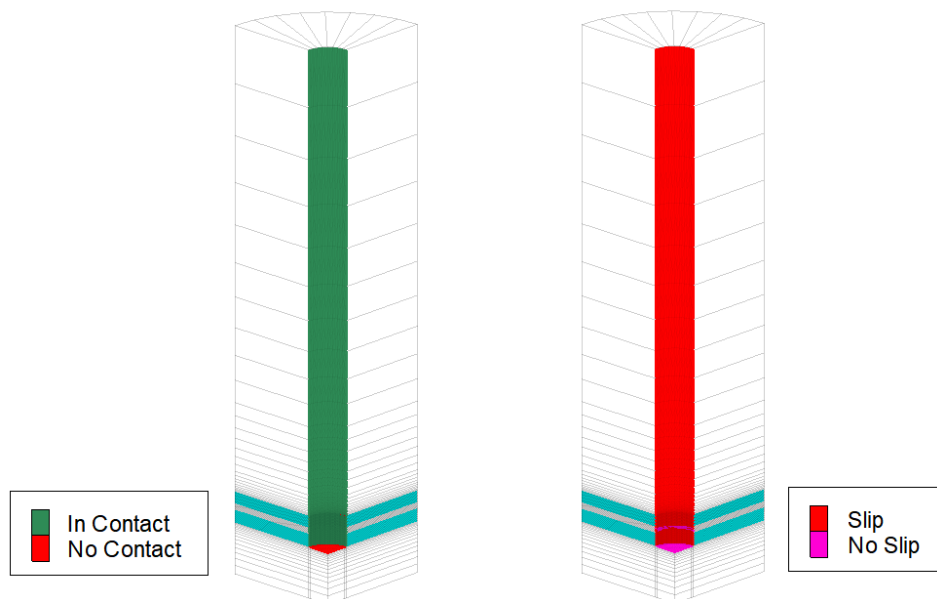
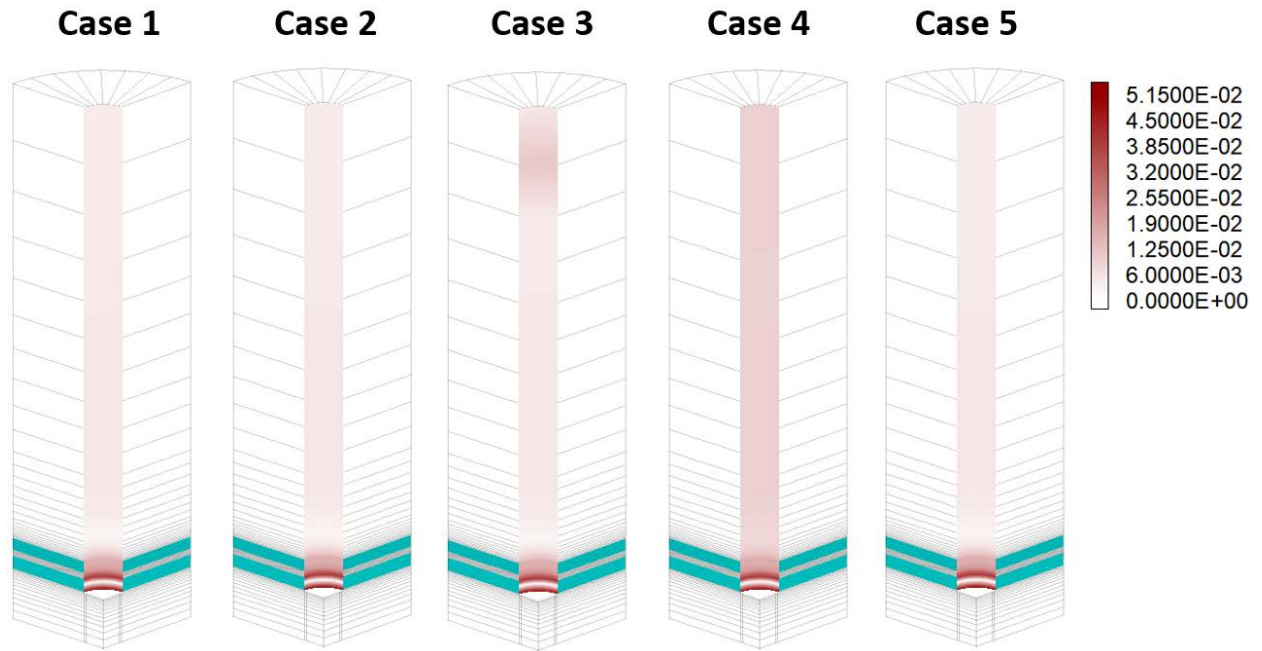


Fig. 5.37 Slip status on interface elements between the pipe and the reservoir formation after 1 year production.



**Fig. 5.38 Shear slip displacement along the interface elements with different interface properties after 1 year production.**

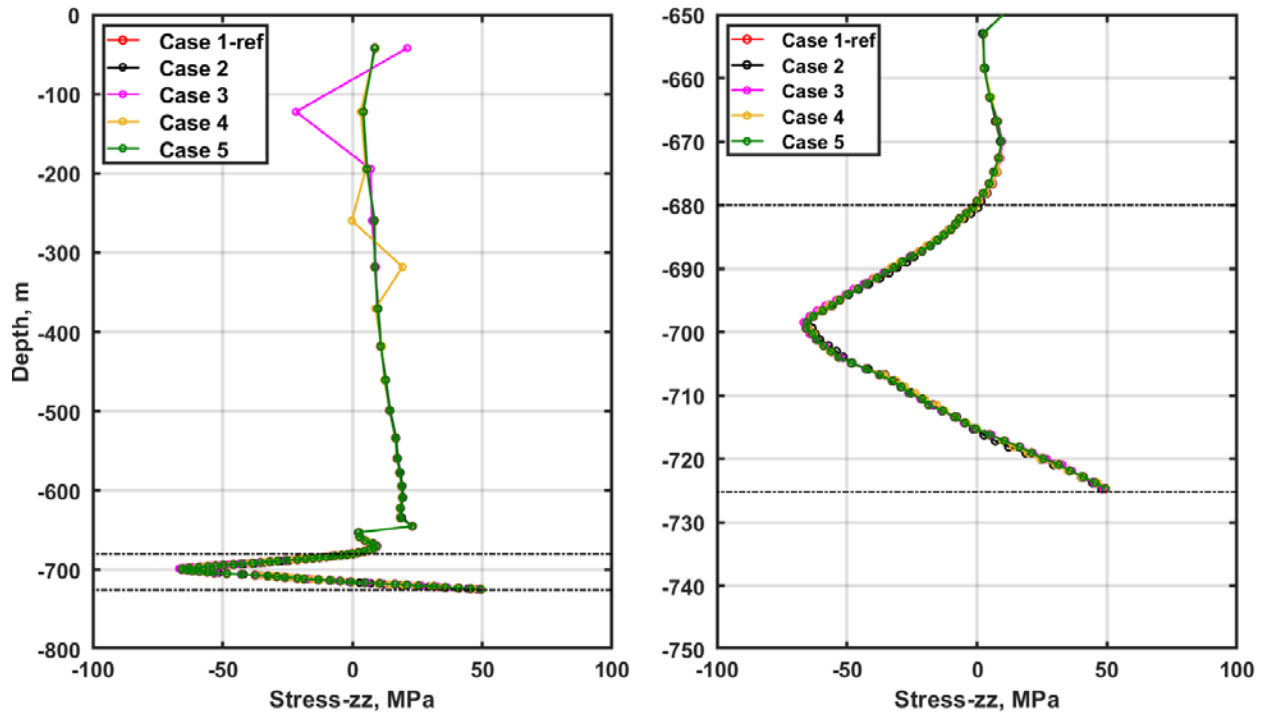


Fig. 5.39 Vertical stress distribution along the vertical direction at the pipe after 1 year production.

## 6. Simulation-Based Analysis of System Behavior at the Ignik-Sikumi and Ulleung Hydrate Deposits (Task 6 by Kneafsey, T., Moridis, G. J.)

The objective of the task was to assess the production potential of these deposits under a variety of production methods. This numerical study includes the investigation of simple depressurization-based dissociation as the baseline method of gas production. The role of Lawrence Berkeley National Laboratory in this task was to provide training, guidance and supervision of Texas A&M graduate students performing the numerical studies. Because this task involved analysis of the coupled flow, thermal and geomechanical behavior during gas production from gas hydrate deposits: the Ignik-Sikumi deposit in Alaska and UBGH2-6 in the Ulleung Basin of Korea were considered for analysis, and most of the focus was placed on UBGH2-6 in the Ulleung Basin of Korea.

In this work, we investigated the feasibility of natural gas production from a layered marine gas hydrate reservoir using the properties and conditions corresponding to the UBGH2-6 site of the Ulleung Basin in the Korean East Sea. For the depressurization process, the investigation involved coupled flow-geomechanical simulations. The studies in this task involved collaboration between Texas A&M University and LBNL, KIGAM (in an advisory role in the Ulleung investigation) and US DOE. The goals of this work were to:

1. instruct new modelers the interrelated coupled processes related to production of gas from hydrate under different conditions,
2. understand sensitivity of production to various formation and operational parameters.
3. Understand the effect of spatial heterogeneity on production.

Summarized from Moridis et al. 2019:

Heterogeneity variations included heterogeneity in a single parameter:  $k$ ,  $\varphi$  and  $SH$ , simultaneous heterogeneity in two parameters, i.e.,  $k$  and  $\varphi$ , heterogeneity in all three parameters, i.e.,  $k$ ,  $\varphi$  and  $SH$ . Two material groups were considered: a sandy (hydrate-bearing) medium, and a clay (mud) medium which comprises the overburden, underburden and the interlayers between the sandy hydrate-bearing sediments (HBS). For Young's modulus we used linear functions of  $SH$  in the hydrate-bearing media. We used a constant Poisson's ratio and the Biot coefficient was  $b = 0.8$ . (Rutqvist and Moridis, 2009; Rutqvist et al., 2009). Field and laboratory data available from the sites provided the physical property data to be used in the analysis. In addition, we also analyzed the geomechanical system response during the 14-day depressurization test, including the evolution of stress and strain during production.

The TOUGH+Millstone suite was used to perform the coupled thermal, flow, and geomechanical analysis (Moridis et al., 2017). The first component of the suite is the extensively used TOUGH+HYDRATE simulator (Moridis et al., 2017), which has been used for numerous investigations of gas production from hydrates (Li et al., 2010; Moridis et al., 2007; Moridis and Reagan, 2007a; Moridis and Reagan, 2007b; Moridis and Reagan, 2011a; Moridis and Reagan, 2011b; Moridis et al., 2011a; Moridis et al., 2011b; Moridis and Sloan, 2007). Due to the size and computational requirements of this system, the MPI-parallel pT+H simulator (Zhang and Moridis, 2008) was used for the reservoir-scale simulations.

Millstone is a newly developed finite-element geomechanical simulator (Moridis et al., 2017) that offers the unique capability of both 3D and 2D axisymmetric formulations. It provides the functionality of automatically interpolating between different flow and geomechanical meshes to allow the use of unstructured grids without any adverse numerical problems. The TOUGH+Millstone suite can either be run fully coupled, in which the geomechanical response is calculated every Newton iteration of the flow time stepping, or in a one-way coupled scheme, in which the geomechanical response is postprocessed from snapshots of the flow simulation.

The work expands and furthers previous investigations in support of a proposed field test. The target system is location in deep water and consists of 13 m of alternating hydrate-bearing sand and soft mud layers and will be produced using a vertical well. We assess production potential during a 14-day field test, examine sensitivity to heterogeneity in permeability, porosity, and initial hydrate saturation, and assess the geomechanical response of the system to short-term production. Producing gas from the system appears to be technically feasible, however, low production rates and relatively large water production rates are expected during the field test. Expected subsidence and reservoir compaction is limited given the current data and the short timeframes of the production test.

The results of the analysis are contained in Moridis et al. (2019), and summarized here.

1. The gas release and production rates are generally low and the affected region of the reservoir is limited. The water production accompanying gas production from this deposit appears manageable (in terms of absolute rates and volumes) under all the scenarios investigated in this study; however, in relative terms the water-to-gas ratio is very high during the 14-day production test and stabilizes relatively early.
2. The maximum subsidence at the seafloor is predicted to be 0.016m, but the maximum subsidence and uplift of the top and bottom of the reservoir, respectively, is predicted to have a magnitude of 0.22m.
3. Reservoir heterogeneity decreases the magnitude of the geomechanical response.

## **PRODUCTS**

### **2016**

Kim J., 2016 Development of Advanced field-wide simulation for gas hydrate deposits, in the meeting of 2nd International Code Comparison Study: Modeling THM Effects on Gas Production from Hydrate Bearing Reservoirs, Lawrence Berkeley National Laboratory, CA, 11 Dec.

### **2017**

Ahn, T., Lee, J., Lee, J.Y., Kim, S.J., Seo, Y.J., 2017 Depressurization-induced production behavior of methane hydrate in a meter-scale alternate layer of sand and mud, the 9th International Conference on Gas Hydrates (ICGH), Denver, Colorado, Jun. 25-30.

Kim, J., Lee, J.Y., 2017, Rigorous simulation of coupled non-isothermal flow and largely deformable geomechanics for gas hydrate deposits, the 9th International Conference on Gas Hydrates (ICGH), Denver, Colorado, Jun. 25-30.

Yoon, H.C., Kim J., 2017 The order of accuracy of the fixed-stress type two-pass and deferred correction methods for poromechanics, 2017 SPE Reservoir Simulation Conference, 20-22 Feb., Montgomery, Texas, SPE-182664-MS

### **2018**

Kim, J., 2018a, A new numerically stable sequential algorithm for coupled finite-strain elastoplastic geomechanics and flow, *Computer Methods in Applied Mechanics and Engineering*, 335: 538-562

Kim, J., 2018b, Unconditionally stable sequential schemes for all-way coupled thermoporomechanics: Undrained-adiabatic and extended fixed-stress splits, *Computer Methods in Applied Mechanics and Engineering*, 341:93-112

Yoon, H.C., Kim, J., 2018, Spatial stability for the monolithic and sequential methods with various space discretizations in poroelasticity, *International Journal for Numerical Methods in Engineering*, 114:694-718

Yoon H.C., Kim, J., Lee, J.Y., 2018, Field-wide Simulation and Analyses of the Geomechanical Responses with Different Depressurizations for the Gas Hydrate Deposit Located in Ulleung Basin, South Korea, AGU (American Geophysical Union) Fall Meeting, Washington D.C, Dec. 10-14

### **2019**

Adams, J., Akkutlu, I.Y., Moridis, G.J., 2019. Modeling of hydrate formation hysteresis in porous media. SPE-195540 presented at the SPE EUROPEC featured at 81th EAGE Conference and Exhibition, London, UK, June 3-6

Kim, J., Lee J.Y, 2019, Wellbore stability and possible geomechanical failure in the vicinity of the well during pressurization at the gas hydrate deposit in the Ulleung Basin, 53rd US Rock Mechanics/Geomechanics Symposium, 24-29 Jun, New York, NJ

Kim, J., Lee S., Moridis G.J., 2019, Advanced Simulation for Strongly Coupled Non-isothermal Flow and Geomechanics for the Gas Hydrate Deposits, SIAM Conference on Mathematical & Computational Issues in the Geosciences, Houston, TX, Mar. 11-14

Moridis, G.J., Reagan, M.T., Queiruga, A.F., Kim, S.J. 2019 System Response to Gas Production from a Heterogeneous Hydrate Accumulation at the UBGH2-6 Site in the Ulleung Basin of the Korean East Sea, *Journal of Petroleum Sciences and Engineering* 178: 655-665

Yoon, S., Kim, J., 2019, The Modeling of Fault Activation and Induced Seismicity by using CoupledFlow-geomechanics Simulation and its Field Application, SIAM Conference on Mathematical & Computational Issues in the Geosciences, Houston, TX, Mar. 11-14

Yoon, S., Kim, J., 2019, The fast marching method for simulation of coupled flow and geomechanics and fault activation, 53rd US Rock Mechanics/Geomechanics Symposium, 24-29 Jun, New York, NJ

Yoon, S., Lee, H., Kim, J., Shinn, Y.J., 2019, Numerical investigation on geomechanical responses of a pilot-scale CO<sub>2</sub> storage site, South Korea, 53rd US Rock Mechanics/Geomechanics Symposium, 24-29 Jun, New York, NJ

Yoon, H.C, Guo, X., Kim, J., Killough, J., 2019 Flexible and practical parallel implementation for coupled elastoplastic geomechanics and non-isothermal flow, *International Journal of Rock Mechanics and Mining Sciences* 120:96-107

## 2020

Yoon, H.C., Zhou, P. , Kim, J., 2020, Robust modeling of hysteretic capillary pressure and relative permeability for two phase flow in porous media, *Journal of Computational Physics*, Vol 402, 108915

Several papers will be submitted for publication.

## References

Adams, J.J., Akkutlu, I.Y., Moridis, G.J., 2019. Modeling of Hydrate Formation Hysteresis in Porous Media, SPE Europec featured at 81st EAGE Conference and Exhibition. Society of Petroleum Engineers, London, England, UK, pp. 20.

Azzi, A., et al., 2010, Gas–liquid two-phase flow division at a micro-T-junction, *Chemical Engineering Science* 65.13: 3986-3993.

Bagherzadeh, S. A., Moudrakovski, I. L., Ripmeester, J. A., & Englezos, P., 2011. Magnetic Resonance Imaging of Gas Hydrate Formation in a Bed of Silica Sand Particles. *Energy & Fuels*, 25(7), 3083-3092. doi:10.1021/ef200399a

Buchanan, P., Soper, A. K., Thompson, H., Westacott, R. E., Creek, J. L., Hobson, G., & Koh, C. A., 2005. Search for memory effects in methane hydrate: structure of water before hydrate formation and after hydrate decomposition. *The Journal of chemical physics*, 123(16), 164507.

Gupta, A., Lachance, J., Sloan, E. D., & Koh, C. A., 2008. Measurements of methane hydrate heat of dissociation using high pressure differential scanning calorimetry. *Chemical Engineering Science*, 63(24), 5848-5853. doi:<https://doi.org/10.1016/j.ces.2008.09.002>

Delli, M.L., and Grozic, J.L.H., 2014, Experimental determination of permeability of porous media in the presence of gas hydrates, *J. Petroleum Science and Engineering* 120: 1-9

Honarpour, M., Mahmood, S.M., 1988, Relative-permeability measurements: An overview, *Journal of petroleum technology* 40.08: 963-966.

Johnson, A., Patil, S., Dandekar, A., 2011, Experimental investigation of gas-water relative permeability for gas-hydrate-bearing sediments from the Mount Elbert Gas Hydrate Stratigraphic Test Well, Alaska North Slope, *Marine and Petroleum Geology* 28.2: 419-426.

KIGAM, 2007, *Studies on Gas Hydrate Development & Production Technology*, KIGAM Research Report, NP2007-018-2007(1), P. 677

KIGAM, 2011, *Studies on Gas Hydrate Development & Production Technology*, KIGAM Research Report, GP2010-016-2011(2), P.811

KIGAM, 2014, *Studies on Productivity for Test Production in 2014*, consulting report to KNOC,, IP2012-017-2014(1), P. 139

KIGAM, 2015, *Studies on Gas Hydrate Development & Production Technology*, KIGAM Research Report, GP2012-025-2015(4), P.860

Kim, B. Y., & Akkutlu, I. Y., 2017. A New Laboratory Setup for Phase Equilibria Studies of Methane Hydrate in Porous Media. Paper presented at the Advances in Laboratory Testing and Modelling of Soils and Shales.

Kim, J., 2018a, A new numerically stable sequential algorithm for coupled finite-strain elastoplastic geomechanics and flow, *Computer Methods in Applied Mechanics and Engineering*, 335: 538-562

Kim, J., 2018b, Unconditionally stable sequential schemes for all-way coupled thermoporoelasticity: Undrained-adiabatic and extended fixed-stress splits, *Computer Methods in Applied Mechanics and Engineering*, 341:93-112

Kim, J., Lee, J.Y., 2019, Wellbore stability and possible geomechanical failure in the vicinity of the well during pressurization at the gas hydrate deposit in the Ulleung Basin, 53rd US Rock Mechanics /Geomechanics Symposium, 24-29 Jun, New York, NJ

Kim, J., Moridis, G. J., 2012, Modeling and numerical simulation for coupled flow and geomechanics in composite gas hydrate deposits, 46th U.S. Rock Mechanics/Geomechanics Symposium, Chicago, IL, 24-27 Jun.

Kim, J., Moridis, G.J., Rutqvist, J., 2012, Coupled flow and geomechanical analyses for gas production in the PBU-L 106 C hydrate deposit in Alaska, *Journal of Petroleum Science and Engineering*, 92-93: 143-157

Kim, J., Moridis, G.J., Yang, D., Rutqvist, J., 2012, Numerical studies on two-way coupled flow and geomechanics in hydrate deposits, *SPE Journal*, 17(2):485-501

Kim, J.-T., Kim, A.-R., Cho, G.-C., Kang, C.-W., Lee, J.Y., 2019, The effects of coupling stiffness and slippage of interface between the wellbore and unconsolidated sediment on the stability analysis of the wellbore under gas hydrate production, *Energies* 2019, 12, 4177

Kneafsey, T.J. et al., 2007. Methane Hydrate Formation and Dissociation in a Core-Scale Partially Saturated Sand Sample. *Journal of Petroleum Science and Engineering*, 56: 108-126.

Kneafsey, T.J., et. al., 2010, Permeability of laboratory-formed methane-hydrate-bearing sand: measurements and observations using X-ray computed tomography.

Lee, J. D., Susilo, R., Englezos, P., 2005. Kinetics of structure H gas hydrate. *Energy & Fuels*, 19(3), 1008-1015.

Lei, L., Seol, Y., Choi, J.-H., Kneafsey, T.J., 2019. Pore habit of methane hydrate and its evolution in sediment matrix – Laboratory visualization with phase-contrast micro-CT. *Marine and Petroleum Geology*, 104: 451-467.

Lekvam, K., Ruoff, P., 1997 Kinetics and mechanism of methane hydrate formation and decomposition in liquid water. Description of hysteresis. *Journal of Crystal Growth*, 179(3), 618-624. doi:[https://doi.org/10.1016/S0022-0248\(97\)00166-8](https://doi.org/10.1016/S0022-0248(97)00166-8)

Li, G., Moridis, G.J., Zhang, K. Li, X.-S., 2010. Evaluation of Gas Production Potential from Marine Gas Hydrate Deposits in Shenhu Area of South China Sea. *Energy & Fuels*, 24(11): 6018-6033.

Linga, P., Haligva, C., Nam, S. C., Ripmeester, J. A., Englezos, P., 2009. Gas Hydrate Formation in a Variable Volume Bed of Silica Sand Particles. *Energy & Fuels*, 23(11), 5496-5507. doi:10.1021/ef900542m

Max, M.D., 2003, ed. *Natural Gas Hydrate in Oceanic and Permafrost Environments*. Vol. 5, Springer Science & Business Media.

McGuire, P. L., 1981 Methane hydrate gas production: evaluating and exploiting the solid gas resource.

Moridis, G. J., Collett, T. S., Boswell, R., Kurihara, M., Reagan, M. T., Koh, C., & Sloan, E. D., 2009 Toward Production From Gas Hydrates: Current Status, Assessment of Resources, and Simulation-Based Evaluation of Technology and Potential. *SPE Reservoir Evaluation & Engineering*, 12(05), 745-771. doi:10.2118/114163-PA

Moridis, G., Kowalsky, M.B. and Pruess, K., 2007. Depressurization-Induced Gas Production From Class 1 Hydrate Deposits. *SPE Reservoir Evaluation & Engineering*, 10(5): 458-481.

Moridis, G.J., Queiruga, A.F. and Reagan, M.T., 2017. The T+H+M Code for the Analysis of Coupled Flow, Thermal, Chemical and Geomechanical Processes in Hydrate-Bearing Geologic Media, 9th Int. Conference on Gas Hydrates, Denver, CO, USA.

Moridis, G.J. and Reagan, M.T., 2007a. Gas Production From Oceanic Class 2 Hydrate Accumulations, Offshore Technology Conference. Offshore Technology Conference, Houston, Texas, U.S.A., pp. 33.

Moridis, G.J. Reagan, M.T., 2007b. Strategies for Gas Production From Oceanic Class 3 Hydrate Accumulations, Offshore Technology Conference. Offshore Technology Conference, Houston, Texas, U.S.A., pp. 29.

- Moridis, G.J. Reagan, M.T., 2011a. Estimating the upper limit of gas production from Class 2 hydrate accumulations in the permafrost: 1. Concepts, system description, and the production base case. *JPSE*, 76(3): 194-204.
- Moridis, G.J. Reagan, M.T., 2011b. Estimating the upper limit of gas production from Class 2 hydrate accumulations in the permafrost: 2. Alternative well designs and sensitivity analysis. *JPSE*, 76(3): 124-137.
- Moridis, G.J., Reagan, M.T., Boyle, K.L. and Zhang, K., 2011a. Evaluation of the Gas Production Potential of Some Particularly Challenging Types of Oceanic Hydrate Deposits. *Transport in Porous Media*, 90(1): 269-299.
- Moridis, G.J., Reagan, M.T., Queiruga, A.F., Kim, S.J. 2019 System Response to Gas Production from a Heterogeneous Hydrate Accumulation at the UBGH2-6 Site in the Ulleung Basin of the Korean East Sea, *Journal of Petroleum Sciences and Engineering* 178: 655-665
- Moridis, G.J., Seol, Y., Kneafsey, T., 2005. Studies of reaction kinetics of the methane hydration reaction in porous media, Fifth International Conference on Gas Hydrates, Trondheim, Norway.
- Moridis, G.J., Silpngarmert, S., Reagan, M.T., Collett, T., Zhang, K., 2011b. Gas production from a cold, stratigraphically-bounded gas hydrate deposit at the Mount Elbert Gas Hydrate Stratigraphic Test Well, Alaska North Slope: Implications of uncertainties. *Marine and Petroleum Geology*, 28(2): 517-534.
- Moridis, G.J., Sloan, E.D., 2007. Gas production potential of disperse low-saturation hydrate accumulations in oceanic sediments. *Energy Conversion and Management*, 48(6): 1834-1849.
- Naar, J., Wygal, R.J., Henderson, J.H., 1962, Imbibition relative permeability in unconsolidated porous media, *Society of Petroleum Engineers Journal* 2.01: 13-17.
- Nuth, M., Laloui, L., 2008 Advances in modeling hysteretic water retention curve in deformable soils, *Computers and Geotechnics* 35:835–844.
- Ohmura, R., Ogawa, M., Yasuoka, K., & Mori, Y. H., 2003. Statistical study of clathrate-hydrate nucleation in a water/hydrochlorofluorocarbon system: Search for the nature of the “memory effect”. *The Journal of Physical Chemistry B*, 107(22), 5289-5293.
- Oyama, H., Konno, Y., Masuda, Y., & Narita, H., 2009. Dependence of Depressurization-Induced Dissociation of Methane Hydrate Bearing Laboratory Cores on Heat Transfer. *Energy & Fuels*, 23(10), 4995-5002. doi:10.1021/ef900179y
- Pini, R., Benson, S.M., 2013, Simultaneous determination of capillary pressure and relative permeability curves from core-flooding experiments with various fluid pairs, *Water Resources Research* 49.6: 3516-3530.
- Pruess, K., Oldenburg, C., Moridis, G.J., 1999 TOUGH2 User’s Guide, Version 2.0. Report LBNL-43134, Lawrence Berkeley National Laboratory, CA.
- Rees, E. V., Kneafsey, T. J., Seol, Y., 2011 Methane hydrate distribution from prolonged and repeated formation in natural and compacted sand samples: X-ray CT observations. *Journal of Geological Research*, 2011.

- Rodger, P. M., 2000 Methane hydrate: melting and memory. *Annals of the New York Academy of Sciences*, 912(1), 474-482.
- Seol, Y., Myshakin, E., 2011 Experimental and Numerical Observations of Hydrate Reformation during Depressurization in a Core-Scale Reactor. *Energy & Fuels*, 25(3), 1099-1110. doi:10.1021/ef1014567
- Seol, Y., Kneafsey, T.J., 2011, Methane hydrate induced permeability modification for multiphase flow in unsaturated porous media, *Journal of Geophysical Research: Solid Earth* 116.B8.
- Simo, J.C., Hughes, T.J.R., 1998, *Computational Inelasticity*, Springer, Heidelberg.
- Yamamoto, K., Terao, Y., Fujii, T., Ikawa, T., Seki, M., Matsuzawa, M., Kanno, T., 2014 Operational overview of the first offshore production test of methane hydrates in the Eastern Nankai Trough. Paper presented at the Offshore Technology Conference, Houston, Texas. <https://doi.org/10.4043/25243-MS>
- Yoon, H.C, Guo, X., Kim, J., Killough, J., 2019 Flexible and practical parallel implementation for coupled elastoplastic geomechanics and non-isothermal flow, *International Journal of Rock Mechanics and Mining Sciences* 120:96-107
- Yoon, H.C., Kim, J., 2018, Spatial stability for the monolithic and sequential methods with various space discretizations in poroelasticity, *International Journal for Numerical Methods in Engineering*, 114:694-718
- Yoon, H.C., Zhou, P. , Kim, J., 2019, Robust modeling of hysteretic capillary pressure and relative permeability for two phase flow in porous media, *Journal of Computational Physics*, Vol 402, 108915
- Zhang, K. and Moridis, G.J., 2008. A Domain Decomposition Approach for Large-Scale Simulations of Coupled Processes in Hydrate-Bearing Geologic Media, 6th International Conference on Gas Hydrates, Vancouver, British Columbia, Canada.